LIÈGE université
Sciences Appliquées

ÉCOLE NATIONALE DES PONTS ET CHAUSSÉES

INSTITUT POLYTECHNIQUE DE PARIS

Effect of pore water chemistry on the hydro-mechanical behavior of poorly indurated Boom Clay (C-H-M coupling)

A thesis submitted in partial fulfillment of the requirements
for the degree of Doctor of Philosophy (PhD) in Engineering Science and Ecole doctorale N°531 – SIE
(Sciences, Ingénierie et Environment)

Presented by

Hassan AL MAIS

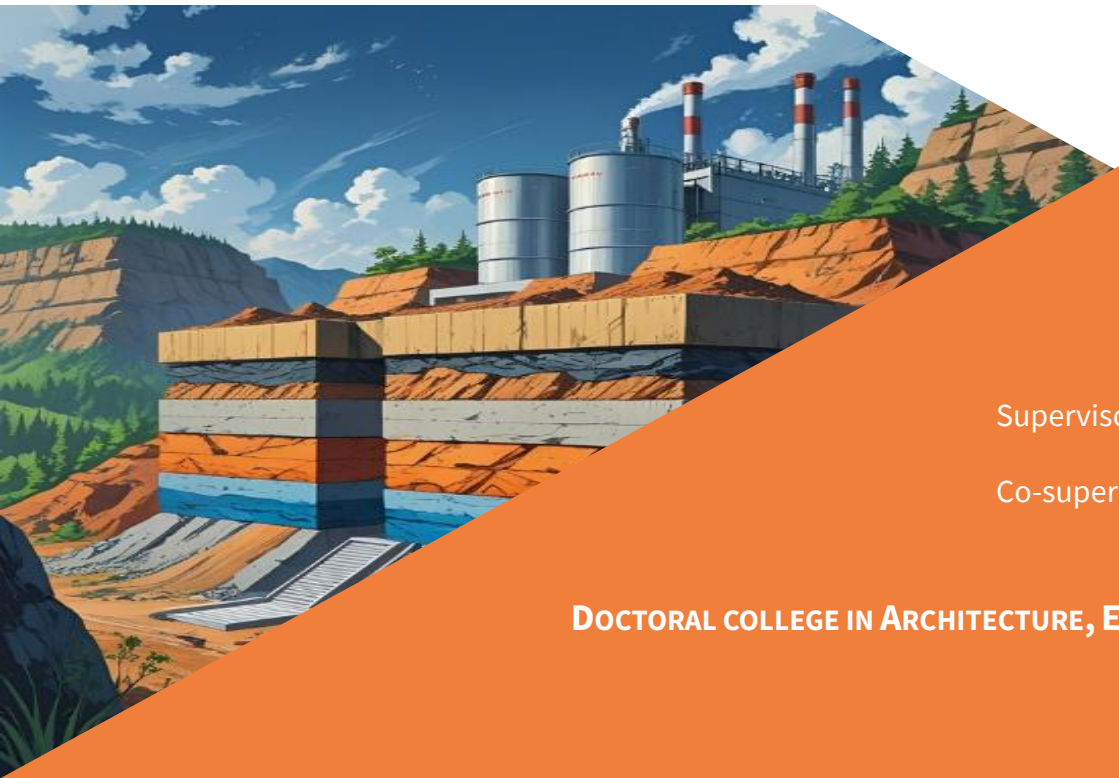

Supervisor: Frédéric COLLIN

Co-supervisor: Yu-Jun CUI

DOCTORAL COLLEGE IN ARCHITECTURE, ENGINEERING AND GEOLOGY

JUNE 2025

University of Liège

Faculty of Applied Sciences

Urban & Environmental Engineering

École nationale des ponts et chaussées

Géotechnique

Laboratoire NAVIER/CERMES

Effect of pore water chemistry on the hydro-mechanical behavior of poorly indurated Boom Clay (C-H-M coupling)

Thesis submitted in partial fulfilment of the requirements

for the degree of Philosophy Doctor (Ph.D.) in Applied Sciences and Ecole doctorale N°531 – SIE (Sciences, Ingénierie et Environment)

Presented by

Hassan AL MAIS

June 2025

Funding:

This research work was conducted in the framework of a public-public collaboration between SCK CEN, ONDRAF/NIRAS and EURIDICE, and was funded by the Belgian Nuclear Research Center (SCK CEN) in partnership with Liège University and École Nationale des Ponts et Chaussées.

Composition of the Jury:

Prof. Frédéric COLLIN	Director	Université de Liège
Prof. Yu-Jun CUI	Co-Director	École nationale des ponts et chaussées
Prof. Olivier CUISINIER	Reporter	Université de Lorraine
Prof. Jian-Fu SHAO	Reporter	Université de Lille
Prof. Anne-Cathérine DIEUDONNÉ	Examinator	TU Delft
Prof. Bertrand FRANÇOIS	Examinator	Université de Liège
Dr. Séverine LEVASSEUR	Examinator	ONDRAF/NIRAS
Dr. Elie VALCKE	Examinator	SCK CEN
Dr. Temenuga GEORGIEVA	Invited (Mentor)	EURIDICE
Dr. Suresh SEETHARAM	Invited (Co-Mentor)	SCK CEN

Acknowledgments

August 2019, a freshly graduated civil engineer with dreams of building a better future. That dream took shape when he applied for a Master's program in Rock and Soil Mechanics in France. A few months later, he received an acceptance from CentraleSupélec and École des Ponts et Chaussées—an opportunity that would change his life. Leaving everything behind, he embarked on a new journey, unaware of how challenging, yet transformative, it would be.

Arrived in Paris in 2020, in the midst of the COVID-19 pandemic. Social contact was limited, and adapting to life in a $9m^2$ student room, far from everything familiar, was difficult. Classes were online, interactions were distant, and the sense of isolation was overwhelming. But persistence paid off. He completed his Master's degree and secured an internship at the Navier Laboratory at École des Ponts, which marked a true turning point in his academic and personal path.

Four years later, through many ups and downs, he is proud to have fulfilled his dream of earning a PhD in the field he deeply loves. This achievement, however, would not have been possible without the unwavering support of many incredible people. I hope I will not forget anyone, and if I do, I ask for your forgiveness.

First and foremost, I would like to thank **Yu-Jun**, for believing in me and giving me this opportunity. I know there may have been doubts at the beginning, but I was determined to turn those doubts into trust. Our discussions and meetings laid the foundation of the geomechanics knowledge I hold today. My deepest gratitude also goes to the entire geotechnical team at **CERMES**, my second home. Thank you to the technical staff for your help and for all the moments we shared in the laboratory.

I would also like to express my sincere thanks to **Frédéric**, whom I respectfully call the "LAGAMINE Hero." You introduced me to a new way of thinking and helped me understand numerical modeling and finite element analysis. Although it was unfamiliar at first, and "the magical mystery" of LAGAMINE was not easy to master, you made it accessible and enriching. Thanks also to all my colleagues in **Liège**—thank you for the coffee breaks, tarte au riz, and all the great times we had together.

This PhD would not have been possible without the support of **SCK CEN** and the kind team that was always available to help. Special thanks to **Elie** and **Suresh** for your constant guidance.

One of the most enriching parts of this journey was working with the team at **EURIDICE**. I sincerely thank all the colleagues and the technical team for their support and collaboration. A special thanks to **Temenuga** for her encouragement and helpful discussions. It was truly a pleasure to work with all of you. A special mention to **Arnaud**, who made every trip to Mol easier and more enjoyable with his kindness and support.

From **ONDRAF/NIRAS**, I sincerely thank **Séverine** for her help and kindness. Your support and words will never be forgotten.

Finally, my deepest gratitude goes to my family in Lebanon—especially my parents and my sisters. **Baba** and **Mama**, thank you for your sacrifices, your faith in me, and your unwavering presence. This work is dedicated to you. None of this would have been possible without your love and support.

And last but not least, research often leads to unexpected discoveries—not just in science, but in life. To you**, *Souad***, you have been my most precious discovery. Your heart is pure, and your presence has been a gift. Thank you for being here. Thank you for being you.

Hassan

June 2025

Abstract

Deep geological disposal is one of the technological options for the long-term management of radioactive waste by isolating harmful radionuclides from the biosphere through a system of engineered and geological barriers. In Belgium, Boom Clay is considered a reference host formation due to its low permeability, high retention capacity, self-sealing behavior, and favorable mechanical properties. Among the waste forms intended for disposal, Eurobitum waste, produced by bituminization of reprocessing effluents, contains high concentrations of $(Na,Ca)NO_3$. Under repository conditions, the bitumen matrix gradually absorbs water and swells, resulting in the progressive release of the embedded salts that diffuse into the surrounding clay formation. This hypersaline plume induces chemical perturbations that can affect the hydro-mechanical behavior of Boom Clay by altering its microstructure, swelling capacity, and strength.

This thesis presents an investigation of the influence of salinity (Ionic Strengths: 0.015 M, 1.0 M, and 2.0 M) and sodium occupancy (60% and 90%) on the hydro-mechanical behavior of Boom Clay by combining a dedicated experimental campaign with the development of a chemo-mechanical constitutive modeling approach. The experimental program includes swelling pressure measurements under constant-volume conditions, salinization and desalinization tests under oedometric conditions, high-pressure oedometric tests, undrained shear strength tests, and microstructural analyses using mercury intrusion porosimetry. The results demonstrate that increasing salinity leads to a reduction in swelling pressure, an increase in shear strength, and modifications of the aggregate structure, especially at high ionic strengths, which also result in increased hydraulic conductivity. While the observed effects of ionic strength are qualitatively consistent with findings reported for other clay materials, the study provides new insights into the role of sodium occupancy—particularly its potential influence on interlayer spacing—in shaping the chemo-hydro-mechanical response of Boom Clay.

To interpret and predict these coupled effects, a chemo-mechanical constitutive model named ACC2-Chem was developed. The starting point was the ACC-2 elasto-plastic model, initially formulated under in-situ pore water conditions (Ionic Strength = 0.015 M), by introducing a cohesion parameter into both the yield surface and the plastic flow rule to better represent the mechanical response of Boom Clay. In parallel, a new chemo-elastic volumetric strain model was developed to describe the elastic deformations induced by changes in ionic strength and sodium occupancy. This chemo-elastic model was then coupled with ACC-2, resulting in the integrated ACC2-Chem model that captures the chemo-hydro-mechanical interactions in Boom Clay. The model was implemented in the finite element code LAGAMINE and calibrated using set of laboratory data. Its validity was verified by reproducing the main trends observed in salinization/desalinization and triaxial tests at the laboratory scale.

Finally, 2D repository-scale simulations were conducted to evaluate the long-term chemo-hydro-mechanical behavior of Boom Clay under high salinity perturbations using a decoupled approach. The simulations capture the phenomenological evolution of the repository through four sequential phases: (1) an initial excavation phase lasting one day, (2) a 100-year operational phase under drained conditions, (3) a 300-year post-operational equilibrium phase, and (4) a 500-year swelling and/or diffusion phase simulating long-term interactions between Eurobitum waste and Boom Clay.

The above findings have contributed to the current understanding of the behavior of Boom Clay under short term exposure to chemically perturbed environments, and has provided theoretical underpinning for a mathematical framework that may support safety and performance assessments for the geological disposal of bituminized radioactive waste in Belgium.

Keywords: Radioactive waste disposal, Boom Clay, Ionic strength, Sodium occupancy, Swelling pressure, microstructure, shear strength, C-H-M coupling, numerical modelling.

Résumé

Le stockage géologique profond constitue l'une des options technologiques pour la gestion à long terme des déchets radioactifs, en isolant les radionucléides dangereux de la biosphère grâce à un système de barrières à la fois géologiques et artificielles. En Belgique, l'argile de Boom est considérée comme formation hôte de référence en raison de sa faible perméabilité, de sa capacité élevée de rétention, son propriété d'auto-colmatage et de ses propriétés mécaniques favorables. Parmi les formes de déchets destinées au stockage, les déchets Eurobitum, issus de la bitumisation des effluents de retraitement, contiennent de fortes concentrations de $(Na,Ca)NO_3$. En conditions de stockage, la matrice bitumineuse absorbe progressivement l'eau et gonfle, entraînant la libération progressive des sels piégés, qui diffusent dans la formation argileuse environnante. Ce panache hypersalé provoque des perturbations chimiques susceptibles d'affecter le comportement hydro-mécanique de l'argile de Boom en modifiant sa microstructure, sa capacité de gonflement et sa résistance.

Cette thèse présente une étude de l'influence de la salinité (forces ioniques : 0.015 M, 1.0 M et 2.0 M) et de l'occupation sodique (60 % et 90 %) sur le comportement hydro-mécanique de l'argile de Boom, en combinant une campagne expérimentale dédiée avec le développement d'une approche de modélisation constitutive chimio-mécanique. Le programme expérimental comprend des mesures de pression de gonflement en conditions de volume constant, des tests de salinisation et de désalinisation en œdomètre, des essais œdométriques sous haute pression, des essais de résistance au cisaillement non drainés, ainsi que des analyses microstructurales par intrusion de mercure. Les résultats montrent qu'une augmentation de la salinité entraîne une réduction de la pression de gonflement, une augmentation de la résistance au cisaillement, ainsi que des modifications de la structure des agrégats, en particulier à fortes forces ioniques, ce qui se traduit également par une augmentation de la conductivité hydraulique. Bien que les effets de la salinité observés soient qualitativement cohérents avec ceux rapportés pour d'autres matériaux argileux, l'étude apporte de nouvelles connaissances sur le rôle de l'occupation sodique, notamment son influence potentielle sur l'espacement interfoliaire, dans le comportement chimio-hydro-mécanique de l'argile de Boom.

Pour interpréter et prédire ces effets couplés, un modèle constitutif chimio-mécanique nommé ACC2-Chem a été développé. Le point de départ a été le modèle élasto-plastique ACC-2, initialement formulé sous les conditions de l'eau interstitielle in situ (force ionique = 0,015 M), par l'introduction d'un paramètre de cohésion dans la surface de rupture et la règle d'écoulement plastique afin de mieux représenter la réponse mécanique de l'argile de Boom. Parallèlement, un nouveau modèle chimio-élastique de déformation volumique a été développé pour décrire les déformations élastiques induites par les variations de salinité et d'occupation sodique. Ce modèle a ensuite été couplé avec ACC-2 pour former le modèle ACC2-Chem, capable de représenter les interactions chimio-hydro-mécaniques de l'argile de Boom. Ce modèle a été implémenté dans le code éléments finis LAGAMINE et calibré à partir d'un ensemble de données expérimentales. Sa validité a été vérifiée par la reproduction des principales tendances observées lors des essais de salinisation/désalinisation et des essais triaxiaux à l'échelle du laboratoire.

Enfin, des simulations 2D à l'échelle du stockage ont été réalisées afin d'évaluer le comportement chimio-hydro-mécanique de l'argile de Boom à long terme sous des perturbations salines

importantes, en utilisant une approche découplée. Les simulations décrivent l'évolution phénoménologique du stockage à travers quatre phases successives : (1) une phase initiale d'excavation d'un jour, (2) une phase opérationnelle de 100 ans en conditions drainées, (3) une phase post-opérationnelle de 300 ans en équilibre, et (4) une phase de gonflement et/ou de diffusion de 500 ans, simulant les interactions à long terme entre les déchets Eurobitum et l'argile de Boom.

Les résultats obtenus ont permis d'améliorer la compréhension du comportement de l'argile de Boom soumis à des perturbations chimiques à court terme, tout en apportant un cadre théorique utile aux évaluations de sûreté et de performance du stockage géologique des déchets radioactifs bituminés en Belgique.

Mots-clés : Stockage géologique, Argile de Boom, Force ionique, Occupation de sodium, Pression de gonflement, Microstructure, Résistance au cisaillement, couplage C-H-M, Modélisation numérique.

Preface

The research presented in this thesis has been partially published in peer-reviewed scientific journals or is currently under review. It has also been the subject of several presentations at international conferences and seminars. The dissemination activities are grouped below according to the two main components of the work: the experimental program and the numerical modeling.

Experimental Work

• *Articles*

[AL Mais et al., 2024] *Effect of sodium occupancy and solute concentration on the swelling pressure and hydraulic conductivity of Boom Clay*. *Canadian Geotechnical Journal*, 2024.

[AL Mais et al., 2025a] *Effects of cyclic infiltration of (Na,Ca)NO_3 solutions on the volume change behavior and microstructure of Boom Clay*. *Journal of Rock Mechanics and Geotechnical Engineering*, 2025a (under revision).

[AL Mais et al., 2025b] *Effect of sodium occupancy and solute concentration on the deviatoric behavior of Boom Clay*. *Canadian Geotechnical Journal*, 2025b (under revision).

• *Conference Posters*

Effect of sodium occupancy and solute concentration on the swelling pressure and hydraulic conductivity of Boom Clay. Clay Conference 2024, Hannover (Germany), 25–28 November 2024.

Numerical Work

• *Conference Presentation*

Effect of pore water chemistry on the hydro-mechanical behavior of poorly indurated Boom Clay: 2D plane strain modelling. 3rd International Conference on Energy Geotechnics, Paris (France), 17–20 June 2025.

Table of Contents

I. Introduction

1. Management of Nuclear Energy

Nuclear power, first introduced in the 1950s, has evolved to become a crucial energy source, particularly for large-scale electricity production (IAEA, 2021). Modern nuclear reactors predominantly rely on Uranium-235 as fuel. The process begins with nuclear fission, where the nucleus of a Uranium-235 atom is struck by a neutron, causing it to split into smaller nuclei while releasing additional neutrons. These newly released neutrons further instigate the fission of surrounding Uranium atoms, resulting in a self-perpetuating chain reaction (IAEA, 2021). This chain reaction releases an immense amount of energy in the form of heat, which is subsequently used to generate steam that drives turbines and ultimately produces electricity. Nuclear power remains a cornerstone of the global energy landscape, contributing significantly to electricity production (Galindo, 2022).

Despite the proven advantages of nuclear energy for societal progress, it is still one of the most contentious methods of generating electricity. The primary concern revolves around the substantial risk of radioactive contamination, which could have far-reaching, potentially catastrophic global effects in the event of a major radionuclide leak from nuclear facilities. Over the past three decades, two high-profile nuclear disasters have deeply influenced public perception of nuclear energy, leaving an enduring skepticism about its safety. Although the likelihood of such an incident occurring is relatively low, the consequences of a significant nuclear accident at any currently operational reactor would be profound, with the potential to affect vast areas, exposing millions of individuals to radiation, and inflicting severe environmental and socio-economic damage both regionally and globally (Lelieveld et al., 2012).

Over time, safety measures in nuclear operations have greatly improved, thanks to the accumulation of operational experience. This has led to the integration of advanced physical safety barriers and provisions designed to enhance the protection of both people and the environment (Högberg, 2013; Levasseur et al., 2022). While these advancements have contributed to a reduction in accident risks, the ongoing challenge

of managing nuclear waste remains one of the most pressing issues facing the nuclear industry.

The classification of radioactive waste varies by country and the specific type of waste produced. The IAEA reference system (Gera, 1974) outlines six main categories based on the radioactivity levels:

- **Exempt Waste (EW)** contains radionuclides at levels nearly identical to natural background radiation, allowing it to be removed from regulatory control without radiation protection measures.
- **Very Short-Lived Waste (VSLW)** includes only radionuclides with very short half-lives, which can be stored temporarily on-site before being disposed of as regular waste.
- **Very Low-Level Waste (VLLW)** consists of materials with low radioactivity that are not harmful to the biosphere and do not require extensive containment or isolation.
- **Low-Level Waste (LLW – Category A)** encompasses a wide range of materials, from small amounts of short-lived radionuclides at higher activity levels to long-lived radionuclides at lower activity levels, all requiring substantial containment for several hundred years.
- **Intermediate-Level Waste (ILW – Category B)** consists of materials with longer-lived radionuclides that need significant isolation and containment for periods extending beyond several hundred years, but without the need for heat dissipation.
- **High-Level Waste (HLW – Category C)** contains the most dangerous materials, with large quantities of long-lived radionuclides and high activity levels that produce considerable heat, requiring immediate cooling and shielding for storage lasting tens of thousands of years.

The ILW/HLW, the most hazardous type, remains dangerous for up to one hundred thousand years, posing significant challenges for its long-term, secure disposal and storage (Horvath and Rachlew, 2016).

For centuries, the common approach to disposing of hazardous solid materials that could not be incinerated involved rapid burial at shallow depths (MacKenzie, 1995). The nuclear industry has since advanced this practice by developing the concept of geological disposal, a method specifically designed to meet rigorous performance standards for the long-term containment of radioactive waste.

In China, the site selection process for a nuclear waste repository began in 1986 under the leadership of the China National Nuclear Corporation (CNNC). Three candidate sites were identified in the Beishan region of Gansu Province, located in the northwest. In 2016, the Xinchang site, situated centrally within the Beishan area, was chosen for the construction of an underground research laboratory (URL), which is currently underway (Wang et al., 2018). This site is intended to serve as the future location of the national repository.

In Japan, the Nuclear Waste Management Organization (NUMO) has managed the site selection process since 2000 (Hara and Yabar, 2012). Following the 2011 Tōhoku earthquake and the Fukushima-Daiichi nuclear disaster, the national government adopted a more proactive role. NUMO is expected to finalize the selection by 2025 and to initiate repository operations by 2035.

In Sweden, the site selection process began in the early 1990s and has been managed by the Swedish Nuclear Fuel and Waste Management Company (SKB) (Arentsen and Van Est, 2023). SKB works in collaboration with Posiva in Finland and with other organizations, including Canada's Nuclear Waste Management Organization (NWMO), as part of a joint research and development initiative aimed at improving nuclear waste management strategies.

In Hungary, the PURAM Waste Management Agency is responsible for managing the site selection process, with completion targeted for 2030 (Vari and Ferencz, 2012).

In Switzerland, the site selection process was initiated in 2008 under the supervision of the Swiss Federal Office of Energy. After 14 years of investigation, the Nördlich Lägern site in the north of the country was selected as the repository location (Schneider and Zuidema, 2011).

In Germany, the legal framework for site selection was established in 2013, with the formal search beginning in 2017. The Federal Company for Radioactive Waste

Disposal (BGE) oversees this process, which is projected to conclude by 2031 (Kurgyis et al., 2024).

In France, the French National Radioactive Waste Management Agency (Andra) began site investigations in 2007 and later selected the Cigéo site near Bure, in the Champagne-Ardenne region. A construction permit for the facility was submitted in 2019, and construction was scheduled to begin in 2022 (Leverd, 2023).

In line with the international recommendations for the safe management of radioactive waste, the geological disposal program in Belgium began in the 1970s with investigations into Boom Clay as a potential host formation. Over several decades, extensive research was conducted to characterize this clay and develop relevant disposal concepts, as detailed by Li et al. (2023) in the history of the HADES underground research laboratory and the Belgian disposal concept. Despite this long-standing effort, formal authorization was only granted in 2014 for ONDRAF/NIRAS—the Belgian Agency for the Management of Radioactive Waste and Enriched Fissile Materials—to propose a national policy for the long-term management of category B and C waste (long-lived low- and intermediate-level waste and high-level waste). In 2022, a royal decree was issued to designate geological disposal as the reference solution.

At present, a Belgian geological disposal facility (GDF) remains an option under consideration rather than a confirmed plan. No specific site or host formation has been selected, and according to the Federal Agency for Nuclear Control (FANC), all potential host formations must remain open for consideration. Nevertheless, ONDRAF/NIRAS continues to develop a generic repository concept involving disposal in poorly indurated clays, either Boom Clay or Ypresian clays, at a reference depth of approximately 400 meters. The objective is to evaluate the technical feasibility of designing, constructing, and operating a GDF that ensures long-term containment and environmental safety. The reference concept is based on a multi-barrier system intended to provide full containment during the thermal phase of high-level waste and spent fuel, while avoiding significant disturbance to the host formation. This concept forms the basis for the recommended strategy in Belgium for the long-term management of category B and C radioactive waste in a single national facility.

A key component of this program is the **HADES Underground Research Laboratory (URL)**, located in the municipality of **Mol**, within the Boom Clay Formation at a depth of approximately 225 meters (ONDRAF/NIRAS, 2020; Van Geet et al., 2023; Li et al., 2023). Initially constructed in the 1980s and later integrated into the national research framework, HADES serves as an essential experimental facility for studying geological disposal in clay. The laboratory has enabled long-term in situ testing of both natural and engineered barrier systems, as well as evaluations of excavation techniques, gallery stability, waste–clay interactions, and THMC (thermo-hydro-mechanical-chemical) processes under repository-relevant conditions (Van Geet et al., 2023; Li et al., 2023).

HADES URL has also contributed to the development of the Belgian disposal concept, by providing reliable data on the behavior of the Boom Clay host formation and the performance of various barrier materials over extended periods. This facility continues to play a central role in both national and international collaborative research efforts related to radioactive waste management (see Figure 1).

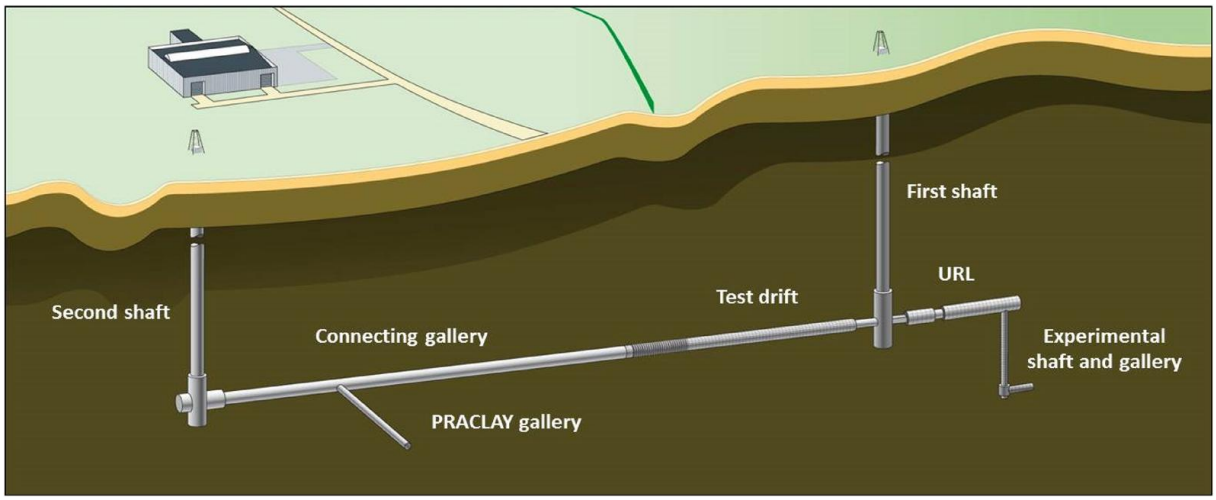

Figure 1 Photograph of the HADES Underground Research Laboratory in Mol, Belgium, illustrating its location within the Boom Clay formation and infrastructure used for in situ experiments (ONDRAF/NIRAS, 2013).

The current Belgian concept for geological disposal distinguishes between two waste categories: **category B** (long-lived intermediate-level waste) and **category C** (high-level heat-emitting waste). For category B waste, which contains long-lived radionuclides posing a radiological risk over timescales ranging from several tens to hundreds of millennia, disposal is planned using Monoliths B. These are large concrete containment structures in which waste drums are immobilized in mortar

(ONDRAF/NIRAS, 2020). Multiple monolith designs exist to accommodate the diversity of primary waste packages, and a single monolith may host waste from different families. Figure 2 shows two representative designs of Monoliths B: one for 200-liter drums and another for compacted waste (ONDRAF/NIRAS, 2013). These monoliths are intended to be emplaced in concrete-lined, horizontal disposal galleries excavated at mid-depth within the host formation. In the Belgian context, Boom Clay—a plastic clay formation—has been extensively studied over several decades as the reference host formation. To manage thermal and mechanical constraints as well as facilitate operational logistics, the disposal galleries for category B waste would be spaced 50 m apart (see Figure 3). All voids within and around the monoliths would be backfilled with cement-based materials. Over time, the facility would saturate with pore water, generating a highly alkaline (pH ≥ 12.5) and reducing environment. This is driven by the presence of cementitious materials and the gradual depletion of oxygen—conditions that are favorable for long-term containment and delay of radionuclide migration.

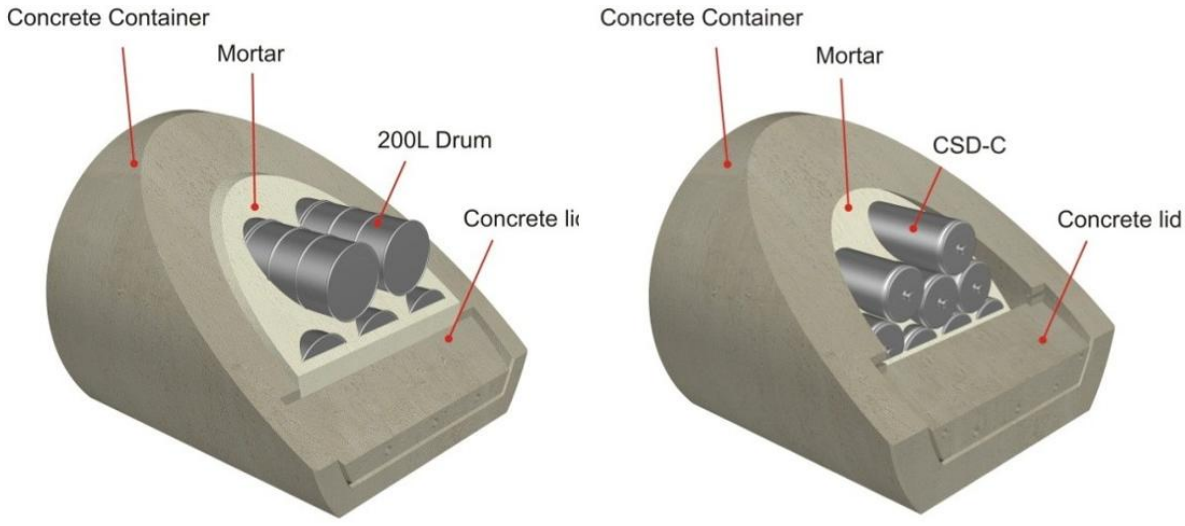

Figure 2 Two Designs of Monoliths for Category B Waste — Left: 200 L Drums; Right: Compacted Waste (ONDRAF/NIRAS, 2013).

For category C waste, ONDRAF/NIRAS has developed the **Supercontainer** concept. Each Supercontainer consists of a stainless steel canister containing high-level waste (HLW) or spent fuel, enclosed within a 3 cm thick carbon steel overpack that is embedded in a thick concrete buffer that on its turn is enclosed in a corrosion-resistant stainless steel envelope. This configuration provides a robust multi-barrier system that protects against mechanical stress, corrosion, and radionuclide release (see Figure 3).

These Supercontainers are intended to be emplaced horizontally in dedicated **C-zone concrete-lined disposal galleries in the host formation** (see Figure 3). The galleries are designed with an inner diameter of approximately **3.5 m** to accommodate the Supercontainers. Along each gallery axis, the containers are spaced **10 cm** apart, while the separation between adjacent galleries for category C waste is set at **120 m** to manage thermal loads and ensure long-term safety (ONDRAF/NIRAS, 2013).

Figure 3 provides a schematic overview of the Belgian deep geological repository concept, illustrating the main components of the Engineered Barrier System (EBS) for high-level waste (HLW). The figure also indicates the galleries designed for the disposal of category B waste in dedicated galleries.

This multi-barrier system, combined with the favorable properties of the reference host formation, is designed to ensure containment, delay radionuclide transport, and provide passive safety over geological timescales. Ongoing research continues to refine knowledge on barrier materials as input to performance assessments and support the long-term safety case (ONDRAF/NIRAS, 2020).

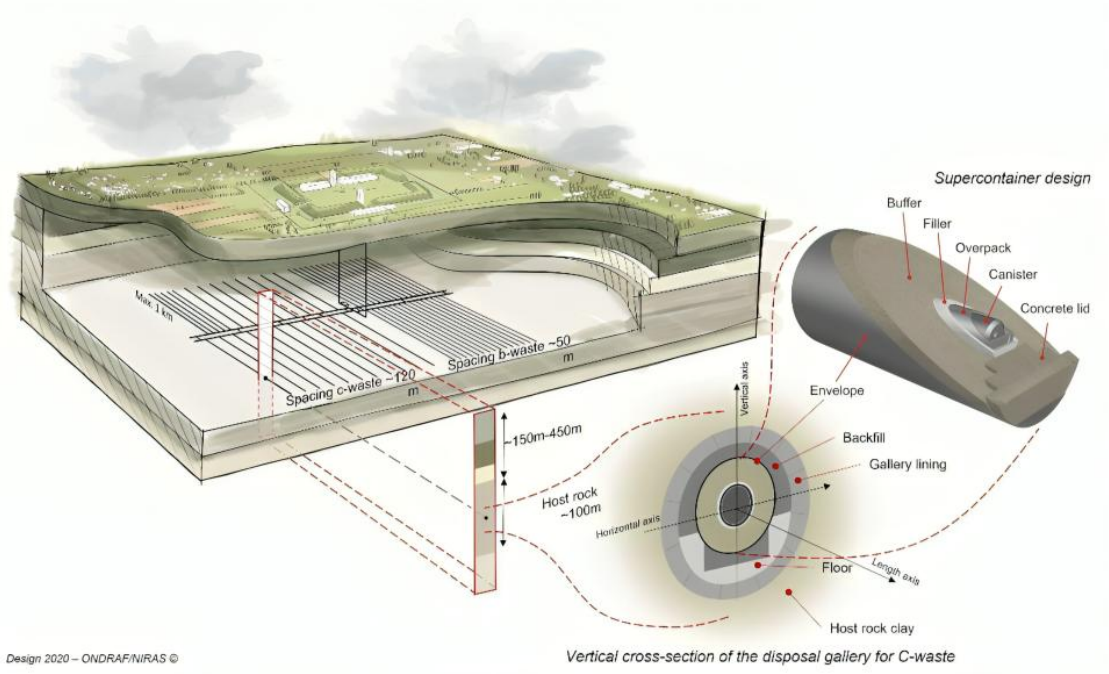

Figure 3 Schematic of the Belgian deep geological repository concept, illustrating the Supercontainer, Monolith B, and the components of the Engineered Barrier System (EBS) within the host formation (ONDRAF/NIRAS, 2020).

2. Context and problem statement

The Boom Clay Formation, a poorly-indurated clay, has been considered as one of the reference host formations for radioactive waste disposal in Belgium (Bernier et al., 2011; X. Li et al., 2023). This selection is based on the favorable properties of this deep Tertiary clay formation, which make it well-suited for geological disposal. The key characteristics of the Boom Clay include its very low permeability, which significantly restricts water flow; its high capacity for retaining and adsorbing radionuclides, which slows their migration; and its ability to self-seal fractures caused during excavation (Horseman et al., 1987; Bernier et al., 2011; X. Li et al., 2023). These properties contribute to its effectiveness as a natural barrier for containing radioactive waste.

The intermediate-level bituminized radioactive waste (BW), known as Eurobitum, was produced at the EUROCHEMIC/BELGOPROCESS reprocessing facility in Mol-Dessel, Belgium (Valcke et al., 2000, 2010). The primary purpose of Eurobitum was to immobilize precipitation sludge and evaporator concentrates generated during the chemical reprocessing of spent nuclear fuel and the cleaning of high-level waste storage tanks. Eurobitum is composed of approximately 20–30% sodium nitrate ($NaNO_3$) by weight and 60% hard bitumen (Mexphalt R85/40), which encapsulates the waste. The remaining material includes sparingly soluble salts such as calcium sulfate ($CaSO_4$), calcium fluoride (CaF_2), and calcium phosphate ($Ca_3(PO_4)_2$), as well as oxides and hydroxides of aluminum (Al), iron (Fe), and zirconium (Zr). Trace amounts of radionuclides, accounting for no more than 0.2% by weight, are also present (CEC, 1989; Valcke et al., 2000, 2010; Weetjens et al., 2010).

In the current concept, this bituminized waste—classified as category B waste—is stored in metallic drums, intended for placement in monoliths, and disposed of in galleries. In geological disposal conditions, Eurobitum interacts with groundwater, leading to water uptake by hygroscopic salts, primarily sodium nitrate ($NaNO_3$) (Valcke et al., 2010; Weetjens et al., 2010). This interaction might disturb the host formation and affect its performance. The process results in two key disturbances:

1. **Geo-mechanical disturbance**: Water uptake causes swelling of the waste and the increase of the internal pressure. If swelling is restricted, it generates high osmotic pressure, leading to mechanical stress on the surrounding clay and potentially damaging the structural integrity of the repository.

2. **Physico-chemical disturbance**: Large quantities of dissolved sodium nitrate and other soluble salts are released into the clay, altering its chemical balance and potentially affecting its ability to act as an effective barrier.

Understanding and assessing these impacts are essential to ensuring the safety and reliability of geological disposal for Eurobitum.

3. Research objectives

As previously mentioned, a significant disturbance that could affect the Boom Clay arises from physico-chemical changes due to exposure to leachate with altered chemical compositions, as is the case for Eurobitum. The leachate, primarily comprising $(Na,Ca)NO_3$ solutions with elevated sodium (Na^+) concentrations, may infiltrate the Boom Clay locally (Valcke et al., 2010; Weetjens et al., 2010). Such infiltration has the potential to alter the hydro-mechanical behavior of the clay, thereby affecting its efficiency as a barrier for radioactive waste containment. The aim of this PhD thesis is to evaluate whether these chemical disturbances could indeed compromise the integrity and performance of the Boom Clay as a geological barrier in the context of deep disposal, through investigating the impact of high salinity resulting from the elevated concentrations of diffused $(Na,Ca)NO_3$ solutions and sodium ion (Na^+) occupancy on the hydro-mechanical behavior of the Boom Clay. The main objectives are:

1. **To assess the effects of salinity on the swelling pressure and hydraulic conductivity of Boom Clay**:
    - Conducting one-dimensional constant-volume swelling pressure tests to investigate the effects of elevated solute concentrations and increased sodium occupancy on the swelling behavior and hydraulic conductivity of Boom Clay.
2. **To evaluate the impact of solute concentration and sodium occupancy on the volumetric behavior and microstructure of Boom Clay**:
    - Performing salinization/desalinization cycles under constant effective stress in oedometer conditions.
    - Assessing the microstructural changes through Mercury Intrusion Porosimetry (MIP).

3. **To investigate the coupled hydro-mechanical processes**:
    - Performing high-pressure oedometer tests (up to 32 MPa) to assess the influence of increased solute concentrations and sodium occupancy on the hydraulic and mechanical properties of Boom Clay.
    - Focusing on key behaviors such as compressibility, deformation, preconsolidation pressure, and compaction under these conditions.
4. **To evaluate the mechanical properties of Boom Clay under saline conditions**:
    - Examining the influence of high ionic strength (IS) and sodium occupancy (Na^+) on the mechanical behavior of Boom Clay by performing undrained triaxial tests under varying effective confining pressures and salinity conditions.
5. **To develop a chemo-hydro-mechanical (C-H-M) elastoplastic constitutive model (ACC2-Chem) for stiff clay**:
    - Enhancing the model by incorporating ionic strength (IS) and sodium occupancy to simulate key experimentally observed chemo-hydro-mechanical processes in low-permeability clay materials.
    - Implementing the developed model within the finite element framework of the LAGAMINE code and verifying its efficiency and robustness.
6. **To apply the developed model across different scales**:
    - Demonstrating the ability of the model to reproduce experimental data at laboratory and in situ scales.
    - Using the model to gain a better understanding of the C-H-M processes active at the scale of a geological disposal system.

This comprehensive study is expected to provide insights into the chemo-hydro-mechanical behavior of Boom Clay under saline conditions and as such to contribute to the design and performance assessment of geological repositories for radioactive waste disposal.

4. Outline of the thesis

This thesis is organized into seven main parts, contributing to a comprehensive understanding of Boom Clay's chemo-hydro-mechanical (CHM) behavior under the influence of saline environments. The structure reflects the logical progression from general background knowledge to detailed experimental work, modeling development, and large-scale application.

The thesis opens with an **Introduction**, which sets the broader context by discussing the global use of nuclear energy and the associated challenges of managing radioactive waste. It explains the rationale for deep geological disposal as a long-term solution and introduces clay formations, particularly Boom Clay, as promising host formation due to their low permeability and strong retention capabilities. A central theme of the thesis is then presented: the chemical perturbations that occur in clayey media when exposed to saline solutions, which may originate from waste packages or engineered barriers. These perturbations can significantly influence the mechanical and hydraulic performance of the clay. The introduction concludes by clearly stating the research objectives and explaining the relevance of the work in the context of geological disposal of radioactive waste.

The second part of the thesis, entitled **State of the Art**, provides a thorough review of the existing knowledge. It begins with an overview of the mineralogical and physicochemical characteristics of clayey soils, emphasizing aspects such as swelling potential, microstructure, and ion exchange capacity. The literature is then reviewed with a focus on the influence of chemical environments, particularly salinity, on the hydro-mechanical behavior of clay. This includes an analysis of existing constitutive models that attempt to account for chemical effects. The chapter concludes with a detailed presentation of Boom Clay, including its geological setting, mineralogical composition, physical and mechanical properties, and observed hydro-mechanical behavior. Special attention is given to the numerical models that have been developed to simulate its response under various loading and chemical conditions.

The third part, **Materials and Experimental Methods**, describes the experimental approach adopted to investigate the CHM behavior of Boom Clay. It begins with a description of the materials, including Boom Clay samples and a range of saline solutions prepared to simulate different porewater chemistries. The preparation

methods are detailed to ensure reproducibility and consistency across tests. The experimental setups are then described, including high- and low-pressure oedometers, a high-pressure triaxial cell, a constant volume cell, and a mercury intrusion porosimeter (MIP). Each device's capabilities are explained in relation to the specific parameters measured. The chapter outlines the protocols followed in each experimental campaign and presents the overall testing program designed to examine the coupled effects of stress and salinity on Boom Clay's behavior.

The fourth part, **Experimental Results**, presents and analyzes the findings from the test program. The results are structured to highlight the influence of saline solutions and sodium occupancy on various aspects of Boom Clay's performance. The effects of salinity on swelling pressure, permeability, mechanical strength, deformation characteristics, and microstructural changes are discussed in depth. These analyses are supported by graphical data and microstructural observations. The section concludes by synthesizing the main experimental insights and preparing the ground for model development.

The fifth part of the thesis focuses on the **Development of an Elasto-plastic Constitutive Model** designed to simulate chemical effects observed during the experimental study. The model is based on the Adapted Cam Clay (ACC-2) framework, an elasto-plastic constitutive formulation used to represent the mechanical behavior of Boom Clay under various loading conditions. The section begins with a conceptual and mathematical overview of the original ACC-2 model, establishing its relevance within the context of geological disposal. The ACC-2 model is then adapted to simulate the response of the Boom Clay when exposed to synthetic porewater. This adaptation includes the introduction of cohesive strength and the recalibration of material parameters, enabling the model to reproduce mechanical responses under in-situ conditions. Following this, a new **purely elastic volumetric microstructural model** is developed to account for the influence of **sodium occupancy** and **ionic strength**, two key parameters identified through experimental investigation. This microstructural model is integrated into the ACC-2 framework, forming an extended version referred to as **ACC2-CHEM**. The extended model includes coupling between chemical and mechanical processes, allowing simulation of coupled chemo-hydro-mechanical (CHM) behavior in clayey media. ACC2-CHEM is implemented into the finite element software **LAGAMINE**, within the existing thermo-hydro-mechanical (THM) formulation,

to enable simulations at both laboratory and repository scales. To verify the model, a series of numerical simulations are carried out to reproduce laboratory-scale experiments, including **salinization–desalinization cycles** and **undrained triaxial compression tests**. These simulations assess the influence of chemical perturbations on swelling pressure, stiffness, and strength of Boom Clay. The model shows a high predictive capacity, successfully replicating key experimental observations and contributing to a deeper understanding of chemical sensitivity in clay formations. The section concludes with an evaluation of the model's performance and a discussion on its potential application in long-term prediction of engineered barrier behavior under variable chemical environments.

The sixth part of the thesis is dedicated to **Repository-Scale Simulations**, with a specific focus on evaluating the long-term chemo-hydro-mechanical (CHM) behavior of Boom Clay in the presence of **intermediate-level bituminized radioactive waste**, particularly **Eurobitum**. To examine these interactions in detail, a series of two-dimensional numerical simulations were performed using the finite element software **LAGAMINE**, into which the newly developed **ACC2-CHEM** model was implemented. The simulation campaign captures the phenomenological evolution of the repository through four sequential phases: (1) an initial gallery excavation phase occurring over a single day, (2) a 100-year operational phase under drained conditions, (3) a 300-year post-operational equilibrium phase, and (4) a 500-year swelling phase simulating the long-term interaction between the Eurobitum and the Boom Clay. During the swelling phase, mechanical expansion of the waste is modeled by applying radial displacements to the concrete lining, thereby mimicking the pressure exerted by the expanding bituminized waste. To isolate and understand the contributions of mechanical and chemical processes, several simulation scenarios were investigated. These included: (i) swelling-induced mechanical perturbations without chemical effects, (ii) combined mechanical swelling and saline plume diffusion, and (iii) pure chemical diffusion without any swelling. By comparing these scenarios, the analysis provides a detailed assessment of the separate and combined influences of mechanical deformation and chemical alteration on the hydro-mechanical response of Boom Clay.

The final chapter, **Conclusions and Perspectives**, summarizes the findings from both the experimental and numerical investigations. It highlights the significant role that

chemical perturbations, especially salinity, play in Boom Clay's hydro-mechanical behavior. The performance of the modified ACC2-CHEM model is evaluated, and its relevance for simulating repository conditions is reaffirmed. The thesis concludes by identifying future research directions, including the application of the model to other clay formations, the integration of thermal effects, and the potential for multi-scale modeling approaches. These perspectives underscore the broader impact of this research on the design and safety assessment of radioactive waste repositories.

II. State of the art

1. Introduction

The behavior of clays, particularly under varying environmental and mechanical conditions, has been a subject of extensive research due to their critical role in geotechnical and environmental applications. Understanding the fundamental aspects of clays is essential for predicting their response to different loading and chemical conditions, which is particularly relevant for applications such as underground waste storage, barrier systems, and civil engineering structures.

This chapter provides a comprehensive review of the state of the art concerning clay materials, with a specific focus on Boom Clay (BC), a reference host formation for radioactive waste disposal. The first section introduces the general characteristics of clays, including their mineral structure and the physicochemical interactions governing their behavior. The second section presents an overview of the behavior and properties of Boom Clay in its in situ conditions, with unperturbed concentration or synthetic Boom Clay water. This includes its geotechnical characteristics, mineralogical composition, pore water chemistry, microstructural features, and hydro-mechanical behavior. Key aspects such as swelling pressure, hydraulic conductivity, volume change behavior, and shear behavior are examined in detail. Additionally, the constitutive modeling approaches for BC are discussed to provide insight into its mechanical representation in numerical simulations.

The third section provides an overview of the effect of concentration on the main properties of clays as reported in the literature. It focuses on the interaction between clays and saline solutions, an important factor influencing the hydro-mechanical response of clayey materials. The effects of salinity on swelling pressure, hydraulic conductivity, volume change behavior, shear strength, and microstructure are reviewed, along with coupled hydro-chemo-mechanical (CHM) modeling approaches. Understanding these effects is crucial for evaluating the long-term stability and performance of clay-based barriers and other geotechnical structures exposed to saline environments.

By synthesizing existing knowledge on these topics, this chapter establishes the necessary foundation for the subsequent experimental and numerical investigations presented in this thesis.

2. General aspects of clays

2.1 Clay mineral structure

Clay is a fine-grained material that results from the chemical and mechanical alteration of various rocks. It can be distinguished from non-clay materials based on the size, shape, and mineral content of its particles. Soil classification systems typically define clay particles as having an effective size of 2 μm or smaller, without considering the mineral type or the quantity of exchangeable cations (Mitchell and Soga, 2005). However, two of the most important properties of the clay size fraction are its mineralogical composition and cation exchange capacity.

Clays are primarily composed of hydrous aluminum silicates. The structure of clay minerals consists of two main types of layers (Grim and Guven, 2011; Meunier, 2003):

1. **Tetrahedral Layer (Figure 4a):** The basic structure is a tetrahedron, with a central silicon atom surrounded by oxygen atoms. These tetrahedra share oxygen atoms to form the tetrahedral layer.
2. **Octahedral Layer (Figure 4b):** The basic structure is an octahedron, with a central aluminum or magnesium atom surrounded by six hydroxyl groups. These octahedra share hydroxyl atoms to form the octahedral layer.

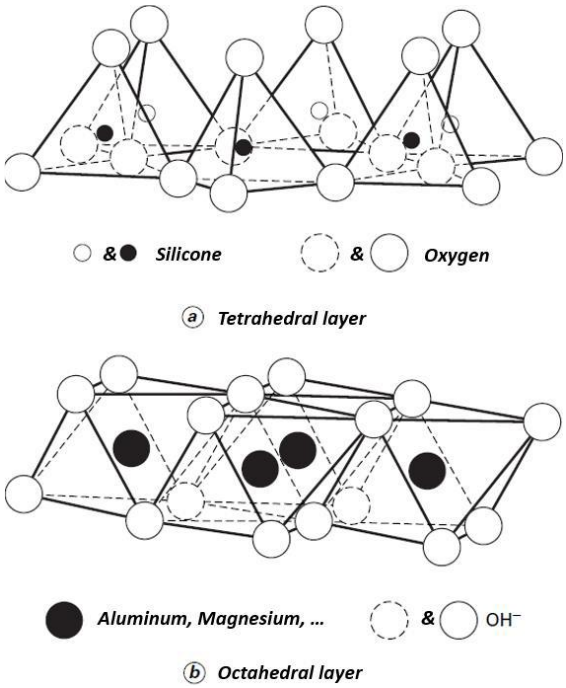

Figure 4 Structure of clay minerals constructing of (a) tetrahedral and (b) octahedral layers (Mitchel and Soga, 2005).

The arrangement of atoms constitutes the tetrahedral and octahedral units, which then form sheets and stack to create layers, as illustrated in Figure 5. These stacked layers combine to produce various clay mineral groups. The basic structures shown in the bottom row of the figure represent the majority of clay mineral types found in soils.

Classifying clay minerals based on their crystal structure and layer stacking sequence is useful, as minerals within the same group generally exhibit similar physical properties. The minerals consist of unit cells made up of two, three, or four sheets.

- **Two-sheet minerals** are composed of a silica tetrahedral sheet and an octahedral sheet, typically aluminum or magnesium based.
- **Three-sheet minerals** feature a dioctahedral or trioctahedral sheet between two silica tetrahedral sheets. These unit layers can be stacked closely or separated by interlayer water or cations, influencing their swelling properties.
- **Four-sheet minerals**, such as chlorite, consist of a 2:1 layer with an additional interlayer hydroxide sheet, which contributes to the mineral's stability and reduces the swelling capacity.

In some soils, there are inorganic, clay-like materials without a clearly identifiable crystal structure, known as allophane or non-crystalline clay (Mitchell and Soga, 2005).

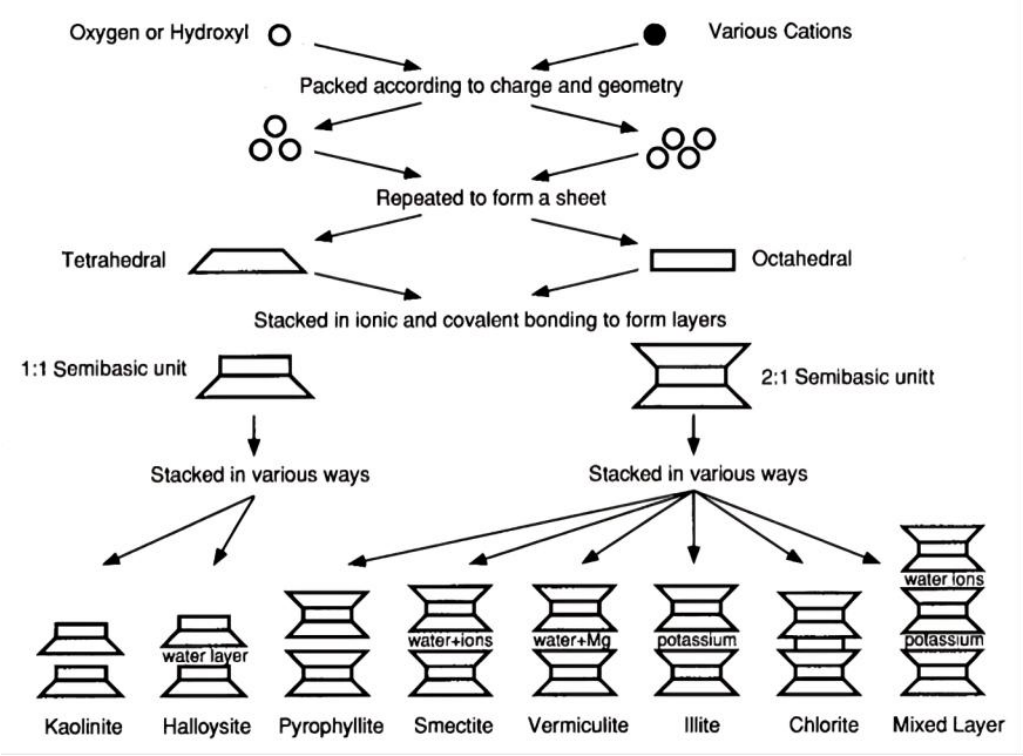

Figure 5 Synthesis pattern for the clay minerals (Mitchell and Soga, 2005).

Kaolinite ($Si_2Al_2O_5(OH)_4$) is the most common 1:1 clay mineral, consisting of a combination of a tetrahedral and an octahedral layer (Figure 6a). This structure allows for the substitution of aluminum (Al^{3+}) with zinc (Zn^{2+}) or iron (Fe^{2+}) atoms in the octahedral layer. However, this isomorphic substitution does not create a significant charge imbalance. Silicon (Si^{4+}) in the tetrahedral layer is rarely substituted in kaolinite; thus, the overall charge of the sheets remains near zero (e.g., Fletcher and Sposito, 1989). When kaolinite sheets are stacked, hydrogen bonds (O-H) are formed, contributing to the stability of the mineral, particularly against water molecule insertion. As a result, water and cations do not penetrate the interlayer space between the sheets, characterizing kaolinite as a non-swelling clay. The sorption sites of kaolinite are located solely on the surface, making it a very weak cation exchanger with a cation exchange capacity (CEC) of approximately $10\,meq/100g\ (= cmol(+)/kg)$. These surface sites are found at the ends of the sheets.

Montmorillonite ($Si_4\left(Al_{2-y}Mg_y\right)O_{10}(OH)_2, yM^+, nH_2O\ with\ M^+as\ a\ cation$) is a 2:1 clay mineral belonging to the smectite family. It consists of an octahedral layer sandwiched between two tetrahedral layers (Figure 6b). In montmorillonite, isomorphic substitution plays a crucial role. Silicon atoms (Si^{4+}) in the tetrahedral layers are replaced by

aluminum (Al^{3+}), and aluminum (Al^{3+}) in the octahedral layers is substituted by magnesium (Mg^{2+}), iron (Fe^{2+}), or chromium (Cr^{3+}), leading to a deficit in structural charge of approximately 0.2 to 0.6 cmol(+)/kg . This permanent negative charge on the particle surfaces is compensated by the adsorption of exchangeable cations and water molecules in the interlayer space (the region between the clay sheets) (e.g., Fletcher and Sposito, 1989). This type of sheet characterizes active clays, which have significant swelling potential and high cation exchange capacity. Montmorillonite exhibits a CEC ranging from $25\ to\ 100\ meq/100g$. Surface sites are also located at the ends of these sheets.

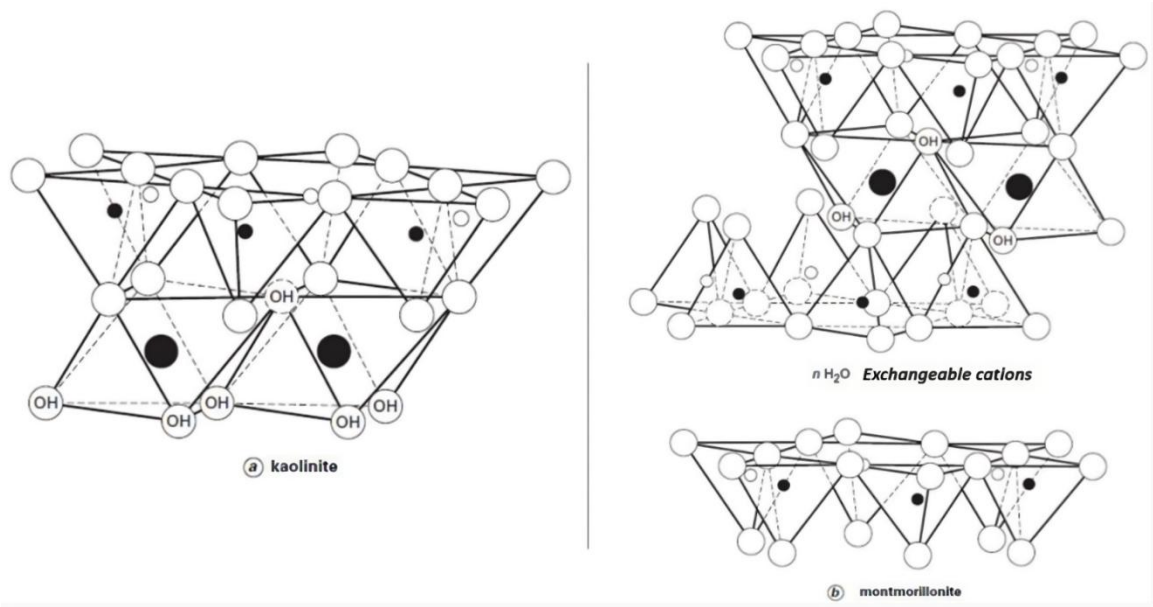

Figure 6 Structure of (a) Kaolinite and (b) Montmorillonite sheets (Mitchell and Soga, 2005).

Illite ($Si_{4-x}Al_x(Al_{2-y}Mg_y)O_{10}(OH)_2,(x+y)K^+$) is a 2:1 clay mineral consisting of an octahedral layer between two tetrahedral layers. In illite, the isomorphic substitution of silicon (Si^{4+}) atoms with aluminum (Al^{3+}) in the octahedral sheet results in a charge deficit on the particle surfaces. The rate of isomorphic substitutions in illite is higher than in montmorillonite, leading to a more significant charge (ranging from 1 to 1.3 molc.kg^{-1}) (e.g., Fletcher and Sposito, 1989). Potassium ions are adsorbed in the interlayer space and strongly bound to the surface of the sheets. These non-exchangeable potassium ions are sufficient to balance most of the charge deficit, reducing the cation exchange capacity. For pure illite, cation exchange is minimal. Illite, therefore, has a lower sorption capacity than montmorillonite. In this mineral, water molecules are absent in the interlayer space (the region between the clay sheets). Illite

is a non-swelling clay with a low cation exchange capacity, and surface sites are present at the ends of the sheets.

Chlorite ($(Mg,Fe)_3(Si,Al)_4O_{10}(OH)_2(Mg,Fe)_3(OH)_6$) is a 2:1:1 non-swelling clay mineral composed of one octahedral sheet sandwiched between two tetrahedral sheets, with a positively charged octahedral layer dominated by magnesium in between. It has a low cation exchange capacity, lower than smectite and similar to illite. Isomorphic substitution occurs when silicon (Si^{4+}) atoms are replaced by aluminum (Al^{3+}) in the octahedral layer, and aluminum (Al^{3+}) is replaced by magnesium (Mg^{2+}) or iron (Fe^{2+}) in the tetrahedral layer. This substitution results in a permanent negative charge that partially neutralizes the positive charge of the interlayer octahedral layer.

2.2 Physical-chemical interactions

The main physicochemical properties of clays are primarily defined by cation exchange capacity (CEC), specific surface area, and specific charge density. Isomorphic substitutions in clay minerals lead to negatively charged particles. To maintain electroneutrality, cations are drawn into interlayer spaces or onto the surfaces and edges of grains. Many of these cations are exchangeable and they can be replaced by other cations when the chemical composition of the solvent changes. The quantity of exchangeable cations is expressed as cation exchange capacity (CEC), measured in meq per 100 g of dried clay. The presence of cations responsible for isomorphic substitutions, especially in smectites, plays a key role in the interlayer bonding within the stacking of sheets. The main cations attracted by the negatively charged surfaces are calcium (Ca^{2+}), magnesium (Mg^{2+}), sodium (Na^{+}), and potassium (K^{+}) (e.g., Rayment and Higginson, 1992). Additionally, due to changes in pore water chemistry, the cations initially adsorbed onto the clay surfaces may be replaced by cations from the surrounding solution. The smaller the cation's hydration radius, the greater the charge density and the stronger its fixation to the clay surfaces. The typical order of cation exchange capacity is (Pusch, 2001; Mata Mena, 2003):

$$Na^{+} < K^{+} < Mg^{2+} < Ca^{2+} \quad (1)$$

Potassium and cesium can easily lose their hydration sphere and become strongly fixed to the clay surfaces, forming an inner-sphere complex. In illite, a cation that has lost its hydration sphere can bind to two clay sheets, preventing the access of other cations (Fletcher and Sposito, 1989; Cornell, 1993). However, a cation with high

replacing power, such as Al^{3+} , can be displaced by one with lower replacing power, such as Na^{+}, through mass action if the concentration of the lower replacing power ion in solution is sufficiently high relative to that of the higher replacing power ion. In addition, the hydrated radius of the exchangeable cation might affect the swelling behavior of the smectite minerals. Cations with smaller hydrated radii, such as $K^{+}$and Na^{+}, can more easily enter the interlayer space of smectite and interact with negatively charged clay surfaces. This results in greater swelling pressures due to the higher degree of hydration within the interlayer. Conversely, cations with larger hydrated radii, such as $Ca^{2+}$and Mg^{2+}, exhibit lower swelling pressures as their hydration shells limit their interaction with clay surfaces and reduce the overall water uptake (Norrish, 1954; Young and Smith, 2000; Mitchell and Soga, 2005). The differences in hydrated radii between monovalent and divalent cations can be attributed to their charge density and hydration energy. According to Marcus (1997) and Mitchell & Soga (2005), divalent cations like Ca^{2+} and Mg^{2+} exhibit higher hydration energy compared to monovalent cations like Na^{+} and K^{+}. Hydration energy refers to the energy released when water molecules surround and interact with a cation.

Divalent cations have a higher charge-to-size ratio than monovalent cations. This increased charge density results in stronger electrostatic interactions with water molecules, leading to the formation of a more tightly bound hydration shell. Consequently, the effective hydrated radius of divalent cations is slightly larger than that of monovalent cations despite their smaller unhydrated ionic radii (Kielland, 1937; Lide and Frederikse, 1995; Marcus, 1997; Mitchell and Soga, 2005).

The approximate hydrated radii for these cations are shown in Table 1.

Table 1 Average values of the hydrated raii of main cations (after Kielland, 1937; Lide and Frederikse, 1995; Marcus, 1997; Mitchell and Soga, 2005).

Cation Type	Hydrated radii (nm)
K^{+}	0.331
Na^{+}	0.358
Ca^{2+}	0.712
Mg^{2+}	0.828

When cations are attracted to the negatively charged surfaces of clay particles, the cation concentration near these surfaces increases in the presence of water. This

creates a concentration gradient between the clay surface and the surrounding solution. While the adsorbed cations naturally tend to diffuse into the solution to equalize the concentration, this movement is restricted by the attraction exerted by the negative electric field of the clay particles. This balance of forces results in the formation of the diffuse double layer (DDL), where the distribution of ions near the clay surface shows a decrease in the clay's negative charge and a corresponding decrease in the cation's positive charge with increasing distance from the surface (Figure 7).

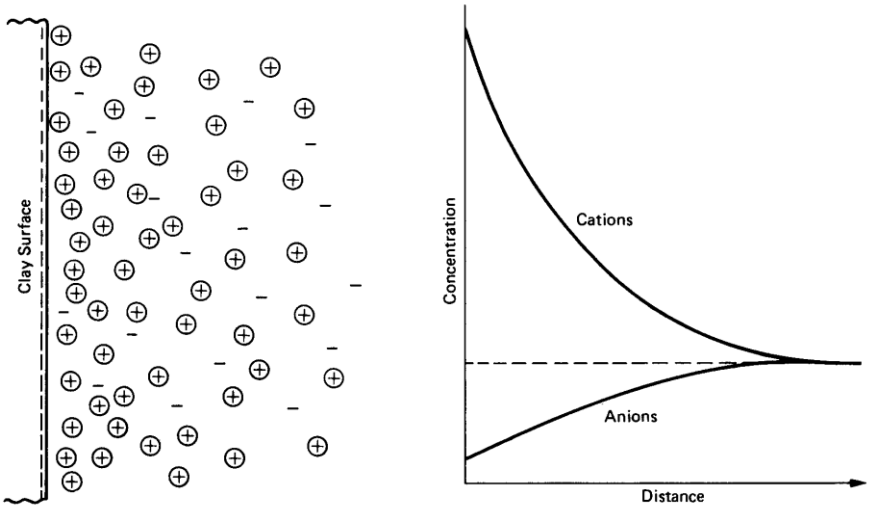

Figure 7 Distribution of ions adjacent to a single clay surface (DDL) (Mitchell and Soga, 2005).

The theory of the DDL was introduced by Gouy (1910) and Chapman (1913) to describe the interaction between clay particles and water, treating the system as a colloidal solution (Van Olphen, 1963). Assuming a negligible Stern layer and a uniformly charged clay layer (Figure 8), the electrical potential Ψ around the clay layer, illustrated in Figure 9(a), can be expressed as a function of the distance from the clay surface. This relationship is given by Eqt.(2) below:

$$\psi = \psi_0 exp\,(-\kappa\chi_c) \tag{2}$$

where ψ_0 is the electrical potential at the clay layer surface and χ_c is the distance from the clay layer surface. κ^{-1} represents the thickness of the diffuse double layer as follows:

$$\kappa^{-1} = \left(\frac{\varepsilon_r \varepsilon_0 \kappa T}{2n_0 e^2 z^2}\right)^{1/2} \tag{3}$$

where ε_r is the dielectric constant of the electrolyte, ε_0 is the dielectric permittivity of vacuum (=8.8542×10^{-12} C^2/J·m), κ is the Boltzmann constant (= 1.38×10^{-23} J/K), T is

the absolute temperature, n_0 is the ion concentration in the electrolyte, e is the electric elementary charge (=1.602 × 10^{-19} C), and z the valency of the ion in the electrolyte.

The thickness of the diffuse double layer (DDL) is influenced by several factors. It decreases with increasing ion valence and the square root of the ion concentration in the pore solution, while it increases with the square root of the dielectric constant and temperature, assuming all other conditions remain constant. These dependencies allow for an estimation of how changes in the system composition can influence particle behavior. A thicker diffuse layer reduces the tendency of particles in suspension to flocculate and increases the swelling pressure in expansive soils (Mitchell and Soga, 2005). An increase in electrolyte concentration reduces the surface potential under a constant surface charge condition, leading to a more rapid decay of potential with distance. This causes the diffuse layer to thin, reducing both the midplane concentration and electrical potential for interacting parallel clay particles at a given spacing. Consequently, interparticle repulsive forces decrease (Figure 9b).

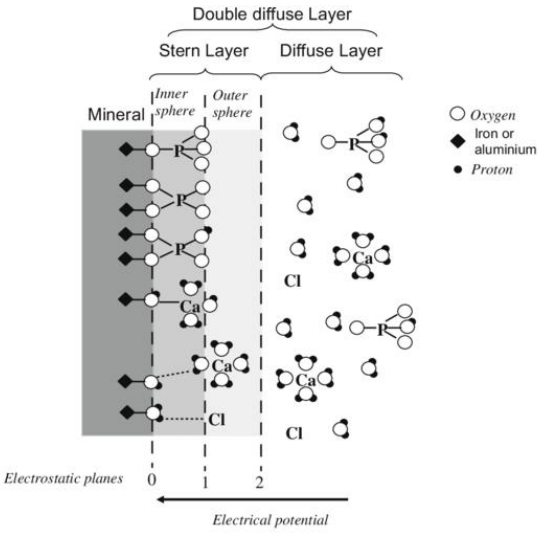

Figure 8 Representation of the diffuse double layer at a mineral surface (Devau et al., 2009).

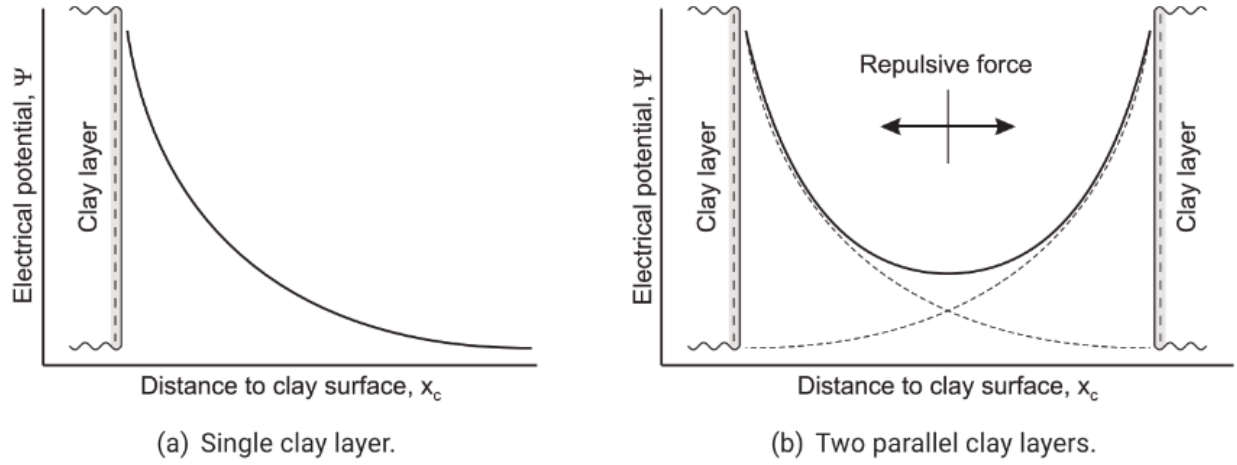

Figure 9 Evolution of the electrical potential as a function of the distance from the clay layer (a) single layer and (b) two parallel layers (Dieudonné, 2020).

3. Clays and saline solutions

3.1 Effect of salinity on the swelling pressure

Swelling pressure is defined as the pressure at which no volume change occurs during wetting. If the soil is subjected to stress lower than its swelling pressure during wetting, it expands; conversely, if the stress exceeds the swelling pressure, the soil collapses. Several methods have been proposed in the literature to determine the swelling pressure of soils, as illustrated in Figure 10 by Zhang et al. (2020):

- **Constant-Volume Method (Path OA in Figure 10 (a))**:
  This method involves using a rigid cell to prevent any volume change in the sample while measuring the total pressure exerted by the soil. Once the pressure stabilizes, the recorded value is taken as the swelling pressure (Nagaraj et al., 2009; Wang et al., 2012; Dieudonné et al., 2024).
- **Zero-Swell Method (Path OBB' in Figure 10(a))**:
  In this approach, a conventional oedometer test is performed, where a small initial load (e.g., 0.1 MPa) is applied before wetting. As the soil hydrates and begins to swell, additional loads are incrementally applied to restore the sample to its original volume once swelling exceeds a predefined threshold (e.g., 0.1%). This process continues until no further swelling is detected, and the applied stress at this stage represents the swelling pressure (Basma and Husein, 1995; Nagaraj et al., 2009; Wang et al., 2012).

- **Pre-Swelling Method (Path OCC' in Figure 10(a))**:
  This method allows the soil sample to swell freely up to a predetermined volume change (Point C, known as pre-swell). After reaching this point, volume change is restricted, and the swelling pressure is measured using a load transducer. The final pressure after stabilization corresponds to the swelling pressure associated with the void ratio at Point C (Wang et al., 2012).
- **Swelling-Consolidation Method (Path ODD' in Figure 10(a))**:
  Here, the sample is first resaturated under a low initial load (e.g., 0.1 MPa). Once the swelling phase is complete, a standard consolidation test is conducted. The swelling pressure is defined as the stress required to restore the soil sample to its original void ratio (Basma and Husein, 1995).
- **Unloading-Reloading Method** (Cui et al., 2013):
  This approach involves performing unloading and reloading cycles in an oedometer test (Figure 10(b)). The bi-linear behavior observed in these curves is used to determine a threshold vertical stress, which separates the regions of low and high slope. Since swelling pressure is defined as the stress at which no further volume change occurs, these threshold stresses are considered representative of the swelling pressure just before or after unloading or reloading.
- **Swelling-Under-Load Method**:
  This method requires multiple identical soil samples (Figure 10(c)). Each sample is subjected to a specific load level before being wetted until swelling stabilizes. The final equilibrium states at various load levels define a "swelling-under-load" curve. The swelling pressure is determined as the stress level (Point A) at which there is no volumetric strain.

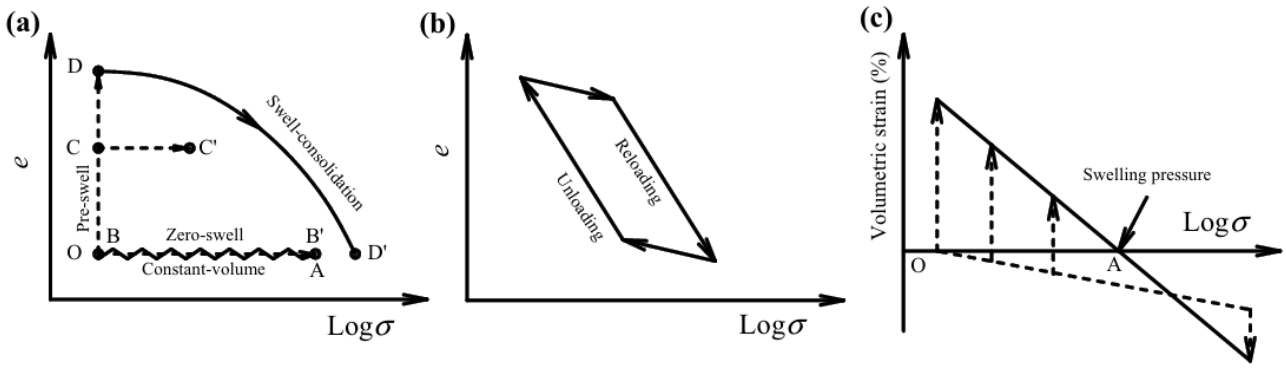

Figure 10 Determination of swelling pressure by a) swell-consolidation method, pre-swell method, zero-swell method, and constant-volume method, b) method proposed by Cui et al. (2013), c) swell-under-load method (Zhang et al., 2020).

Numerous experimental studies have explored the chemical effects on the swelling behavior of clay, consistently indicating that an increase in pore water salinity leads to a significant reduction in swelling pressure while simultaneously enhancing hydraulic conductivity (Studds et al., 1998; Castellanos et al., 2008; Ye et al., 2014). While extensive research has examined the role of cation valence in ion exchange reactions during saline solution percolation, fewer studies have assessed the effects of hydrated radius and cation type on the swelling and hydraulic conductivity of saturated clay, with most investigations focusing on reconstituted or unsaturated clays. Additionally, limited research has addressed the influence of saline plumes from bituminized waste on the physico-chemical and hydro-mechanical behavior of Boom Clay (Mokni, 2011; Bleyen, 2018). The influence of pore fluid composition on clay behavior has been of significant interest across various disciplines, including clay mineralogy, soil physics, geotechnical engineering, and environmental engineering (Bolt, 1956; Mesri and Olson, 1971; Sridharan et al., 1986; Ye et al., 2014a). The hydro-mechanical properties of clays, particularly their sensitivity to pore water salinity, have been widely investigated, with studies showing that the liquid limit of compacted Boom Clay decreases as osmotic suction increases (Mokni et al., 2014), a trend also observed for bentonites (Maio, 1998; Castellanos et al., 2008). These findings align with previous research suggesting that swelling potential decreases with increasing pore water salinity (Musso et al., 2003; Musso, 2013; Rao et al., 2013; Thyagaraj and Rao, 2013), underscoring the critical role of pore fluid chemistry in determining the mechanical behavior of active clays.

According to Norrish (1954), two swelling mechanisms occur at the micro and macro scales during the hydration of smectite. The first mechanism is **crystalline swelling**, which begins in the hydrophilic regions of the clay, specifically at the interlayer basal surfaces. During this initial hydration process, water molecules are progressively and systematically adsorbed into the interlayer space, forming up to four layers of water (Figure 11 (a)). This orderly hydration leads to a rearrangement of the solid matrix, resulting in the subdivision of particles and a reduction in the number of stacked layers per particle (Figure 11 (b)). As water layers intercalate into the interlayer space, the spacing between clay monolayers increases incrementally. For example, the initial interlayer spacing of smectite is 9.6 Å (in the absence of water) and expands to 12.6 Å, 15.6 Å, 18.6 Å, and 21.6 Å with one, two, three, and four layers of water molecules, respectively (Figure 11(a)). The second mechanism, **osmotic swelling**, results from the interaction of the diffuse double layers associated with adjacent clay particles. At higher water contents, the cations adsorbed on the negatively charged surfaces of the clay are restricted in their ability to diffuse freely into the surrounding bulk solution. This creates concentration gradients that generate repulsive forces between the particles as their double layers interact. Swelling pressure, as defined by Mesri et al. (1994), is the pressure required to prevent water movement into or out of the clay and is equal to the repulsive force between two clay particles. Osmotic swelling is a continuous process, expressed as the repulsive swelling pressure (σ_s) between two clay layers, as described in Eqt. (4):

$$\sigma_s = 2n_0 KT(\cosh u - 1) \tag{4}$$

where u is a non-dimensional potential at the mid-plane between the two clay layers and is strongly dependent on the electrical potential ψ around a single clay layer (Eqt. (4)).

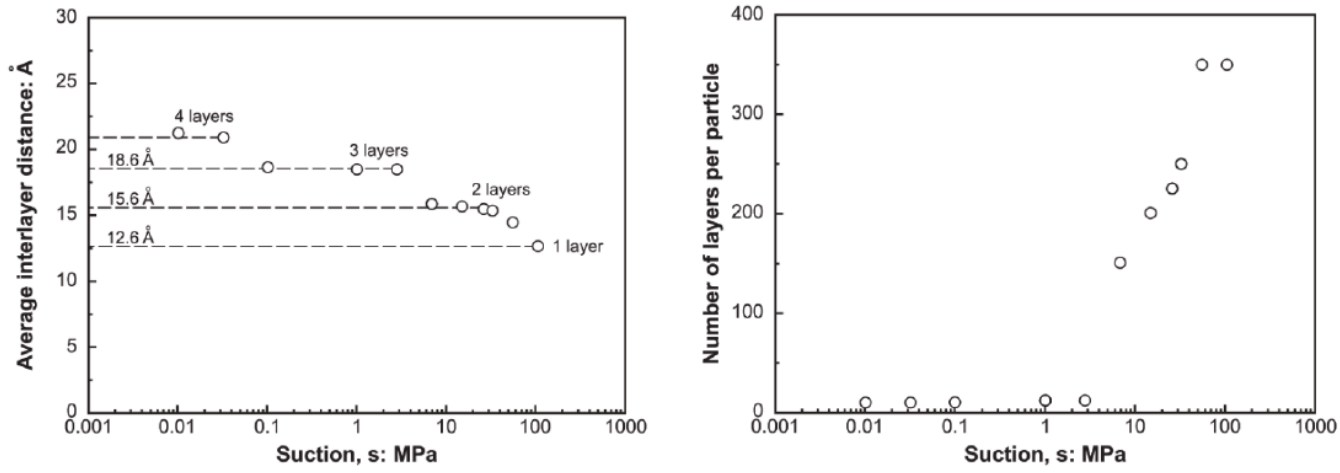

(a) Increase in the number of adsorbed water layers. (b) Decrease in the number of stacked layers per particle.

Figure 11 Hydration effect on particles of MX-80 bentonite (Saiyouri et al., 2000).

Numerous experimental studies have investigated the chemical effects on clay swelling behavior, which consistently demonstrate that increased pore water salinity significantly reduces swelling pressure (Komine et al., 2009; Zhu et al., 2013). Yukselen-Aksoy et al. (2008) and Zhu et al. (2013) observed that specific cations in the pore water, such as sodium and calcium, can alter the mineralogical composition through cation exchange within the interlayer space of montmorillonite sheets. This alteration affects the crystalline swelling process, leading to a reduction in swelling pressure. Figure 12 presents the results of one-dimensional swelling tests on GMZ01 bentonite conducted by Zhu et al. (2013) to examine the effects of solution concentration and cation type. Regardless of the solution type, swelling pressure decreases as the solution concentration increases. Furthermore, for a given concentration, the swelling pressure of compacted GMZ01 bentonite hydrated with NaCl solutions is lower than that hydrated with $CaCl_2$ solutions. The magnitude of this difference depends on the solution concentration. At low salt concentrations, the difference is minor, whereas at higher concentrations, the swelling pressure in the presence of low-valence NaCl solutions is significantly lower than that in high-valence $CaCl_2$ solutions. This suggests that Na^+ has a stronger weakening effect on swelling pressure compared to Ca^{2+}. Additionally, depending on the initial conditions, both ionic strength (IS) and the exchange of adsorbed cations with those in the pore water can reduce the thickness of the diffuse double layer (DDL), thereby influencing osmotic swelling behavior (Castellanos et al., 2008; Siddiqua et al., 2011; Zhu et al., 2013; Du et al., 2021).

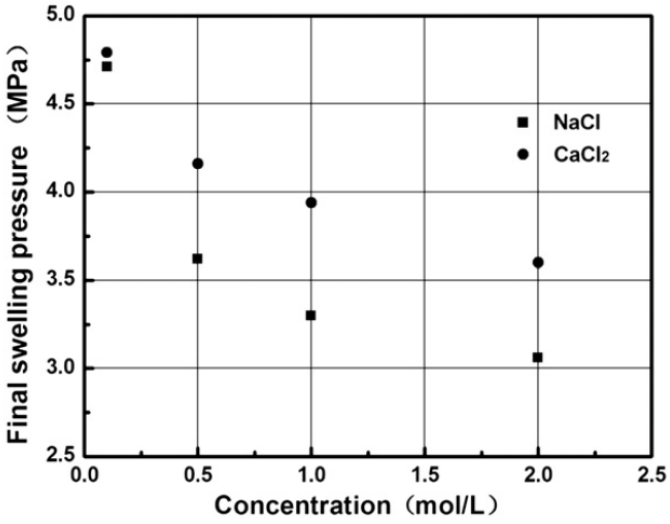

Figure 12 Comparison of influence of cation types on the swelling pressure of GMZ01 (Zhu et al., 2013).

Increasing the salt concentration in pore water weakens the repulsive forces within the diffuse double layer, thereby reducing the swelling potential of clays (Calvello et al., 2005). Numerous studies have shown that salt solutions cause structural collapse in clays, reduce the thickness of the diffuse double layer, increase hydraulic conductivity, and lower swelling potential. Alawaji (1999) demonstrated that the swelling potential of Boom Clay and sand-bentonite mixtures containing $NaNO_3$ or $Ca(NO_3)_2$ solutions decreased by increasing solute concentration. Similarly, Yong (1999) reported that the swelling pressure of sodium montmorillonite decreases with increasing salt concentration, while Karnland (1997) found that the swelling pressure of highly compacted MX−80 bentonite is reduced after exposure to saturated $NaCl$ solutions.

Several other researchers observed that swelling pressure decreases with higher pore water salinity across various types of bentonites (e.g., MX80, Kunigel V1, GMZ01, and FEBEX bentonites) (Suzuki et al. (2008), Rao et al. (2013), Castellanos et al. (2008), Rao and Thyagaraj (2013), Komine et al. ((Komine et al., 2009), Siddiqua (2011), and Zhu et al. (2013). Although many studies have examined the role of cation valence in ion exchange during saline solution percolation, limited research has addressed the impact of hydrated radius and cation type on saturated clay swelling and hydraulic conductivity. Moreover, investigations into the influence of saline plumes, such as those originating from bituminized waste, on the physico-chemical and hydro-mechanical behavior of saturated clays remain scarce (e.g., Mokni, 2011; Bleyen, 2018).

Evans and Quigley (1992) investigated the effects of salt (e.g., copper solutions) leaching from solid waste on sand-bentonite mixtures and found that salt leaching increased permeability while reducing swelling. Di Maio (1997) reported increased free swelling of bentonite after exposure to NaCl, KCl, and $CaCl_2$ solutions, noting that the exchange of Na^+ was reversible, unlike that of Ca^{2+} or K^+.

Further studies highlighted that the swelling pressure of compacted bentonite depends on the type of cation in the interlayer space (Chipera et al. (1995), Musso et al. (2003), Likos and Lu (2010), Villar et al. (2012), Likos and Wayllace (2010), Thyagaraj and Rao (2013), and Zhu et al. (2013). For instance, despite being subjected to the same relative humidity, basal spacing differs between Ca-bentonite and Na-bentonite, resulting in variations in swelling pressure. At 100% relative humidity, Ca-smectite exhibits greater basal spacing and swelling pressures compared to Na-smectite (e.g., Chipera et al.,1995). When Na-bentonite is exposed to $CaCl_2$, partial transformation into Ca-bentonite occurs due to cation exchange between Na^+ and Ca^{2+}. This explains why swelling pressure in the presence of $CaCl_2$ is higher than that with $NaCl$ (Zhu et al., 2013; Chen et al., 2017). Cation exchange, a critical process in clay-water interactions, is governed by the type, valence, concentration, and size of the cations involved.

3.2 Effect of salinity on the volume change behavior

Changes in the chemical composition of pore fluids can significantly affect the volumetric behavior of clays, resulting in cation exchange within various mineralogical units, alterations in electrochemical forces between clay platelets, and variations in osmotic pressure. Numerous studies have shown that the volume change behavior of clayey soils is highly sensitive to pore water chemistry (Karnland, 1997; Studds et al., 1998; Castellanos et al., 2008; Suzuki et al., 2008; Katsumi et al., 2008; Siddiqua et al., 2011). In the literature, four possible mechanisms have been put forward to explain the shrinking/swelling of soil during saline cycling: 1) change in the surface potential of clay lamellae with the salt concentration; 2) change in the Debye length with the salt concentration (contraction or expansion of DDLs); 3) change in osmotic suction with the salt concentration (outflow or inflow of the pore water under osmotic gradient); and 4) exchange of Ca^{2+} and Mg^{2+} cations present in the interlayer space of the montmorillonite sheets with Na^+ cations present in the percolated solutions. The cation

with higher replacing power can also be replaced by the one with lower replacing power depending on its concentration. This is consistent with the results reported by Di Maio (1997) and Mitchell and Soga (2005).

Some experimental studies, including those by Thyagaraj and Das (2014) on compacted red soil and Song et al. (2017) on reconstituted marine clay, have primarily focused on the volumetric behavior of reconstituted soils. Few studies, such as Al Mais et al. (2024, 2025a, 2025b), have examined the cyclic saline effects on the volume change behavior of saturated natural clays. Research on compacted expansive clays subjected to cyclic salinization-desalinization (Musso et al., 2003; Chen et al., 2017; Ye et al., 2017; Zhang et al., 2023) shows that the solution concentration significantly influences the volume change behavior and microstructure of soils. The type of exchangeable cations plays a critical role in determining the composition and behavior of clays (Yukselen-Aksoy et al., 2008). Cation exchange is influenced by several factors, including the size and valence of the cations, as well as the ionic strength of the surrounding solution and the cation fraction present in the clay structure. In addition to chemical composition, the mechanical behavior of clays is strongly influenced by stress levels (Castellanos et al., 2008; Zhang et al., 2012). Under low stress conditions, physicochemical effects are more pronounced due to the larger void ratio and increased distance between clay particles. This configuration allows for greater interaction between clay particles and the surrounding solution, leading to higher shrinkage and significant plastic deformations. Conversely, under high stress levels, clay sheets are more compactly arranged, reducing the void ratio and particle spacing. In this state, the influence of chemical effects diminishes as mechanical factors, such as particle rearrangement and compression, dominate the behavior of the clay. This transition highlights the interplay between stress levels and the relative significance of physicochemical and mechanical influences on clay behavior. It appeared from the aforementioned studies that previous work focused mostly on the effect of solute concentration.

Experimental research, such as that by Thyagaraj and Das (2014) on compacted red soil and Song et al. (2017) on reconstituted marine clay, has primarily investigated volumetric behavior in reconstituted soils. Fewer studies, including Al Mais et al. (2024), have explored cyclic saline effects on the volume change behavior of saturated natural clays. Investigations on compacted expansive clays subjected to cyclic

salinization-desalinization cycles (Musso et al., 2003; Chen et al., 2017; Ye et al., 2017; Zhang et al., 2023) reveal that solution concentration significantly influences soil volume changes and microstructure.

Ye et al. (2014) conducted swelling deformation tests on compacted GMZ01 bentonite (1.70 Mg/m³) infiltrated with deionized water, sodium chloride (NaCl), and calcium chloride ($CaCl_2$) solutions at varying concentrations. The tests examined the impact of solution type and concentration on volume change behavior in compacted specimens. Results showed that specimens infiltrated with NaCl solutions experienced shrinkage ranging from 25% (0.1 M NaCl) to 55% (2.0 M NaCl), while specimens infiltrated with $CaCl_2$ solutions exhibited shrinkage from 30% (0.1 M $CaCl_2$) to 55% (2.0 M $CaCl_2$). These findings indicate that higher shrinkage is observed at higher solution concentrations.

In addition, the chemo-mechanical coupling of clays is strongly pronounced. Under low stress conditions the distance between clay particles increases due to the larger void ratio (Castellanos et al., 2008; Zhang et al., 2012). This configuration allows for greater interaction between clay particles and the surrounding solution, leading to higher shrinkage and significant plastic deformations. Conversely, under high stress levels, clay sheets are more compactly arranged, reducing the void ratio and particle spacing. In this state, the influence of chemical effects diminishes as mechanical factors, such as particle rearrangement and compression, dominate the behavior of the clay. This transition highlights the interplay between stress levels and the relative significance of physicochemical and mechanical influences on clay behavior.

Thyagaraj and Rao (2013) investigated the cyclic salinization–desalinization effects on the swelling behavior of a compacted expansive clay from Southern India under 0.2 MPa vertical stress and found that the total swelling strain increased with increasing salinization–desalinization cycles (Rao et al., 2013). Zhang et al. (2012) reported that the maximum strain of compacted GMZ bentonite exponentially decreased with increasing the Total Dissolved Solids (TDS) from 0 g/L to 12 g/L (0.2 M) in a NaCl-Na_2SO_4 solution, with TDS referring to the combined content of all inorganic and organic substances dissolved in a liquid, usually water. Ye et al. (2014) and Chen et al. (2017) found that a high NaCl concentration solution could induce a smaller swelling strain for GMZ bentonite. Furthermore, Chen et al. (2017) pointed out that the chemical

effect of NaCl on the swelling behavior of GMZ bentonite was hindered as the applied vertical stress exceeded a certain value. Zhang et al. (2016) established an empirical equation to predict the maximum strain of GMZ bentonite with consideration of salt concentration and vertical stress. Meanwhile, the swelling pressure with cyclic infiltrations of distilled water and different concentration NaCl solutions (0.1 M, 1 M, 2 M) was also investigated by Chen et al. (2017). Results indicate that the swelling pressure in the salinization process is quite different from that in the desalinization process even though the percolated solution has the same concentration; the hysteretic phenomenon for the swelling pressure was significant during the cycling processes. Furthermore, the effect of cyclic infiltrations of $CaCl_2$ solution and distilled water on the vertical deformation of compacted GMZ bentonite was experimentally studied by Zhu et al. (2015). However, most of these investigations were limited to the volume change behavior of compacted unsaturated GMZ bentonite experiencing repeated infiltrations of NaCl and $CaCl_2$ solutions.

The cation exchange is mainly controlled by the exchange capacity of the clay minerals (Mata, 2003); the ease with which a cation of one type can replace a cation of another type depends mainly on the valence, relative abundance of the different cation types, and the cation size. On a microscopic scale, the spacing between different unit layers is contingent upon the valence, dimensions, and hydration state of the interlayer cations. The commonly accepted competitive order in cation exchange processes is $Na^+ < K^+ < Mg^{2+} < Ca^{2+}$ (Mata Mena, 2003; Mitchell and Soga, 2005; Zeng et al., 2020). Furthermore, high sodium concentrations may lead to the replacement of divalent ions, such as calcium, which tends to reduce the diffuse double layer (DDL).

Tests conducted on densely compacted GMZ bentonite showed that the changes in volume change behavior were partially reversible during NaCl-water and NaCl- $CaCl_2$ cycling (Chen et al., 2015, 2017). However, in the case of KCl-water cycling, almost no recovery in volume change was observed, likely due to potassium ions strongly binding within the clay layers and causing a structural collapse that limits the clay's ability to swell back to its original volume (Chen et al., 2015, 2017). Chipera et al. (1995) identified that when the relative humidity increases to 100%, the basal spacing is one-layer (~12.5 Å) hydrate state for K-smectite, two-layer (~15 Å) for Na-smectite, while three-layer (~17.5 Å) for Ca-smectite, respectively. Similarly, Villar et al. (2012) reported that the basal spacing of FEBEX bentonite almost increases linearly with

relative humidity, while a stepwise increase is identified in MX80 bentonite. This phenomenon could be explained by their different interlayer cations and their hydrated radius (Likos and Wayllace, 2010). Sridharan et al. (1986) demonstrated that the hydrated cationic radius substantially affects the liquid limit of montmorillonitic soils, a phenomenon more pronounced with monovalent cations than those with higher valences.

In addition, the compressibility of fine-grained soil depends not only on the mechanical properties of the constituent clay minerals but also on the physiochemical properties of the pore fluid like cation valency and salt concentration (1956). Numerous studies have examined the impact of salinity on the compressibility of clays (Barbour, 1986; Barbour and Fredlund, 1989; Maio, 1998; Yang, 1990; Barbour and Yang, 1993; Mokni et al., 2014). Di Maio (1997) conducted oedometer tests on Ponza sodium bentonite saturated with various saline solutions, including KCl, NaCl, and $CaCl_2$. Exposure to NaCl resulted in reversible deformation when the samples were later re-exposed to distilled water. In contrast, KCl and $CaCl_2$ solutions led to ion exchange reactions, causing non-reversible deformations. The Na^+ cations were replaced by Ca^{2+} or K^+ ions, which further influenced the soil's hydro-mechanical behavior. Additionally, clay samples saturated with synthetic water were loaded to a specified stress level and then exposed to highly concentrated NaCl solution. During osmotic consolidation (caused by the brine penetration), which led to a decrease in sample volume and void ratio due to the flow of water from micro to macro pores, the pre-consolidation stress increased, and compressibility decreased. After reaching the new pre-consolidation stress, the sample continued to consolidate along the virgin compression line. As the salt concentration in the pore water increased, the compressibility of the soil decreased further (Barbour, 1986; Barbour and Fredlund, 1989; Yang, 1990; Barbour and Yang, 1993).

3.3 Effect of salinity on soil microstructure

The increase in pore fluid salinity can enhance the osmotic suction due to the presence of dissolved salts, reducing the thickness of the diffuse double layer, resulting in the shrinkage of soil. Consequently, macropores are generated due to particle aggregation, which corresponds to the preferential pathways for fluids (Wang et al., 2019). As reported by Palomino and Santamarina (2005), the fabric associations are

dominated by the ionic concentration. At low ionic concentration, the negatively charged edges and faces of clay sheets lead to a dispersed-deflocculated state. This occurs due to the repulsive forces generated by the diffuse double layer surrounding the clay particles. As a result, the dispersed-deflocculation (DD) mode prevails, allowing the clay particles to remain separated rather than aggregating. As the ionic concentration increases from low to high, the double layer becomes much thinner and van der Waals attraction dominates (Wahid et al., 2011). As a result, the particle associations change from the dispersed mode to the face-to-face (FF) mode, leading to the aggregation of clay platelets. Furthermore, the clay aggregation induced by high-concentration pore fluid salinity can also inhibit the overall shrinkage. The hypothesis of the generation of large interaggregate pores with infiltration of salt solutions can be indirectly justified by the increasing hydraulic conductivity((Karnland, 1997; Castellanos et al., 2008; Zhu et al., 2013; Chen et al., 2015). Following Castellanos et al. (2008), several mechanisms can be involved, such as (i) modification of pore size distribution resulting from clay matrix swelling, and (ii) variations of water molecule mobility associated with exchangeable cations adsorbed on the clay sheet surfaces or in the diffuse double layer. Consequently, when the pore water salt concentration increases, there is a reduction of swelling capacity, thus increasing large flow channel (inter-aggregate) size, causing permeability increase. On the contrary, any decrease in pore water salt concentration results in a thicker DDL, causing a decrease in permeability because of the decrease of the size of large flow channels. The explanations above lead to the same conclusion in terms of microstructure changes: the size of large pores increases by clay aggregation due to the pore water salt concentration increase, and thus the soil permeability is increased.

Musso et al. (2013) investigated the Pore Size Distribution (PSD) for compacted FEBEX bentonite (with an initial dry density of 1.65 Mg/m^3), infiltrated with different solutions under a vertical stress of 0.2 MPa, and found that: (i) the as-compacted specimen exhibited a bimodal pore size distribution feature; (ii) a new pore family was generated in the case of infiltration of distilled water, 0.5 M NaCl and 2.0 M NaCl solutions; (iii) when the infiltration solutions were 3.5 M and 5.5 M NaCl, the large pore size was enlarged, while the bimodal feature was maintained. Moreover, Musso et al. (2003) observed that the pore size distribution (PSD) curve of compacted FEBEX bentonite (with a dry density of 1.4 Mg/m^3 and a bimodal pore size distribution) changed significantly with exposure to different infiltrations. Under a vertical stress of

0.2 MPa, the PSD of bentonite infiltrated with distilled water showed a typical bimodal pattern. However, when the bentonite was subjected to a cycle of infiltration with distilled water followed by a 0.2 M NaCl solution, a new pore family emerged, and the large pore family disappeared. These results suggest that the volume change behavior of clay subjected to cyclic salinization–desalinization was extremely complex at microstructural scale.

3.4 Effect of salinity on the hydraulic conductivity

One of the main characteristics of clay in the context of geological disposal is its low permeability, which functions as a natural barrier to slow down the migration of leached waste. Variations in the electric potential of clay particles, caused by changes in the exchange complex, alter the forces of attraction or repulsion between particles, which in turn affect the properties of the clay. These changes can influence hydraulic conductivity, which typically increases with higher salinity levels (Studds et al., 1998; Pusch, 2001; Mata Mena, 2003; Castellanos et al., 2008; Suzuki et al., 2008; Villar et al., 2012a; Zhu et al., 2013; Chen et al., 2015; Al Mais et al., 2024). During the phase of in situ pore water replacement, it was observed that higher salt solution concentrations led to greater soil compression and increased intrinsic permeability. Typically, permeability decreases with a reduction in void ratio; therefore, the observed increase in permeability must be attributed to other factors. Fernandez and Quigley (1985)) and Cui et al. (2003), while studying natural clay and compacted Jossigny silt with distilled water and non-polar fluids, highlighted the significant impact of percolating fluids with higher salt concentrations. These studies reported notable particle aggregation associated with higher fluid salt concentration, resulting in a pronounced increase in permeability. These findings are consistent with those of Nguyen et al. (2013) and Wang & Anderko (2001).

Similarly, earlier studies on FEBEX bentonite (Castellanos et al., 2008), MX-80 bentonite (Karnland, 1997; Villar et al., 2012a), sodium montmorillonite–sand mixtures (Studds et al., 1998), compacted montmorillonite and illite (Rolfe and Aylmore, 1977), and Friedland Ton clay (a natural clay containing 45% smectite (Pusch, 2001) also demonstrated a clear increase in hydraulic conductivity with rising salinity in the permeating fluid. Castellanos et al. (2008) suggested several mechanisms that may contribute to this phenomenon, including: (i) changes in pore size distribution due to swelling of the clay matrix and (ii) variations in the mobility of water molecules

influenced by exchangeable cations adsorbed on clay surfaces or within the diffuse double layer. As the salt concentration in pore water increases, the swelling capacity of clay particles decreases, resulting in an enlargement of inter-aggregate flow channels and a corresponding increase in permeability. Conversely, a reduction in salt concentration leads to greater development of the diffuse double layer, reducing the size of large flow channels and thereby decreasing permeability.

Zhu et al. (2013) investigated the impact of two saline solutions, NaCl and $CaCl_2$, on the hydraulic conductivity of GMZ10 bentonite. Their findings revealed that hydraulic conductivity increases with rising solute concentration, regardless of the cation type. Specifically, the maximum hydraulic conductivity increased from **2.1×10^{-13} m/s** (when infiltrated with deionized water) to **8.2×10^{-13} m/s** (with 2.0 M NaCl solution) and **4.5×10^{-13} m/s** (with 2.0 M $CaCl_2$ solution). These results confirm that hydraulic conductivity is positively correlated with the concentration of the infiltrating solutions, consistent with observations from prior studies (Karnland, 1997; Studds et al., 1998; Mata Mena, 2003; Suzuki et al., 2008).Figure 13 illustrates the evolution of hydraulic conductivity in GMZ10 bentonite with respect to the concentration of the two solutions, NaCl and $CaCl_2$. It was observed that the hydraulic conductivity of GMZ10 bentonite increases by a factor of **3.25** and **1.54** when the concentrations of NaCl and $CaCl_2$ solutions rise from **0.1 M** to **2.0 M**, respectively. For a given concentration, the hydraulic conductivity values vary between the two solutions, and the difference becomes more pronounced at higher concentrations. The results also show that the hydraulic conductivity of GMZ10 bentonite infiltrated with NaCl solutions is higher than that with $CaCl_2$ solutions at the same concentration. This difference is attributed to the reduced clogging of macro-pores caused by NaCl infiltration compared to $CaCl_2$ infiltration, which leads to relatively higher hydraulic conductivity. This observation aligns with findings from Pusch (2001) and Castellanos et al. (2008), who similarly noted that bentonite's hydraulic conductivity increases more rapidly when sodium is the predominant cation in the infiltrating solution.

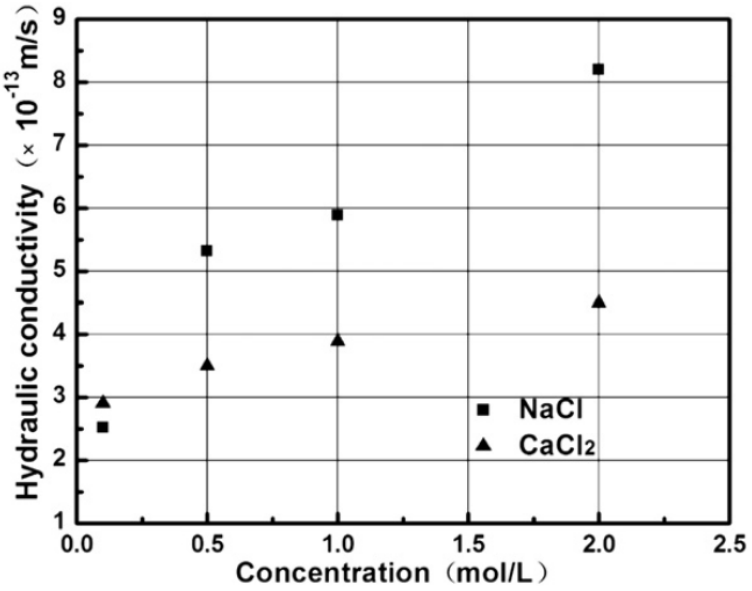

Figure 13 Comparison of influence of cation types on hydraulic conductivity of GMZ01 bentonite (Zhu et al., 2013).

3.5 Effect of salinity on the shear behavior

The impact of salt concentration on the mechanical properties of clay soils has been widely studied, indicating that increasing salinity can significantly affect soil behavior, particularly in terms of stiffness and strength. Salt ions in pore water influence the clay structure by shrinking the diffuse double layer around clay particles, which results in closer particle arrangements and increases the interparticle bonding. This process generally enhances soil stiffness (Van Olphen, 1963; Barbour and Fredlund, 1989; Mitchell and Soga, 2005; Thyagaraj and Rao, 2010, 2013).

Numerous experimental studies have been conducted to investigate the coupling effects between the ionic solutions in the pore water and mechanical behavior of soil (Di Maio and Fenelli, 1997; Musso, 2013; Chen et al., 2017). The shear strength of pure clays exhibits a significant sensitivity to variations in the composition of pore fluids, as these changes influence the electrochemical interactions between clay particles and the overall structural behavior of the clay matrix (Kenney, 1967; Mesri and Olson, 1971; Sridharan et al., 1991; Maio, 1998). Variations in pore fluid composition, such as changes in ionic concentration, pH, or type of dissolved ions, can alter the thickness of the electrical double layer around clay particles, influencing their repulsion or attraction. Although the effects of pore fluid chemistry on reconstituted clays have been extensively explored (Mesri and Olson, 1971; Barbour and Fredlund, 1989; Barbour

and Yang, 1993; Di Maio and Fenelli, 1997; Studds et al., 1998; Cuisinier et al., 2013), few studies have concentrated on the impact of salinization on the mechanical behavior of compacted and natural soils (Musso et al., 2003; Castellanos et al., 2008; Siddiqua et al., 2011; Musso, 2013). However, the effects of variations in pore fluid composition on the shear strength of clays remain insufficiently studied, and no definitive conclusions have been reached regarding their impact within the context of geological disposal.

While many studies considered the impacts of different chemical compounds on the geotechnical properties of clayey soils, there is limited information about the shear strength of clay liners interacting with chemicals (Sridharan and Venkatappa Rao, 1979; Anderson et al., 1985; Arasan, 2010; Ray et al., 2021). Sridharan et al. (2002) assessed the shear strength of remoulded marine clay that was saturated by various salt solutions. By increasing salt concentration, they observed an increase in undrained shear strength for kaolinitic soils, while the behavior was reversed for montmorillonite soils. Ayininuola et al. (2009) studied the saturated subsoil shear strength with various amounts of calcium sulphate. They reported that calcium sulphate salts and calcium ions can induce strong bonds between clay minerals, increasing the internal friction angle and effective cohesion. Moore (1991) investigated the influence of the pore solution chemistry on the residual shear strength of pure kaolinite and montmorillonite, observing that the concentration of Na^{+} or Ca^{2+} ions affected the residual shear strength. It is suggested that the increase in residual shear strength with higher salt concentration is due to enhanced interparticle bonding.

Di Maio and Fenelli (1997) considered the effects of NaCl solution on the residual shear strength for kaolinite and sodium bentonites and for the mixtures of both. In contrast to Moore (1991), they found that the mechanical behavior of kaolinite is not affected by pore fluid salinity. This is consistent with the test results of Wahid et al. (2011). However, Di Maio and Fenelli (1997) also reported that the residual friction angle for bentonite increased as the concentration of NaCl increased, and thus concluded that the enhanced residual shear strength was due to both the nature of clay minerals and the increase in effective interparticle stresses with the increase of salt concentration in pore water. Fang et al. (2019) performed an experimental study on bentonite and bentonite-kaolin mixture to investigate the effect of different concentrations of sodium

chloride on the shear strength. For both soils, the friction angle increased with salt concentration while the cohesion decreased. This observation was explained by the mineral-mineral contact and mineral-water-mineral contact for the clay particles connection. With increase in pore fluid concentration, the electric double-layer repulsion among soil particles decreased, thereby increasing the effective contact stress at the mineral-mineral contact and leading to increased consolidation settlement and a lower water content under vertical stress. This means a larger shear resistance at the mineral-mineral contact point and a thinner absorbed water layer at the mineral-water-mineral contact point, leading to a greater friction angle and a lower cohesion.

Barbour and Yang (1993) summarized osmotic consolidation tests conducted by Yang (1990), Ho (1985), and Barbour (1986) on remoulded and undisturbed samples of glacial till and glaciolacustrine clay, exposed to various solution concentrations. The samples were subjected to specific stress levels and then equilibrated with NaCl solution through diffusion. Following this, they were reloaded to higher stresses. When the water-saturated clay was exposed to NaCl brine, it underwent a decrease in volume. This volume change was accompanied by an apparent increase in preconsolidation stress and a decrease in compressibility, until the new preconsolidation stress was exceeded. Afterwards, the samples continued to consolidate along the same virgin compression line. Similar observations were reported by Barbour and Fredlund (1989). Ho (1985) also showed results for the samples remoulded with brine and then tested in water. A noteworthy observation was that submersion of the samples in water caused a decrease in volume under constant effective stress. Di Maio (1997) investigated the effects of exposure of water-saturated specimens of Ponza bentonite, alternately to pure water and saturated NaCl, KCl, or $CaCl_2$ solutions. Exposure to these three electrolytes produced consolidation of the specimens, large volumetric deformations, and an increase in residual shear strength. The effects of NaCl exposure were reversible when the samples were re-exposed to pure water, while those for KCl and $CaCl_2$ were not, due to ion exchange reactions. The irreversibility observed with KCl and $CaCl_2$ is mainly due to the stronger electrostatic interactions between the clay particles and the potassium (K^+) and calcium (Ca^{2+}) ions. K^+ ions have a lower hydration energy and are more tightly bounded to the clay particles than sodium (Na^+) ions, making their displacement less likely. Additionally, Ca^{2+} ions, being divalent, form even stronger bonds with the clay

particles, further reducing the reversibility of the effects. These stronger ion-clay interactions lead to more permanent changes in the clay structure when exposed to KCl or $CaCl_2$ solutions.

3.6 CHM modelling of clays

In recent years, chemo-hydro-mechanics has gained increasing attention in the field of Environmental Geomechanics. This discipline examines scenarios where, in addition to mechanical loads, environmental factors such as temperature changes or fluxes of heat and mass—often chemically, electrically, or biologically non-neutral—also play a role (Hueckel, 2005). It has long been recognized that the geochemical environment significantly influences the mechanical and hydraulic behavior of highly active clays (Mesri and Olson, 1971; Sridharan et al., 1986; Moore, 1991).

Several models have been developed to simulate hydro-chemo-mechanical coupling in saturated soils (Alonso et al., 1990; Gajo and Loret, 2003; Boukpeti et al., 2004; Hueckel, 2005; Liu et al., 2005; Shao et al., 2006; Guimarães et al., 2013).

Heidug and Wong (1996) extended Biot's equations and Darcy's law to develop an elastic model incorporating chemo-mechanical interactions, including water flow and salt diffusion in porous media, based on non-equilibrium thermodynamics. Hueckel (1997) introduced a chemo-plastic model that accounts for water adsorption/desorption, particle flocculation, and plastic strain during the consolidation and swelling of clay under isothermal conditions. Loret et al. (2002) proposed an elastic-plastic model that considers salt advection/diffusion and water mass transfer between solid and fluid phases, relying on thermodynamic principles. Loret and Simões (2005) applied the Clausius–Duhem inequality to derive coupled fluxes in balance equations. Hueckel and Hu (2009) further advanced a multi-scale formulation to describe chemo-mechanical behavior in sediments. More recently, Musso et al. (2020) developed a model based on elastoplasticity with generalized hardening to capture chemo-mechanical effects on the volumetric behavior of both active and inactive clays.

To study swelling behavior under chemo-mechanical interaction, researchers have employed the double-porosity model, which conceptualizes the medium as comprising microporous matrix blocks surrounded by fluid-filled macropores. Musso et al. (2013) explored the influence of double-structure effects on the chemo-mechanical behavior

of active clays, proposing a model that distinguishes between microstructural and macrostructural components, each characterized by distinct hydraulic pressures and osmotic suctions. Their approach incorporated mass exchange between these two domains. Della Vecchia and Musso (2016) compared single- and double-porosity models for simulating hydro-chemo-mechanical processes in active clays, concluding that while the double-porosity model requires more calibration parameters, it provides a more accurate representation of the initial delay in swelling displacement upon exposure to distilled water. Xu et al. (2017) applied a double-structure model to simulate the response of clay-rock repositories for nuclear waste under chemo-mechanical loading and unloading. Navarro et al. (2017) developed a hydro-mechanical model incorporating the chemical potential of water in both micro- and macrostructures to evaluate salt solution effects on bentonite swelling. Additionally, Yustres et al. (2017) demonstrated that integrating reactive transport models with hydrogeomechanical frameworks enhances the simulation of MX-80 bentonite behavior across different pore water chemistries, which is critical for designing bentonite barriers.

Cation exchange has been incorporated into various models of chemo-mechanical interaction in both saturated and unsaturated clays (Gajo and Loret, 2003; Guimarães et al., 2013; Idiart et al., 2020). Gajo and Loret (2003) introduced a model to account for volume change behavior in saturated clay upon contact with different pore water solutions due to cation exchange. Guimarães et al. (2013) explicitly incorporated cation exchange within a double-structure model for unsaturated expansive clays, distinguishing between macrostructural and microstructural levels. The total void ratio, e, is expressed as the sum of the macrostructural void ratio, e_M, and the microstructural void ratio, e_m. The macrostructure consists of aggregated particles and macropores, resembling a granular fabric, while the microstructure is governed by physicochemical interactions at the clay particle scale. Idiart et al. (2020) expanded the Barcelona Basic Model to incorporate cation exchange effects on the swelling behavior of both saturated and partially saturated bentonites.

Several studies have also explored the behavior of unsaturated expansive soils under physicochemical interactions (Gens and Alonso, 1992; Rahardjo et al., 2008; Chen and Hicks, 2013; Ma et al., 2016; Song and Menon, 2019). Gens and Alonso (2008) extended a low-activity clay model by distinguishing between microstructural and

macrostructural levels to describe the swelling behavior of expansive soils. Yan (2018) modified the Barcelona Basic Model (BBM) to evaluate the response of saturated soils to chemo-mechanical coupling by replacing matric suction with osmotic suction.

4. Boom Clay

4.1 Stratigraphy

The Boom Clay Formation is located along the river Rupel to the south of Antwerp (Figure 14). The river also lends its name to the Rupelian age. The sediments of the Boom Clay Formation were deposited during the Rupelian period (33.1 to 28.1 Ma) (Vandenberghe et al., 2014).

Boom Clay has been primarily used in the production of bricks and roof tiles. Even today, several quarries continue to operate in the Rupel region to extract this clay for industrial use. In addition to its industrial applications, the Boom Clay Formation is considered as a potential host formation for the disposal of highly active and long-lived radioactive waste in Belgium (ONDRAF/NIRAS, 2013). For this reason, its properties have been extensively studied over the past decades.

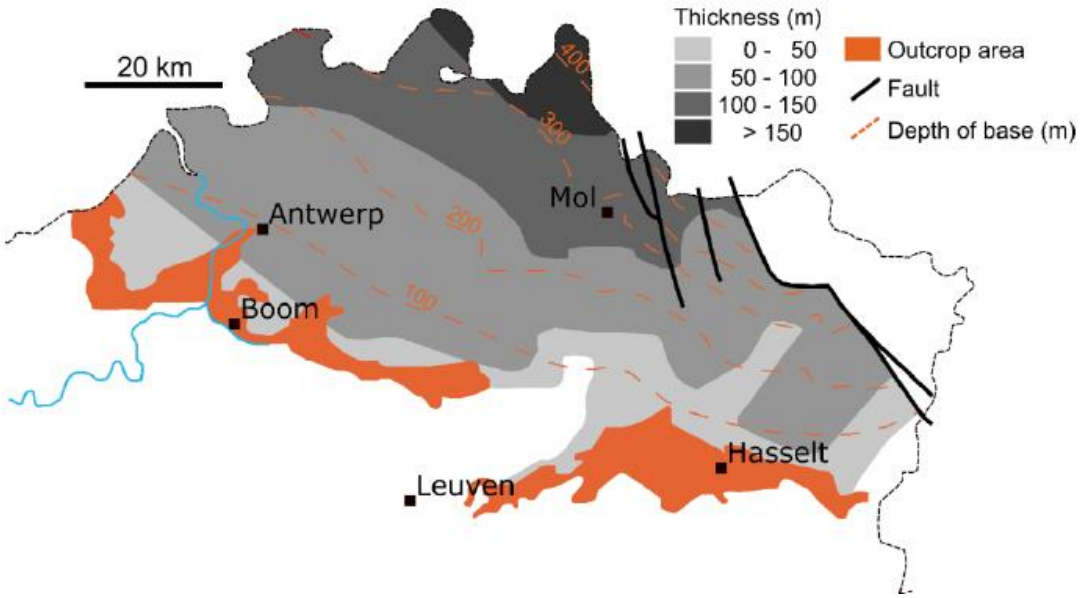

Figure 14 Geological map of the outcrop area of the Boom Clay Formation and its continuation in the subsoil of northeast Belgium (ONDRAF/NIRAS 2000).

The stratigraphy of the Boom Clay Formation has been extensively studied and documented (Vandenberghe et al., 2014). The Boom Clay sequence is divided into

three distinct lithological units, along with a fourth unit referred to as the Transition Formation (Figure 15).

At the base of the sequence lies the Belsele-Waas Member, which differs from the rest of the Boom Clay due to the presence of two thick silty layers. Initially, the boundary between the Belsele-Waas Member and the overlying Terhagen Member was defined at the base of the clay layer containing septaria horizon S10. However, a more recent decision redefined this boundary at the top of the uppermost thick silty layer, as it is more clearly identifiable on resistivity and natural gamma-ray well logs (Zeelmaekers et al., 2015).

The Terhagen Member consists primarily of grey clay interspersed with a few black-stained layers. In its lower part, dispersed carbonate is present, as evidenced by calcite deposits on the septae walls of three septaria horizons. A notable feature of this unit is a distinct pinkish to brownish layer, known as the "Red Band". The top of the Terhagen Member is defined by the sudden and systematic appearance of black bands in the overlying clay, creating a clear transition to the next unit. This boundary is also identifiable in natural gamma-ray logs, where a sharp increase in gamma-ray intensity marks the transition (Vandenberghe et al., 2014).

Above the Terhagen Member, the Putte Member is characterized by the systematic presence of black bands rich in organic matter of vegetal origin. This organic content is associated with significant pyrite deposits, with some septaria horizons, such as S50, featuring pyrite crystal formations on the septae surfaces. Near the base of this member, a distinctive "double layer" (DB) consisting of two successive coarse silt layers can be observed. The upper boundary of the Putte Member is determined based on resistivity and gamma-ray well logs, where a noticeable increase in resistivity values indicates a transition to a siltier lithology (Vandenberghe et al., 2014). The HADES Underground Research Facility (URF) is situated within the Putte Member of the Boom Clay Formation.

The silty unit above the Putte Member was initially referred to as a "Transition Zone" due to its gradual shift into the overlying formations. However, (Zeelmaekers et al. (2015) later reclassified this unit as a distinct lithological member, now known as the Boeretang Member. This unit contains progressively more silty clay than silt-poor clay bands, making it easily distinguishable. The top of the Boeretang Member, and

consequently the top of the Boom Clay as a whole, is defined where the characteristic alternations of the Boom Clay cease.

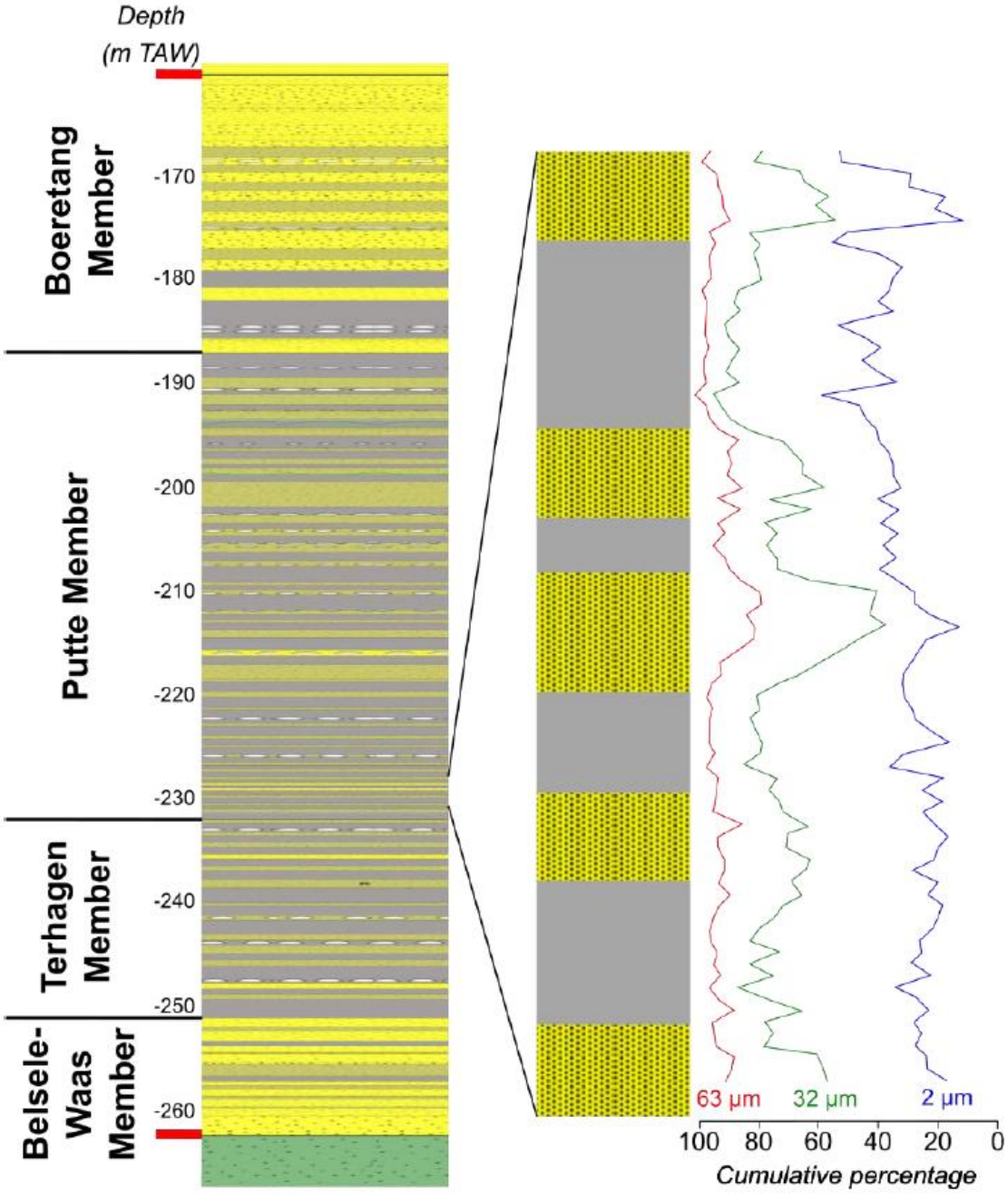

Figure 15 Micro stratigraphical log of the Boom Clay Formation (Vandenberghe et al., 2014).

4.2 Mineralogy

Boom Clay is a sedimentary deposit primarily composed of siliciclastic minerals, fossils, and organic matter (Honty, 2010). Its mineralogical composition has been extensively studied since the 1970s, driven by its use as a raw material, a lithostratigraphic marker, an indicator of relative sea-level variations, and its potential

as a host formation for radioactive waste disposal. The initial investigation into Boom Formation as a reference host for radioactive waste disposal (De Beer, 1978) prompted further research (Horseman et al., 1987; Frederickx et al., 2018; Awarkeh, 2023).

Non-clay minerals in Boom Clay are typically identified through optical microscopy, whereas quantification is generally performed using X-ray diffraction (XRD) analysis (Frederickx et al., 2021). However, clay minerals cannot be easily distinguished using optical microscopy and must be identified and quantified solely through XRD. The mineralogical composition of Boom Clay is presented in Table 2. It consists of 60% of clay minerals (20-30% of smectite, 30-40% illite/smectite and 10-20% kaolinite, and others) and 40% non-clay minerals (20% of quartz, 10% of feldspars, 5% of calcite, and others).

Zeelmaekers (2015)) quantified the clay mineralogy in the <2 µm fraction, assuming that this fraction represents the entire clay mineral population. However, recent findings by Jacops et al. (2020) indicate that clay minerals are also present in coarser fractions, and their composition differs from the <2 µm fraction.

This observation necessitates a dual approach: first, quantifying the clay minerals found in fractions larger than 2 µm to assess the uncertainty in the study of Zeelmaekers (2015) original quantification method. Frederickx et al. (2021) conducted a study to evaluate the representativeness of the <2 µm fraction for the entire 2:1 clay mineral population of the Boom Clay, as mineralogical analyses of this fraction are often extrapolated to the whole formation. By analyzing different size fractions, the study demonstrated that the >2 µm fraction contains a significantly higher proportion of illite compared to the <2 µm fraction.

Despite these compositional differences, the impact on the overall whole-rock mineral composition remains limited due to the small proportion of clay minerals in the >2 µm fraction. Additionally, Frederickx et al. (2021) quantified muscovite and glauconite in each fraction separately and combined the results to determine the whole-rock mineralogical composition. The main clay fraction, corresponding to particles <2 µm, is presented in Table 3, showing that this fraction is primarily composed of illite (14-30%), smectite + illite/smectite interstratifications (20-60%), and kaolinite (10-30%). Differences in mineralogical studies are mainly attributed to variations in analytical

methods or sample variability, depending on whether a single sample or an average over the entire Boom Clay Formation is considered.

Table 2 Mineralogical composition of the Boom Clay (wt.%).

Reference	Clay Mineral	Quartz	K-feldspars	Calcite	Pyrite	Others
Awarkeh (2023)	59.1 – 69.2	21.1 – 28.7	5.6 – 7.4	0.6 – 1	1.1 – 2.6	1.6 – 1.9
Frederickx et al. (2019)	49.3	35.5	7	0.7	1.3	6.3
Zeelmaekers et al. (2015)	51.6	34.4	6.9	1	1.6	4.5
De Craen et al. (2004)	30 – 60	15 – 60	1 – 10	1 – 5	1 – 5	6
Belanteur et al. (1997)	72	28	-	-	-	-
Merceron et al. (1993)	65	20 – 25	4 – 5	-	4.5	3.5
Horseman et al. (1987)	70	30	-	-	-	-
Decleer et al. (1983)	56	24 – 58	6.5 – 11	0 – 4.3	0.7 – 2.5	-

Table 3 Clay fraction mineralogy of the Boom Clay (wt. %).

Reference	Illite	Smectite	Illite/Smectite	Kaolinite	Others
Awarkeh (2023)	23.8 – 26.4	8.9 – 13.6	39.4 – 40.9	16.9 – 18.5	5.9 – 6.7
Frederickx et al. (2019)	21.8	23.5	35.5	7.1	12.2
Zeelmaekers et al. (2015)	22.1	27.5	29.7	15.3	5.4
De Craen et al. (2004)	21	44		28	11
Belanteur et al. (1997)	28	31	-	42	-
Merceron et al. (1993)	20 – 30	20 – 40	0 – 25	20 – 30	7.5
Horseman et al. (1987)	27	31	-	41	-
Decleer et al. (1983)	14 – 24	43 – 65	-	19 – 35	-

4.3 Microstructure

Several researchers have investigated the microstructure of Boom Clay using various techniques (Nguyen, 2013; Bésuelle et al., 2014; Gonzalez-Blanco and Romero Morales, 2017; Awarkeh, 2023; Al Mais et al., 2025b).

The Mercury Intrusion Porosimetry (MIP) technique is widely applied to qualitatively and quantitatively determine the pore size distribution (PSD) of soils by injecting mercury into the pore network as presented in Figure 16. These results indicate that the PSD of Boom Clay is unimodal, with a predominant micropore diameter ranging between 0.07 and 0.09 µm.

Scanning Electron Microscopy (SEM) observations on intact Boom Clay samples revealed that clay particles are densely stacked and oriented parallel to the bedding plane, as shown in Figure 17 (Nguyen, 2013). In contrast, in the perpendicular direction, juxtaposed particles were identified, highlighting the anisotropic nature of Boom Clay. The analysis of SEM images indicates that macropores are approximately 5 µm in size, while micropores measure around 0.5 µm.

Furthermore, X-ray Computed Tomography (X-ray CT) was employed by Bésuelle et al. (2014) to obtain high-resolution, non-destructive 3D reconstructions of Boom Clay samples before testing. Figure 18 illustrates that these samples contain a significant number of inclusions, which are not always visible to the naked eye. Additionally, the presence of pre-existing cracks within the Boom Clay samples prior to testing were identified, which may influence failure mechanisms by promoting fracture along these pre-existing cracks.

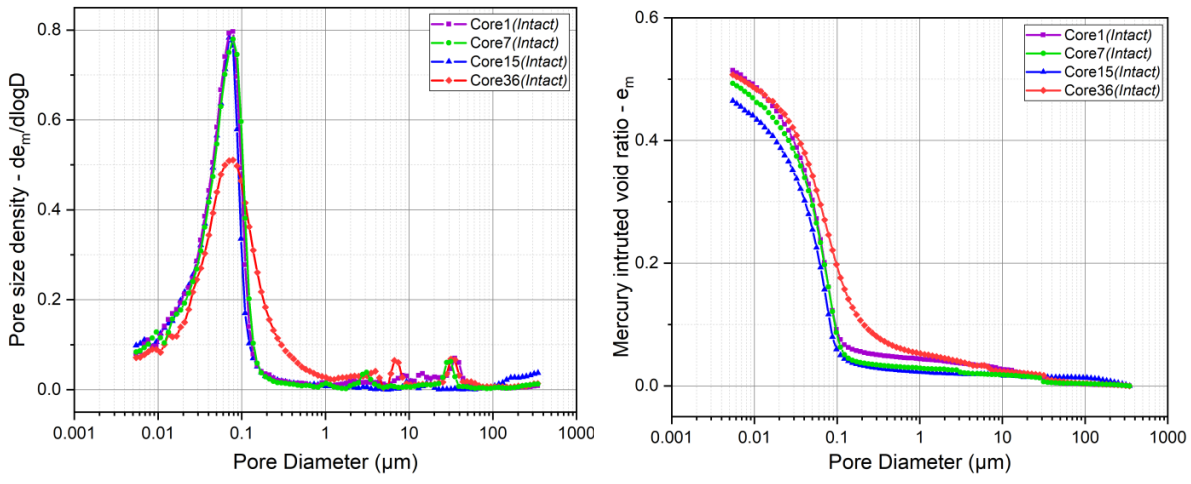

(a) (b)

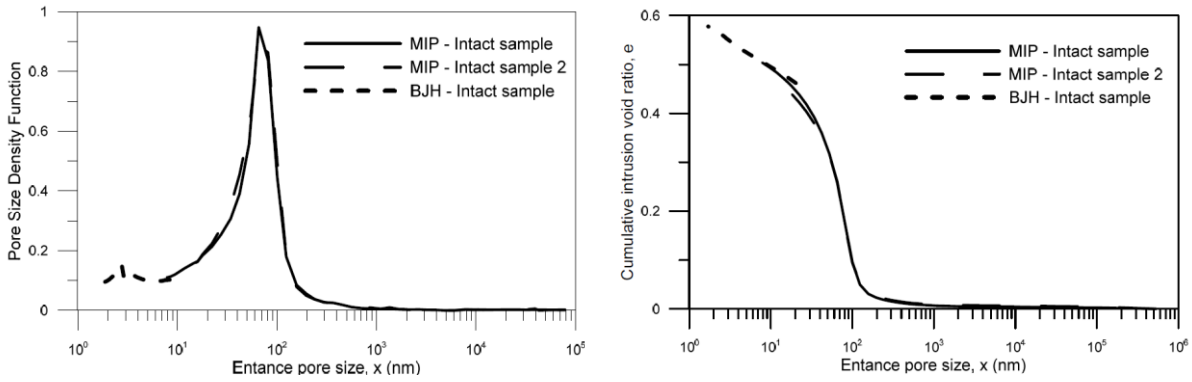

(c) (d)

Figure 16 (a) PSD function of intact Boom Clay, and (b) Cumulated intruded void ratio of intact Boom Clay obtained with MIP (Awarkeh, 2023; Gonzalez-Blanco, 2017).

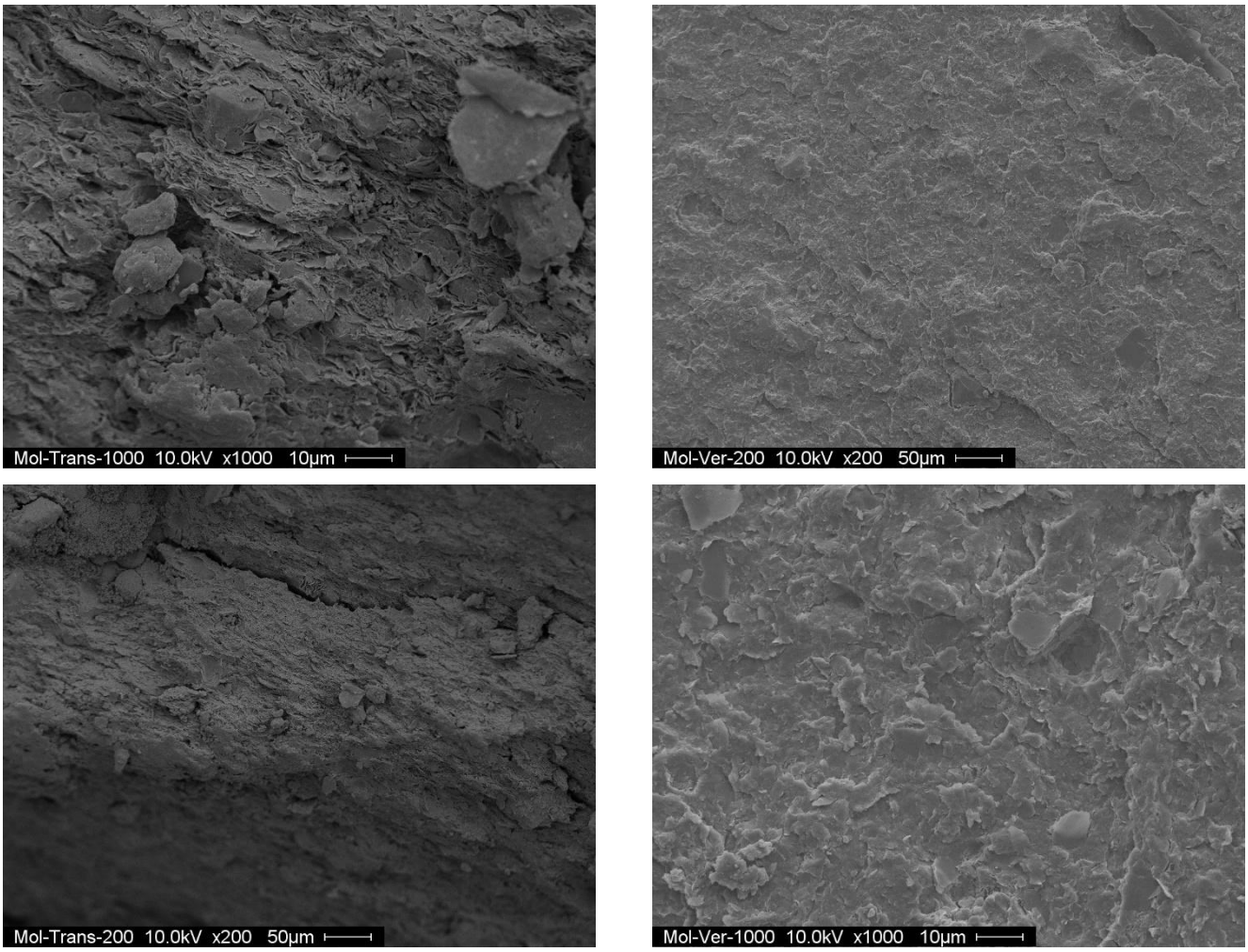

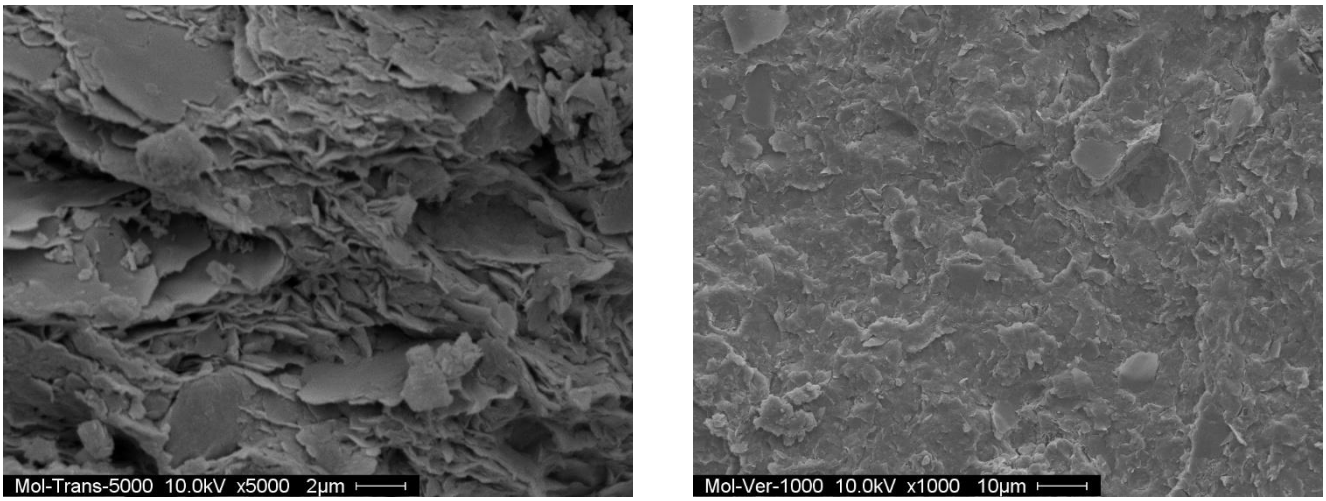

Figure 17 *SEM observations of intact Boom Clay (BM-223m) parallel (left) and perpendicular (right) to the bedding plane (Nguyen, 2013).*

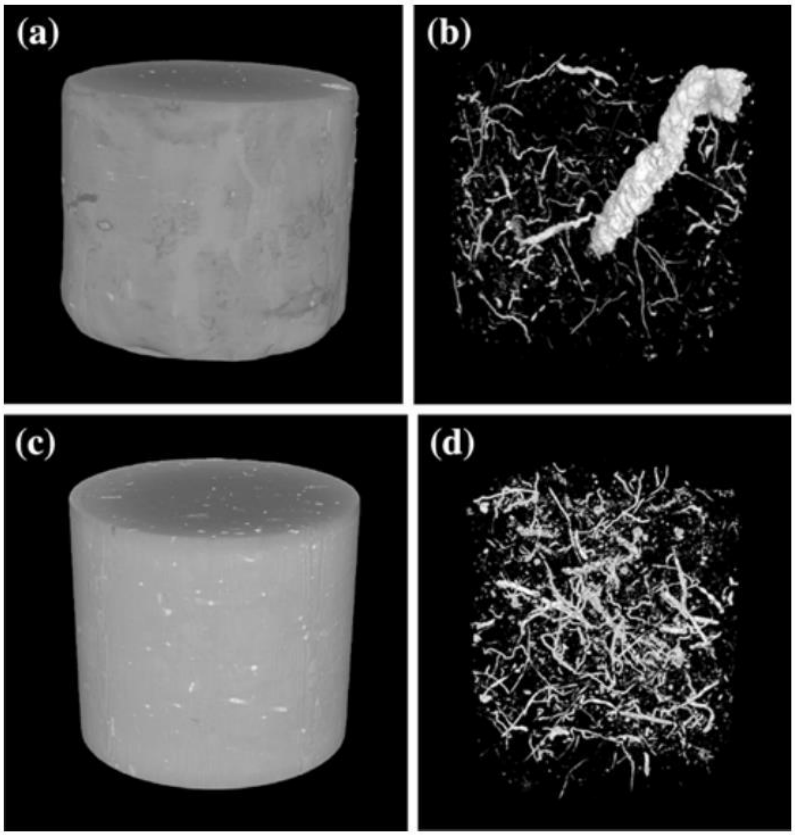

Figure 18 X-ray CT 3D reconstruction before testing of two specimens: (a) and (c) 3D reconstruction of the surface of the specimens; (b) and (d) 3D reconstruction of the inclusions inside the specimens (Bésuelle et al., 2014).

Nguyen (2013) conducted Mercury Intrusion Porosimetry (MIP) tests on intact Boom Clay saturated with synthetic Boom Clay water, as well as on two other samples where the in situ pore water was replaced with NaCl solutions at concentrations of 15 g/L (test BO3) and 30 g/L (test BO4). The samples were then subjected to an unloading–reloading–unloading path under low vertical stresses ranging from 0.05 MPa to 3.2 MPa. The results, presented in the Figure 19, show that intact Boom Clay exhibited a mono-modal pore-size distribution, with a dominant pore size of approximately 0.15 µm, classified as mesopores according to Romero et al. (Romero et al., 1999). However, for the samples percolated with NaCl solutions, the pore-size distributions became more or less bi-modal, with the creation of a new micropore population around 0.06 µm, while the mesopore population shifted slightly to a larger size of 0.25 µm. Under the combined effects of chemical and mechanical loading, it was observed that pores smaller than 0.06 µm remained unaffected. Meanwhile, the density of intermediate pores ranging from 0.06 µm to 0.2 µm decreased, whereas the density of larger pores, greater than 0.3 µm, increased. Moreover, when comparing the BO3 and BO4 samples, it was found that the density of the mesopore population was higher in BO4, which had a NaCl concentration of 30 g/L, than in BO3, which had a lower NaCl concentration of 15 g/L. This suggests that increasing the NaCl concentration enhances the microstructural modifications in Boom Clay.

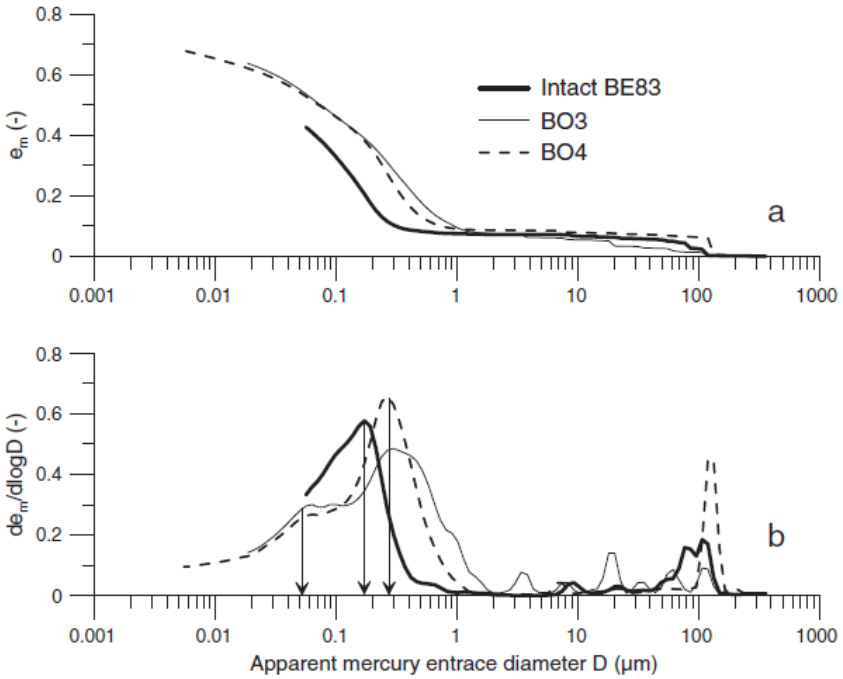

Figure 19 Results of MIP tests on Boom Clay: (a) cumulative curves, and (b) derived curves (Nguyen et al., 2013).

Mokni et al. (2014) investigated the combined effects of matric and osmotic suction on the microstructure and specific surface area of compacted Boom Clay. At low water content (w = 20%), an increase in osmotic suction led to a reduction in the dominant macro- and micropore peaks, as well as a decrease in the micropore fraction. Simultaneously, an increase in the macropore fraction was observed. Similar findings were reported by Castellanos et al. (2008) for compacted bentonite samples treated with sodium chloride (NaCl) saline solution. These changes were attributed to the shrinkage of micropores (Castellanos et al., 2006). The nitrogen adsorption-desorption technique also showed a decrease in the diameter of the dominant micropores as osmotic suction increased, along with a reduction in the specific surface area. This suggests that pore water salinity influences the size of clay particles.

Field emission scanning electron microscopy (FESEM) images of Boom Clay samples prepared with either distilled water or a highly concentrated sodium nitrate ($NaNO_3$) solution (π = 31 MPa) at w = 20% revealed a significant difference in the size of the clay particles (Figure 20). For the sample prepared with distilled water, the particles underwent considerable swelling, allowing them to merge due to their larger size (Figure 20a). These particles were softer due to the absorption of a substantial amount of water. However, for the sample prepared with sodium nitrate solution, the particles were smaller (Figure 20b), consistent with the findings of Mokni et al. (2014).

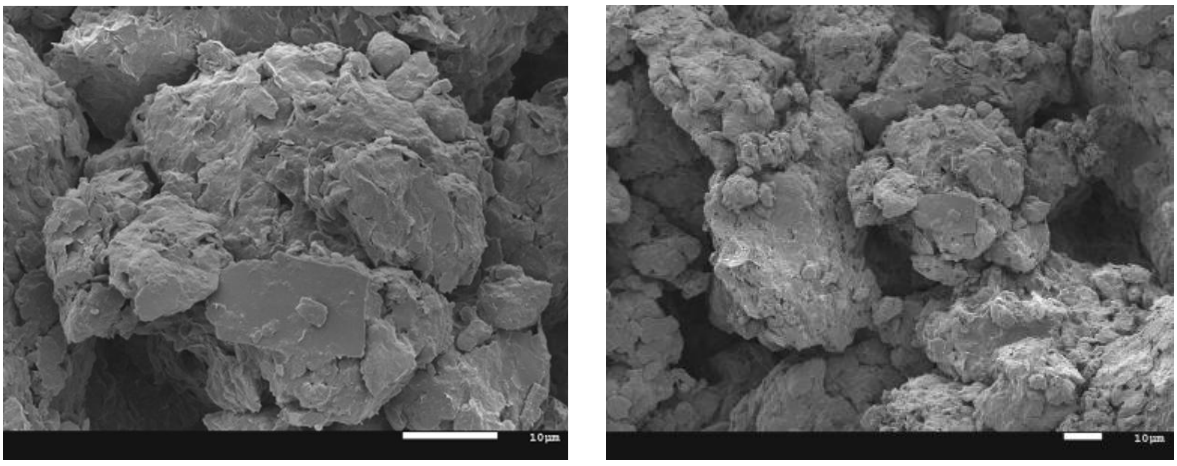

(a) (b)

Figure 20 FESEM photomicrographs of compacted Boom Clay samples at different osmotic suctions and w=20%: samples prepared at osmotic suctions (a) $\pi = 31\ MPa$; (b) $\pi = 0\ MPa$ (e.g., Mokni et al., 2014).

4.4 Geotechnical characteristics

Boom Clay is classified as a stiff, plastic, overconsolidated clay. It is characterized by very low permeability and relatively high swelling pressure. At the level of the Underground Research Laboratory (URL) in Mol, the total vertical stress and pore water pressure are approximately 4.5 MPa and 2.2 MPa, respectively (Bernier et al., 2011; Nguyen, 2013). The K_0 value, representing the coefficient of earth pressure at rest, has been determined through laboratory testing and various in situ methods, including pressuremeter tests, dilatometer tests, self-boring pressuremeter (SBP) tests, hydrofracturing tests, borehole breakout analysis, and back-analysis of stresses in the segmental concrete lining. The K_0 value for Boom Clay ranges between 0.7 and 0.8 (Horseman et al., 1987; Delage et al., 2007).

The fundamental geotechnical properties of Boom Clay —such as bulk density (ρ), dry bulk density (ρ_d), solid phase density (ρ_s), water content (ω), initial void ratio (e_0), and initial degree of saturation (Sr_0) — along with the initial in-situ conditions (site location, core depth, and lithological characteristics), are summarized in Table 4. These properties were obtained from the current study and supplemented by data from the literature.

The analyzed Boom Clay samples exhibit near-complete saturation, with a specific gravity ranging from approximately 2.65 to 2.7 Mg/m^3. Minor variations in physical properties are attributed to the inherent heterogeneity of Boom Clay and differences in depth and location, such as between the Mol site (190 to 293 m depth) and the Essen site (218 to 256 m depth). Additionally, the liquid limit (ω_L) of Boom Clay (BC) reported ranges from 56 to 70%, while the plastic limit (ω_P) varies between 19% and 23%. Consequently, the plasticity index (IP) falls within the range of 37 to 47 (Horseman et al., 1987; Lima, 2011; Gonzalez-Blanco and Romero Morales, 2017).

Table 4 Geotechnical properties of the Boom Clay obtained in this study and reported in the literature.

Core property				Parameters					
Reference	Site	Depth (m)	Member	ρ (Mg/m^3)	ρ_d (Mg/m^3)	ρ_s (Mg/m^3)	w $(\%)$	e_0 $(-)$	Sr_0 $(-)$
This study	Mol	225	Putte	2.05	-	-	20.2-23.4	0.54-0.62	0.94-1
Awarkeh (2023)	Mol	225	Putte	2	1.7-1.75	-	21-23.5	0.54-0.65	0.93-1
Gonzalez-Blanco (2017)	Mol	223	Putte	2-2.06	16.63-1.69	2.67	22.63-23.9	-	1
Bésuelle et al. (2014)	Mol	223	Putte	-	-	-	20-25	-	-
Lima (2011)	Mol	223	Putte	-	1.65-1.71	2.67	20-25	-	0.91-1
Deng et al. (2011)	Essen	218-256	Putte Terhagen	-	-	2.64-2.68	26.5-29.7	0.7-0.785	0.97-1
De Craen et al. (2004)	Mol	190-293	Transition Putte Terhagen Belsele-Waas	1.9-2.1	-	2.65	19-24	-	-
Horseman et al. (1987)	Mol	247	Terhagen	2.02-2.08	1.63-1.69	2.7	22.8-25.2	0.646	-

4.5 Pore water composition

The pore water of Boom Clay (BCPW) at the Mol site primarily consists of a 15 mM $NaHCO_3$ solution, with major cations such as Na^+, K^+, Mg^{2+} and Ca^{2+} present at concentrations that vary depending on the vertical position within the clay layer. Extraction of pore water from the Boom Clay formation has been conducted using both in situ and laboratory techniques.

For in situ extraction, piezometers are employed. These devices are installed at various orientations and depths within the clay, with filters positioned at different levels to collect pore water. Laboratory methods, such as mechanical squeezing and leaching, are also used to extract pore water. These techniques require careful sampling and preservation of clay cores to minimize potential geochemical alterations. The reliability and significance of the extracted data are evaluated through statistical analyses and

geochemical modeling, which have helped establish a reference composition for Boom Clay pore water at the Mol site. The pore water composition of Boom Clay is presented in Table 5.

This pore water is characterized by relatively high concentrations of dissolved organic carbon (78–263 mg C L^{-1}) and contains humic acids (HA) and fulvic acids (FA) with a wide range of molecular sizes. It also has a partial CO_2 pressure (pCO_2) ranging from $10^{-2.8}$ to $10^{-2.4}$ atm. The reference chemical composition of BCPW, derived from samples collected using piezometers in the HADES Underground Research Laboratory (URL), has been documented by De Craen et al. (2004).

Table 5 Pore water composition of Boom Clay (De Craen et al., 2004).

Element	mg/L	mmol/L
Na	359	15.6
K	7.2	0.2
Ca	2.0	0.05
Mg	1.6	0.06
Fe	0.2	0.003
Si	3.4	0.1
Al	$0.6x10^{-3}$	$2.4x10^{-5}$
B		
HCO_3^-	878.9	14.4
TIC	181.3	15.1
Alkalinity (meq/L)	15.12	
Cl	26	0.7
Total S	0.77	0.02
SO_4^{2-}	2.2	0.02
F	-	-

4.6 Physicochemical properties

The physico-chemical properties of Boom Clay have been extensively studied, both in the context of geological disposal research and its use as a raw material for industrial applications. One of the important physico-chemical properties of Boom Clay is its cation exchange capacity (CEC), which refers to the clay's ability to adsorb cations in a form that can be readily exchanged with competing ions (Bache, 1976).

Due to their negatively charged layers, clay minerals can retain cations on their surfaces. In the case of illite and mica, potassium cations are permanently fixed within

the interlayer spaces to partially compensate for the layer charge. The remaining charge, which is particularly significant in smectite, is balanced by cations that are not permanently fixed and can be easily replaced by competing ions.

Several studies have investigated the CEC of Boom Clay using different cationic complexes to replace adsorbed cations (Baeyens and Henrion, 1985; Fernandez and Quigley, 1985; Honty, 2010; Zeelmaekers et al., 2015; Frederickx et al., 2018). These studies report considerable variability in CEC values (Table 6), with average values ranging from 19.9 ± 3.1 cmol(+)/kg to 30.0 ± 3.9 cmol(+)/kg. The variations can be attributed to (i) differences in the methodologies used to determine CEC, (ii) variations in the clay content of the analyzed samples, and (iii) a lack of independent controls to validate the measured CEC values. The fluctuations in CEC are primarily influenced by the smectite content, which contributes approximately 90% to the total CEC, and thus vary depending on the sampling location within the Boom Clay profile at the Mol-1 borehole.

Frederickx et al. (2018) determined the CEC of Boom Clay samples from the Mol site using two different techniques. The copper(II) triethylenetetramine (Cu-trien) method (Meier and Kahr, 1999; Ammann et al., 2005; Honty, 2010), modified to account for Ca-bearing mineral phases (Dohrmann and Kaufhold, 2009), was used alongside the cobalt(III) hexamine (CoHex) method, which served as a reference technique (Ciesielski et al., 1997; Dohrmann and Kaufhold, 2009). The study reported an average CEC value of 22.2 ± 5.0 cmol(+)/kg.

For undisturbed Boom Clay, the primary exchangeable cations are Na^{+} (47%), Ca^{2+} (20%), Mg^{2+} (20%), and K^{+} (12%) (Honty, 2010; Bleyen, 2018).

Table 6 Summary of average CEC values of Boom Clay samples.

Reference	Borehole location	CEC (cmol(+)/Kg)	Ion changer
Frederickx et al. (2018)	HADES URF	22.2 ± 5	Cu-trien
Zeelmaekers et al. (2015)	ON-Mol-1	19.9 ± 3.1	Cu-trien
Fernandez et al. (2010)	HADES URF	26.7 ± 2.5	$CsNO_3$
Honty (2010)	HADES URF	21.8 ± 4.3	Cu-trien
Maes et al. (2003)	ON-Mol-1	20.4 ± 1.8	$^{137}CsCl$

Baeyens et al. (1985)	HADES URF	30.0 ± 3.9	Ag-thiourea
Baeyens et al. (1985)	HADES URF	23.3 ± 3.1	$^{45}Ca(NO_3)_2$
Baeyens et al. (1985)	HADES URF	24.4 ± 3.4	$^{85}Sr(NO_3)_2$

4.7 Hydro-mechanical behavior

4.7.1 Swelling pressure

Due to its clay mineral composition and overconsolidated nature, Boom Clay exhibits a significant swelling capacity. The swelling pressure is highly dependent on the dry density of soil. An increase in dry density (or a decrease in void ratio) reduces the distance between clay particles, increasing the mid-plane potential u, which in turn raises the swelling pressure.

Several researchers have measured the swelling pressure of Boom Clay using different techniques. Horseman et al. (1987) obtained values ranging from $\sigma_s = 0.3 - 1.7\ MPa$ using the zero-swell method. Sultan (2010) reported a swelling pressure of $\sigma_s = 0.48\ MPa$ with the swell-consolidation method. Coll (2005) determined values between $\sigma_s = 0.5 - 2.0\ MPa$ using the swell-under-load method, while Lima (2011) measured a swelling pressure of $\sigma_s = 3.7\ MPa$ via the swell-consolidation method.

To further investigate the swelling pressure, Cui et al. (2013) applied their unloading-reloading loop method to oedometer tests conducted on Boom Clay samples from both the Essen and Mol sites (Figure 21). A linear relationship between swelling stress and the void ratio just before unloading or reloading has been found. They estimated a swelling pressure of $1\ MPa$ for a void ratio of 0.6, corresponding to the initial state of Boom Clay.

The discrepancies in swelling pressure values across studies are primarily attributed to differences in sample extraction methods, variations in the saturation procedures applied before testing (which can alter the clay's microstructure), and the use of different measurement techniques.

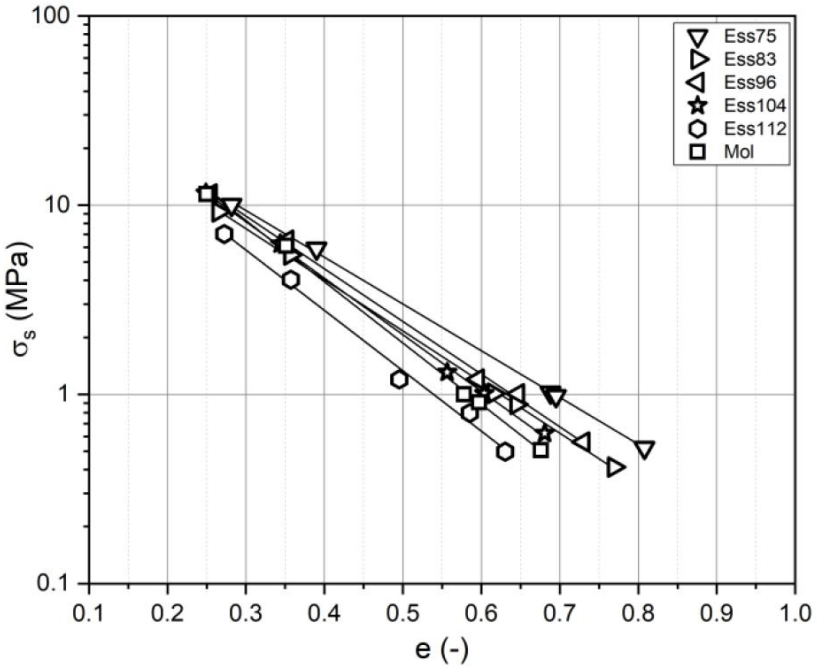

Figure 21 Swelling stress versus the void ratio just before unloading or reloading for Boom clay (from Essen and Mol sites) (Cui et al., 2013).

Numerous experimental studies have explored the chemical effects on the swelling behavior of clay (Studds et al., 1998; Calvello et al., 2005; Ye et al., 2014a). These studies consistently indicate that an increase in pore water salinity leads to a significant reduction in swelling pressure (Komine et al., 2009; Zhu et al., 2013) while simultaneously enhancing hydraulic conductivity (Castellanos et al., 2008; Zhu et al., 2013). While extensive research has examined the role of cation valence in ion exchange reactions during saline solution percolation, fewer studies have assessed the effects of hydrated radius and cation type on the swelling and hydraulic conductivity of saturated clay. Most of these investigations have focused on reconstituted clays or unsaturated materials. Furthermore, there is limited research (Mokni, 2011; Bleyen, 2018) on how saline plumes originating from bituminized waste influence the physico-chemical and hydro-mechanical behavior of Boom Clay.

4.7.2 Hydraulic conductivity

Hydraulic conductivity measurements of Boom Clay have been conducted for over 30 years as part of various national (Yu et al., 2013) and international research programs (Barnichon and Volckaert, 2000; Bernier et al., 2011; Ma et al., 2016). A vast dataset of hydraulic conductivity (K) values has been obtained through fluid flow and tracer experiments, both in situ at the HADES Underground Research Facility (URF) in Mol,

Belgium, and in laboratory settings using undisturbed clay core samples. These core samples were extracted from several deep boreholes across northeastern Belgium, covering an area of several thousand square kilometers.

Previous studies on Boom Clay consistently report hydraulic conductivity values in the range of approximately 10^{-12} m/s (Aertsens et al., 2004; Delage et al., 2007; Wemaere et al., 2008; Bernier et al., 2011; Deng et al., 2011; Al Mais et al., 2024). The horizontal hydraulic conductivity ($4.8 - 6.2 \times 10^{-12}\ m/s$) is higher than the vertical conductivity ($2 - 2.4 \times 10^{-12}\ m/s$), with an anisotropy ratio (K_h/K_v) of approximately 2.5. In other members of the Boom Clay Formation, such as Boeretang and Belsele-Waas, the presence of silty zones with higher sand content leads to increased hydraulic conductivity values ($K_h = 5 - 5.7 \times 10^{-12}\ m/s,\ K_v = 1.6 - 2.8 \times 10^{-12}\ m/s$). Conversely, the Putte and Terhagen Members are considered more suitable for underground geological disposal due to their lower permeability, homogeneity, and overall consistency. These findings were obtained using various experimental techniques such as small-scale core measurements (a few centimeters) to piezometer-scale (several decimeters) and even gallery-scale tests (spanning several meters to tens of meters). The interpretation of these measurements is based on Darcy's law, which describes a linear relationship between flow discharge and hydraulic gradient under steady-state conditions. However, Darcy's law is valid within certain limits, and deviations from Darcy-type flow have been widely reported in clayey materials (Horseman et al., 1987).

Another type of laboratory experiment used to determine hydraulic conductivity is the percolation test. In this setup, a clay sample is confined between two filters in a permeation cell and continuously percolated with Boom Clay interstitial water under a constant pressure gradient. Tritiated water (HTO) and iodide were used as unretarded tracers. The outflowing water is collected, and the tracer concentration is monitored over time. The tracer injection can be applied either at the inlet (boundary value problem, BVP) or in the middle of the clay sample (initial value problem, IVP). The imposed hydraulic pressure difference generally ranges between 1.23 and 1.35 MPa, and the hydraulic conductivity is derived from the measured water flux and the applied pressure gradient. Detailed descriptions of percolation experiments are provided by Aertsens et al. (2004).

Another common technique is the permeameter test, which involves placing undisturbed clay samples (5 cm long, 3.8 cm in diameter, with a sample volume of ~57

cm³) into a rigid stainless steel cylindrical cell with sintered stainless steel filters at both ends. Deionized water is injected at the bottom of the sample under a constant upward pressure of approximately 0.63 MPa. The outflowing water is collected in a sealed flask placed on a precision balance to monitor flow stability. The test is considered complete when measurements over five consecutive days indicate a stable flow through the clay sample (Wemaere et al., 2008).

For in situ hydraulic conductivity measurements, several techniques have been applied, including single-point piezometer tests, interference tests, and large-scale in situ tests. These methods are detailed in the work of Yu et al. (2013), who conducted a critical review of both laboratory and in situ hydraulic conductivity measurements for the entire Boom Clay Formation. Table 7 summarizes the hydraulic properties of the Boom Clay Formation.

Table 7 Summarize the hydraulic properties of the Boom Clay Formation.

Parameter	Unit	Value
K	*m/s*	1.5 – 4 x 10^{-12}
K_v	m/s	2 – 3.5 x 10^{-12}
K_H	m/s	4 – 5.5 x 10^{-12}
K_H/K_v	-	2.5

4.7.3 Compression behavior

When clay is subjected to an external load, it undergoes compression due to the rearrangement of particles and the expulsion of pore water. Upon unloading, if the clay remains in contact with water, it tends to swell as it reabsorbs moisture and attempts to recover its original volume. This swelling behavior is particularly pronounced in overconsolidated clays and expansive geomaterials, where volume changes can be substantial. The compressibility of soil is also strongly influenced by its composition, particularly particle size distribution and plasticity. In clayey materials, mineralogical composition plays a key role in determining both physicochemical interactions and mechanical responses, affecting consolidation and swelling behavior. These effects are reflected in the values of the compression index (Cc) and the swelling index (Cs). The compression index, which quantifies a soil's compressibility, is typically below 0.5 for natural clay soils (Wood, 1990; Mitchell and Soga, 2005). According to Mitchell and Soga (2005), soils are classified based on Cc values as follows: low compressibility (Cc < 0.2), moderate compressibility (0.2 ≤ Cc ≤ 0.4), and high compressibility (Cc > 0.4).

Similarly, the swelling index (Cs) is generally less than 0.1 for non-expansive soils and greater than 0.2 for expansive soils. These indices provide essential insights into soil behavior.

The compressibility and swelling behavior of clay are typically assessed through oedometer tests, which examine the relationship between applied stress and volumetric strain under controlled drainage conditions. During loading, soil undergoes compression due to particle rearrangement, which may result from sliding at interparticle contacts and/or grain crushing.

From an oedometer test, a consolidation curve is generated by plotting vertical strain or void ratio against the logarithm of time for each loading step, as illustrated in Figure 22. After the loading phase, unloading can be applied to observe the soil's rebound behavior. The compressibility parameters derived from the consolidation curve include the compression index (Cc) and the swelling index (Cs), which represent the slopes of the loading and unloading paths, respectively. Their determination follows the equations presented in Eqt. *(5)*.

Additionally, the yield stress (σ'_y) can be obtained from the compressibility curve using Casagrande's method, while the preconsolidation pressure (p'_c) is defined as the maximum stress that the soil has experienced in its history. These parameters are essential for understanding the deformation characteristics of soils and predicting its mechanical behavior under different loading conditions.

(5)
$$C_{c,s} = -\frac{de}{d\log\sigma'_v}$$

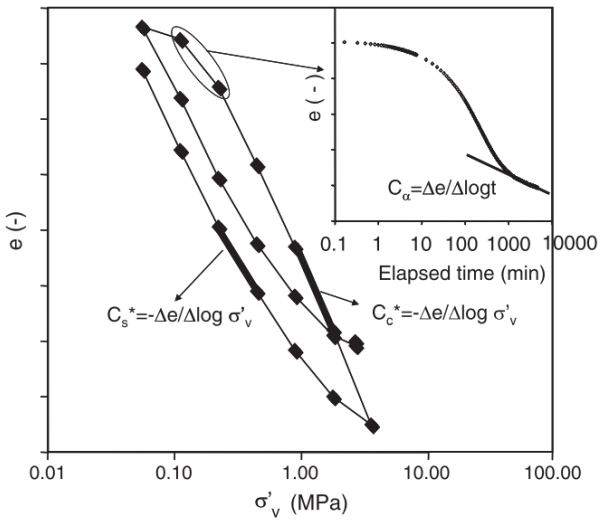

Figure 22 Consolidation and compressibility curves after saturation phase in oedometer tests (Deng et al., 2012).

Several studies have been conducted to characterize the Boom Clay by determining its volume change parameters (p_c', $C_c = \lambda \times \ln 10$ and $C_s = \kappa \times \ln 10$), as summarized in Table 8. The values reported in the literature, compiled in Table 8, consistently indicate a preconsolidation pressure ranging between 5 and 6 MPa.

Delage et al. (2007) highlighted the importance of conducting sample saturation under in situ effective stress conditions (approximately 2.5 MPa for Boom Clay) to prevent microstructural changes caused by swelling. In the selected tests presented in Table 9, no significant swelling was observed during saturation, ensuring that the microstructure and compression behavior remained unaffected. Swelling was effectively minimized by maintaining saturation under the in situ effective stress of 2.5 MPa in the studies by Deng et al. (2011), Le (2007), and Nguyen (2013); under 1 MPa in Coll (2005); under 3 MPa in Lima (2011); under low stress with a gradual increase in Horseman et al. (1987); and under low stress (<1 MPa) with reduced loading time in Baldi et al. (1988).

The influence of applied stress during saturation on preconsolidation pressure has been clearly demonstrated in multiple studies. When saturation was conducted under low applied stress (<0.1 MPa), significant swelling was observed—Le (2007) reported a swelling of 17% compared to the typical range of 0.7–2.3%, while Coll (Coll, 2005) found an 11% increase. This excessive swelling altered the clay's microstructure, subsequently affecting the preconsolidation pressure values, which decreased to 0.8 MPa (Lê, 2007), 2.1 MPa (Lima, 2011), and 0.43 MPa (Sultan et al., 2010) after saturation under low stress.

Table 8 Volume change parameters: preconsolidation pressure, compressibility and swelling parameters of the Boom Clay Formation.

Reference	Preconsolidation pressure (MPa)	κ (-)	λ (-)
Horseman et al. (1987)	6 MPa	0.046	0.178
Baldi et al. (1991)	6.0773 MPa	0.01279	0.1103
Sultan (1997)	0.37 MPa	0.0072	0.0728
Coll (2005)	5 MPa	0.075	0.218
Le (2008)	5 MPa	0.0145-0.0341	0.077-0.1173
Deng et al. (2011)	-	0.150	0.410
Lima (2011)	5.0	0.107	0.360
Nguyen (2013)	5.3	0.16	0.42

Table 9 Summarize of the volume change parameters of the Boom Clay Formation.

Parameter	Unit	Value
p_c'	MPa	5 – 6
C_c	-	0.05 – 0.15
C_s	-	0.25 – 0.40

Regarding the effect of saline composition on the compressibility of the BC, oedometer experiments on Boom Clay samples were conducted, initially prepared with distilled water or different concentrations of $NaNO_3$ solution under controlled matric suction (e.g., Mokni, 2011). Two samples were prepared with distilled water: one had a matric suction of 500 kPa, and the other was saturated (matric suction equal to zero). The results showed that as matric suction increased, the compressibility of Boom Clay increased. This finding contradicted the approach proposed by Alonso et al. (1990), even though the pre-consolidation vertical stress under unsaturated conditions was higher than that under saturated conditions. Furthermore, three samples were prepared with $NaNO_3$ solution at varying concentrations. An increase in osmotic suction resulted in a slight reduction in soil compressibility (e.g., Mokni et al., 2014).

To investigate the effects of mixed chemo-mechanical loading, oedometer tests were performed on Boom Clay samples that were initially saturated with distilled water and then exposed to different concentrations of $NaNO_3$ solution in two scenarios: In the first scenario, the sample was prepared with distilled water and exposed to a highly concentrated $NaNO_3$ solution under a vertical stress of 50 kPa (Mokni et al., 2014). After chemical consolidation occurred, the sample was loaded up to 1000 kPa. The decrease in sample volume was accompanied by an increase in pre-consolidation stress and a reduction in compressibility until the new pre-consolidation stress was reached. After this point, the sample continued to consolidate along the virgin compression line. These results were consistent with previous findings (Barbour, 1986; Barbour and Fredlund, 1989; Yang, 1990; Barbour and Yang, 1993).

In the second scenario, the sample was initially prepared with distilled water and exposed to a dilute $NaNO_3$ solution under a vertical stress of 200 kPa. Once chemical consolidation occurred, the sample was loaded to 1000 kPa and then exposed to a highly concentrated $NaNO_3$ solution. In this case, no increase in pre-consolidation stress was observed because the sample had already reached the elasto-plastic state

due to the high applied stress. The addition of the highly concentrated $NaNO_3$ solution did not induce volume reduction. This suggests that volume changes under chemical loading depend on the applied stress (Mokni et al., 2014). The magnitude of collapse for unsaturated clays decreases with saturation by saline solutions, especially when the applied stress is high, becoming insignificant in cases of very high applied stresses (Toll et al., 2008). Upon re-exposure to distilled water, the two samples showed minimal swelling, indicating that the effect of increasing pore water salinity is irreversible (e.g., Mokni et al., 2014).

Additional oedometer tests were conducted on Boom Clay samples initially saturated with $NaNO_3$ solution and exposed to distilled water in two scenarios: In the first, the sample was prepared with $NaNO_3$ solution and exposed to distilled water under a vertical stress of 500 kPa. The sample experienced a volume decrease (Mokni et al., 2014), confirming the findings of Barbour and Yang (Barbour and Yang, 1993). This suggests that clays are compressed under significant mechanical loading when exposed to a solution with a different salt concentration than that of the in situ pore water. If a sample is initially prepared with distilled water, its exposure to a saline solution will shrink the DDL, increase the effective stress, contract the clay particles, and lead to compression of the sample (Barbour and Yang, 1993). However, when clays are initially mixed with a saline solution, their exposure to distilled water causes the stiff, salinized particles to absorb water and lose rigidity, making the solid skeleton subject to contraction under significant mechanical stress (Mokni et al., 2014).

In the second scenario, the sample was initially prepared with $NaNO_3$ solution and exposed to distilled water under a vertical stress of 2000 kPa (4 times higher than in the previous study). No volume change was detected. This suggests that under significant mechanical loading (low porosity), the impact of changing pore fluid concentration becomes insignificant, and the volumetric deformation of clays under chemical loading remains highly dependent on the mechanical loading (e.g., Mokni, 2011).

4.7.4 Shear behavior

For most clay and claystone formations, shear strength is typically evaluated using triaxial tests conducted under various confining pressures. Research on the shear strength of Boom Clay has been ongoing for over four decades. Studies utilizing

standard drained and undrained triaxial compression tests indicate that Boom Clay exhibits a nonlinear stress-strain response, as illustrated in Figure 23. Additionally, loading-unloading triaxial tests (Rousset et al., 1989) reveal that Boom Clay follows an elasto-plastic behavior with a limited purely elastic zone. Additionally, Coll (2005) determined the uniaxial compressive strength of Boom Clay to be between 2 and 2.5 MPa.

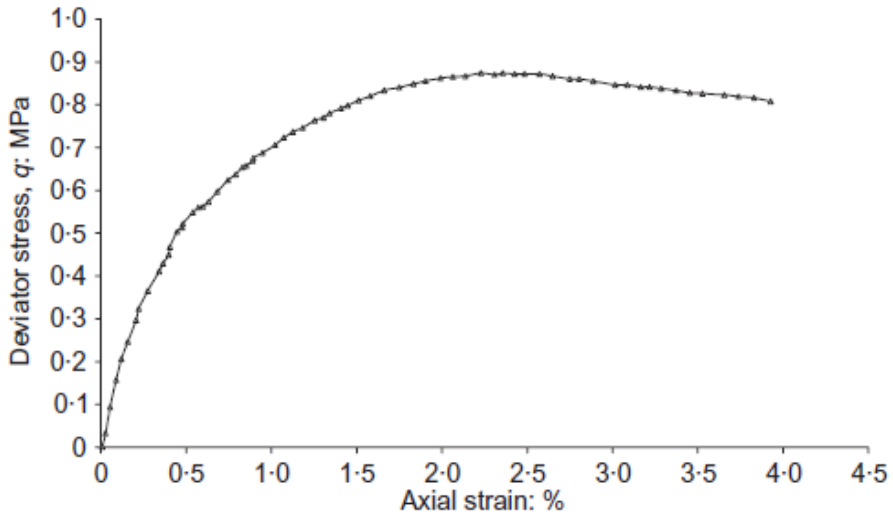

Figure 23 Stress-strain curve from drained triaxial compression test on Boom Clay (Bernier et al., 2007).

In triaxial drained tests on overconsolidated Boom Clay, the plastic zone is distinguished by a peak strength, separating the deformation process into plastic hardening and subsequent plastic softening. To characterize the shear strength of Boom Clay, multiple triaxial tests under both drained and undrained conditions have been conducted by various researchers (Horseman et al., 1987; Baldi et al., 1988; Rousset et al., 1989; Coll, 2005; Lê, 2007; Lima, 2011; Awarkeh, 2023).

Li (2010) conducted consolidated undrained triaxial shear tests to investigate the hydro-mechanical behavior of Boom Clay. The tests were carried out at an extremely low shearing rate (20 μm/min), with deformation and pore pressure continuously monitored. The results indicate that the shear strength under an effective confining stress of 2.5 MPa is approximately 3.0 MPa. Scanning Electron Microscopy (SEM) analysis of the clay's microstructure before and after shearing revealed a more pronounced directional arrangement in the post-shear samples, suggesting microstructural reorientation due to loading.

Lima (2011) performed three undrained triaxial tests on Boom Clay samples. The results indicate that increasing the confining pressure leads to a higher peak deviator stress. The tests were conducted at very low confining pressures, representative of an overconsolidated state, leading to strain-softening behavior, where the deviator stress initially peaks before decreasing to residual strength (Figure 24, left). The stress path in the mean effective stress–deviatoric stress plane during undrained tests for overconsolidated Boom Clay follows an almost linear trajectory, as shown in Figure 24 (right). The low compressibility of the clay-water mixture suggests that volumetric deformation in these tests is theoretically negligible.

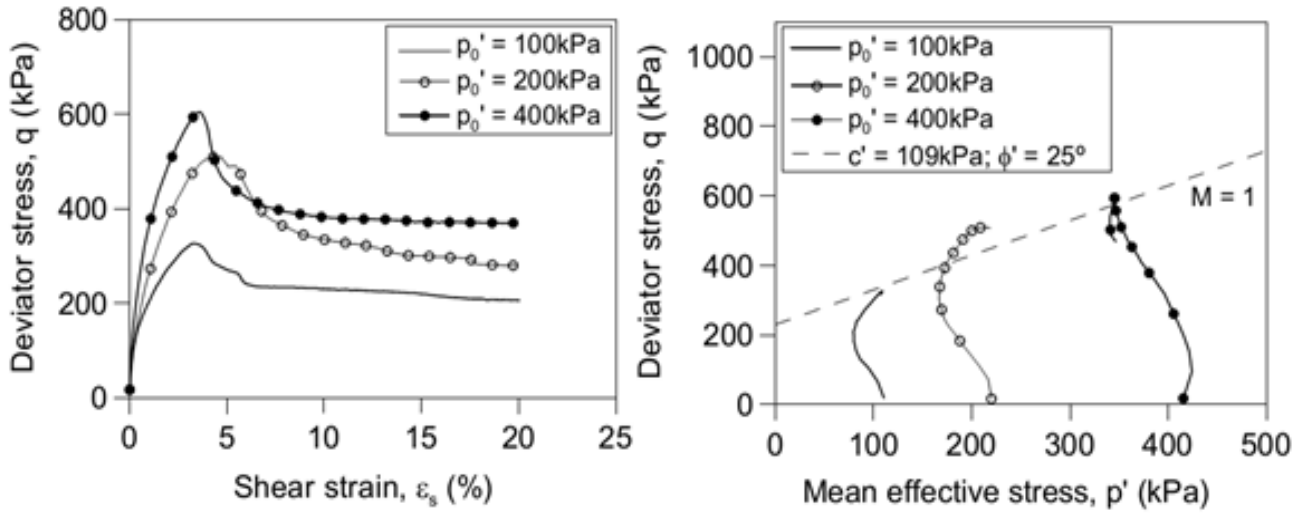

Figure 24 Undrained triaxial test at different confining pressures (Lima, 2011).

Various mechanical parameters are derived from triaxial tests under different conditions, as summarized in Table 10. Additionally, the failure envelope, presented in Figure 25, provides the shear strength parameters: cohesion (c') and friction angle (φ') as summarized by Dizier et al. (2018). The variability in the experimental data is attributed to differences in test conditions, particularly the saturation process, sample heterogeneity, and variations in applied shear rates. Based on the approach proposed by Petley (1999), a bilinear failure criterion is applied to the failure envelope of Boom Clay (Figure 23). Instead of a single set of cohesion (300 kPa) and friction angle (18°) values (Bernier et al., 2011), the $p' - q$ plane is divided into two distinct regions around a vertical effective stress of 2.5 MPa . The relevant strength properties of Boom Clay in drained conditions are presented in Table 10.

Table 10 Summarized elastic and shear properties of Boom Clay in drained and undrained conditions (after Dizier et al., 2018).

Parameter	Unit	Drained	Undrained
Poisson's ratio	-	0.125	0.4
Young's Modulus	MPa	120 – 350	500 – 900
Cohesion c'	MPa		
< 2.5 MPa		0.015	
> 2.5 MPa		0.60	
Friction angle φ	°		
< 2.5 MPa		25	
> 2.5 MPa		13	
Critical state slope M	-	0.6 – 0.870	

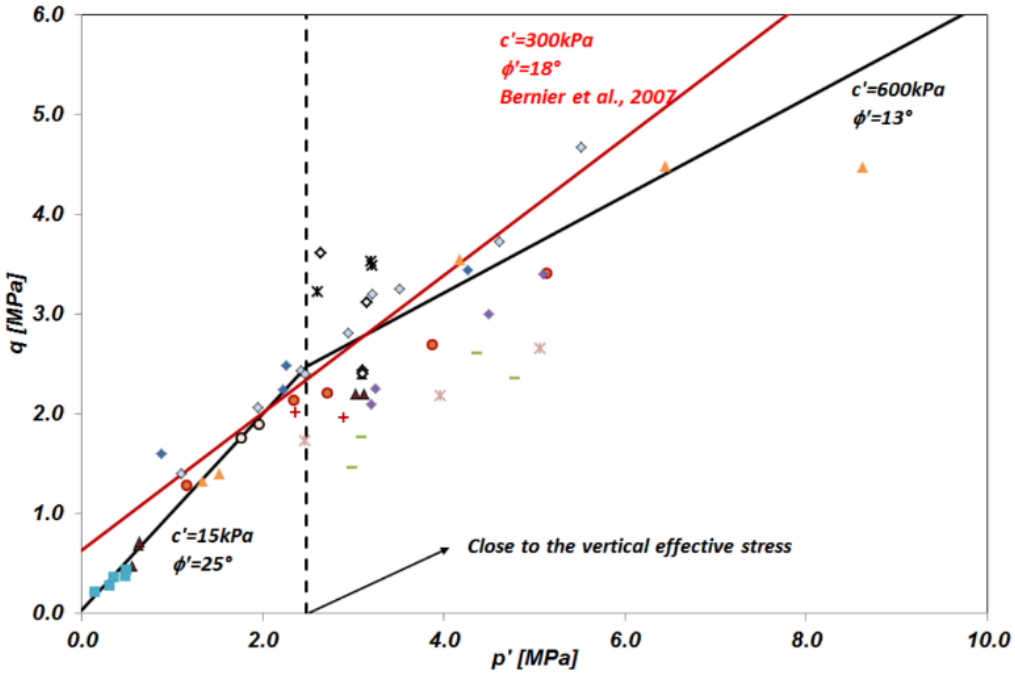

Figure 25 Failure envelope from drained triaxial compression test on Boom Clay (Dizier et al., 2018)

Few studies investigating the shear behavior of natural intact clays as BC. Mokni (2011) performed a series of direct shear tests on Boom Clay powder mixed with $NaNO_3$ solution. The results demonstrated that under partially saturated conditions, an increase in salinity caused a slight decrease in both compressibility and shear strength. Note that the samples prepared with $NaNO_3$ solution exhibited a reduction in water content at a given matric suction. This reduction in shear strength could be attributed to the lower water content of soil, which is equilibrated with the electrolyte at the given

matric suction. Therefore, the observed decrease in strength may be primarily due to the change in water content, which influences the mechanical response of the material under these specific conditions.

4.8 Constitutive modelling of BC

Over the past five decades, significant efforts have been made to develop more comprehensive models for soil behavior, driven by advancements in numerical methods and their mutual interaction with experimental research. However, achieving a perfect representation of soil behavior remains an ongoing challenge. Unlike materials in mechanical and structural engineering, soil exhibits complex mechanical responses, including nonlinearity, anisotropy, and time-dependent behavior when subjected to stress. Several factors influence soil behavior, with key aspects including soil composition (e.g., the proportion of fine-grained particles), loading history (such as overconsolidation ratio and stress path), and drainage conditions (Potts, 2002). Due to this complexity, numerous constitutive models have been developed to describe soil behavior with varying degrees of sophistication.

These models range from elastic models (e.g., Duncan and Chang, 1970) that assume reversible deformations, to elasto-plastic models (e.g., Roscoe and Burland, 1968) that account for permanent deformations beyond a yield surface, and elasto-viscoplastic models (e.g., Sekiguchi, 1976; Adachi and Oka, 1982; Borja and Kavazanjian, 1985) that incorporate time-dependent effects. The choice of model depends on the complexity of the problem and the key soil behaviors that need to be captured.

Concerning the constitutive modeling of Boom Clay, most conventional constitutive models have been employed with minor adaptations to better capture its hydro-mechanical behavior (Labiouse, 1997; Sultan et al., 2010; Della Vecchia et al., 2011; François et al., 2014; Hong et al., 2016).

Labiouse (1997) developed an adaptation of the Mohr-Coulomb model to incorporate the characteristics of pore water and the intrinsic drained properties of Boom Clay. This extended formulation highlights that the extent of the plastic zone, as well as the distribution of stresses and pore pressures, is influenced not only by the soil's strength parameters — commonly considered in total stress approaches — but also by the deformability of both the soil matrix and pore water. The developed model was applied to quantify the hydro-mechanical response of Boom Clay during the excavation of an

underground gallery, demonstrating the significance of pore water interactions in controlling stress redistribution and plastic deformation.

Further research has sought to refine these constitutive models by capturing the time-dependent behavior, anisotropy, and complex coupled hydro-mechanical interactions that characterize the Boom Clay.

Sultan et al. (2010) developed an elasto-plastic constitutive model that accounts for both initial and induced anisotropy in Boom Clay. The model is defined by eight parameters ($\kappa, G, \lambda, M, a, \mu, \alpha, b$) and introduces a normalized yield surface based on experimental results, particularly the preconsolidation pressure and the effective earth pressure coefficient (K_0). The proposed yield surface formulation incorporates changes in shape that occur during the hardening process. To capture the evolution of anisotropy, an anisotropic hardening rule was introduced, linking hardening behavior to the stress history and the ratio between shear and volumetric strains. Additionally, the radial increment of plastic loading (dR) was incorporated as a hardening parameter, further refining the model's ability to describe anisotropic behavior. Several simulations were performed to validate the model, yielding satisfactory results. However, as the model was developed based on triaxial stress conditions, its ability to fully characterize the anisotropic elasto-plastic behavior of natural clay remains incomplete. The need for further investigations, particularly considering more generalized stress states should be more clarified.

Della Vecchia et al. (2011) investigated the effects of hydro-mechanical coupling in both natural and compacted Boom Clay from a constitutive modeling perspective. To capture the complex behavior of these materials, the authors employed a fully coupled hydro-mechanical constitutive model based on elasto-plasticity with generalized hardening. The study integrated experimental data with fabric analysis using mercury intrusion porosimetry (MIP) to better understand the microstructural characteristics of natural and compacted Boom Clay. The findings were interpreted within the framework of classical elasto-plasticity with generalized hardening, focusing on the relationship between microstructural features and macroscopic behavior. The results highlighted the significant influence of microstructure on the phenomenological modeling of Boom Clay, demonstrating how structural differences between natural and compacted states affect the hydro-mechanical response of the BC material.

Ya et al. (2014) proposed a constitutive model that integrates a transversely isotropic elastic formulation with a modified Mohr-Coulomb criterion to comprehensively describe the mechanical behavior of Boom Clay. This model incorporates an elastic damage law that accounts for transverse isotropy, along with a plastic hardening law and a plastic damage law to capture the nonlinear elastic, hardening, and softening behavior of the material. The parameters of the proposed constitutive model were derived through direct analytical calculations and implemented in the finite element software ABAQUS. However, the authors emphasized the need for further experimental and theoretical studies to obtain additional data for a more in-depth understanding of the anisotropic damage behavior of Boom Clay.

To enhance the understanding of Boom Clay rheology, particularly regarding mechanical anisotropy and softening processes, François et al. (2014) developed a hardening/softening Drucker–Prager model — a frictional elasto-plastic model — that incorporates elastic and plastic cross-anisotropy. This model was implemented in the LAGAMINE finite element code (Collin et al., 2002). The proposed model introduces the elastic cross-anisotropy into an extended Drucker–Prager plasticity formulation, which accounts for hardening and softening behaviors. The plastic cross-anisotropy is introduced through a cohesion parameter that varies depending on the angle between the major principal stress and the normal to the bedding plane. The behavior is considered isotropic on the bedding plane, while the only anisotropic direction is perpendicular to the bedding. To properly model strain localization processes, a hydro-mechanical second-grade regularization method was applied. Numerical simulations using this model revealed the formation of shear bands around an excavated hole, with results that closely match the "chevron" fracture patterns observed in the field.

Recently, Hong et al. (2016) developed an enhanced constitutive model called the Adapted Cam Clay model (ACC-2), based on the Modified Cam Clay (MCC) model but incorporating two yield surfaces. The inner yield surface is an additional feature within the conventional outer yield surface, where elastic strains develop inside, and plastic strains initiate outside. This modification allows plastic strains to form even at small strain levels, improving the model’s ability to describe the behavior of natural stiff clays. ACC-2 employs a progressive plastic hardening mechanism, integrating a combined volumetric-shear hardening law associated with the inner yield surface. The formulation of the constitutive equations is derived from the consistency condition of

the inner yield surface. However, the model does not account for soil anisotropy. Despite this limitation, ACC-2 successfully captures several key characteristics of natural stiff clays, as observed in experiments, including:

- A limited elastic zone,
- The presence of strain hardening and softening,
- A smooth transition from elastic to plastic behavior.

The performance of the ACC-2 elasto-plastic model was assessed by simulating the behavior of natural Boom Clay under oedometer and triaxial conditions. The simulation results were then compared to experimental data from the literature, demonstrating the model's effectiveness in reproducing the key mechanical responses of Boom Clay.

5. Conclusion

This chapter has provided a detailed review of the key aspects governing the behavior of clay materials, with a particular emphasis on Boom Clay. The discussion began with the fundamental properties of clays, highlighting their mineralogical structure and the physicochemical interactions that control their response to mechanical and chemical changes. The specific characteristics of Boom Clay were then explored, covering its geotechnical properties, pore water composition, mineralogy, microstructure, and hydro-mechanical behavior. The various mechanisms influencing its swelling, permeability, volume change, and shear strength were critically examined, along with constitutive models used to simulate its behavior.

Furthermore, the effects of saline solutions on clays were analyzed, emphasizing their impact on swelling pressure, hydraulic conductivity, volume change behavior, shear strength, and microstructural alterations. The chapter also reviewed CHM modeling approaches, which are essential for accurately predicting clay behavior under complex environmental conditions.

Overall, this state-of-the-art review highlights the significant progress made in understanding clay behavior while also identifying knowledge gaps that warrant further investigation. Specifically, the literature review revealed that no studies have considered the occupancy of cations in percolated saline solutions. Additionally, most existing research has been conducted on unsaturated, reconstituted, or slurry soils, whereas no work has provided a comprehensive understanding of intact Boom Clay in

the context of radioactive waste disposal. To address these gaps, this thesis aims to perform laboratory experiments to characterize the CHM behavior of Boom Clay, develop a CHM model based on the experimental results, and conduct 2D plane strain simulations. These investigations will contribute to a more holistic understanding of Boom Clay's response under varying hydro-chemo-mechanical conditions.

III. Materials and experimental methods

1. Introduction

This chapter presents the characterization of the tested material along with the experimental techniques and protocols employed in this study. It first describes the Boom Clay samples, their conditioning with saline solutions, and the geochemical analyses performed to determine the cation exchange capacity (CEC) and sodium occupancy. The chapter then details the preparation techniques used to ensure sample consistency across experiments. Finally, the experimental procedures—including swelling pressure tests, salinization/desalinization tests, high-pressure oedometer tests, mercury intrusion porosimetry (MIP) tests, and triaxial tests—are presented to assess the hydro-mechanical behavior of Boom Clay under various conditions.

2. Materials

2.1 Boom Clay samples

Boom Clay (BC) core samples were extracted from the HADES Underground Research Laboratory (URL) in Mol, Belgium, at a depth of 223 meters. At this depth, the total vertical stress (σ_v) and pore water pressure (u) are approximately 4.5 MPa and 2.25 MPa, respectively (Bernier et al., 2011; Nguyen, 2013; X.-L. Li et al., 2023).

The core samples used in this study are obtained from two drilling campaigns in June 2017 and May 2023 from the Connecting Gallery, specifically from boreholes R78-79W and CG76-77W The borehole was oriented horizontally towards the west, extending to a final length of 43.3 meters at a depth of 223meters (Figure 26). To prevent potential desaturation, the extracted Boom Clay samples were immediately vacuum-sealed in thermo-welded aluminum-reinforced foil, as illustrated in Figure 27.

For this study, four core samples, each with a diameter of approximately 98 mm and lengths ranging from 500 mm to 1000 mm, were sent to the Navier Geotechnical Laboratory CERMES for testing. The primary difference between these cores lies in their horizontal distance from the intrados of the Connecting Gallery lining, measured

at 2.2 m, 13.2 m, 16.2 m, and 28.1 m, respectively. Table 11 provides a summary of the key characteristics of the Boom Clay cores analyzed in this study.

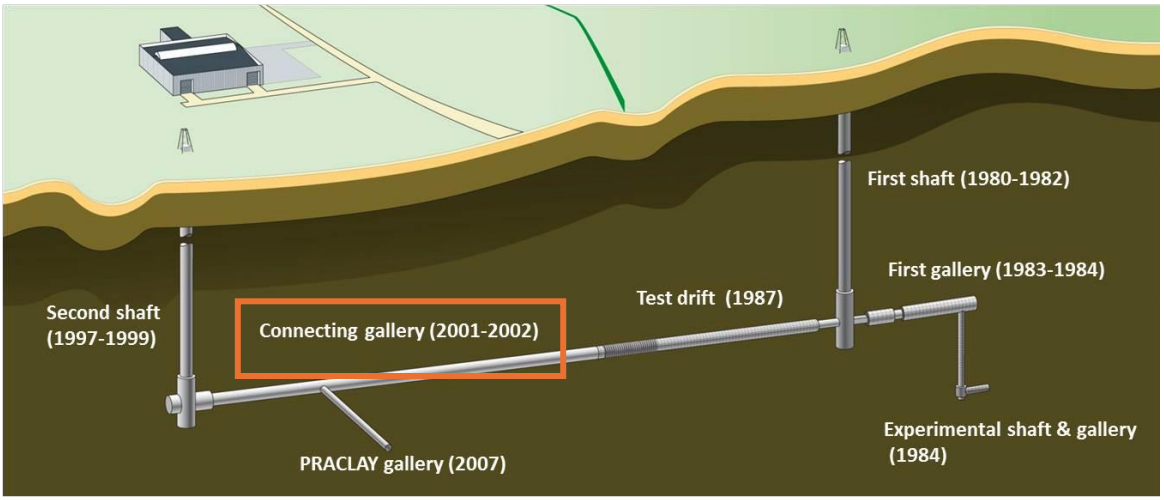

Figure 26 The HADES URL in the Boom Clay Formation at Mol, Belgium and location of cores (EURIDICE).

Figure 27 The Boom Clay cores vacuum-sealed in aluminum-reinforced foil.

Table 11 Details of Boom Clay cores used in this study.

Material	Core	Member	Date of drilling	Localization	Depth (m)	Length (m)	Diameter (m)
Boom Clay	28.1	Putte	2017	R78-79W_Core 2.2	225	0.9	0.1
	2.2	Putte	2017	R78-79W_Core 28.1	225	0.8	0.1

	16.2	Putte	2023	CG76-77W_Core 16.2	225	1	0.1
	13.2	Putte	2023	CG76-77W_Core 13.2	225	0.5	0.1

In this study, a series of characterization tests was conducted on the four Boom Clay cores. The bulk density (ρ) was determined using a geometric method, which involved measuring the dimensions of a specimen prepared with a cutting ring using a caliper. The water content (w) was measured by weighing the sample before and after oven-drying for 24 hours at 110 °C, following the NF P 94-049-2 (1996) standard. Based on these measurements, the initial void ratio (e_0) and initial degree of saturation (S_{r0}) were calculated.

The geotechnical properties obtained in this study align well with values reported in the literature, as summarized in Table 12.

Table 12 Geotechnical properties of Boom Clay cores used in this study.

Unit	Core property			Parameter			
	Site	**Depth**	**Member**	$\boldsymbol{\rho}$	$\boldsymbol{w}$	$\boldsymbol{e_0}$	$\boldsymbol{S_{r0}}$
		m		$\boldsymbol{Mg/m^3}$	%	**(-)**	**(-)**
This study	Mol	225	Putte	1.99 - 2.11	20 - 23.6	0.54 - 0.62	0.93 - 1

Additionally, a microstructural analysis was conducted using Mercury Intrusion Porosimetry (MIP), at the Navier Geotechnical Laboratory. Figure 3isplay the MIP results for intact samples from the four different cores. The mercury pressure applied during the test ranged from 3 kPa to 227 MPa, which allowed for the analysis of pore diameters spanning from 343 μm to 5 nm (Sun and Cui, 2020).

Figure 28(a) shows the intruded mercury void ratio, which ranges between 0.5 and 0.55. It is important to note that MIP does not capture all the pores in the sample, as the technique is limited by the pressures applied, which may not reflect the total void ratio of the sample accurately. From the MIP results, the pore size distribution of the Boom Clay (BC) samples is observed to follow a unimodal pattern. The pore sizes

predominantly range from 0.07 to 0.09 μm, as shown in Figure 28(b). The results are consistent across the four cores, indicating similar microstructural characteristics.

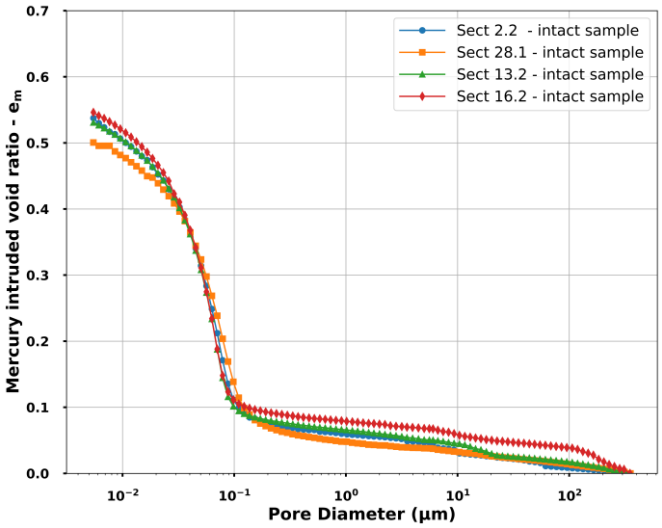

(a)

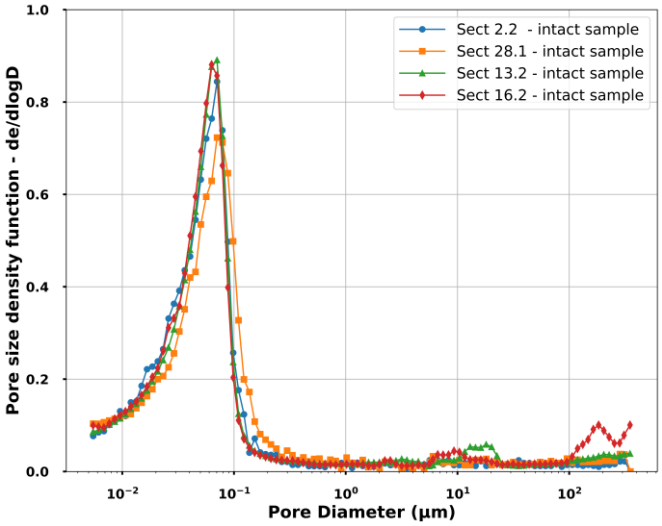

(b)

Figure 28 MIP results of Boom Clay cores used in this study: (a) Cumulative mercury intruded void ratio, (b) Pore size density.

2.2 Conditioning of Boom Clay samples

As previously mentioned, this study focuses on a specific intermediate-level radioactive waste form relevant to Belgium, known as Eurobitum. Eurobitum is a bituminized radioactive waste (BW) that primarily consists of precipitation sludges generated from the chemical reprocessing of spent nuclear fuel. A distinguishing characteristic of Eurobitum is its high content of $NaNO_3$ (typically between 20 and 30

wt%), along with notable amounts of $CaSO_4$ (4–6 wt%) and other chemical compounds such as CaF_2 and $Ca_3(PO_4)_2$ (Valcke et al., 2009).

The $NaNO_3$ plume will increase the Na^+ occupancy and Na^+ solution concentration of the Boom Clay surrounding the disposal gallery (e.g., Weetjens et al., 2010). The response of this $NaNO_3$-affected Boom Clay to the geomechanical (or CHM) perturbation induced by unrestricted swelling of the Eurobitum waste might be different from that of undisturbed BC. To study this, BC samples were percolated with salt solutions with different ionic composition and ionic strength. To explore a broad range of sodium occupancies and solution concentrations, five different salt solutions were considered. These solutions varied in total concentration, Na^+ and Ca^{2+} concentrations, and their respective ratios, all compared to the natural pore water chemistry of intact Boom Clay (see Table 13). In this study, only Na^+ and Ca^{2+} were examined. Sodium occupancy was calculated using (6), where ion concentration (meq/g) is divided by the total cation exchange capacity (CEC) of the clay. The ionic strength (IS) was calculated using Eqt.(7), where c_i represents the ion concentration and z_i represents the ionic charge.

(6) $$occupancy\ (\%) = \frac{concentration\ of\ exchangeable\ cation}{CEC} \times 100$$

(7) $$IS = \frac{1}{2}\sum_{i=1}^{n} c_i z_i^2$$

Table 13 represents a summary of the concentration and composition of each solution consisting of sodium nitrate $(NaNO_3)$ and calcium nitrate $(Ca(NO_3)_2)$. Additionally, a synthetic BC solution with a sodium bicarbonate $(NaHCO_3)$ concentration of 15 mmol/L (simulating in situ BC pore water chemistry (De Craen et al., 2004), was investigated as a reference for comparison purposes. It is worth noting that the cation occupancy refers to the total contribution of a specific cation to the overall exchangeable cations in the clay material. For instance, a 90% sodium occupancy implies that 90% of the exchangeable cations in the sample are sodium, while the remaining 10% consist of magnesium, calcium, potassium, and other elements.

Table 13 Saline solutions used in this study.

Solution	Na^+ - Occupancy (%)	$NaNO_3$ $(mmol/L)$	$Ca(NO_3)_2$ $(mmol/L)$	Ionic Strength (M)	Pore Volume replacements
1	60%	900	70	1.0	3
2	60%	1600	230	2.0	6
3	90%	2000	-	2.0	5
4	20%	320	340	1.0	3
5	10%	165	400	1.0	3

Higher sodium occupancies (60% and 90%) and total concentrations (1 M and 2 M) were derived from the work of Weetjens et al. (2010), who used coupled geochemical and transport models to predict the evolution of Na^+ concentration and occupancy for a hypothetical Eurobitum disposal in Boom Clay. The lower Na^+ occupancies (10% and 20%) with a 1 M total concentration were arbitrarily selected. Additionally, a natural reference system with a Na^+ occupancy of approximately 35 ± 7% (Frederickx et al., 2018)—representing the initial sodium occupancy in Boom Clay in contact with a 15 mM $NaHCO_3$ BC synthetic solution was included in the study (De Craen et al., 2004). Recent findings by Honty et al. (2022) from experimental investigations on Boom Clay pore-water chemistry confirm that present-day BC pore water is a dilute $NaHCO_3$ solution with a concentration ranging between 10 and 20 mM and an alkaline pH slightly above 8. To estimate the sodium occupancies and concentrations under equilibrium conditions, the equations proposed by Baeyens et al. (1985) were applied to define the composition of the (Na,Ca) nitrate solutions used for conditioning Boom Clay samples to 60% and 90% occupancy at total concentrations of 1 M or 2 M. Additionally, to determine the number of pore volumes of percolation solution (with $NaNO_3$ as the dominant solute) required to achieve high sodium occupancy in Boom Clay cores, a geochemical code was employed to compute the necessary pore volume replacements.

The geochemical modeling calculations were performed by L. Wang, SCK CEN, using *The Geochemist's Workbench (GWB)* software (Bethke, 2022). The thermochemical database used was the *Thermoddem* database (Blanc et al., 2012), version V1.10_15Dec2020, available at https://thermoddem.brgm.fr/.

The chemical model used in this study consists of the clay mineral composition and pore water composition in equilibrium with the clay. The mineralogical composition of Boom Clay was simplified based on previous mineralogical studies (Frederickx et al., 2021), while the current reference chemical model was adopted from Wang et al. (Wang et al., 2023). The mineral assemblage representing Boom Clay includes seven key minerals: quartz, kaolinite, chlorite, calcite, dolomite, siderite, and pyrite. When equilibrated with pore water, this assemblage successfully reproduces the observed geochemical characteristics of in situ pore water sampled at the Mol site in Belgium (Honty et al., 2022). Cation exchange properties of Boom Clay were also incorporated into the model, with data on selectivity, cation exchange capacity (CEC), and cation occupancies sourced from Frederickx et al. (2018). For equilibrium calculations, one liter of pore water (equivalent to one pore volume) was equilibrated with a cation exchange capacity corresponding to 4 kg of clay, mimicking a porosity of 20 wt%. Given that Boom Clay has a CEC of 22.2 cmol/kg (2018), the model clay was assigned 0.88 eq CEC (4 × 0.22 eq) in the system.

To condition the clay core to achieve the target Na^+ occupancies, three scenarios were considered:

1. Exposure to 2 M $NaNO_3$ to attain 90% Na^+ occupancy.
2. Exposure to 1 M $NaNO_3$ to attain 90% Na^+ occupancy.
3. Exposure to a mixed solution with 1 M ionic strength (comprising 856 meq/L $NaNO_3$ and 144 meq/L $Ca(NO_3)_2$) to achieve 60% Na^+ occupancy.

GWB was configured to allow the three different inlet solutions to "react" with the model clay, which included clay minerals, cation exchange sites, and the initial Boom Clay pore water in the first pore volume. Reaction path calculations were performed using the "flush" model setup, enabling the inlet water to gradually replace the original pore water until the desired sodium occupancy was achieved.

The key results of the equilibrium calculations are summarized as follows (see Figures Figure 29, Figure 30 and Figure 31):

1. Approximately 4.5 pore volumes (pv) of 2 M $NaNO_3$ were required to reach 90% Na^+ occupancy in the clay core (Figure 29).
2. Approximately 10 pv of 1 M $NaNO_3$ were needed to reach 90% Na^+ occupancy (Figure 30).
3. Approximately 2.6 pv of a solution containing 856 meq/L $NaNO_3$ and 72 mM $Ca(NO_3)_2$ were needed to attain 60% Na^+ occupancy in the clay core (Figure 31).

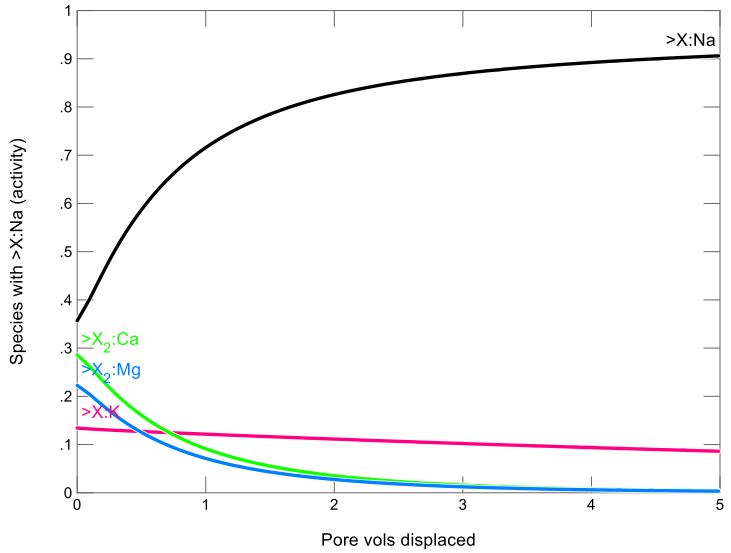

Figure 29 Cation exchange occupancies as function of displacement of pore volumes of inlet pore waters. Inlet concentration: High IS: 2 M $NaNO_3$.

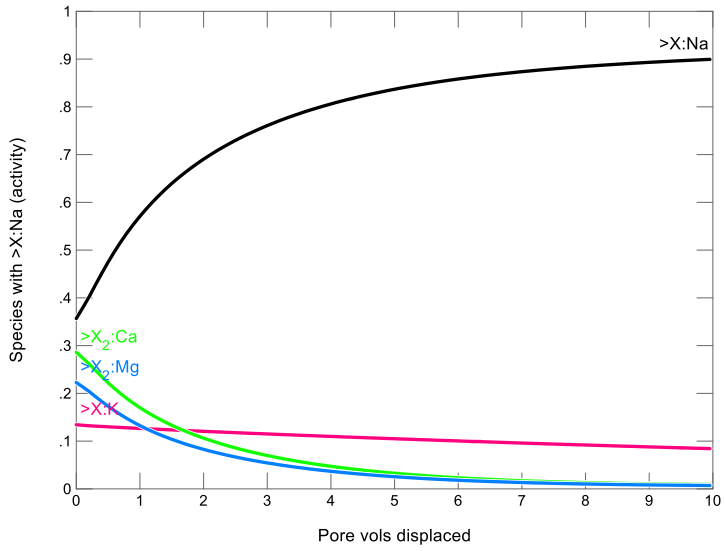

Figure 30 Cation exchange occupancies as function of displacement of pore volumes of inlet pore waters. Inlet concentration: Medium IS: 1 M $NaNO_3$.

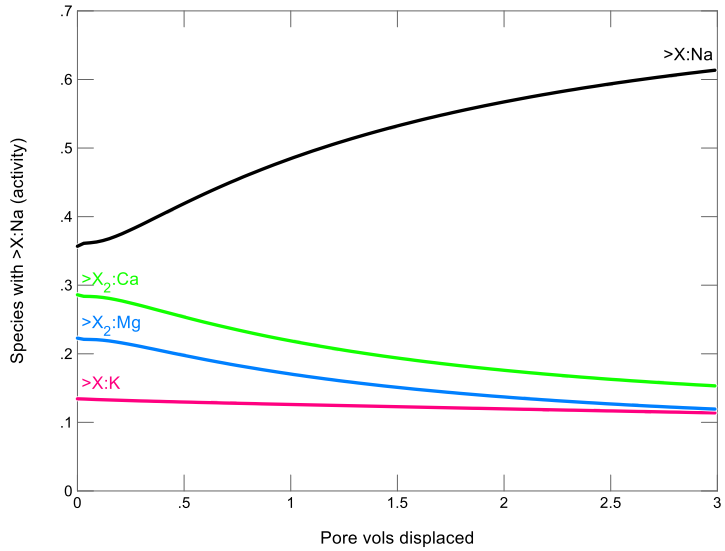

Figure 31 Cation exchange occupancies as function of displacement of pore volumes of inlet pore waters. Inlet concentration: Medium IS: 856 meq/L NaNO3 and 72 mM $Ca(NO_3)_2$.

2.3 Geochemical analysis

Before initiating the experimental program, a geochemical analysis was conducted on Boom Clay samples that had been previously conditioned by percolation with various saline solutions. This analysis aimed to determine the cation exchange capacity (CEC) of the clay and the actual sodium occupancy of Boom Clay.

For this purpose, five undisturbed Boom Clay samples (1, 2, 3, 4 and 5) were prepared with a diameter of 50 mm and a length of 10 mm. These samples were placed in oedometer cells and subjected to an effective stress of 2.25 MPa correspond to the effective stress at the HADES URL level. Each sample was successively percolated with solutions containing high sodium occupancies (Na-percolated) and solute concentrations, as summarized in Table 13. The percolation process was carried out using a constant pressure and volume (CPV) and an interface cell, where the injected solution volume was carefully monitored.

The clay cores were considered to have reached equilibrium with the percolation solution once the required pore volume number for a given solution was achieved. At this stage, the clay was expected to transition into a nearly homoionic sodium clay. Throughout the experiment, percolated water was collected at the outlet, ensuring a volume of 10–20 mL was available for cation analysis. To prevent biochemical alterations, the water samples were stored in a refrigerator until further analysis. Moreover, the chemical composition of the water collected from the clay samples was analyzed using Inductively Coupled Plasma (ICP) to quantify the cations present in the solution (Varian 720-ES ICP-OES, Agilent, Santa Clara, California, USA). If the clay reaches full equilibrium with the injected solution after percolating the required pore volume, the cation occupancy of the clay should match that of the injected solution.

Following the percolation phase, the oedometer cells were dismantled, and the clay cores were carefully extracted using a manual press inside an argon-filled glovebox to prevent oxidation. Each core was then manually sliced into 14 cross-sections, each approximately 2 mm thick and tested as follows:

- The water content of each section was determined gravimetrically by weighing the slices before and after drying at 120 °C overnight, repeating the process until a stable weight was achieved. In general, this lasted for 4 days.
- A clay powder was prepared from each slice by drying at 70 °C for one week in an anaerobic glovebox (under Ar atmosphere) to avoid oxidation. Once dried, the slices were removed from the glovebox, crushed using a mortar and pestle, and sieved to a grain size of <0.125 mm. The samples were then stored in a desiccator until further characterization, particularly for CEC determination and cation occupancy analysis.

- In addition, the final 10–20 mL of percolated solution, collected from the upper base of the oedometer tests after complete exchange with the sample, was analyzed using ICP-AES to determine sodium and calcium concentrations. This analysis allowed for a comparison between the Na and Ca concentrations in the percolated solution and those in the initial percolation (inlet) solution.

The cation exchange capacity (CEC) was measured using clay powder obtained from the top, center, and bottom of the percolated clay cores. The $[Cu\ Trien]^{2+}$ method, based on copper (II) triethylenetetramine as an index cation, was applied following the procedure of Amman et al. (2005) and previously used for Boom Clay by Honty (2010). A 0.01 M solution of $[Cu\ Trien]^{2+}$ was prepared to exchange cations in the clay with Cu^{2+}. Different masses of dried clay (100, 200, and 300 mg) were mixed with 40 mL of distilled water and 10 mL of $[Cu\ Trien]^{2+}$ solution, then ultrasonically dispersed and shaken for 30 minutes. After centrifugation, the concentration of $[Cu\ Trien]^{2+}$ in the supernatant was determined using UV-VIS spectrophotometry (Perkin Elmer, Lambda 40) by measuring absorbance at 577 nm. In addition, 250 mL of the supernatant was diluted using 4.75 mL of deionized water, after which the exchangeable cations, the index cation, and sulfur were measured by ICP analysis (Varian 720-ES ICP-OES, Agilent, Santa Clara, California, USA). The amount of adsorbed $[Cu\ Trien]^{2+}$ was calculated using Beer-Lambert's law with a molar absorption coefficient of 0.245 $dm^3\ mol^{-1}\ cm^{-1}$. Finally, the CEC was determined as the difference between the added and non-adsorbed $[Cu\ Trien]^{2+}$, and the average CEC was computed from the values obtained for different clay masses.

Additionally, the concentration of key cations commonly found in Boom Clay (Na^+, Ca^{2+}, K^+, Mg^{2+}, and Sr^{2+}) was measured in the solutions obtained from the CEC analysis. These concentrations were used to calculate the cation occupancy of the sodium-exchanged clay cores, following the approach of Bleyen et al. (2018). A correction was applied to the Na^+ concentration by subtracting the amount of Na^+ present in the pore water from the total Na^+ measured in the CEC measurement solution.

Table 14 presents the measured and expected concentrations of calcium (Ca^{2+}) and sodium (Na^+) in the percolated samples, along with the corresponding sodium occupancy and ionic strength (IS). The determined sodium occupancies and

concentrations from the five different treatments are compared against their pre-calculated values, ensuring consistency in the experimental setup.

The results demonstrate a strong agreement between the experimentally determined sodium occupancies and the values predicted by geochemical simulations. This indicates that after percolating the required pore volume, the sodium occupancy of the clay samples successfully reaches the expected equilibrium state. This consistency validates the reliability of the geochemical modeling approach and confirms that the ion exchange processes in Boom Clay behave as anticipated under the imposed saline conditions. The findings further reinforce that the methodology used for conditioning the clay samples effectively simulates real occupancy changes within the clay matrix.

Table 14 Measured and expected concentrations of Ca^{2+} and Na^{+} in the percolated samples.

Sample	Ca Pre-calculated Meq/l	Ca Determined Meq/l	Na Pre-calculated Meq/l	Na Determined Meq/l	Na (%) - IS (M) Pre-calculated	Na (%) – IS (M) Determined
S1	144	105	856	954.6	60% - 1.0 M	66% - 1.05 M
S2	144	22.3	856	1049.2	60% - 1.0 M	83% - 1.07 M
S3	-	22.85	1980	2244.6	90% - 2.0 M	90.1% - 2.2 M
S4	-	11.85	1980	2451	90% - 2.0 M	93% - 2.4 M
S5	-	37.4	1980	2184.4	90% - 2.0 M	88% - 2.1 M

The CEC values determined by photometric analysis (CEC(Cu-VIS)) and those obtained through ICP analysis (CEC(Cu-ICP)) exhibit a strong correlation, as shown in Table 15. The average CEC for the entire sample set (n = 5) was 18.0 ± 2.5 cmol(+)/kg using photometric analysis and 18.5 ± 2.0 cmol(+)/kg using ICP analysis. These values are in good agreement with previous findings, notably the average CEC of 21.8 ± 4.3 cmol(+)/kg reported by Honty (2010) for a broader set of Boom Clay samples (n = 8).

The consistency between the two analytical methods confirms the reliability of the CEC measurements and highlights the robustness of the applied methodologies. Small variations between the two techniques may be attributed to differences in sensitivity and detection limits. Nonetheless, the overall agreement suggests that both methods are effective in characterizing the cation exchange capacity of Boom Clay under the tested conditions (Frederickx et al., 2021).

Table 15 CEC values from VIS and ICP analysis.

Sample	CEC(Cu-VIS) $cmol(+)/Kg$	CEC(Cu-ICP) $cmol(+)/Kg$
S1	21.7	20.54
S2	15.63	17.38
S3	16.86	18.53
S4	20.66	22.26
S5	16.42	16.66

3. Experimental procedures

3.1 Preparation technique of samples

Before initiating sample preparation, it is crucial to determine the orientation of the bedding plane, as the inherent anisotropy of Boom Clay significantly influences mechanical behavior. As illustrated in Figure 32(a), bedding planes are clearly visible to the naked eye immediately after opening the core. To ensure precise sample extraction, a core block (5-10 cm) is carefully cut using a wire saw machine, as shown in Figure 32(b).

In this study, particular attention was given to the loading direction, which was deliberately chosen to be perpendicular to the bedding planes. .

(a) (b)

Figure 32 After core opening: (a) Bedding plane determination, and (b) The wire saw machine used for preparing the samples.

Regarding the preparation of samples for swelling pressure, salinization/desalinization test and high pressure oedometer test, the core was divided into four slices, each 20 mm thick (see Figure 33(a)). Subsequently, manual trimming was carried out using a sharp blade cutter and a cutting ring (Figure 33(b,c)) to prepare a sample with a diameter of 50 mm and a height of 10 mm (Figure 33(d)). Special attention was paid to preserving the initial water content. The preservation process involved wrapping the samples with Parafilm made of wax blends, followed by placing them in high-density vacuum storage bags, and finally, vacuum-packing them using a fast vacuum.

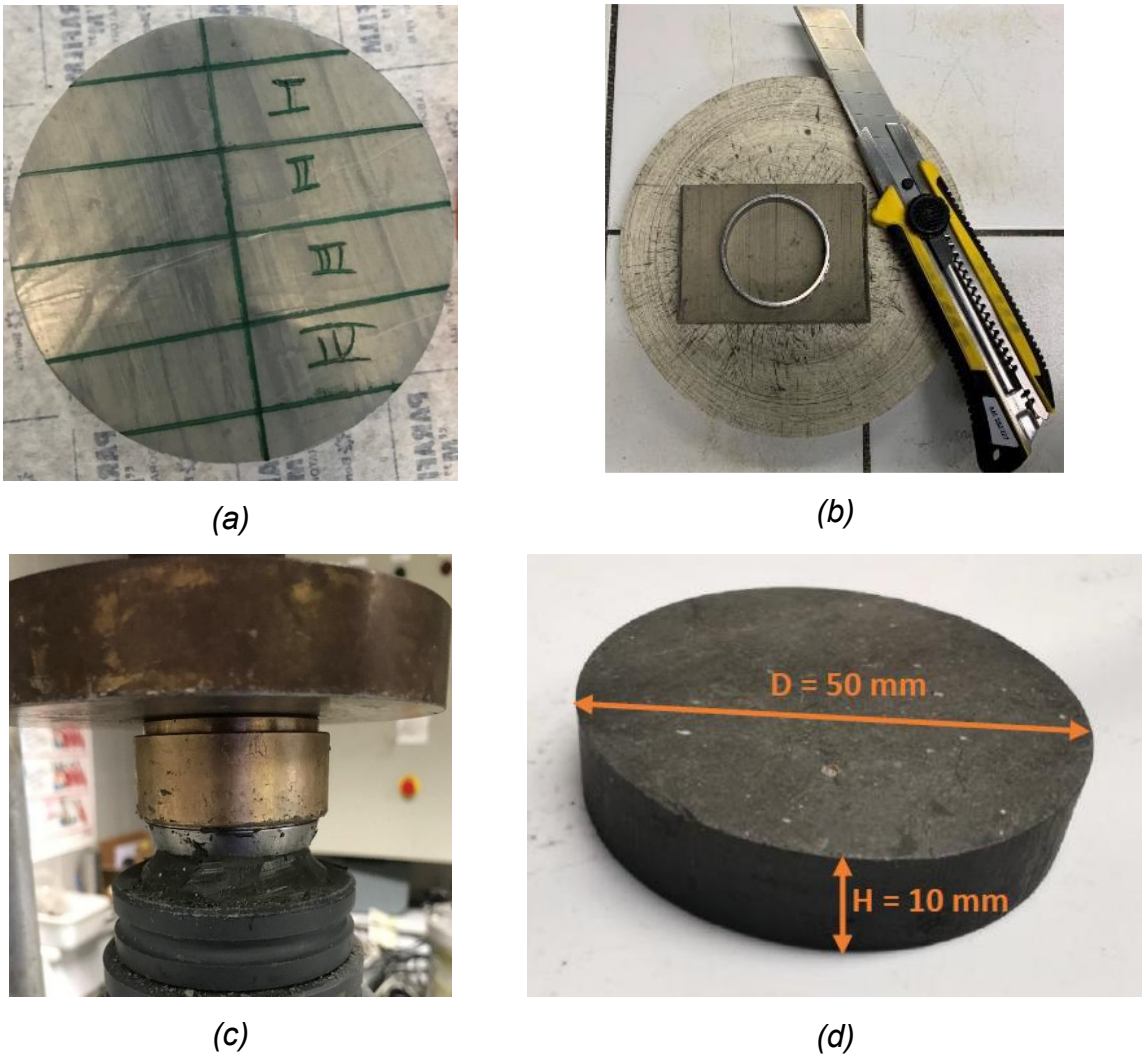

(a) *(b)*

(c) *(d)*

Figure 33 Sample preparation technique for swelling, salinization/desalinization and oedometer tests.

For the preparation of triaxial test samples, a cuboid section was first extracted from the core block (Figure 34a, b). The sample was then manually trimmed using a sharp blade cutter and a soil lathe (Figure 34c) to achieve a cylindrical shape with a diameter of 38 mm and a height of 76 mm (Figure 34d).

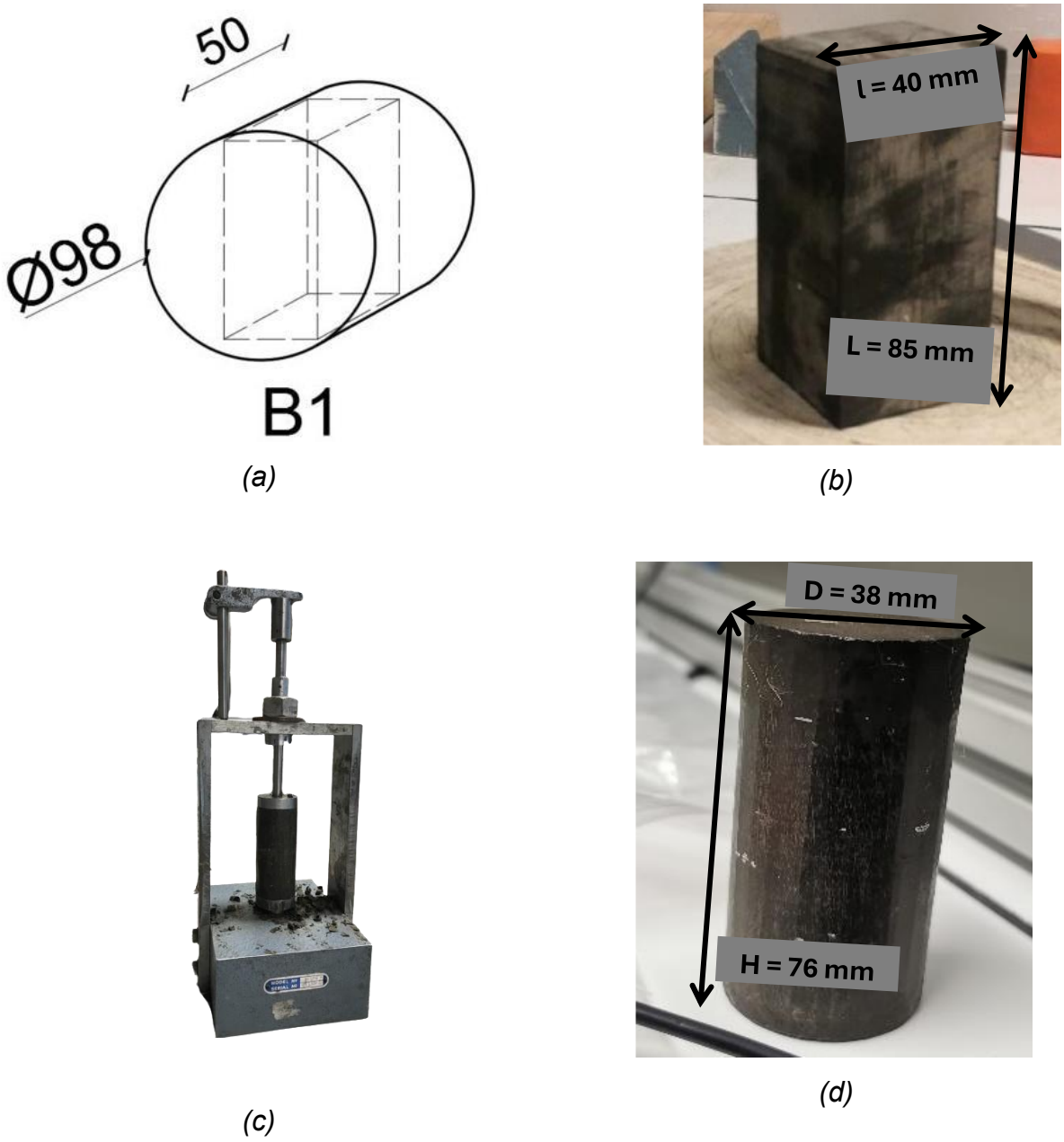

Figure 34 Sample preparation technique for triaxial tests.

During sample preparation, numerous specimens fractured while being prepared. As illustrated in Figure 35 and Figure 36, these failures were primarily attributed to the presence of natural discontinuities, pre-existing cracks, or localized concentrations of pyrite inclusions within the clay matrix. These factors compromised the structural integrity of the samples, making them more susceptible to breakage during handling and testing.

In total, 84 samples were prepared for the experimental campaign. However, a significant portion,17 triaxial samples and 22 specimens designated for other tests, experienced breakage, as detailed in Table 16. The high failure rate underscores the

challenges associated with working with Boom Clay, particularly in ensuring sample integrity for mechanical testing.

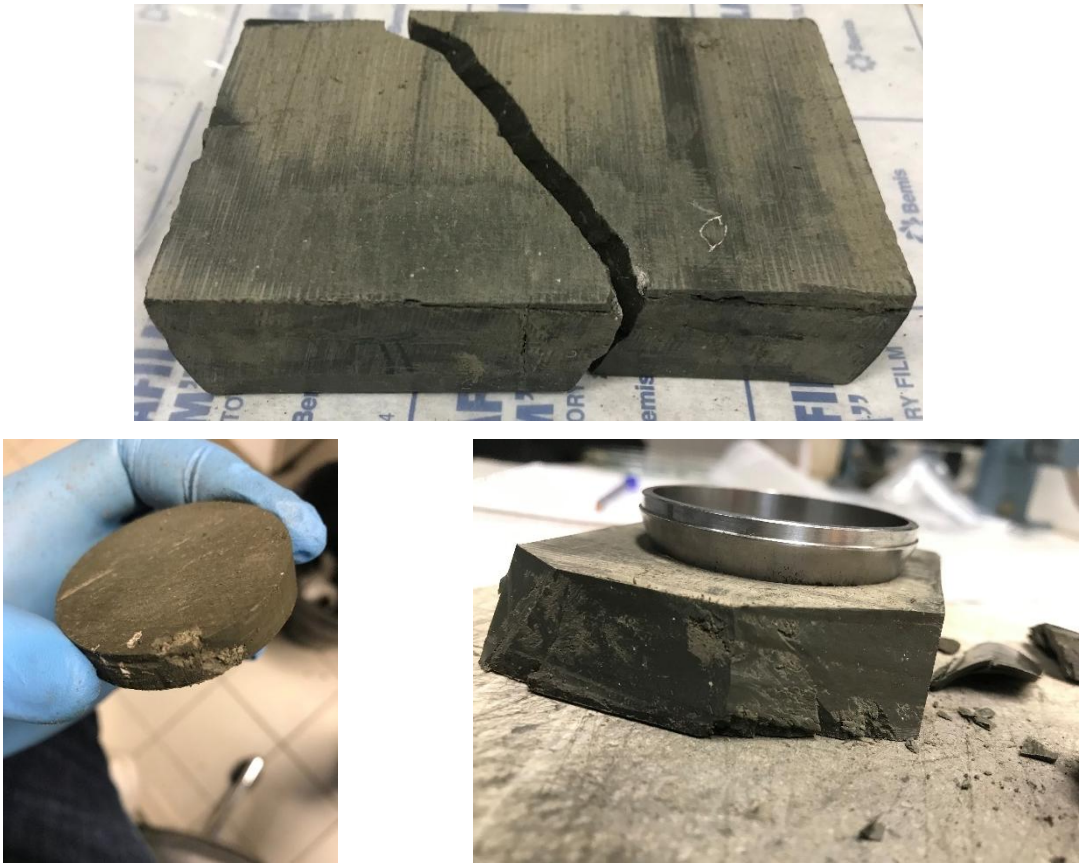

Figure 35 Cracked samples during the preparation for swelling, salinization/desalinization and oedometer tests.

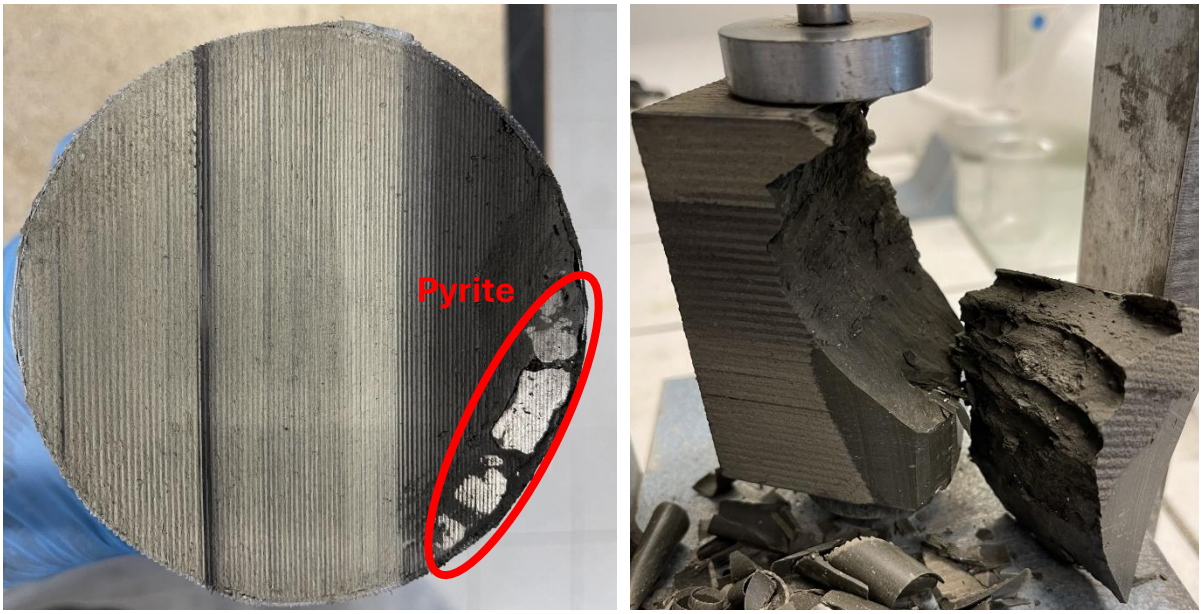

Figure 36 Cracked samples during the preparation for triaxial tests.

Table 16 Total number of prepared samples, i.e., Cracked and tested samples, for each type of experiment.

Test type	Cracked samples	Tested samples
Swelling samples	7	10
Salinization/desalinization samples	5	5
Oedometer samples	10	20
Triaxial samples	17	10
Total	39	45

3.2 Swelling pressure test

For the swelling pressure test and the determination of hydraulic conductivity, five main apparatuses were utilized: a low-pressure oedometer frame, an oedometer cell, a volume and pressure controller (CPV), an interface cell, and a constant volume cell.

The low-pressure oedometer was developed at CERMES, within the Navier Laboratory in France. It features a lever arm mechanism that amplifies the applied load by a factor of 10, allowing for a maximum axial stress of 3.2 MPa to be exerted on a specimen with a 50 mm diameter (Figure 37). This design enables precise control over stress application, making it suitable for swelling pressure measurements.

Figure 37 Low pressure oedometer apparatus.

The oedometer cell, presented in Figure 38, consists of three main components: a piston, a cell wall, and a base. The base is equipped with two valves, which facilitate the saturation of the porous discs before testing. This setup ensures proper hydration of the sample, which is critical for obtaining accurate hydraulic conductivity measurements.

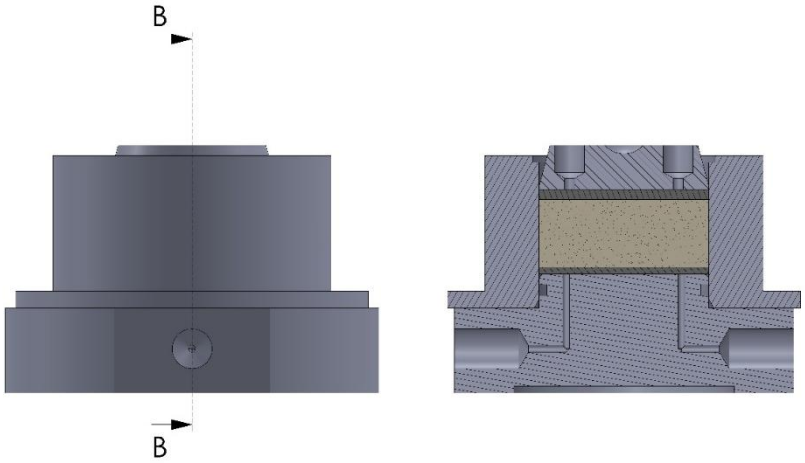

Figure 38 Oedometer cell.

The CPV (Controller of Pressure and Volume) is a precision instrument designed to regulate either water pressure or injection volume. It can inject water while applying a specific pressure and simultaneously monitor the injected volume, or it can maintain a constant injection volume while tracking pressure variations (Figure 39). This dual functionality allows for precise control over fluid flow during experiments.

The interface cell is a compact, two-compartment chamber separated by an impermeable membrane as shown in Figure 40. The upper compartment contains distilled water, which transmits the applied pressure from the CPV. The lower compartment holds saline water, which is injected into the oedometer cell via the drainage system to ensure complete sample saturation. The primary role of the interface cell is to act as a barrier, preventing direct contact between the CPV and the saline solution, thereby minimizing the risk of corrosion and ensuring the longevity and accuracy of the CPV system.

Figure 39 CPV and Interface cell.

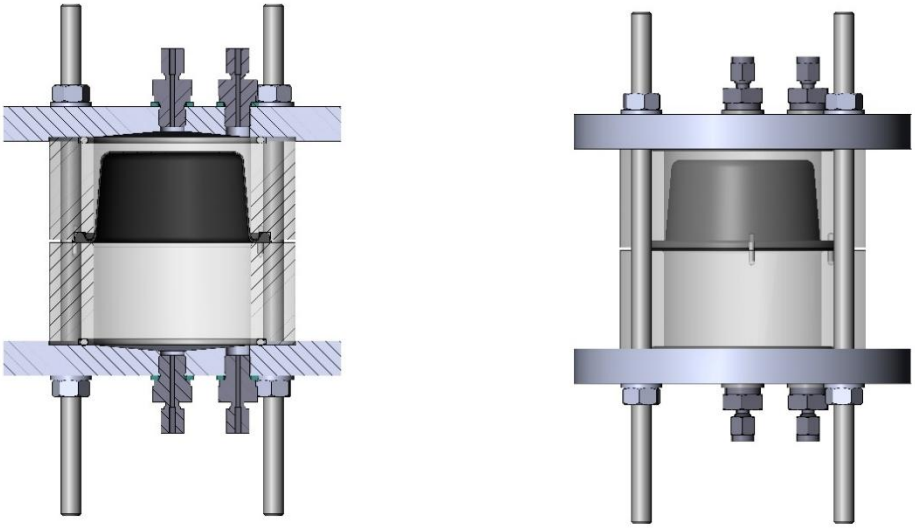

Figure 40 Interface cell.

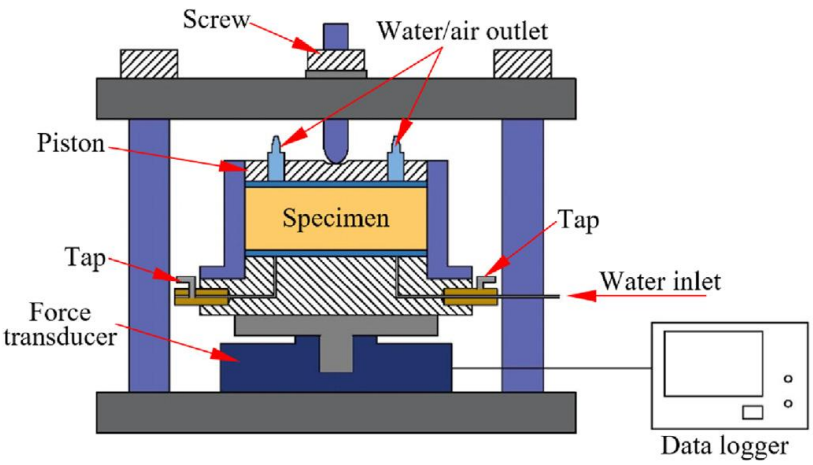

Figure 41 Constant volume cell.

The constant volume cell consists of two axial bars, as shown in Figure 41, and a force transducer fixed at the bottom. A piston is positioned at the top to secure the upper part of the oedometer cell, preventing any displacement and ensuring the constant volume method is maintained for swelling pressure and hydraulic conductivity determination. The force transducer is connected to a data logger, allowing continuous monitoring and recording of the applied stress throughout the test.

The test procedure for swelling pressure and hydraulic conductivity involved carefully placing the sample inside an oedometer cell, positioned between two dry metallic porous disks, each covered with filter papers on the top and bottom. To minimize lateral surface friction, the inner walls of the cell were greased. The oedometer cell was fitted with two valves at its base to allow for the saturation of the porous discs, while vertical drainage was enabled through the top porous disks. The sample was loaded stepwise up to the in situ effective stress of 2.25 MPa. Afterwards, saturation was carried out using the desired solution and an infiltration cell connected to a controller of pressure and volume (CPV). To achieve the desired Na^+ occupancies of 60% at 1.0 M, 60% at 2.0 M, and 90% at 2.0 M, a percolation of 3, 6, and 5 times the pore volume of the sample was applied. For solutions with 20% and 10% sodium occupancies and 1.0 M concentration, 3 pore volumes were enough, as these solutions contain a high amount of calcium, and less pore volume replacements were required to achieve the desired sodium occupancy due to the easier replacement of the divalent cation Ca^{2+} versus the monovalent cation Na^+ (Mitchell and Soga, 2005). Once the specified percolated volume was achieved, the saturation phase was deemed completed. For the BC

synthetic solution (15 mmol/L $NaHCO_3$), a minimum of two times the pore volume was percolated to ensure thorough sample saturation.

After saturation, excess water from the saturation phase was removed from the cell by air flushing, and the sample was rapidly unloaded and transferred to the constant-volume cell to initiate the swelling pressure test. During this transfer process, negative internal suction developed, maintaining the sample volume almost constant. This behavior was proved by sacrificing several tests after the saturation phase and fast unloading, during which the total suction induced by the fast unloading was measured using a chilled-mirror dew-point hygrometer (WP4) (Ying et al., 2021). The "stress release suction" refers to the suction generated by the rapid unloading without water supply. In this process, the clay undergoes a sudden reduction of external pressure while its volume remains constant due to the stress release suction (T.T. Le et al., 2011; Zhang et al., 2022; Yang et al., 2024). Table 17 presents the measured total suction and the osmotic suction related to the (Na,Ca)NO_3 concentration for the three main solutions (BC synthetic solution, 1.0 M and 2.0 M), calculated using Equation (8) proposed by Beyer et al. (2005). The difference between the measured total suction by WP4 and the calculated osmotic suction leads to the suction due to the fast unloading of the BC sample without contact with water, referred to as the stress release suction (Zhang et al., 2022; Yang et al., 2024). Notably, an internal negative stress release suction of approximately 3.5 MPa was observed for the BC synthetic solution, which is quite high. For solutions with Na=60% and IS=1.0 M, and Na=90% and IS=2.0 M, the released stress release suctions were found to be 4.25 and 5 MPa, respectively. It is clear that the measured total suction increases with the increasing solution concentration, which is mainly attributed to the increase in osmotic suction.

(8) $$\pi = \frac{-RT\rho_L}{M_w} ln\left[1 - \left(\frac{cM_s}{\rho_L}\right)^2\right]$$

Where R=8.31 $J/(mol\ K)$ is the gas constant, T =293 K is the temperature, M_w=18.016 $Kg/kmol$ is the molar mass of water, M_s=85 $Kg/kmol$ is the molar mass of sodium nitrate, ρ_L (Kg/m^3) is the liquid density, and c (mol/l) is the concentration.

Table 17 Total suction measured using WP4.

Solution	Total Suction (MPa)	Osmotic Suction (MPa)	Stress Release Suction (MPa)
BC Synthetic Solution	3.5	0	3.5
Na = 60%; $IS = 1.0\ M$	5.0	0.75	4.25
Na = 90%; $IS = 2.0\ M$	9.0	4	5

Once the oedometer cell was properly placed in the constant-volume cell (Zeng et al., 2019), the first desired solution from a reservoir was percolated under low pressure (50 kPa) into the first valve at the base of the cell to evacuate any air, and then the second valve was closed as water started to flow out. The swelling pressure was measured by the force transducer installed at the bottom of cell and was recorded by a data logging system. In this procedure, the injection pressure was gradually raised until a stable pressure (100 kPa), regulated by the CPV. This pressure was maintained between the upper and lower sections of the sample throughout the test. To minimize the disturbance to the microstructure and to prevent hydraulic fracturing, the water injection pressure was intentionally kept below 1/10 of the ultimate swelling pressure. When the recorded swelling pressure was stable for 48 h, the test was considered as completed. Afterwards, the hydraulic conductivity was determined.

To determine the saturated hydraulic conductivity, the constant hydraulic head method was employed. The CPV monitored and recorded the injected solution volume. The test was terminated when the volume of injected solution was equal to that necessary for replacing the desired number of pore volumes for each solution.

Subsequent to the injection test, the injection pressure was decreased to 50 kPa, allowing assessment of the impact of the injection pressure on the swelling pressure. Once the swelling pressure stabilized, the solution within the water/salt-solution converter was substituted with the next concentration solution, following the aforementioned protocol.

The saturated hydraulic conductivity, k_s (m/s), was calculated using Darcy's law:

$$k_s = \frac{\Delta Q}{A.i} = \frac{\Delta Q.l}{A.\Delta h} = \frac{\Delta Q.l}{A.(h_1 - h_2)} = \frac{\Delta Q.l}{A.(100-0)} \quad (9)$$

where ΔQ represents the inflow rate monitored by the CPV (m^3/s), A denotes the cross-sectional area of the test sample (m^2), i stands for the hydraulic gradient, l is the height

of the sample (m), Δh signifies the difference in water head (m), h_1 corresponds to the water head at the inflow point, and h_2 refers to the water head at the outflow point. For example, if the water pressure applied at the inflow point was 1.0 MPa, h_1 was maintained at 100 m; h_2 was considered zero due to the presence of a thin layer of water at the outflow point.

3.3 Salinization/desalinization test

Before conducting the chemical loading/unloading test, the sample was carefully positioned inside the oedometer cell, sandwiched between two dry metallic porous disks covered with filter papers at the top and bottom. To reduce the lateral surface friction, the interior of the cell wall was coated with grease. The oedometer cell was equipped with two valves in its base to facilitate saturation of the porous discs, while vertical drainage was permitted through the top porous disks.

The experimental protocol began by placing the oedometer cell into the low-pressure oedometer apparatus, which had a lever arm that multiplied the load by 10. The in situ effective stress of 2.25 MPa was applied in steps until displacement stabilization ($\varepsilon_a = 5 \times 10^{-3} mm/24h$). Afterwards, saturation was carried out by injecting the BC reference solution (15 mmol/L - 0.015 M $NaHCO_3$) using an infiltration cell connected to a controller of pressure and volume (CPV). The sample was considered as fully saturated after percolating two times its pore volume ($V_{1\text{-pore}}$ = 8 cm^3). After the saturation, the sample was gradually unloaded to the final effective vertical stress. The chemical loading/unloading cycle was then initiated under low pressure (50 kPa) using a CPV to regulate the volume of water injected. The first valve at the base of the cell was opened to evacuate any trapped air. Once water started to flow out, the second valve was closed. To achieve the targeted occupancies of 60% - IS = 1.0, 60% - IS = 2.0, and 90% - IS = 2.0, a percolation of 3, 6, and 5 times the pore volume was applied with the respective (Na,Ca) nitrate solutions listed in Table 13. Once the specified percolated volume was reached, the infiltration phase was considered as completed and the next solution was switched for continuing the infiltration cycle. During the salinization/desalinization cycle the vertical displacement was measured using a digital comparator to an accuracy of 0.001 mm.

The shrinkage/swelling strains are defined as the ratio of the height change (induced by salinization/desalinization) to the height of the sample under its final vertical stress prior to the infiltration, as follows:

(10) $$\epsilon_T = \frac{\Delta H_T}{H_0} \times 100\%$$

where H_0 is the sample height (mm) at the final vertical stress before the chemical loading/unloading cycles and ΔH_T is the total vertical displacement (mm). The cumulative strain is defined as the ratio of the cumulative changes in specimen height over the new specimen height after each salinization/desalinization process.

3.4 MIP test

Mercury Intrusion Porosimetry (MIP) is widely recognized as both a qualitative and quantitative technique for characterizing the pore structure of porous materials. This method operates by injecting mercury, a non-wetting fluid, into a porous sample under increasing pressure while recording the corresponding reduction in pore diameter occupied by mercury.

In this study, macrostructural analysis was conducted using an Autopore IV 9500 porosimeter (Micromeritics Instrument Corp.) at a controlled ambient temperature of 20 ± 1 °C. The applied mercury pressure ranged from 3 kPa to 228 MPa, allowing the investigation of pore entrance diameters between 350 μm and 5 nm (Sun and Cui, 2020).

Prior to MIP testing, the sample was dehydrated using the freeze-drying method described by Delage and Pellerin (1984) to prevent significant shrinkage and preserve the original microstructure. Small soil specimens were rapidly frozen after vacuum immersion in liquid nitrogen at $-210°C$, which had already been pre-frozen under vacuum to prevent boiling and structural disturbance. The frozen samples were then placed in a vacuum freeze dryer for 24 hours to facilitate ice sublimation, a key feature of this method.

Following the drying process, the sample was inserted into a penetrometer consisting of a sample cup attached to a metal-clad, precision-bore glass capillary stem (Figure 42). The microstructural procedure consists of two main parts as the device features two mercury intrusion ports:

- Low-pressure port: Operating between 0.003 MPa and 0.2 MPa
- High-pressure port: Operating between 0.2 MPa and 228 MPa

Based on the applied pressure, the entrance pore diameter, ranging from 0.005 µm to 350 µm, was determined using Laplace's law (Eqt. (11)) as described by Delage and Lefebvre (1984).

$$d = -\frac{4\gamma \cos\theta}{P} \quad (11)$$

where d is the corresponding pore diameter, γ is the surface tension of mercury (0.485 N/m), θ is the contact angle (130°), and P is the mercury pressure.

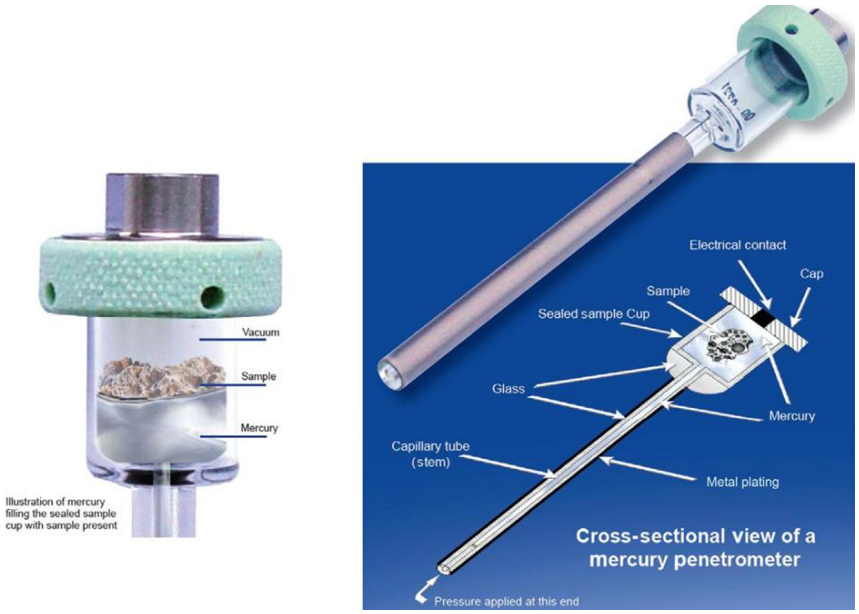

Figure 42 Schematic of automated mercury injection high-pressure penetrometer: www.micromeritics.com.

One of the primary limitations of Mercury Intrusion Porosimetry (MIP) is its inability to capture all types of pores within a material. Specifically, it cannot detect enclosed pores that are entirely surrounded by aggregated particles, as these remain inaccessible to mercury intrusion (Romero and Simms, 2008). Additionally, the technique struggles to measure constricted pores, where access is limited by narrow pore throats, preventing mercury from fully penetrating the pore space. Furthermore, MIP is ineffective in characterizing extremely small pores—those smaller than $\boldsymbol{0.005\,\mu m}$—due to the constraints of the maximum applied mercury pressure, which limits its ability to intrude into the finest pore networks (Delage et al., 2007). As a result, MIP provides valuable insight into pore size distribution.

3.5 High-pressure Oedometer test

The high-pressure oedometer was developed at CERMES, within the Navier Laboratory in France (Marcial et al., 2002). It is equipped with a double-lever system,

where one lever amplifies the applied load by a factor of 5 and the second by 10, allowing for a maximum axial stress of 64 MPa to be exerted on a 50 mm diameter specimen (Figure 43).

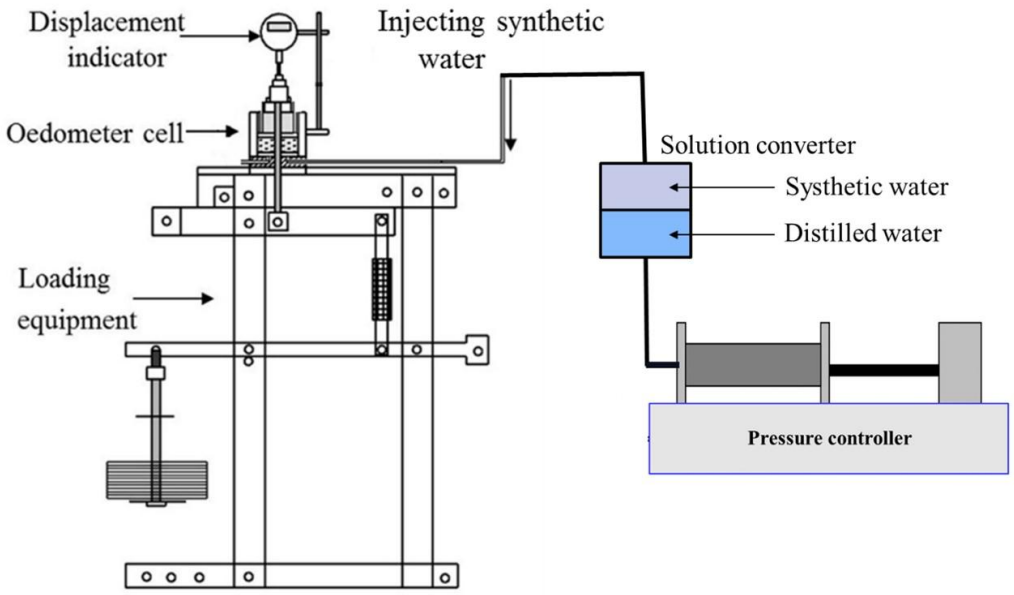

Figure 43 High pressure oedometer apparatus, CPV and interface cell.

Due to the vertical stacking of multiple components, including the frame and the oedometer cell, as well as the significant stresses involved, calibration was necessary to account for the system compression when interpreting total displacement measurements. This calibration was performed by applying the same loading path and measuring the self-deformation of the cell, as in the actual tests, but on an empty cell without a sample. Under cyclic loading and unloading within a stress range of $\sigma_v' = 0.125 - 32\ MPa$, the system exhibited a response that was largely reversible.

The procedure for conducting a high-pressure oedometer test with unloading/reloading cycles is as follows:

- Application of in-situ effective stress ($\sigma_v' = 2.25\ MPa$): The stress was applied in increments until displacement stabilization was achieved.
- Saturation process: A specified volume of pore fluid was percolated through the sample, with two pore volumes used for Boom Clay synthetic water. Water was introduced under low pressure through the first valve at the base of the cell, allowing air to be expelled through the second valve positioned over the dry porous disc. The second valve was closed as soon as water began to flow out.

- Loading/unloading cycles: These tests were performed to examine the compressibility and swelling behavior of soils under different percolated solutions, particularly assessing the influence of saline solutions on compressibility, swelling, and preconsolidation pressure. A loading/unloading cycle was conducted, ranging from 0.25 MPa to 32 MPa, with the load doubling at each step. The unloading sequence followed the same stepwise procedure. Each loading or unloading step continued until displacement stabilization was reached, defined by a vertical strain rate of less than 0.005 mm/8 h.

According to AFNOR (Afnor, 1994), volume change stabilization is considered achieved when the vertical strain rate falls below $5 \times 10^{-4}/8\,h$, equivalent to a displacement rate lower than $0.005\,mm/8\,h$.

3.6 Triaxial test

A self-compensating triaxial cell made by Geodesign called “HP3” (see Figure 44(a)) was used (Nguyen, 2013). The axial deviator stress is applied by a self-compensating hydraulic system without the effect of confining pressure on the piston. The measurement of the axial force is ensured by an internal force sensor with a capacity of 25 kN, corresponding to a maximum axial stress of 22 MPa. The self-compensating cell consists of three parts: cap, side wall, and base (Figure 44 (b)) and is supplied by: a pore pressure controller of pressure and volume (CPV), a confining pressure CPV, a deviator stress CPV, and a solution converter. The triaxial cell includes two axial LVDTs and three radial LVDTs to measure the local displacement of the sample with an accuracy of 0.001 µm (Figure 44 (c)).

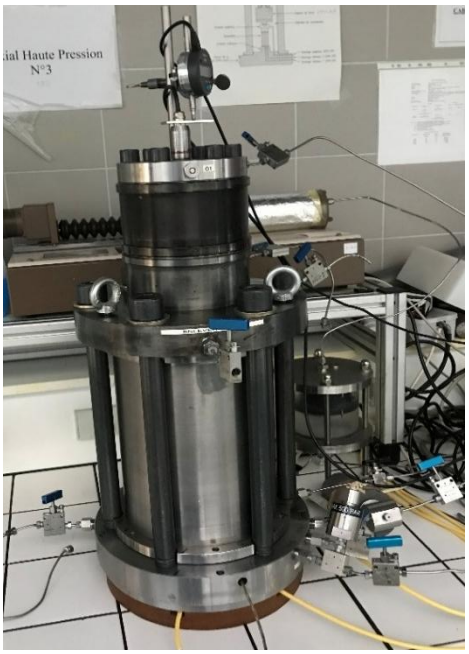

(a)

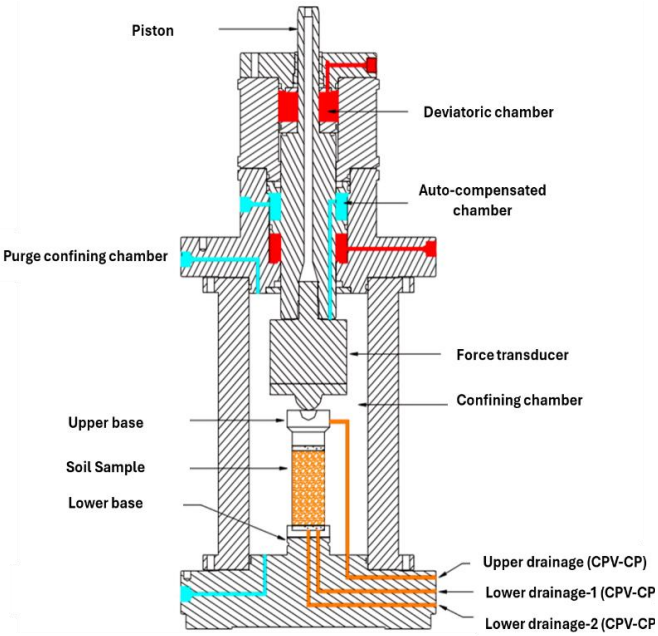

(b)

(c)

(d)

Figure 44 (a, b) triaxial cell HP3 (c) LVDTs (d) sample covering.

For the undrained triaxial test, the specimen is first covered with a geotextile membrane to accelerate the saturation process (Figure 44(d)). The specimen is then placed between two dry metallic porous disks and encased within a neoprene membrane in the triaxial cell base, with LVDT rings positioned around it (Figure 44c). To ensure that the neoprene membrane is not punctured and is watertight, a vacuum is applied to the

specimen, and the pressure is monitored over time. If the pressure remains stable, the membrane can withstand the pressure and the absence of leakage is confirmed. The subsequent steps are carried out in the following order: installation of the side wall, filling the cell with silicone oil, and replacing the self-compensating cover or cap.

The triaxial tests were conducted following the French standards (Afnor, 1994). The procedure followed during the undrained triaxial test is as follows:

- The specimen is isotropically consolidated in steps in drained conditions until the effective confining stress reaching the in-situ effective stress ($\sigma_3' = 2.25\ MPa$; loading steps: 0.2 MPa → 0.4 MPa → 0.6 MPa → 0.8 MPa→ 1 MPa→ 1.2 MPa→ 1.4 MPa→ 1.6 MPa→ 1.8 MPa→ 2 MPa→ 2.25 MPa). It is important to note that the initial vacuum was removed once the confining pressure is equal to 500 kPa ($\sigma_3' = 500\ kPa$).

- Once the volumetric deformation of the specimen stabilized at an effective confining stress of $\sigma_3' = 2.25\ MPa$, the saturation process was initiated using the desired solutions. Saturation was proceeded by applying a stepwise back pressure up to 1 MPa while maintaining a constant effective confining stress of 2.25 MPa ($\sigma_3' = \sigma_3 - u = 2.25\ MPa$) to prevent swelling of the specimen and to preserve any microstructural modification. The desired solution was injected via Controller of Pressure and Volume (CPV) into the drainage system through one of the two outlets on the lower base for the upper and lower injections. The remaining outlet was left open to purge air from the tubes and porous stones. Once the air was purged, the remaining outlet was closed, and the saturation began.

- The saturation time was standardized across all tests at 35 days. Following the saturation period, the Skempton coefficient ($B = \frac{\Delta u}{\Delta \sigma_3}$) was verified by: (i) isolating the specimen from the CPV system to create undrained conditions with an initial pore pressure of $u = 1\ MPa$; and (ii) slightly increasing the confining pressure by an increment of $\Delta\sigma_3 = 200\ kPa$. To achieve a degree of saturation $S_r = 99\%$ and with a pore pressure of 1 MPa, the Skempton coefficient B must be equal to or greater than 0.85 (Afnor, 1994). Nearly all specimens tested in this study have reached or exceeded this value. Once the measurement of the Skempton coefficient is completed, the confinement pressure was reduced to $\sigma_3' = 2.25\ MPa = \sigma_3 - 1\ MPa$, and the drainage system was opened.

- After the saturation, all specimens were isotopically consolidated to 6 MPa, representing the preconsolidation pressure of Boom Clay under in situ-conditions (Horseman et al., 1987). This step was performed to minimize the effects of initial anisotropy, as well as potential heterogeneities or small fractures that might have resulted from hand trimming during sample preparation, ensuring that all specimens shared the same initial conditions. Subsequently, the specimens were unloaded to three final effective confining pressures: 1 MPa, 2.25 MPa, and 4.5 MPa, corresponding to three overconsolidation ratios (OCR) of 6, 2.6, and 1.3, respectively. The selection of these stress levels was motivated by the need to cover the two main volumetric strain domains - an effective confining pressure of 1 MPa (OCR = 6) was used to examine the dilatantancy behavior of Boom Clay, while 4.5 MPa (OCR = 1.3) enabled the study of its contraction behavior. The intermediate confining pressure of 2.25 MPa represents the in-situ effective stress, with an OCR of 2.6, capturing the transition between contraction and dilation. Finally, the water valves were closed, and the specimens were sheared at a constant rate of 5 µm/min (Afnor, 1994) with the stress and pore pressure continuously measured. The test was stopped when the axial strain reached between 5% and 10% ($\varepsilon_a = 5 - 10\ \%$).

3.6.1 Saturation process

As mentioned previously, the saturation process was maintained for 35 days for all specimens. This duration was determined based on numerical simulations of the evolution of concentration profiles and sodium occupancy within Boom Clay specimens. These simulations were conducted using the HPx framework (Jacques et al., 2018) implemented within HYDRUS 5 (Šimůnek et al., 2024). The HPx framework integrates PHREEQ (Parkhurst and Appelo, 2013) as the geochemical solver with the HYDRUS flow and transport model, enabling detailed assessment of coupled hydrogeochemical processes. In this study, an axisymmetric two-dimensional (2D) geometry (height: 38 mm; radius: 19 mm) was utilized. The model employed a fixed concentration boundary condition at the top and along the outer edges of the cylindrical specimen.

The key properties of Boom Clay were assumed as follows: porosity of 0.35, saturated hydraulic conductivity of $4 \times 10^{-12}\ m/s$ (Al Mais et al., 2024), and an effective diffusion coefficient of $10^{-10}\ m^2/s$. The boundary solution comprised a 2 M $NaNO_3$ solution,

while reactions involving Na^+ and the Boom Clay matrix were described using the cation exchange model from Wang et al. (2023). Table 18 summarizes the key parameters of the geochemical exchange model, which serves as the basis for simulating the cation exchange processes in Boom Clay under the defined experimental conditions.

The initial water composition of Boom Clay was defined in equilibrium with conditions outlined by Wang et al. (2023), characterized by a pH of 8.2 and ionic concentrations of Na, K, Ca, and Mg set at 1.34×10^{-2}, 2.07×10^{-4}, 7.02×10^{-5}, and 4.94×10^{-5} M, respectively. The initial cation exchange complex occupancy of Boom Clay was approximately 34.6%, 16.4%, 28.9%, and 20.1% for Na, K, Ca, and Mg, respectively (Frederickx et al., 2018). These parameters collectively ensured the accurate representation of chemical and hydraulic processes during the simulation and experimental phase.

Table 18 Parameters of the exchange model for the Boom Clay (Wang et al., 2023).

Capacity	**0.88 eq/l**
Cation Exchange – (Bc^- represents the cation exchanger)	
	LogK
$Bc^- + Na^+ = NaBc$	0
$Bc^- + K^+ = KBc$	1.4815
$2Bc^- + Ca^{2+} = CaBc$	0.9618
$2Bc^- + Mg^{2+} = MgBc$	0.9344

Figure 45 illustrates the temporal evolution of sodium occupancy (β_{Na}, %) at fixed elevations (z=0 mm and z=19 mm) with varying radial distances (r=0, 5, 10, and 15 mm). It can be observed that the sodium occupancy at the center (z=0) and radial distances of 10 mm and 15 mm approaches 95%. In contrast, at z=0 and r=0 mm, it was found to stabilize at around 85%. These results indicate that the chosen saturation protocol, which involves saturating the specimen from both the top and bottom boundaries, is effective in achieving near-uniform sodium occupancy within 35 days.

At the center of the specimen, the potassium (K^+) occupancy was found to be approximately 14%, while the calcium (Ca^{2+}) and magnesium (Mg^{2+}) occupancies were found to be less than 1%, reflecting the dominance of sodium (Na^+) exchange under the experimental conditions.

Figure 46 presents the spatial distribution of sodium occupancy across the Boom Clay (BC) samples, highlighting the gradient of Na^+ (β_{Na}) from high-concentration boundaries to the center. Near the boundaries with elevated concentrations, the sodium occupancy is close to 100%, confirming the effective cation exchange and the full saturation.

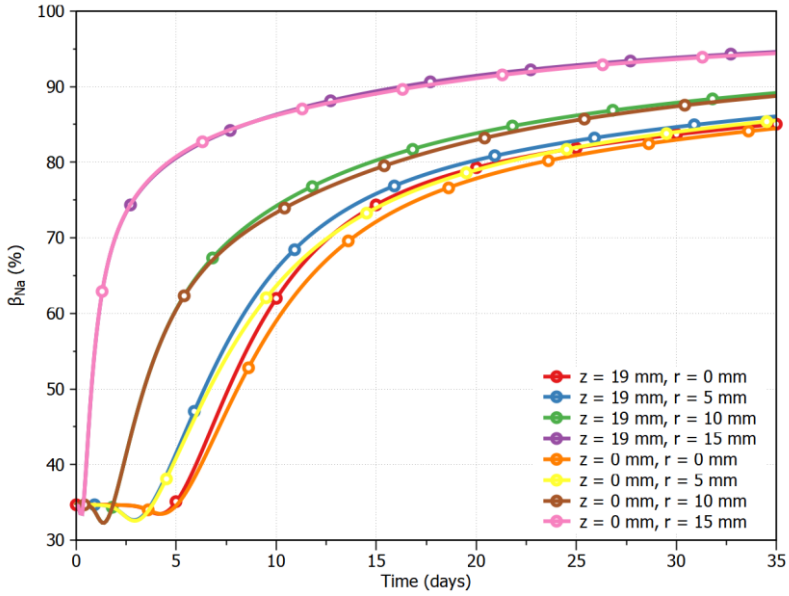

Figure 45 Sodium Occupancy (β_{Na}) in Boom Clay at different observation points over time.

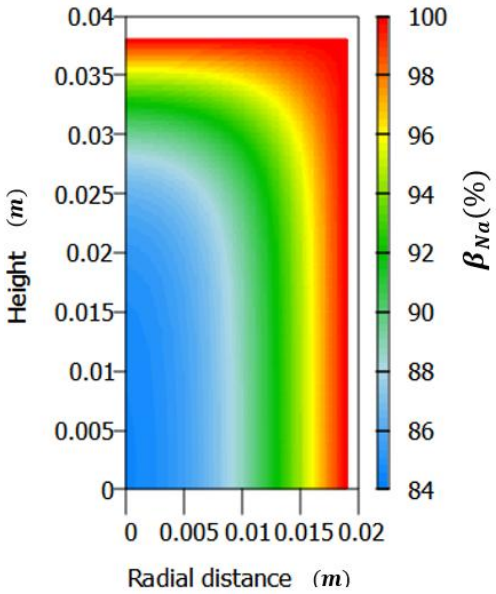

Figure 46 Spatial distribution of Sodium Occupancy (β_{Na}) in Boom Clay after 35 days.

4. Conclusion

This chapter provided a comprehensive overview of the materials and methodologies used in this study. The characterization of Boom Clay, including conditioning and geochemical properties, established well-defined initial conditions for the experiments. Preparation techniques ensured consistency across samples, while the experimental procedures enabled a systematic investigation of the hydro-mechanical response of the clay.

IV. Experimental results and discussion

1. Introduction

The hydro-mechanical behavior of Boom Clay (BC) can be significantly influenced by changes in pore water chemistry, particularly the presence of high-salinity solutions and varying sodium (Na^+) occupancies. Understanding these effects is essential for evaluating the long-term performance of Boom Clay in repository conditions, especially in scenarios where salinity variations arise from the leaching of bituminized waste.

This study systematically investigates the impact of sodium occupancy and solute concentration on the swelling behavior, hydraulic conductivity, compressibility, volume change, and shear response of Boom Clay. A series of laboratory experiments were conducted, including swelling pressure tests, high-pressure oedometer tests, salinization-desalinization tests, and isotropically undrained triaxial tests. These experiments utilized different percolating solutions: a synthetic BC solution (0.015 M $NaHCO_3$) representing in-situ pore water chemistry and (Na,Ca)NO_3 solutions to yield target sodium occupancies of 10%, 20%, 60%, and 90% at concentrations of 1.0 M and 2.0 M.

This study focuses on key hydro-mechanical parameters, such as swelling capacity, hydraulic conductivity, preconsolidation pressure and shear strength, to assess how Boom Clay responds to varying saline conditions. High sodium occupancies (60% and 90%) were selected to replicate the expected conditions in areas exposed to nitrate-rich plumes from bituminized waste disposal, while lower occupancies (10% and 20%) provide comparative insights. Additionally, microstructural changes were examined through mercury intrusion porosimetry (MIP) tests to analyze how salinity affects the clay fabric and porosity evolution.

The results from different experimental approaches allow better understanding the coupled hydro-mechanical-chemical interactions in Boom Clay. The findings will serve as a foundation for developing constitutive models that incorporate salinity effects, enabling relevant numerical analysis of BC behavior at both laboratory and in-situ scales.

2. Effect of (Na,Ca)NO_3 concentration and Na^+ occupancy on the swelling pressure and hydraulic conductivity of BC

a. Introduction

This part examines the impact of sodium occupancy and solute concentration on the swelling behavior and hydraulic conductivity of Boom Clay. One-dimensional swelling pressure tests were performed on intact samples that were first percolated with either a $NaHCO_3$ solution, representing the in-situ porewater composition, or (Na,Ca)NO_3 solutions of varying concentrations (1 mol/L and 2 mol/L) and Na/Ca ratios, corresponding to different sodium occupancies of 10%, 20%, 60%, and 90%. The percolation process was conducted in oedometer cell under an in-situ vertical effective stress of 2.25 MPa. After percolation, the oedometer cell was transferred to a constant-volume cell to measure the swelling pressure and the hydraulic conductivity. Higher sodium occupancies (60% and 90%) were selected to simulate the response of Boom Clay to the saline plume which was predicted by coupled geochemical and transport simulations (see Chapter 3) with consideration of salt leaching from bituminized waste. Lower occupancies (10% and 20%) were included for comparison. Table 19 represents the concentration and composition of each solution consisting of sodium nitrate ($NaNO_3$) and calcium nitrate ($Ca(NO_3)_2$). Additionally, a synthetic BC solution with a sodium bicarbonate ($NaHCO_3$) concentration of 15 mmol/L (IS= 0.015 M) (simulating intact BC pore water chemistry as recommended by De Craen et al., 2004), was investigated as a reference for comparison purposes.

Table 19 Composition of Saline Solutions.

Solution	***Na^+ - Occupancy (%)***	***$NaNO_3$ $(mmol/L)$***	***$Ca(NO_3)_2$ $(mmol/L)$***	***Ionic Strength (M)***	***Pore Volume Replacement***
1	60%	900	70	1.0	3
2	60%	1600	230	2.0	6
3	90%	2000	-	2.0	5
4	20%	320	340	1.0	3
5	10%	165	400	1.0	3

A total of nine swelling pressure tests and five hydraulic conductivity measurements were conducted. The samples were taken from two different cores: the first, labeled R78-79W_Core 28.1, and the second, R78-79W_Core 2.2 (Table 20). The first core was extracted approximately 28.1 m horizontally from the intrados of the Connecting Gallery at the HADES underground laboratory level, representing intact Boom Clay. In contrast, the second core was taken 2.2 m away, within the excavation damaged zone (EDZ) of the CG. To preserve their properties, all cores were coated with wax and stored in an airtight chamber at a temperature of 20 °C and a relative humidity of approximately 99%. The test results provide insight into the influence of solution concentration and sodium occupancy on swelling potential and hydraulic conductivity.

Table 20 Geometry, initial water content and initial void ratio of the specimens tested.

Test	*Sample localization*	D_0 (mm)	H_0 (mm)	ρ (g/cm^3)	W_0 (%)	e_0	S_r
1	R78-79W_Core 28.1 Block5-SliceI	49.11	10.00	2.07	22.6	0.565	1.00
2	R78-79W_Core 28.1 Block5-SliceIII	49.90	9.90	2.02	20.0	0.565	0.93
3	R78-79W_Core 2.2 Block2-SliceIII	49.90	9.92	2.06	21.0	0.554	1.00
4	R78-79W_Core 2.2 Block3-SliceIII	49.86	10.07	2.03	22.3	0.595	0.99
5	R78-79W_Core 28.1 Block6-SliceII	49.66	9.89	2.04	21.7	0.575	0.99
6	R78-79W_Core 28.1 Block5-SliceIV	49.76	9.95	2.04	23.63	0.603	1.00
7	R78-79W_Core 28.1 Block6-SliceI	49.83	9.75	2.03	23.43	0.605	1.00
8	R78-79W_Core 28.1 Block9-SliceI	49.90	9.78	2.04	21.7	0.576	0.99
9	R78-79W_Core 28.1 Block9-SliceII	49.86	9.99	2.04	20.8	0.569	0.97

b. Experimental results

i. Effect of solute concentration on swelling pressure

The impact of the solution concentration on the swelling pressure of BC is illustrated in Figure 47. It appears that the stabilized swelling pressure decreased from 0.75 MPa (BC synthetic solution, 0.015 M $NaHCO_3$) to 0.425 MPa (1.0 M (Na,Ca)NO_3) and further to 0.29 MPa (2.0 M (Na,Ca)NO_3). In other words, the swelling pressure of BC decreases with the increase in infiltration solution concentration. This finding aligns with the results reported by various researchers (Castellanos et al., 2008; Komine et al., 2009; Siddiqua et al., 2011; Zhang et al., 2012). Moreover, the swelling pressure experiences a rapid initial growth during solution percolation and eventually stabilizes. The duration of the tests was defined by the time required for the swelling pressure to stabilize. A higher salt concentration led to a reduction of the swelling process duration. Specifically, the stabilization time was approximately 1 h for a concentration of 2.0 M, and extended to 2 h for a concentration of 1.0 M. In the case of BC synthetic solution, the evolution of swelling pressure achieved complete stabilization after 10 h. This phenomenon can primarily be attributed to the infiltration being driven by the matric suction gradient during primary swelling, and to the transportation of salts and cation exchange, which led to an increase in osmotic suction during the secondary swelling (Rao and Shivananda, 2005). At higher concentrations, a more pronounced suction gradient is generated, due to the difference of the osmotic suction of injected solution. This led to a lower swelling pressure.

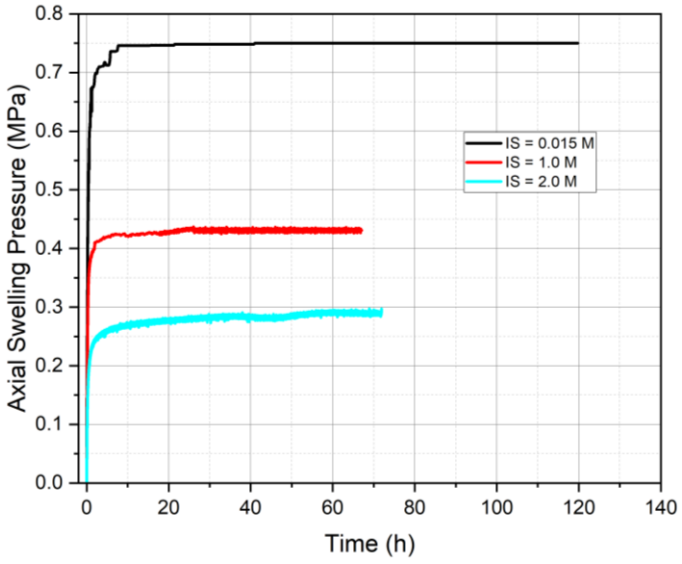

Figure 47 Evolution of the swelling pressures over time with different solute concentrations.

ii. Effect of sodium occupancy on swelling pressure

The impact of the sodium occupancy on swelling pressure is illustrated in Figures Figure 48, Figure 49 and Figure 50. Figure 48 shows three duplicate swelling pressure tests (tests 1, 2 and 3), all with the same experimental procedure and infiltration solutions. It can be observed that as the sodium solution concentration increased from 1.0 M to 2.0 M while maintaining a constant sodium occupancy of 60%, the swelling pressure decreased. Subsequently, at 2.0 M concentration, increasing the occupancy to 90% leads to a further reduction in the swelling pressure. Note that the close alignment of the three curves highlights the high repeatability of the results. Figure 49 shows the results of two additional swelling pressure tests (tests 4 and 5). The first test began with the percolation of BC synthetic solution, followed by an increase in concentration up to 1.0 M with a 60% occupancy, resulting in a reduction of swelling pressure. Additionally, holding the sodium occupancy constant while increasing the solute concentration led to a further decrease in swelling pressure. Likewise, when the sodium occupancy was increased at the same solution concentration, the swelling pressure continued to decrease, underlining the comparable influence of occupancy and concentration on the swelling pressure. Another pair of tests (tests 6 and 7) were initiated with higher solute concentration and sodium occupancy (90% - 2.0 M) (Figure 50), and a decrease in both parameters revealed a very slight increase in swelling pressure. This slight increase of the swelling pressure might be explained by the larger number of pore volume replacements needed to establish a new equilibrium with decreasing solute concentration, in contrast to the case for increasing concentration. Summarizing, the swelling pressure decreased as sodium occupancy and solute concentration increased, while a slight increase in the swelling pressure was detected with decreasing solute concentration and sodium occupancy.

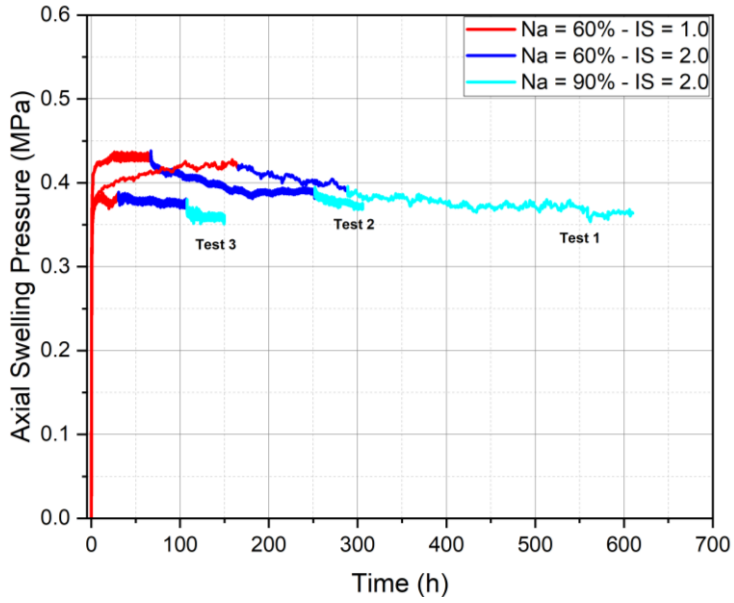

Figure 48 Evolution of the swelling pressure of samples percolated with different saline solutions (Na=60%- IS=1.0 M→ Na=60%- IS=2.0 M→ Na=90%- IS=2.0 M).

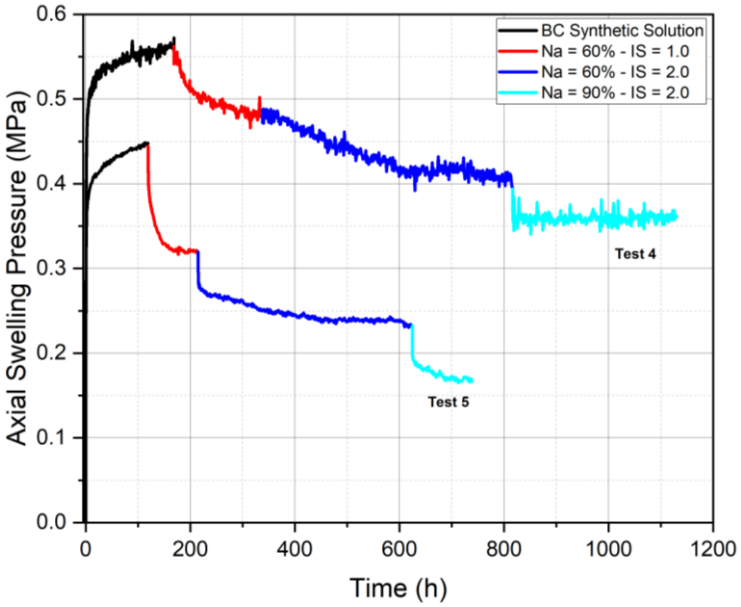

Figure 49 Evolution of the swelling pressure of samples percolated with different saline solutions (BC synthetic solution → Na=60%- IS=1.0 M→ Na=60%- IS=2.0 M→ Na=90%- IS=2.0 M).

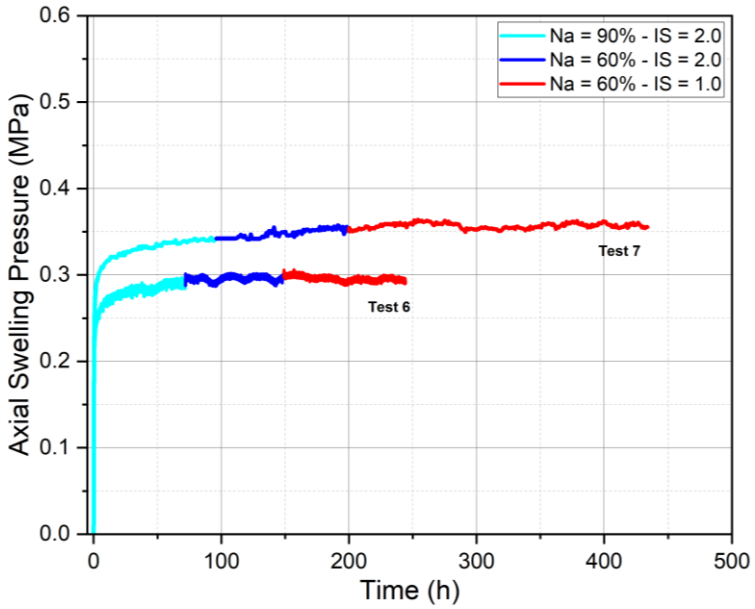

Figure 50 Evolution of the swelling pressure of samples percolated with different saline solutions (Na=90%- IS=2.0 M→ Na=60%- IS=2.0 M→Na=60%- IS=1.0 M).

iii. Effect of sodium occupancy and solute concentration on hydraulic conductivity

Figure 51 shows the impact of the solution concentration and occupancy of sodium, on the evolution of the hydraulic conductivity of BC samples that are consecutively equilibrated with the different solutions. At the outset, all samples were percolated with BC synthetic solution, yielding a value of hydraulic conductivity K equal to $4.5 \times 10^{-12}\, m/s$, which aligns with the findings from existing literature (Horseman et al., 1987; Yu et al., 2013). In particular, the *K* values for the BC reported in the literature under the in-situ conditions (BC synthetic solution) vary from $1.5 \times 10^{-12}\, to\, 4 \times 10^{-12}$ (Yu et al., 2013). In this study, the highest recorded K value changes from 5.8 × 10^{-12} m/s (resulting from BC synthetic solution) to 9.9 × 10^{-11} m/s (using a 1.0 M (Na,Ca)NO_3 solution with 60% Na^+ occupancy), and further to 1.03 × 10^{-10} m/s (with a 2.0 M (Na,Ca)NO_3 solution, 60% Na^+ occupancy), and finally reaching 1.23 × 10^{-10} m/s (with a 2.0 M $NaNO_3$ solution, 90% sodium occupancy). Interestingly, the hydraulic conductivity is positively correlated with the concentration of infiltrating sodium solutions. This observation is congruent with the findings reported by other researchers (Villar, 2007; Chen et al., 2015), who explored the effects of saline and alkaline solutions on the hydraulic conductivity of MX80 bentonite/granite mixture (with a ratio of 30/70 in dry mass) and GMZ01 bentonite, respectively. This pattern is also in agreement with the outcomes from various other studies. Karnland et al. (1992)

identified an increase in permeability for compacted MX-80 bentonite by half an order of magnitude when permeant salinity was elevated from distilled water to 3.5 M NaCl. Similarly, Villar (2005) highlighted a 135% higher hydraulic conductivity for compacted MX-80 bentonite when exposed to saline water (0.5 M salinity) compared to de-ionized water. Castellanos et al. (2008) discovered these fluctuations to be comparable in scale to those observed in compacted FEBEX bentonite.

These results are not consistent with those presented in the study by Bleyen et al. (Bleyen, 2018), who observed the evolution of hydraulic conductivity for a Boom Clay core (length = 3 cm, diameter = 3.8 cm) consecutively percolated with Real Boom Clay pore Water (RBCW) and with RBCW containing 0.1, 0.5, or 1 M $NaNO_3$ over a total test duration of approximately 10 years. The percolation tests were conducted in oedometer cell with a constant effective stress of 2.75 MPa. It was observed that immediately after switching to a higher concentration (i.e., a higher ionic strength), the hydraulic conductivity increased rapidly but only slightly, by approximately 25%. Conversely, when Na^+ exchange occurred over longer time, the hydraulic conductivity began to decrease. This behavior was attributed to the decrease in Electrical Diffuse Layer (EDL) thickness for the increase of the hydraulic conductivity. The effect was counteracted in the following weeks and months by Na^+-M^{2+} cation exchange processes and, to some extent, by the subsequent deterioration of the microstructure ("slaking") due to the ion exchange with sodium. Note that the test duration was almost 10 years, and it is known that the hydraulic conductivity of clay cores under continuous vertical stress decreases slowly with time (~10% after 6 years; N. Maes, SCK•CEN, personal communication, 2013 , in: Bleyen et al., 2018), probably due to the creep of the clay. All this has to be kept in mind when interpreting the results of these tests and comparing them to the tests done in this work.

It is worth noting that in this study, the determination of hydraulic conductivity was instantaneous after directly switching to a higher solution concentration and sodium occupancy under constant volume condition, thereby representing the immediate hydraulic conductivity after such switch. Furthermore, over time, the hydraulic conductivity of Boom Clay may decrease due to its self-sealing capacity, which can lead to the closure of some macropores. Further investigations are required to better understand such complex process.

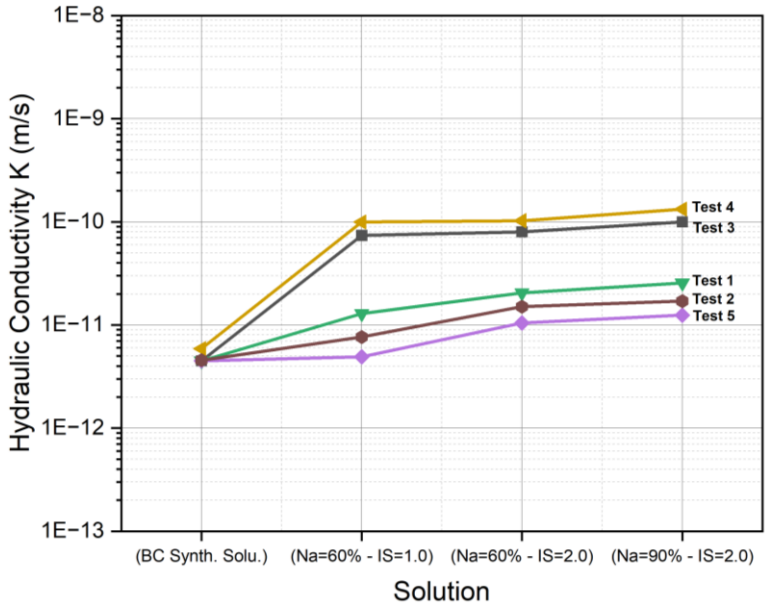

Figure 51 Evolution of hydraulic conductivity with varying sodium occupancy and solute concentration (BC synthetic solution → Na=60% - IS=1 M → Na=60% - IS=2 M → Na=90% - IS=2 M).

To further investigate the influence of sodium occupancy on swelling pressure, two more tests with Na^+ occupancies of 10% and 20% were performed. The procedure started with the infiltration of the BC synthetic solution, followed by percolation involving a solution containing 1.0 M solution concentration with 20% (Figure 52) and 10% (Figure 53) sodium occupancy, respectively. The solutions infiltrated into these samples are prepared by mixing sodium nitrate ($NaNO_3$) and calcium nitrate $Ca(NO_3)_2$, leading to an increase of calcium fraction in the solution due to the increase of $Ca(NO_3)_2$ concentration.

The evolutions of swelling pressure with 20% and 10% Na occupancy are illustrated in Figure 52 and Figure 53, respectively. It is seen that the infiltration of the BC synthetic solution led to a swelling pressure of 0.6 MPa and 0.75 MPa, respectively. This synthetic solution was maintained until two pore volume replacements were completed. The subsequent part of the graph can be divided into two phases: initially, there is a slight decrease in swelling pressure, followed by an increase. For the sample with 10% Na^+ occupancy a greater increase was observed compared to the 20% sample. The initial decrease in both cases align with the DDL theory and the compression of clay platelets along with the decreased thickness of the DDL. As infiltration continues with a solution containing fewer sodium cations and more calcium cations, the calcium cations, which have a larger hydrated radius than sodium cations,

begin to replace the Na^+ cations situated within the interlayer space, triggering an increase in swelling pressure.

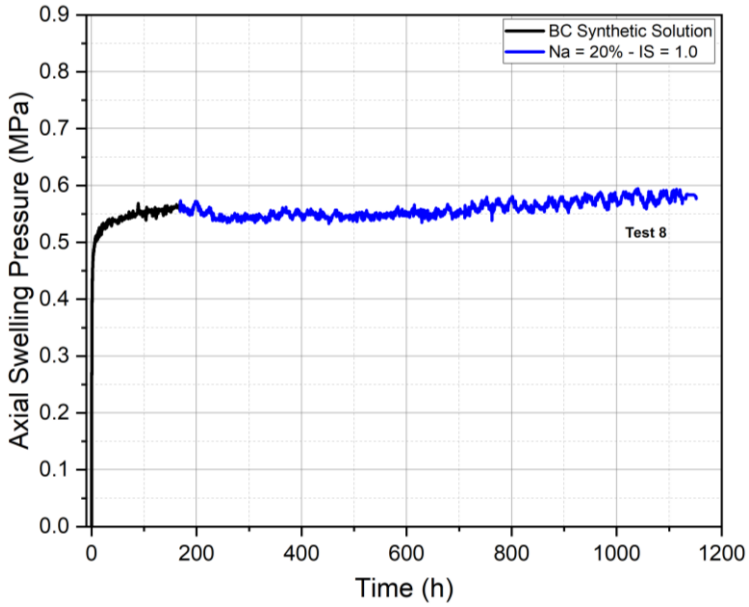

Figure 52 Evolution of swelling pressure of a sample with BC synthetic solution and Na=20% - IS =1.0 M.

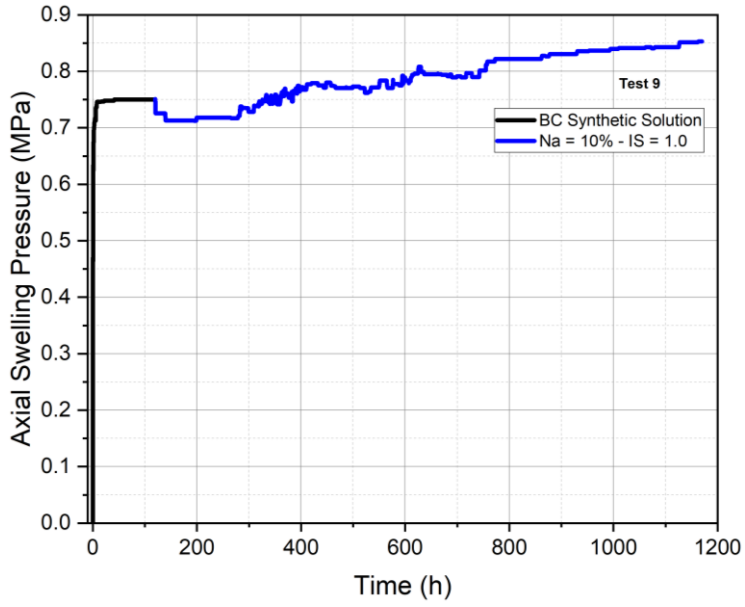

Figure 53 Evolution of swelling pressure with BC synthetic solution and Na=10% - IS=1.0 M.

c. Discussion

i. Effect of solute concentration on swelling pressure

Various studies showed that the swelling capacity of clayey material is lower in saline water; the higher the dissolved salt concentration, the lower the swelling pressure (Studds et al., 1998; Karnland et al., 2005, 2006; Castellanos et al., 2008; Katsumi et al., 2008; Suzuki et al., 2008; Siddiqua et al., 2011). The swelling behavior of unsaturated clayey soil upon exposure to water or electrolytes is commonly governed by two primary mechanisms: crystalline swelling and diffuse double-layer (DDL) swelling (Madsen and Müller-Vonmoos, 1989; Savage, 2005). Crystalline swelling is prompted by the hydration of initially dehydrated exchangeable cations (K^+, Na^+, Ca^{2+}, and Mg^{2+}) between the unit layers of montmorillonite. This mineral has a structure with a single alumina octahedral sheet enclosed between two silica tetrahedral sheets (TOT). The DDL swelling leads to more extensive and prolonged swelling, often referred to as long-term swelling. The swelling potential of expansive clays is influenced by factors such as overburden stress, unloading conditions, water exposure, and water content. Various researchers have studied the swelling characteristics of bentonite. Evans and Quigley (1992) explored the effects of salt (copper solution) leaching from solid waste on permeability and swell percentage in sand-bentonite mixtures. They found that salt leaching increased permeability while decreasing swelling. Similarly, Simons and Reuter (1985) investigated the influence of salt leaching from waste and absorption, revealing changes in ions and electrostatic forces that led to the decrease in swelling pressure and increase in hydraulic conductivity. Di Maio (1998) observed an increase in free swelling of bentonite after interaction with water following exposure to NaCl, KCl, and $CaCl_2$ solutions. The exchange of Na^+ was found to be reversible, unlike the exchange of Ca^{2+} or K^+.

The results from this study illustrate a decrease in swelling pressure as sodium concentrations increase. This behavior can be qualitatively explained by the diffuse double layer (DDL) theory. On a mesoscopic scale (1 - 10 μm), the ionic strength of the solution governs the repulsion forces between particles and influences osmotic pressure within micro-pores (0.01 - 1 μm) (Matuso, 1977). As the cation concentration in the pore water increases, the thickness of the diffuse double layer and the repulsive

force decrease (Mitchell and Soga, 2005). Consequently, a lower swelling pressure was observed for the specimens percolated with saline solutions.

ii. Effect of sodium occupancy on swelling pressure

For a specific type of clay, its structure is influenced by two main factors: (i) the ionic composition of the exchange complex and (ii) the pH level. The characteristics of the exchange complex are primarily affected by the valence, concentration, size, and hydration properties of the cations. Alterations in the chemical composition of the pore fluid bring about distinct impacts on clays. These changes might lead to cation exchanges between mineralogical units, variations of the electrochemical forces acting among different platelets, and variations in osmotic pressure. The cation exchange reaction is mainly controlled by the exchange capacity of the clay minerals (Mata, 2003). The ease with which a cation of one type can replace a cation of another type depends mainly on the valence, relative abundance of the different cation types, and the cation size. On a microscopic scale (interlamellar space of montmorillonite sheets), the spacing between different unit layers is contingent upon the valence, dimensions, and hydration state of the interlayer cations. When the cations present in the pore water possess considerable replacing potential, cation exchange can occur, potentially altering the clay type. The commonly admitted competitive order is $Na^{+} < K^{+} < Mg^{2+} < Ca^{2+}$ (Mata Mena, 2003; Mitchell and Soga, 2005; Zeng et al., 2020). Furthermore, high sodium concentrations in infiltrated saline solution samples may lead to the replacement of divalent ions, such as calcium, which tends to reduce the diffuse double layer (DDL). Alawaji (1999) also indicated that the swelling potential diminishes with elevated sodium concentration in the liquid composition.

Martens et al. (2011) performed a series of laboratory percolation experiments on undisturbed and saturated Boom Clay cores. Real Boom Clay pore Water (RBCW) and RCBW with additional $NaNO_3$ with concentrations up to 1 M were injected in four steps into clay cores. The concentration of Na, K, Ca, Mg and Sr in the eluted water were measured. It was found that after every switch of the $NaNO_3$ concentration, the concentration profiles of K, Ca, Mg and Sr showed a sharp rise, followed by a slow decrease. It was also found that as a result of injecting high concentrations of sodium, the Boom Clay is transformed into Na-clay with almost 100% Na occupancy at exchange clay sites. Reactive coupled transport modelling with PHREEQC-2 was used

to describe the experimentally observed elution curves for the cations. The model could fairly well describe the experimentally observed cation concentrations in the eluted water, confirming that cation exchange is indeed the dominant mechanism regulating the cation elution in the percolation experiments.

Infiltration of sodium cations into the interlayer spaces between montmorillonite sheets results in a decrease in swelling potential. This reduction could be attributed to the hydrated radius of the sodium cation. The adsorption of cations with varying hydrated radii by fine clayey soil emerges as a pivotal factor impacting swelling potential. The principal hydrated radii reported in the literature are presented in Table 21. Notably, sodium cations possess a smaller hydrated radius compared to calcium and magnesium. The disparities among the hydrated radii presented in Table 21 may be attributed to the differing methods used to estimate the hydrated radius of each cation. The values provided by Mitchel and Soga (2005) were derived from the equations of Stern's theory as described by van Olphen (1965), which account for both single and interacting flat double layers. These equations enable the calculation of charge within each layer and the potential at their interface. It is plausible that these variations are linked to the number of water molecule layers surrounding the cation, a quantity that likely varies depending on the scenarios, such as very low ionic strength (IS) solutions, high IS solutions, or within the water layer in contact with a clay sheet in a dense clay matrix. The values of the hydrated radius given by Kielland (1937) were based on a revised and extended table of ionic activity coefficients, largely computed by independent means, taking into consideration the diameter of the hydrated ions as estimated by various methods. For sufficiently dilute solutions, the well-known Debye-Hückel formula was used. The effective diameters of the hydrated ions (noted as a_i) were approximately calculated by different methods, such as from the crystal radius and deformability according to the equation for cations given by Bonino (1933), or from the ionic mobilities or its empirical modification given by Young and Smith (2000). Sridharan et al. (1986) demonstrated that the hydrated cationic radius substantially affects the liquid limit of montmorillonite, a phenomenon more pronounced with monovalent cations than with higher valences.

Though limited data exists on the impact of the hydrated cationic radius on the swelling pressure of clays, it can be inferred that an increase in hydrated cationic radius results in a greater interlayer space, consequently yielding higher swelling capacity.

Specifically, the hydrated radius of the Na^+ ion is approximately 10% larger than that of K^+, while it is approximately 30%-40% smaller than those of Mg^{2+} and Ca^{2+}.

Table 21 Hydrated radius of cations (a_i).

Cation	Kielland (1937)	Mitchell and Soga (2005)	Lide and Frederikse (1995)
Na^+	0.4-0.45 nm	0.56-0.79 nm	0.358 nm
K^+	0.3 nm	0.38-0.53 nm	0.331 nm
Mg^{2+}	0.8 nm	1.08 nm	0.628 nm
Ca^{2+}	0.6 nm	0.96 nm	0.812 nm
Al^{3+}	0.9 nm	-	-

iii. Effect of sodium occupancy and solute concentration on hydraulic conductivity

During the pore water replacement, it appeared that higher concentrations of salt solution and sodium occupancy led to lower swelling pressure and higher hydraulic conductivity. According to Castellanos et al. (2008), several mechanisms may be at play, including alterations in pore size distribution due to the swelling of the clay matrix, and variations in water molecule mobility associated with exchangeable cations present on clay sheet surfaces (interlayer space) or within the diffuse double layer. As a result, an increase in salt concentration of the pore water leads to a reduced swelling capacity of clay particles, thereby enlarging the size of larger flow channels (inter-aggregate) and subsequently increasing the permeability.

Additionally, an increase in sodium occupancy leads to a decrease in swelling pressure and interlayer spacing between montmorillonite sheets, giving rise to the formation of more micro-fissures. This phenomenon could explain the observed increase in hydraulic conductivity with rising sodium occupancy. Conversely, a reduction in pore water salt concentration amplifies the development of the diffuse double layer, causing a decrease in permeability due to the decreased size of larger flow channels. In other words, aggregation of clay enlarges macro-pores as a consequence of increased pore water salt concentration, ultimately increasing soil permeability.

The influence of pore water salt concentration and sodium occupancy on permeability remained consistent: higher concentrations or occupancy resulted in higher

permeability. Numerous findings on compacted swelling clays demonstrated a correlation between pore water salinity and permeability increase. For instance, FEBEX bentonite exhibited a 184% rise in hydraulic conductivity with a NaCl concentration of 0.22 M compared to distilled water. Similarly, with a NaCl concentration of 5.5 M, the permeability (*K)* has doubled. MX-80 bentonite displayed a 5 to 6-fold increase in permeability (*K)* when shifting from distilled water to 3.5 M NaCl, as confirmed by Karnland et al. (1992). Villar (2005) reported a 135% increase in *K* for MX-80 bentonite using a 0.5 M NaCl solution in comparison to pure water. Experiments by Pusch (2001) showed a two-order of magnitude increase in *K* with a salinity rise from 0% to 20% on Friedland Ton clay, a natural clay containing 45% smectite. Furthermore, Castellanos et al. (2008) and Pusch (2001) concluded that sodium induces a greater increase in permeability than calcium.

3. Effect of salinization/desalinization cycle of (Na,Ca)NO_3 and Na^+ occupancy on the volumetric behavior and microstructure of BC

a. Introduction

In this section of study, both the effects of sodium occupancy and solute concentration on the volume change behavior and microstructure of BC were investigated. In total, six different salinization-desalinization tests were conducted, involving the infiltration of a synthetic BC solution (0.015 M $NaHCO_3$; De Craen et al., 2004) and (Na,Ca)NO_3 solutions of different concentrations and with different sodium (Na^+) occupancies. Two concentrations of (Na,Ca)NO_3 —1 mol/L and 2 mol/L — were considered, along with two different Na/Ca ratios, resulting in two target Na^+ occupancies of 60% and 90%. Note that such high occupancies (60% and 90%) simulate the response of the BC to the $NaNO_3$ plume identified by the classical advection-diffusion-retardation transport simulations regarding the leaching of $NaNO_3$ from Eurobitum (Weetjens et al., 2010; Al Mais et al., 2024). The MIP analyses were conducted on three sample types: intact samples, samples saturated with synthetic BC solution, and samples subjected to one single cycle of salinization-desalinization under constant effective vertical stresses of 0.4, 0.8, 1.6 and 2.25 MPa. Based on the test results, the effects of solute concentration and sodium occupancy on the volume change and microstructure were analyzed. The

samples were taken from four different cores: R78-79W_Core 28.1, R78-79W_Core 2.2, CG76-77W_Core 16.2 and CG76-77W_Core 13.2 (Table 22).

In addition, the basic properties of the tested samples were determined and are shown in Table 4. It appears that the water content is in the range of 20.6%< w_0 <23.6%, and the saturation is in the range of 94%< S_r <100%. Note that the specific solid density (G_s) of BC is 2.65 Mg/m³ (De Craen et al., 2004). The void ratio was calculated based on the G_s, as well as the total volume and mass of each sample. Since the samples were hand-trimmed and prepared from different cores, they may exhibit some variabilities. Thereby, the initial void ratios of the tested samples range from 0.565 to 0.6 (Table 22). To minimize the impact of these variabilities, each sample was percolated under fixed vertical stress with cycles of different solute concentrations and sodium occupancies. The loading direction for the samples was chosen to be perpendicular to the bedding plane.

Table 22 Geometry, initial water content and initial void ratio of the tested specimens.

Test	Sample localization	D_0 (mm)	H_0 (mm)	ρ (g/cm³)	W_0 (%)	e_0 (-)	S_r (-)
1	R78-79W_Core 28.1 Block7-SliceII	49.84	10	2.02	20.6	0.582	0.94
2	R78-79W_Core 28.1 Block13-SliceIII	49.85	9.6	2.06	21.6	0.565	1
3	R78-79W_Core 2.2 Block3-SliceIV	49.74	9.62	2.04	23.5	0.599	1
4	R78-79W_Core 2.2 Block2-SliceIII	49.76	9.94	2.04	23.6	0.6	1
5	CG76-77W_Core 16.2 Block3-SliceIV	49.81	9.74	2.04	22.36	0.59	0.99
6	CG76-77W_Core 13.2 Block1-SliceI	49.5	9.6	2.05	23	0.586	1

Table 23 presents the specifications for the salinization/desalinization tests (1–6), including the test paths and corresponding vertical stresses. The void ratio and the height of each sample just before starting the chemical loading/unloading cycles under the specified vertical stress are also presented. The void ratio ranges from 0.554 to 0.636, while the height varies between 9.4 and 10 mm, due to the variability of the samples, as mentioned previously. All the tests were performed at a controlled ambient temperature of 20 ± 1 °C.

Table 23 Specification for the cyclic salinization/desalinization tests.

Test	Vertical stress (MPa)	Void ratio (-)	H_0 (mm)	Salinization/desalinization path
1	2.25	0.562	9.56	60%-1.0/60%-2.0/90%-2.0/60%-2.0/60%-1.0
2	1.6	0.547	9.91	60%-1.0/60%-2.0/90%-2.0/60%-2.0/60%-1.0
3	0.8	0.606	9.65	60%-1.0/60%-2.0/90%-2.0/60%-2.0/60%-1.0
4	0.4	0.6	9.92	60%-1.0/60%-2.0/90%-2.0/60%-2.0/60%-1.0
5	0.4	0.636	10	60%-1.0/60%-2.0/90%-2.0/60%-2.0/60%-1.0
6	0.4	0.554	9.4	60%-1.0/90%-2.0/60%-2.0/60%-1.0

b. Experimental results

i. Effect of sodium occupancy and solute concentration on the volume change behavior

The chemical loading/unloading cycle tests involved the infiltration of (Na,Ca)NO_3 solutions with varying solute concentrations and sodium occupancies (Na^+) under different vertical stresses. During the salinization/desalinization process under different vertical stresses, clear stabilization was not always achieved before transitioning to the next solution. Equilibrium was considered reached after achieving the desired pore volume replacement through percolation.

The impacts of (Na,Ca)NO_3 concentration and sodium occupancy on the volumetric strain measured during the salinization/desalinization cycle are illustrated in Figure 54. The specimens are tested under vertical stresses of 2.25 (Figure 54.a), 1.6 (Figure Figure 54.b), 0.8 (Figure 54.c) and 0.4 (Figure 54.d.e.f) MPa. During the first salinization step (60%-1.0 M), the BC exhibits a compression/shrinkage behavior under all vertical stresses and the shrinkage continues with increasing solute concentration (60%-2.0 M) and sodium occupancy (90%-2.0 M). In contrast, swelling behavior is recorded during the desalinization steps. The BC thus undergoes shrinkage with increasing infiltration solution concentration and sodium occupancy, and swelling with decreasing solute concentration and sodium occupancy. This finding aligns with the results reported by various researchers (Thyagaraj and Rao, 2013; Chen et al., 2019; Zhang et al., 2023). Moreover, it can be observed from Figure Figure 54(b) that the BC exhibits larger swelling after injecting BC synthetic solution after the

salinization/desalinization cycle under vertical stress of 1.6 MPa. However, slight swelling is detected for the sample percolated with BC synthetic solution after the salinization/desalinization cycle under 0.4 MPa (Figure 54(d)). It can thus be inferred that the solute concentration and the sodium occupancy have similar effect on the volume change behavior. As the solute concentration increases (from 1.0 M to 2.0 M) while maintaining a constant sodium occupancy of 60%, the BC experiences a shrinkage. Subsequently, raising the occupancy to 90% whilst maintaining the concentration of 2.0 M, leads to further compression. Likewise, when the sodium occupancy is elevated at the same concentration, the shrinkage behavior continues, underlining the similar influence of both occupancy and concentration on the volume change behavior.

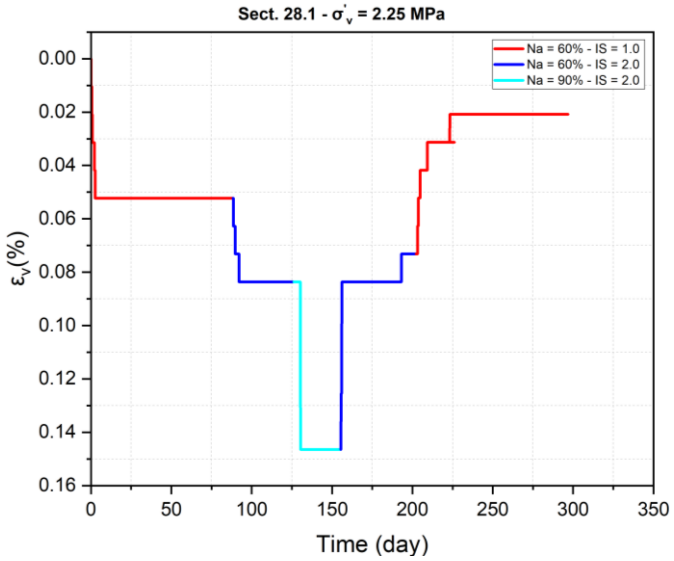

(a)

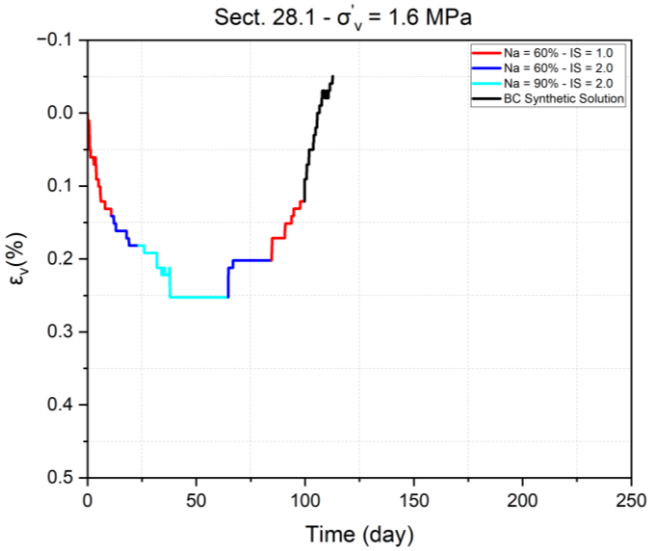

(b)

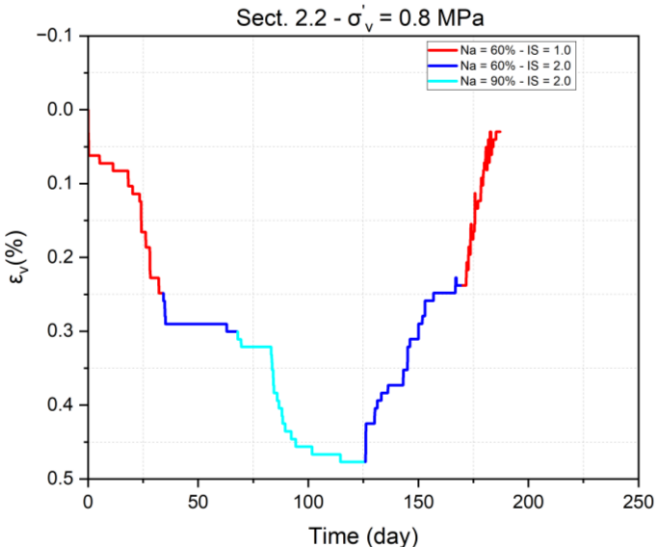
Sect. 2.2 - σ'v = 0.8 MPa
Na = 60% - IS = 1.0
Na = 60% - IS = 2.0
Na = 90% - IS = 2.0
εv(%)
Time (day)

(c)

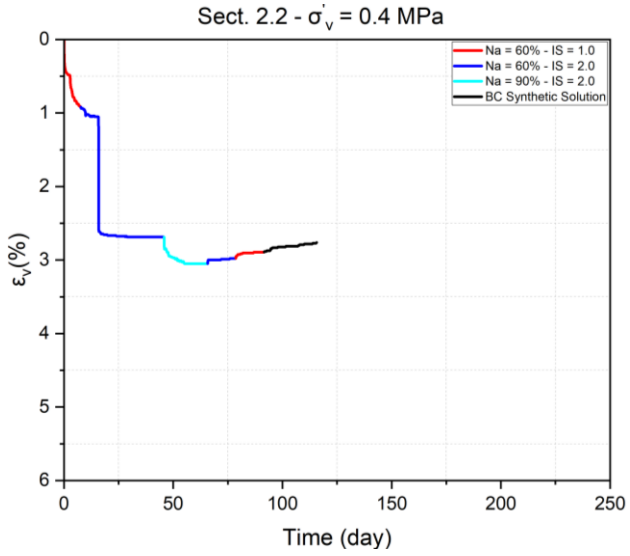
Sect. 2.2 - σ'v = 0.4 MPa
Na = 60% - IS = 1.0
Na = 60% - IS = 2.0
Na = 90% - IS = 2.0
BC Synthetic Solution
εv(%)
Time (day)

(d)

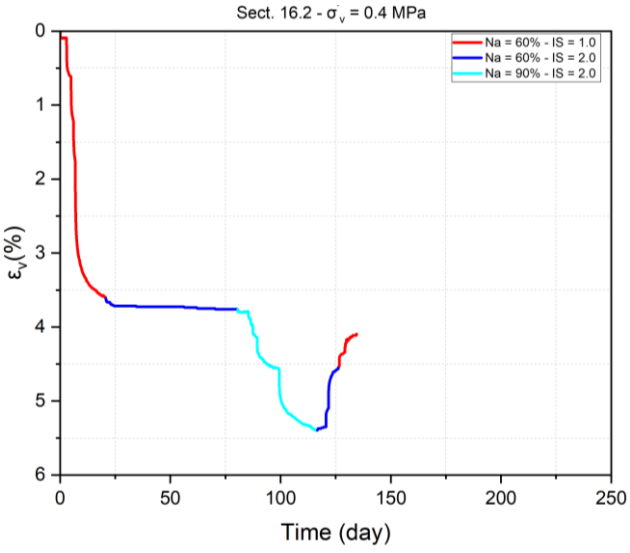
Sect. 16.2 - σ'v = 0.4 MPa
Na = 60% - IS = 1.0
Na = 60% - IS = 2.0
Na = 90% - IS = 2.0
εv(%)
Time (day)

(e)

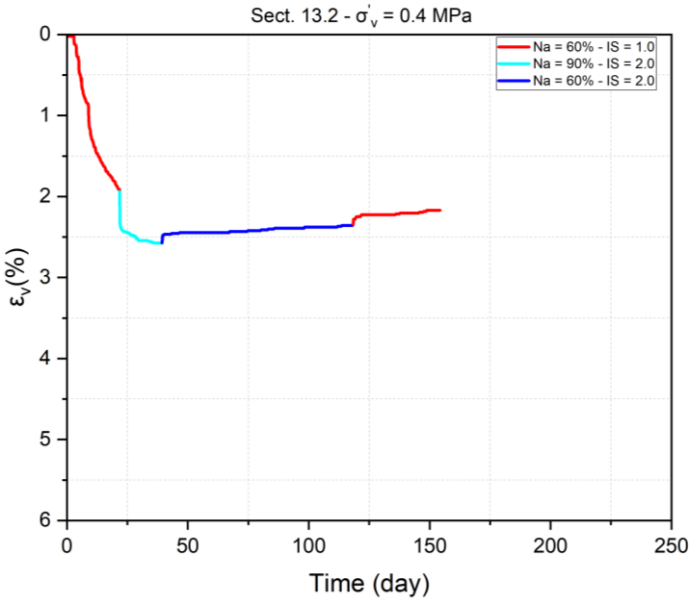

(f)

Figure 54 Volumetric strain evolution with time under different vertical stresses: (a) σ'_v = 2.25 MPa ;(b) σ'_v = 1.6 MPa ;(c) σ'_v = 0.8 MPa ;(d, e, f) σ'_v = 0.4 MPa.

ii. Effect of vertical stress on vertical strain

Figure 55 illustrates the total vertical strain during salinization (full line) and desalinization (dashed line) as function of the vertical stress. During salinization, the total vertical strain is approximately 0.20% under a vertical stress of 2.25 MPa. As the vertical stress decreases, the vertical strain increases, reaching about 3.6% under 0.4 MPa. This indicates that the effect of salinization is more pronounced at lower vertical stresses, suggesting that the physico-chemical effects are dominant in the lower stress range. From the desalinization data points, it can be observed that the final strain after swelling is nearly zero for stresses ranging from 0.8 to 2.25 MPa. This reversible behavior indicates that the strain induced by salinization is almost fully recovered after the desalinization. In contrast, under 0.4 MPa, the final strain after swelling is still around 3%, showing that only 0.6% of the induced strain has been recovered. This suggests that the effect of the physico-chemical processes is reversible and recoverable for stresses above 0.8 MPa. Thereby, two distinct zones can be defined, separated by 0.8 MPa, which is close to the swelling pressure of Boom Clay under in situ conditions (Horseman et al., 1987; Nguyen, 2013). In the higher stress zone (above 0.8 MPa), the behavior is predominantly reversible (elastic zone), with the physico-chemical effects being insignificant (Cui et al., 2013). By contrast, in the lower stress zone (below 0.8 MPa), the behavior becomes irreversible (plastic zone), and the

physico-chemical effects are more pronounced (Cui et al., 2013). It is noteworthy that switching between solutions depends on the number of pore volumes required for each solution.

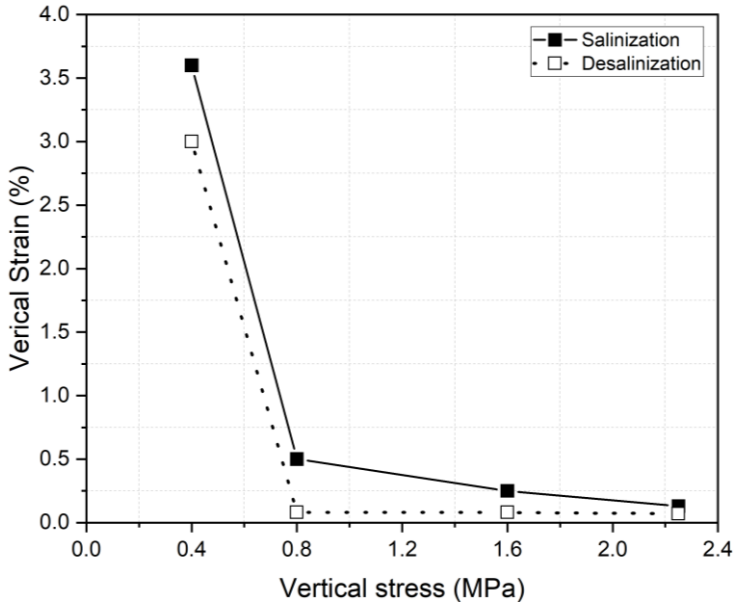

Figure 55 Vertical strain versus vertical stress in the salinization/desalinization cycle.

iii. Effect of sodium occupancy and solute concentration on the microstructure of BC

The effect of solute concentration occurs on the mesoscopic scale, affecting the pore sizes ranging from 1 μm to 10 μm. In contrast, cation occupancy impacts the microscopic scale (less than 1 μm), specifically within montmorillonite interlayer spaces. However, this microscopic scale cannot be detected using MIP analyses due to the limitation of the MIP technique. Therefore, this study focuses only on investigating the effect of solute concentration on the microstructure of BC.

Figure 56 displays the MIP results for the specimens subjected to a salinization/desalinization cycle under vertical stresses of 0.4 (Figure 56.a, b), 0.8 (Figure 56.c, d), and 2.25 (Figure 56.e, f) MPa. Regardless of the applied vertical stress, all specimens exhibit a unimodal pore size distribution. The predominant pore sizes range from 0.07 to 0.1 μm, with the emergence of macropores between 10 and 50 μm, as well as pores exceeding 100 μm. For the specimens percolated at 0.4 MPa, the pore structure can be divided into two distinct categories: small pores ranging from 0.07 to 1.0 μm and larger pores between 10 and 200 μm. This observation is consistent with the findings from Musso et al. (2013) and Zhang et al. (2023). In contrast, the

specimens percolated at 0.8 and 2.25 MPa maintained a unimodal distribution, characterized by the presence of macropores exceeding 100 μm. This behavior can be attributed to the increased osmotic suction, which leads to the shrinkage of the diffuse double layer, resulting in soil shrinkage that creates fissures and preferential flow paths (Yuan et al., 2019; Zhang et al., 2023). This indicates that salinization/desalinization may lead to changes of the soil microstructure by generating larger pores. As vertical stress decreases, both the dominant pore size and the corresponding density of the micropores tend to increase following the chemical loading/unloading cycles. This behavior is attributed to the shrinkage of soil and the formation of aggregates, which is significantly enhanced under higher concentrations of (Na,Ca)NO_3. As the concentration of dissolved ions increases, the ionic strength of the pore water rises, effectively compressing the diffuse double layer. This compression reduces the electrostatic repulsion between adjacent clay particles, facilitating closer contact and promoting aggregation (Delage and Lefebvre, 1984; Guerra et al., 2017). Larger aggregates lead to the formation of larger macropores within the soil structure. After the chemical loading and unloading cycle, irreversible fissures develop in the soil matrix. These fissures tend to be more pronounced under lower vertical stresses, suggesting that the mechanical effects of salinization/desalinization are more significant when the soil is less constrained. Additionally, the observed macropore sizes follow a consistent trend that correlates with the applied vertical stresses. As vertical stress increases, the size and extent of the macropores decrease, suggesting that higher stress levels reduce the physicochemical effects in terms of soil structure. Consequently, the interaction between the clay particles, influenced by factors such as salt concentration, leads to changes in microstructure that are more significant under lower stresses.

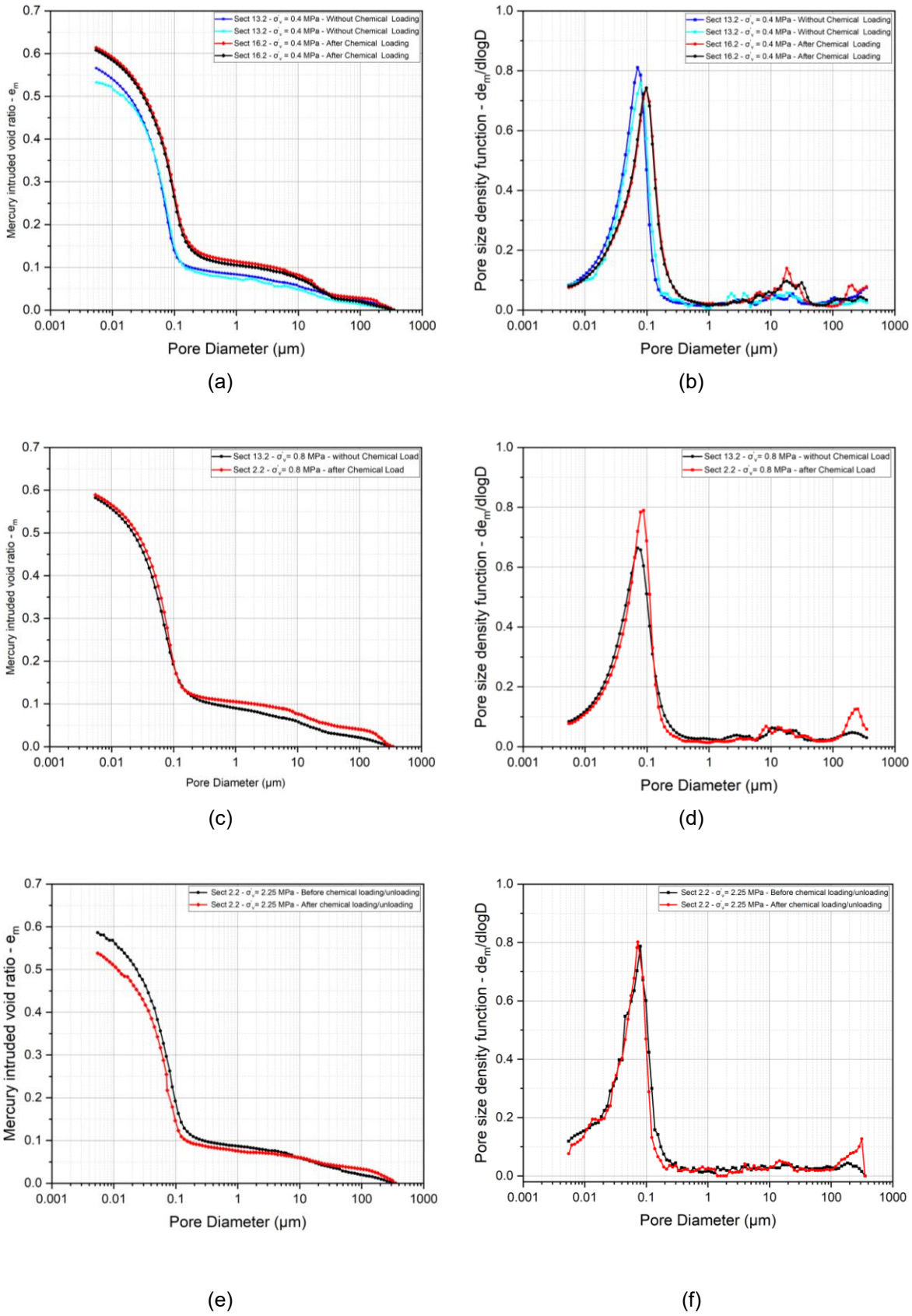

Figure 56 Cumulative curves (a, c, e) and density function curves (b, d, f) of BC specimens before and after chemical loading/unloading cycle.

c. Discussion

i. Effect of sodium occupancy, solute concentration and vertical stress on volumetric strain

According to the double structure theory, the hydration swelling of clay particles occurs on the microstructural level (within the clay aggregates), and the rearrangement of the clay structure is observed on the macrostructural level (between the clay aggregates) (Gens and Alonso, 1992). The physicochemical interaction on the microstructural level was assumed to be independent of the macrostructure, while microstructural deformation was assumed to be elastic and strongly affecting the clay macrostructure. In contrast, macrostructural deformation can be partially plastic. The double structure theory can adequately explain the volume change behavior of BC with respect to the sodium concentration and occupancy (Ye et al., 2017; De La Morena et al., 2018). The effect of solute concentration can be explained by the Diffuse Double Layer theory (DDL) (Madsen and Müller-Vonmoos, 1989; Savage, 2005), while the sodium occupancy controls the interlamellar space between montmorillonite sheets. This mineral has a structure with a single alumina octahedral sheet enclosed between two silica tetrahedral sheets (TOT) (Mitchell and Soga, 2005). Various studies showed that the volume change behavior of clayey soil is strongly dependent on the pore water chemistry (Studds et al., 1998; Karnland et al., 2005, 2006; Castellanos et al., 2008; Katsumi et al., 2008; Suzuki et al., 2008; Siddiqua et al., 2011): the higher the dissolved salt concentration, the larger the shrinkage.

In the literature, four possible mechanisms have been put forward to explain the shrinking/swelling of clayey soil during saline cycling: 1) change in the surface potential of clay lamellae with the salt concentration; 2) change in the Debye thickness with the salt concentration (contraction or expansion of DDLs); 3) change in osmotic suction with the salt concentration (outflow or inflow of the pore water under osmotic gradient); and 4) exchange of Ca^{2+} and Mg^{2+} cations present in the interlayer space of the montmorillonite sheets with Na^{+} cations present in the percolated solutions. The cation with higher replacing power can also be replaced by the one with lower replacing power depending on its concentration. This is consistent with the results reported by Di Maio (1998) and Mitchell and Soga (2005). Previous studies (Studds et al., 1998; Karnland et al., 2005; Castellanos et al., 2008; Katsumi et al., 2008; Siddiqua et al., 2011) did

not comprehensively address the role of cation exchange in clay behavior. As a result, the effects of cation characteristics, including type, valence, and hydrated ionic radius, were not fully considered. This gap in the literature has led to an incomplete understanding of how specific cation properties influence the swelling behavior of clay, especially under variable ionic environments. In some studies, the shrinking/swelling behavior has been mainly attributed to the DDL theory (Attard, 1996; Bradbury and Baeyens, 2003; Suzuki et al., 2005).

Alteration in the chemical composition of pore fluid can bring about distinct impacts on clays, leading to cation exchanges at the level of different mineralogical units, variations in the electrochemical forces acting among different platelets, and fluctuations in osmotic pressure. The cation exchange is mainly controlled by the exchange capacity of the clay minerals (Mata Mena, 2003); the ease with which a cation of one type can replace a cation of another type depends mainly on the valence, relative abundance of the different cation types, and the cation size. On a microscopic scale, the spacing between different unit layers is contingent upon the valence, dimensions, and hydration state of the interlayer cations. The commonly accepted competitive order in cation exchange processes is $Na^{+} < K^{+} < Mg^{2+} < Ca^{2+}$ (Mitchell and Soga, 2005; Sun et al., 2018; Zeng et al., 2020). Furthermore, high sodium concentrations may lead to the replacement of divalent ions, such as calcium, which tends to reduce the diffuse double layer (DDL).

The results obtained in this study confirm the above findings that increasing solute concentration and sodium occupancy leads to the shrinkage of BC while swelling behavior has been detected with decreasing both. The effect of sodium concentration can be qualitatively explained by the diffuse double layer (DDL) theory. On a mesoscopic scale, the ionic strength of the solution governs repulsion forces between particles and osmotic pressure within micro-pores. Additionally, as the cation concentration of pore water increased, the repulsive force between the diffuse double layer and the thickness of the diffuse double layer decreased (Mitchell and Soga, 2005). Consequently, a higher shrinkage was observed for the specimens percolated with saline solutions.

Concerning sodium occupancy, infiltration of sodium cations into the interlayer spaces between montmorillonite sheets results in an increase in shrinkage potential. This increase could be attributed to the replacement of calcium which has large hydrated

radius by sodium which has smaller hydrated radius (Al Mais et al., 2024). The adsorption of cations with varying hydrated radii by fine clayey soil emerges as a pivotal factor impacting the swelling potential. The hydrated radii reported in the literature are presented in Table 4. Notably, sodium cations possess a smaller hydrated radius compared to calcium and magnesium. Sridharan et al. (1986) demonstrated that the hydrated cationic radius substantially affects the liquid limit of montmorillonitic soils, a phenomenon more pronounced with monovalent cations than those with higher valences.

Though limited data exists about the impact of hydrated cationic radius on the volume change behavior of clayey soils, it can be qualitatively concluded that – for a given valency – an increase in hydrated cationic radius results in a greater net interlayer space, consequently yielding higher swelling capacity. Specifically, the hydrated radius of the Na^+ ion is approximately 10% larger than that of K^+, while it is approximately 30%-40% smaller than that of Mg^{2+} and Ca^{2+} (Kielland, 1937; Mitchell and Soga, 2005). Tests conducted on densely compacted GMZ bentonite showed that the changes in volume change behavior were partially reversible during NaCl-water and NaCl- $CaCl_2$ cycling (Chen et al., 2015, 2017). However, in the case of KCl-water cycling, almost no recovery in volume change was observed, likely due to the potassium ions strongly binding the clay layers and causing a structural collapse that limits the clay ability to swell back to its original volume (Chen et al., 2015, 2017). Chipera et al. (1995) identified that when the relative humidity increases to 100%, the basal spacing is one-layer (~12.5 Å) hydrate state for K-smectite, two-layer (~15 Å) for Na-smectite, while three-layer (~17.5 Å) for Ca-smectite, respectively. Similarly, Villar et al. (2012) reported that the basal spacing of FEBEX bentonite almost increases linearly with relative humidity, while a stepwise increase is identified in MX80 bentonite. This phenomenon could be explained by their different interlayer cations and their hydrated radius (2010).

The clay structure, combining the arrangement of the clay particles and the interparticle forces acting between them, forms the basis of the clay microstructure associated with the pore spaces. Due to the complexity of clay soil structure, the definition of pore spaces is based on two basic fabric elements: elementary particle (microstructural units) and particle assemblages (macrostructure) (Wong and Varatharajan, 2014). Elementary particle arrangements are made up of several single particles linked

together by physicochemical interactions and bonds. These elementary particles are also known as flocs, clusters, aggregate groups or peds. Their structure is characterized by a dense and parallel arrangements (face-to-face contacts) and a low internal porosity. Micropores (intra-aggregate or interlamellar pores; less than 2 μm) are defined by the small pore spaces within the elementary particle. Particle assemblages (greater than 100 μm) correspond to an aggregation of several elementary particles, forming the soil skeleton. The pore spaces within particle assemblages and between the elementary particles correspond to the macropores (interaggregate or intramatrix pores).

Regarding the vertical stress, results from this study show that the effect of solute concentration and sodium occupancy are less pronounced with increasing vertical stress. This behavior can be explained by the physicochemical interactions and fabric arrangement. At higher stresses, the physicochemical effects induced by the face-to-face arrangement of clay particles are restrained by the mechanical stress, which limits the development of spaces between the particles. However, unloading the clay sample to a lower stress leads to the formation of macropores and particle rotation due to electrostatic forces (Cui et al., 2013). This occurs as the electrical double layer between clay particles expands, suggesting that pore water chemistry and cation type may have a more pronounced effect on the volume change behavior of clays.

ii. Effect of solute concentration on microstructure

The increase in pore fluid salinity can enhance the osmotic suction due to the presence of dissolved salts, reducing the thickness of the diffuse double layer, resulting in the shrinkage of soil. Consequently, macropores are generated due to particle aggregation, which corresponds to the preferential pathways for fluids (Wang et al., 2019). As reported by Palomino and Santamarina (2005), the fabric associations are dominated by the ionic concentration. At low ionic concentration, the negatively charged edges and faces of clay sheets lead to a dispersed-deflocculated state. This occurs due to the repulsive forces generated by the diffuse double layer surrounding the clay particles. As a result, the dispersed-deflocculation (DD) mode prevails, allowing the clay particles to remain separated rather than aggregating. As the ionic concentration increases from low to high, the double layer becomes much thinner and the van der Waals attraction dominates (2011). As a result, the particle associations change from the dispersed mode to the face-to-face (FF) mode, leading to the

aggregation of clay platelets. Furthermore, the clay aggregation induced by high-concentration pore fluid salinity can also inhibit the overall shrinkage. The hypothesis of the generation of large interaggregate pores with infiltration of salt solutions can be indirectly justified by the increasing hydraulic conductivity (Karnland et al., 2006; Castellanos et al., 2008; Zhu et al., 2013; Chen et al., 2015). Following Castellanos et al. (2008), several mechanisms can be involved, such as (i) modification of pore size distribution resulting from clay matrix swelling, and (ii) variations of water molecule mobility associated with exchangeable cations adsorbed on the clay sheet surfaces or in the diffuse double layer. Consequently, when the pore water salt concentration increases, there is a reduction of swelling capacity, thus increasing large flow channel (inter-aggregate) size, causing permeability increase. On the contrary, any decrease in pore water salt concentration results in a thicker diffuse double layer, causing a decrease in permeability because of the decrease of the size of large flow channels. The explanations above lead to the same conclusion in terms of microstructure changes: the size of large pores increases by clay aggregation due to the pore water salt concentration increase, and thus the soil permeability is increased.

Besides, the thorough percolation with (Na,Ca)NO_3 solution may also cause the Na-Ca and Na-Mg ion exchange in smectite. In this case, calcium and magnesium ions inside the interlayer space of montmorillonite sheets are replaced by sodium ions in the pore solution, leading to higher shrinkage and creation of macro-pores.

4. Effect of (Na,Ca)NO_3 and Na^+ occupancy on the compressibility of BC

a. Introduction

In this section of study, the effect of saline solutions on intact Boom Clay samples is investigated to better understand their influence on compressibility, swelling behavior under oedometer conditions, and preconsolidation pressure. Eight high-pressure oedometer tests were conducted (Table 24). After applying the in situ effective stress of 2.25 MPa, the samples were percolated with different solutions: three tests were performed using a solution with 60% sodium occupancy and a solute concentration of 1.0 M, another three tests with a solution containing 90% sodium occupancy and a solute concentration of 2.0 M, while the remaining two tests were percolated with Boom Clay synthetic water (0.015 M $NaHCO_3$).

Table 24 Specifications of the high-pressure oedometer tests.

Test	Saline solution	Void ratio (-)	H_0 (mm)	Loading/unloading stages (after saturation)
1	Na = 60% - IS = 1.0M	0.574	10.8	Unloading I (2.25 → 0.25 MPa) Loading I (0.25 → 16 MPa) Unloading II (16 → 0.25 MPa) Loading II (0.25 → 32 MPa) Unloading III (32 → 0.25 MPa)
2	Na = 60% - IS = 1.0M	0.566	10.09	Unloading I (2.25 → 0.25 MPa) Loading I (0.25 → 16 MPa) Unloading II (16 → 0.25 MPa) Loading II (0.25 → 32 MPa) Unloading III (32 → 0.25 MPa)
3	Na = 60% - IS = 1.0M	0.583	9.82	Unloading I (2.25 → 0.25 MPa) Loading I (0.25 → 16 MPa) Unloading II (16 → 0.25 MPa) Loading II (0.25 → 32 MPa) Unloading III (32 → 0.25 MPa)
4	Na = 90% - IS = 2.0M	0.567	10.78	Unloading I (2.25 → 0.25 MPa) Loading I (0.25 → 16 MPa) Unloading II (16 → 0.25 MPa) Loading II (0.25 → 32 MPa) Unloading III (32 → 0.25 MPa)
5	Na = 90% - IS = 2.0M	0.587	10.0	Unloading I (2.25 → 0.25 MPa) Loading I (0.25 → 16 MPa) Unloading II (16 → 0.25 MPa) Loading II (0.25 → 32 MPa) Unloading III (32 → 0.25 MPa)
6	Na = 90% - IS = 2.0M	0.586	10.28	Unloading I (2.25 → 0.25 MPa) Loading I (0.25 → 16 MPa) Unloading II (16 → 0.25 MPa) Loading II (0.25 → 32 MPa) Unloading III (32 → 0.25 MPa)
7	IS = 0.015 M	0.576	9.78	Unloading I (2.25 → 0.25 MPa) Loading I (0.25 → 16 MPa) Unloading II (16 → 0.25 MPa) Loading II (0.25 → 32 MPa) Unloading III (32 → 0.25 MPa)
8	IS = 0.015 M	0.55	9.61	Unloading I (2.25 → 0.25 MPa) Loading I (0.25 → 16 MPa) Unloading II (16 → 0.25 MPa) Loading II (0.25 → 32 MPa) Unloading III (32 → 0.25 MPa)

Once saturation was achieved, the samples underwent a controlled loading and unloading sequence. They were first unloaded to 0.25 MPa, then loaded to 16 MPa, followed by unloading back to 0.25 MPa. The second loading phase increased the stress to 32 MPa, after which the samples were finally unloaded to 0.25 MPa. This procedure consisted of three loading stages and two unloading stages.

All samples were taken from a single core, labeled R78-79W_Core 28.1 (Table 25), which was extracted approximately 28.1 m horizontally from the Connecting Gallery at the HADES underground laboratory level, representing intact Boom Clay. The fundamental properties of the samples, including water content and saturation, were determined and are summarized in Table 25. The initial water content ranged between 20.34% and 21.68%, while the degree of saturation varied between 95% and 100%. All tests were performed at a controlled temperature of 20 °C following the guidelines established by the French standard (AFNOR, 1997). More details can be found in the procedures section.

Table 25 Geometry, initial water content and initial void ratio for the tested specimens.

Test	*Sample localization*	D_0 (mm)	H_0 (mm)	ρ (g/cm^3)	W_0 (%)	e_0 (-)	S_r (-)
1	R78-79W_Core 28.1 Block2-SliceI	49.67	10.8	2.03	20.64	0.574	0.95
2	R78-79W_Core 28.1 Block6-SliceIII	49.84	10.09	2.05	21.5	0.566	1.00
3	R78-79W_Core 28.1 Block9-SliceIII	49.82	9.82	2.03	21.68	0.583	0.98
4	R78-79W_Core 28.1 Block2-SliceII	49.82	10.78	2.03	20.34	0.567	0.95
5	R78-79W_Core 28.1 Block5-SliceII	49.85	10.0	2.03	21.58	0.587	0.97
6	R78-79W_Core 28.1 Block7-SliceI	49.84	10.28	2.02	21.21	0.586	0.95
7	R78-79W_Core 28.1 Block9-SliceII	49.89	9.78	2.04	21.61	0.576	0.99
8	R78-79W_Core 28.1 Block13-SliceII	49.87	9.61	2.06	21.05	0.55	1.0

b. Experimental results

Figure 57, Figure 58, and Figure 59 present typical compression curves obtained from tests percolated with solutions containing Na = 60% and 1.0 M, Na = 90% and 2.0 M, and Boom Clay synthetic water, respectively.

The initial step in the tests involved gradually applying the in situ vertical effective stress ($\sigma'_{v0} = 2.25\ MPa$) without exposing the soil sample to water, as shown by the grey dashed line. This loading resulted in only slight compression for all specimens, with a noticeable change in slope at $\sigma'_v = 1.6\ MPa$. At the end of this initial loading phase, the degree of saturation (S_r), estimated for each step based on measured volume changes assuming a constant water content ($w = w_0$), reached 100% for all tests. Le et al. (2011) also observed that Boom Clay samples from the Mol site at a depth of 223 m (BM223) achieved full saturation under a vertical stress σ'_v of 1.6 MPa, indicated by the measured suction dropping to zero.

The results during saturation of the samples with Boom Clay synthetic water and the injection of 1.0 M and 2.0 M solutions are shown in Figure 60. For the test saturated with Boom Clay synthetic water (Test 8), a slight increase in the void ratio was observed, indicating a small amount of swelling upon contact with water. The void ratio increased from 0.519 to 0.527, suggesting that the applied effective stress of 2.25 MPa corresponds closely to the in situ effective stress at the HADES level. Furthermore, the concentration of Boom Clay synthetic water appears to closely match in situ conditions.

For tests 1 and 5, which were saturated with 1.0 M and 2.0 M solutions, respectively, no swelling was observed, and the void ratio remained almost constant. This suggests that the high concentration of the saline solutions effectively saturated the samples without inducing swelling, highlighting the influence of the solute concentration on the swelling of the BC material under in situ conditions.

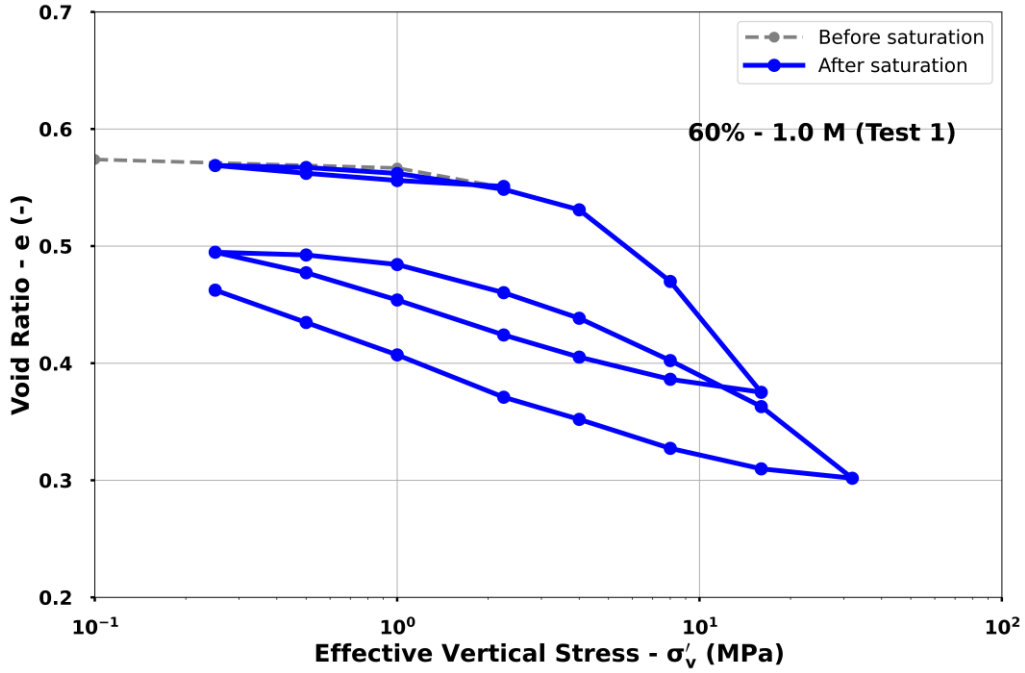
Before saturation
After saturation
60% - 1.0 M (Test 1)
Void Ratio - e (-)
0.7
0.6
0.5
0.4
0.3
0.2
10^{-1}
10^{0}
10^{1}
10^{2}
Effective Vertical Stress - σ'_v (MPa)

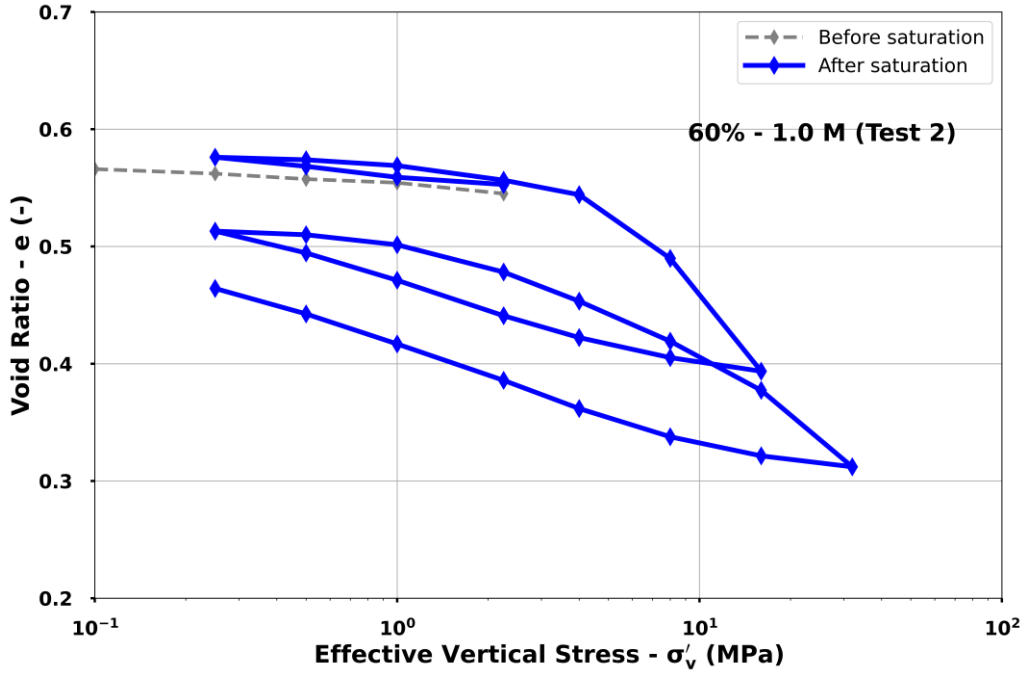
Before saturation
After saturation
60% - 1.0 M (Test 2)
Void Ratio - e (-)
0.7
0.6
0.5
0.4
0.3
0.2
10^{-1}
10^{0}
10^{1}
10^{2}
Effective Vertical Stress - σ'_v (MPa)

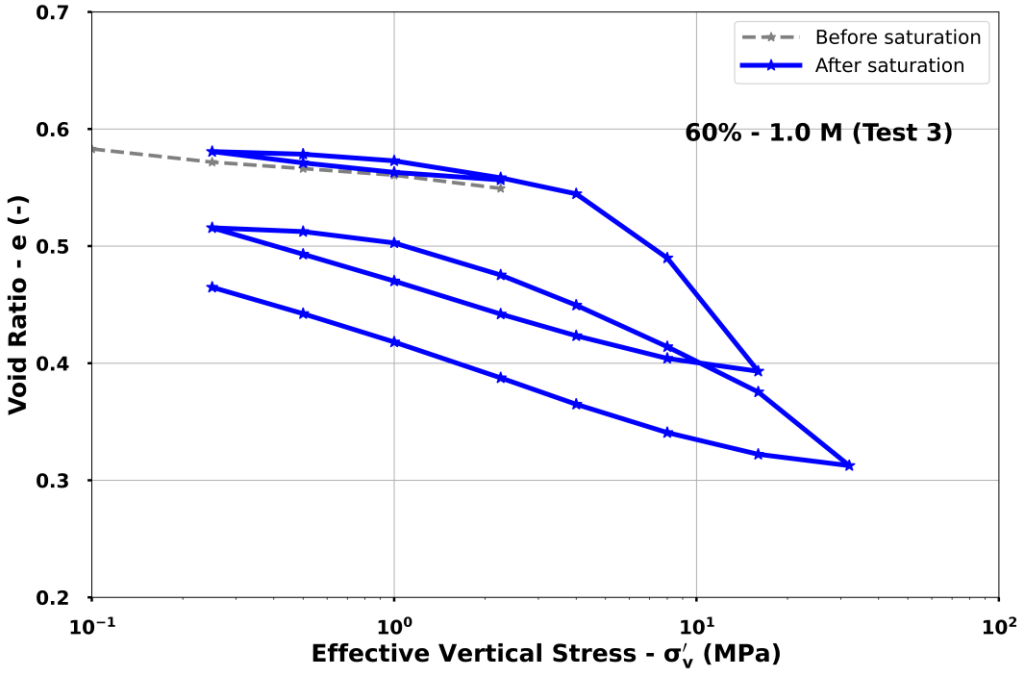

Figure 57 Compressibility curves for samples saturated with Na=60% - IS=1.0M.

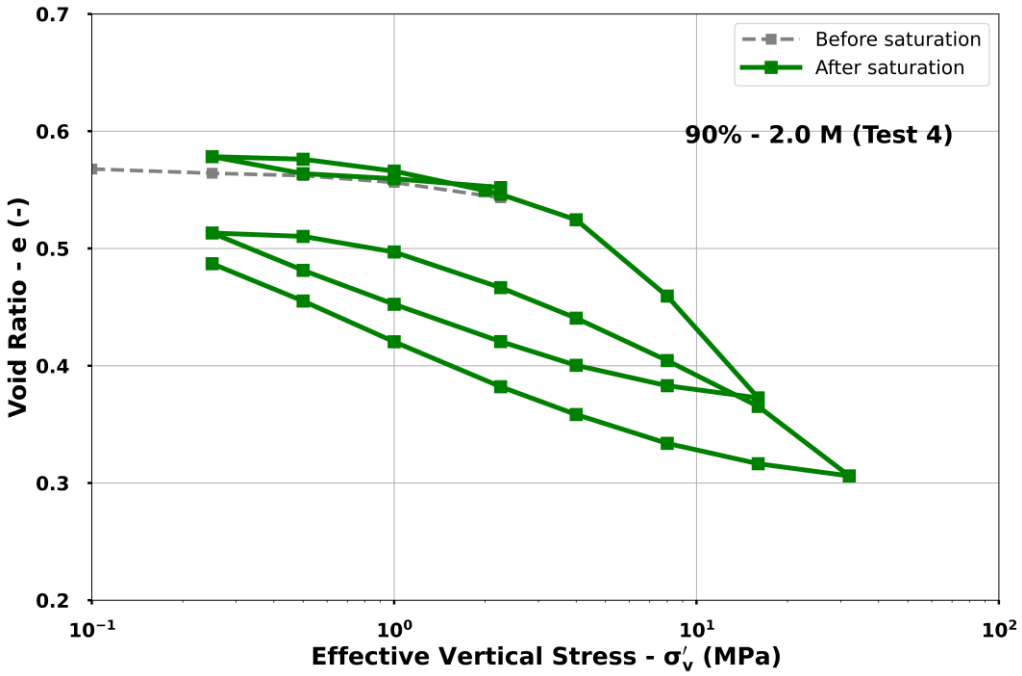

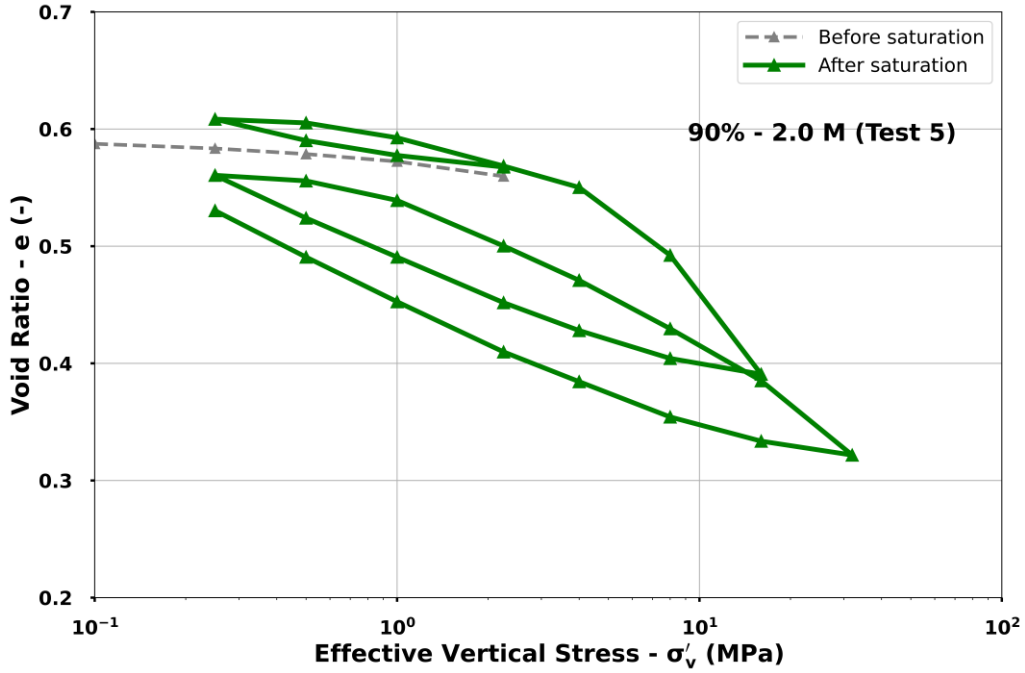

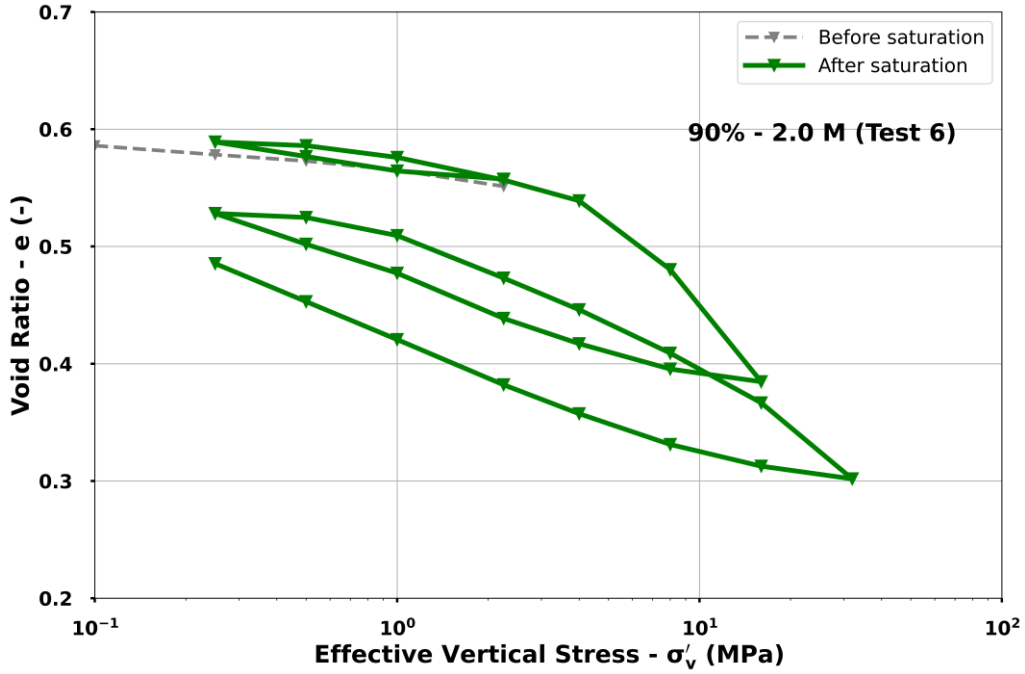

Figure 58 Compressibility curves for samples saturated with Na=90% - IS=2.0M.

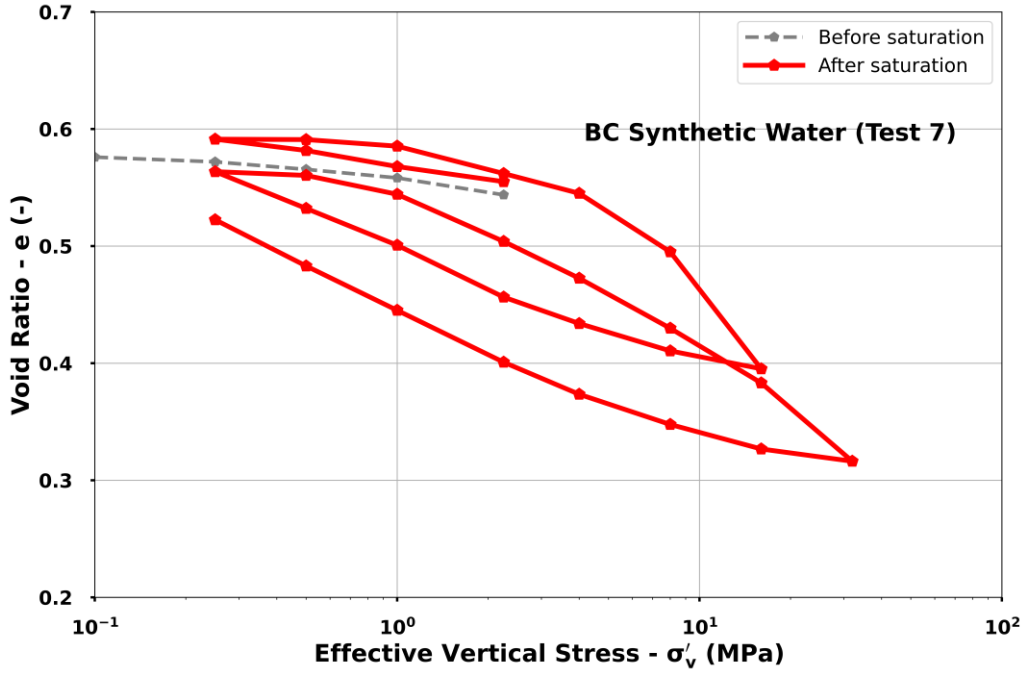

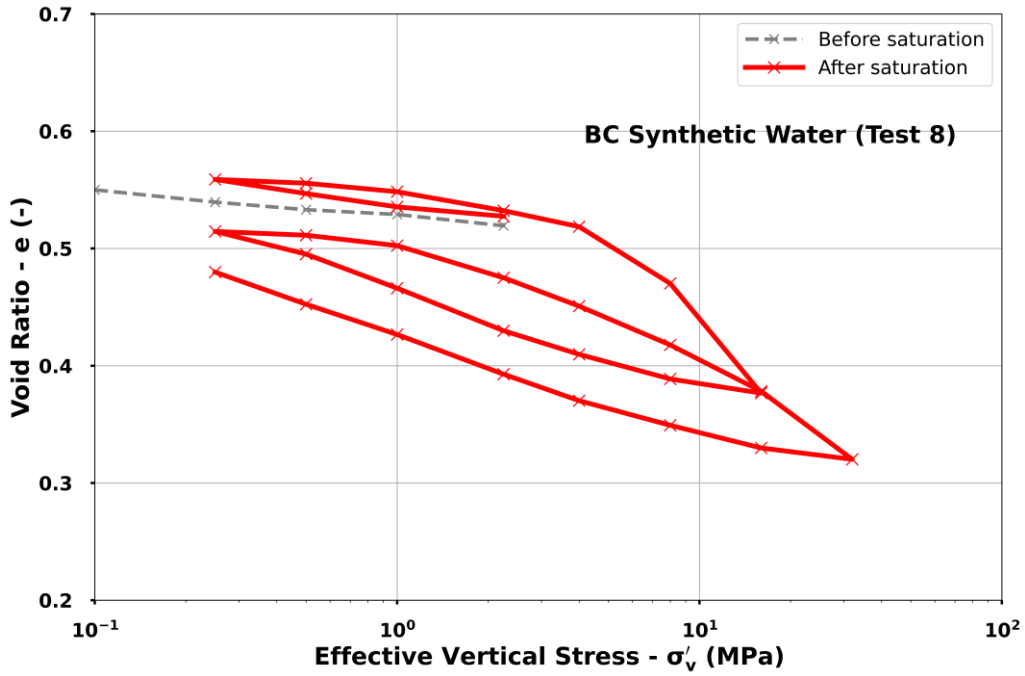

Figure 59 Compressibility curves for samples saturated with the BC synthetic water.

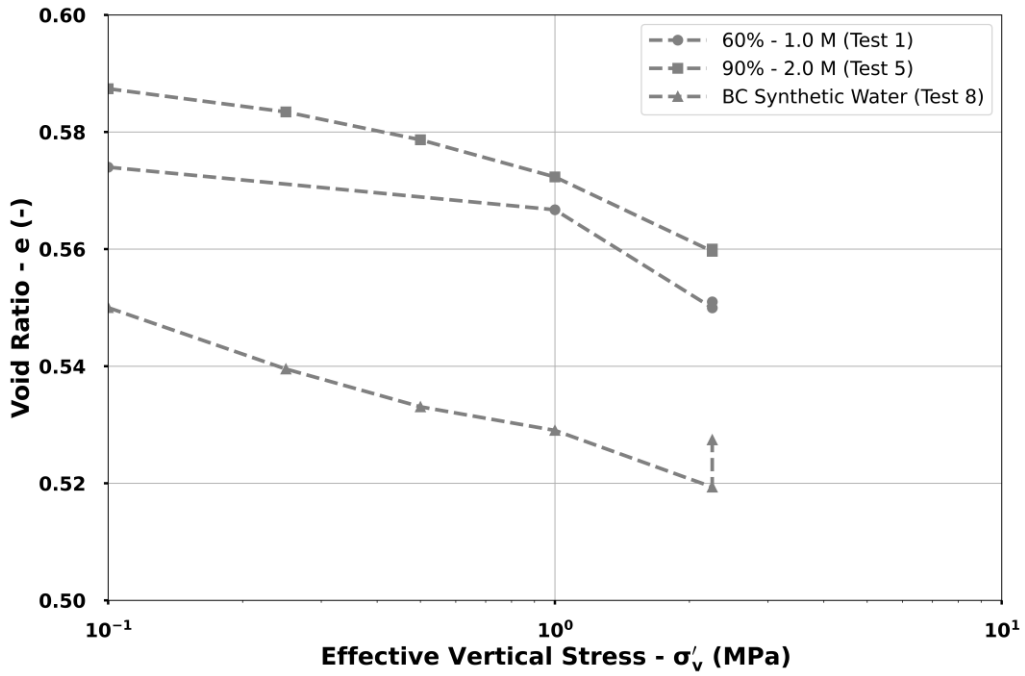

Figure 60 Saturation phase under in situ condition with different solute concentration.

After the saturation stage, the sample was gradually unloaded to 0.25 MPa, and then the loading/unloading cycles began. The compressibility curves, which describe the variation of void ratio as a function of the logarithm of vertical effective stress, exhibit a trilinear trend during the loading stages (Loading I and II) in high-pressure oedometer tests. This behavior is characterized by gradual yielding. During the first loading phase after saturation (Loading I), the void ratio remains nearly unchanged between the application of 0.25 MPa and 2.25 MPa. However, when the vertical effective stress reaches 4 MPa, a change in slope occurs, indicating the onset of structural rearrangement. As the stress further increases to 16 MPa, the slope becomes significantly steeper, as the preconsolidation pressure of Boom Clay ($P_c' = 6\,MPa$) is exceeded. The gradual yielding observed throughout the loading process reflects the progressive breakdown of the soil structure, a phenomenon that continues during the subsequent loading cycles. Upon unloading (Unloading II and III), the BC samples exhibited significant swelling. However, the final void ratio attained after full unloading to 0.25 MPa did not return to its initial value, indicating irreversible changes. This suggests that the microstructure of the clay underwent rearrangement or partial destruction due to the applied loading path, further altering its swelling behavior.

Another important aspect to consider is the response of Boom Clay during both loading and unloading, particularly after exposure to high stresses (16 or 32 MPa). The vertical

threshold stress for each loading and unloading path, which distinguishes zones with different compression slopes, is illustrated in Figure 61 for Test 7. The observed trilinear compression curve (Loading I) can be divided into a bilinear response within the overconsolidated range. The first yield point corresponds to the threshold stress (σ'_{s1}), marking the transition from an initial low-slope region to a steeper slope within the overconsolidated state. This is followed by a second yield point, which separates the overconsolidated zone from the normally consolidated zone. Beyond this point, the slope becomes steeper, indicating the transition into the normally consolidated state. A similar behavior is observed during unloading (Unloading II and III). Initially, in the mechanical rebound phase, the void ratio exhibits only a small variation, reflecting elastic deformation. However, once the applied mechanical stress becomes lower than the threshold stress, the slope increases significantly, indicating higher swelling of BC. Figure 62 shows the variation of threshold stresses with respect to the void ratio corresponding to each stress level for different salt concentrations. It can be observed that, regardless of loading or unloading, the threshold stress, known as the swelling pressure, decreases with increasing salt concentration. Additionally, for the unloading path, applying higher stress results in a lower void ratio, and the threshold stress increases. For a void ratio of 0.55, the swelling pressure was found to range from 0.8 to 1 MPa with synthetic solution. These results are consistent with those previously presented for the swelling pressure of BC with synthetic water, where a value of 0.75 MPa was determined using the constant volume method.

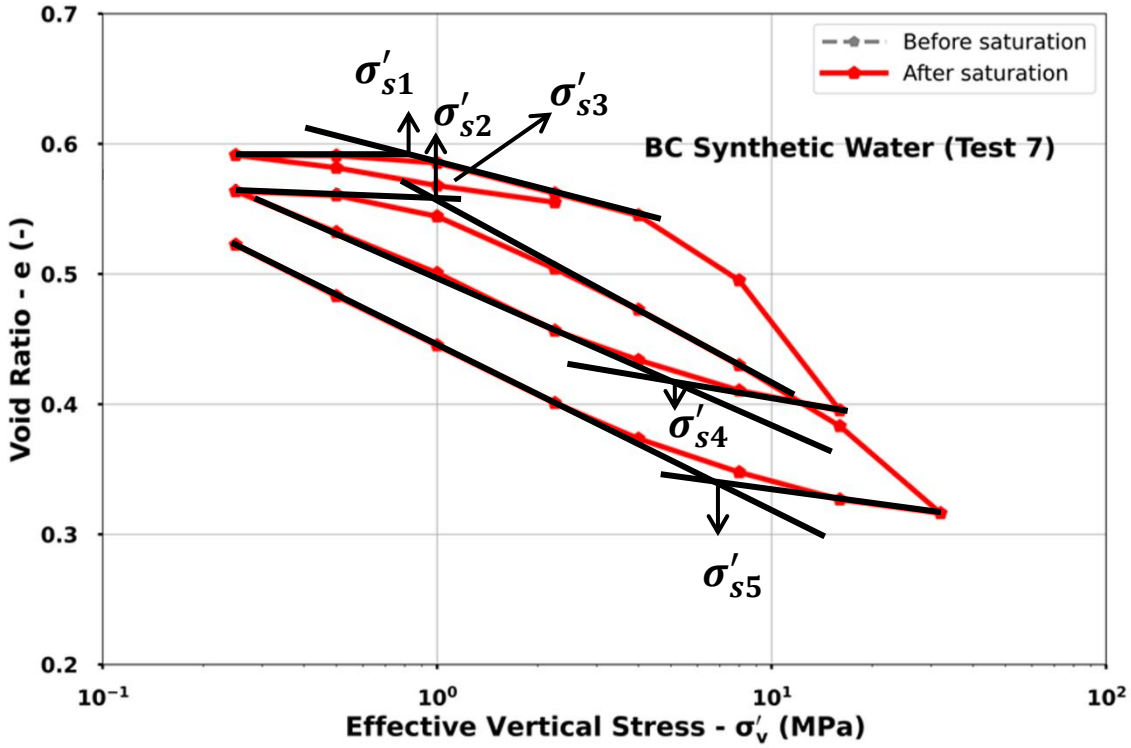

Figure 61 Determination of threshold stress from Test 7 oedometer test with loading/unloading loops.

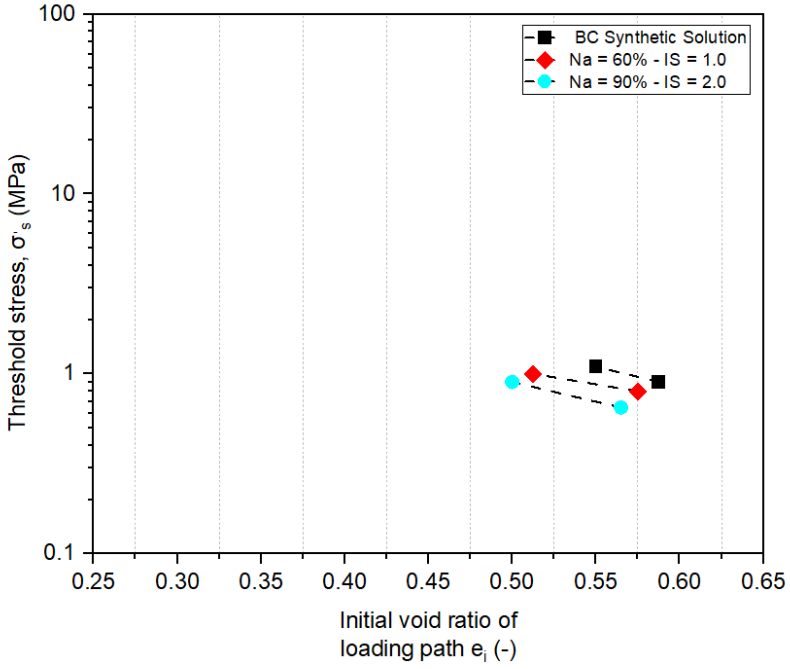

(a)

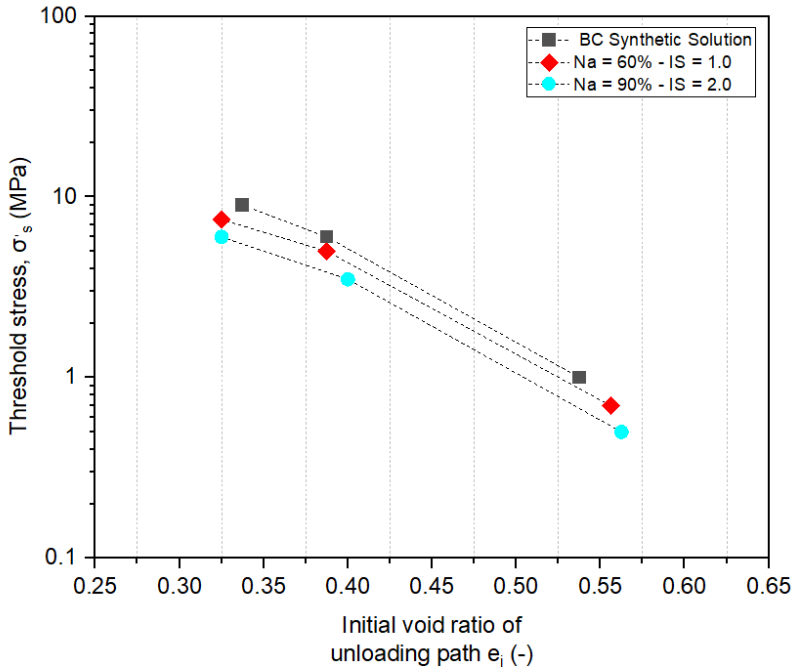

(b)

Figure 62 Threshold stress for loading (a) and unloading (b) paths with different saline solutions.

For a more comprehensive analysis of the effect of solute concentration on the mechanical behavior of BC, the compression curves obtained after the saturation phase were utilized. These curves provide valuable insights into the compressibility parameters, including the *compression index (Cc), the swelling index (C*s), and the preconsolidation pressure (P_c'), under different saline conditions. The compression index (*Cc) and the swelling index (C*s) are derived from the slopes of the loading and unloading stages, respectively, reflecting the soil's response to applied stress and its ability to swell or compress. Additionally, the Casagrande method was applied to determine the preconsolidation pressure, a critical parameter that identifies the point at which the soil shifts from elastic to plastic deformation. Note that the determination of such parameters is essential and will be helpful for the development of the constitutive law, which accounts for the effect of saline solutions on the hydro-mechanical behavior of intact Boom Clay.

Figure 63 and Figure 64 illustrate the compression slope (C′c) and swelling slope (C′s) for each loading (I and II) and unloading (II and III) step, plotted against the mean vertical stress (σ_v'). A clear influence of pore water salt concentration on the compression and swelling behavior is observed. The sample saturated with BC

synthetic water exhibited the highest values for both C′c and C′s, indicating greater compressibility and swelling. These values decreased progressively for samples percolated with $Na = 60\% - IS = 1.0\ M$ solution and $Na = 90\% - IS = 2.0\ M$ solution, respectively.

It is also evident that as the vertical stress (σ_v') increases, the differences in compression and swelling behavior between the different samples diminish. This suggests that the influence of pore water salt concentration becomes less pronounced at higher stress levels. Additionally, the differences in C′c and C′s between the samples with (Na, Ca)NO_3 solutions at concentrations of 1.0 M and 2.0 M were minimal when compared to the differences observed between samples with BC synthetic water (0.015 M). These findings are consistent with the results reported by Nguyen et al. (2013), who investigated the effect of saline solutions (NaCl) on Boom Clay and Ypersian clay.

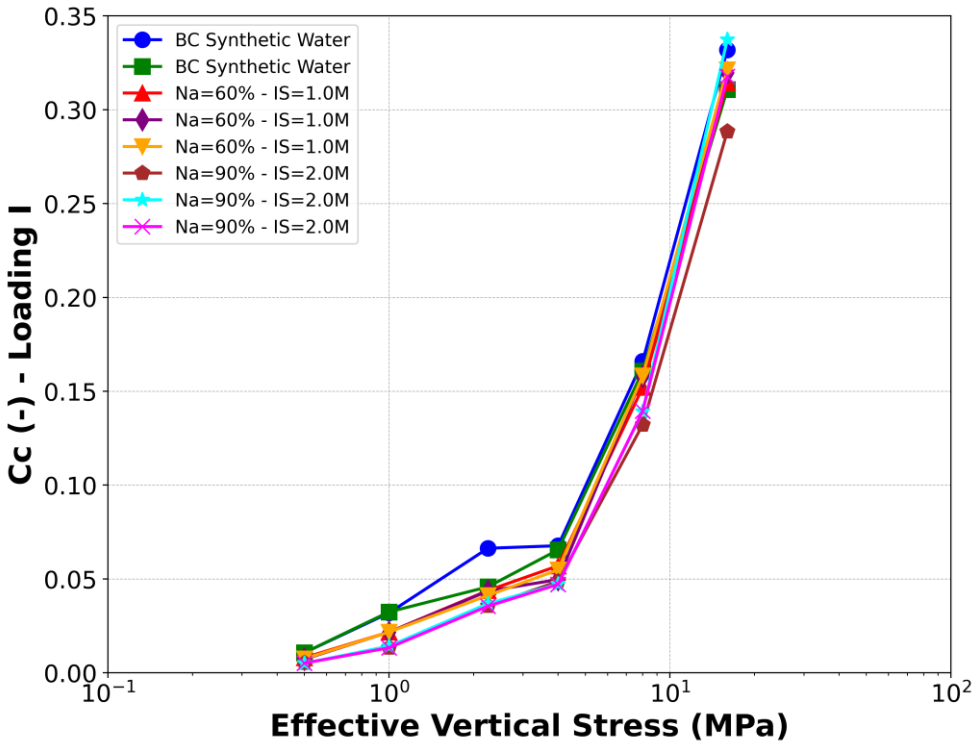

(a)

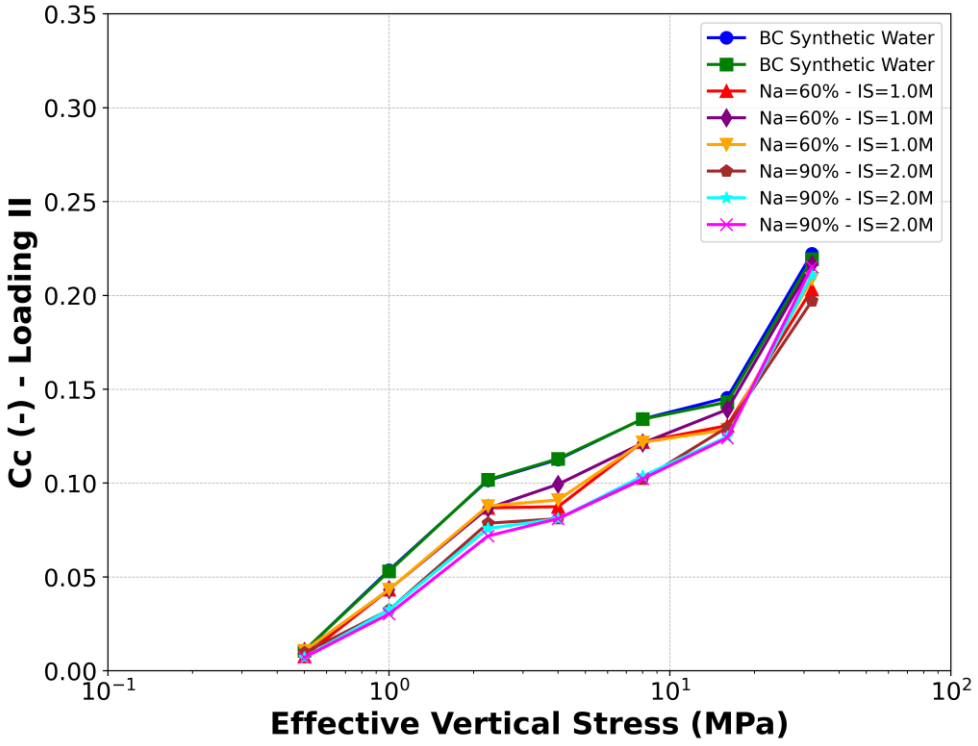

(b)

Figure 63 Variations of compression slopes with vertical stress for Loading I (a) and Loading II (b).

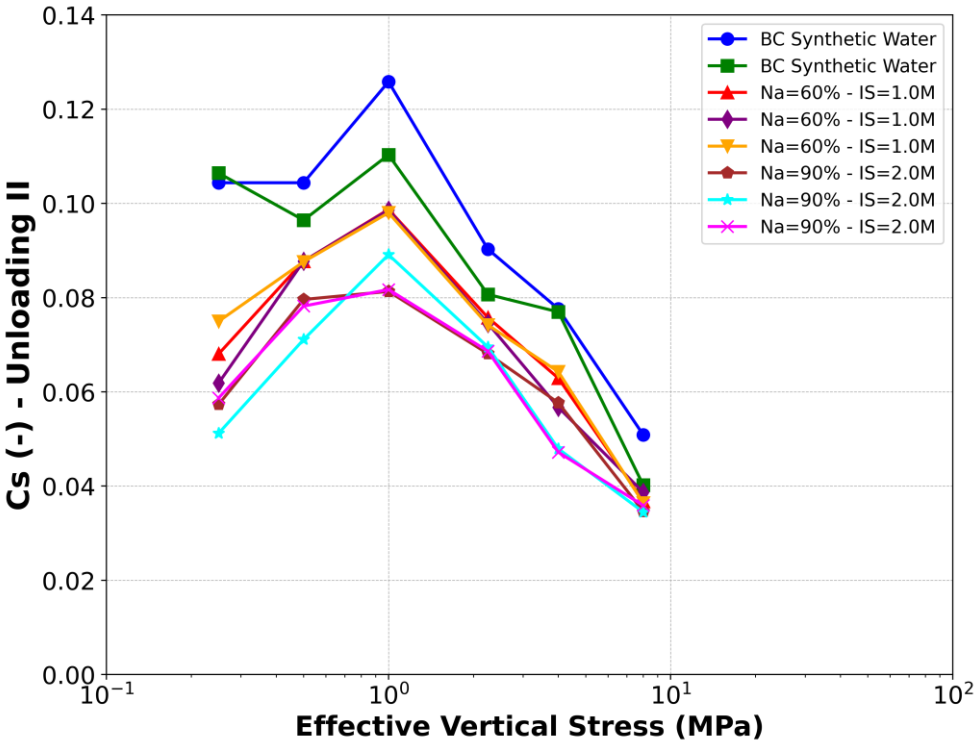

(a)

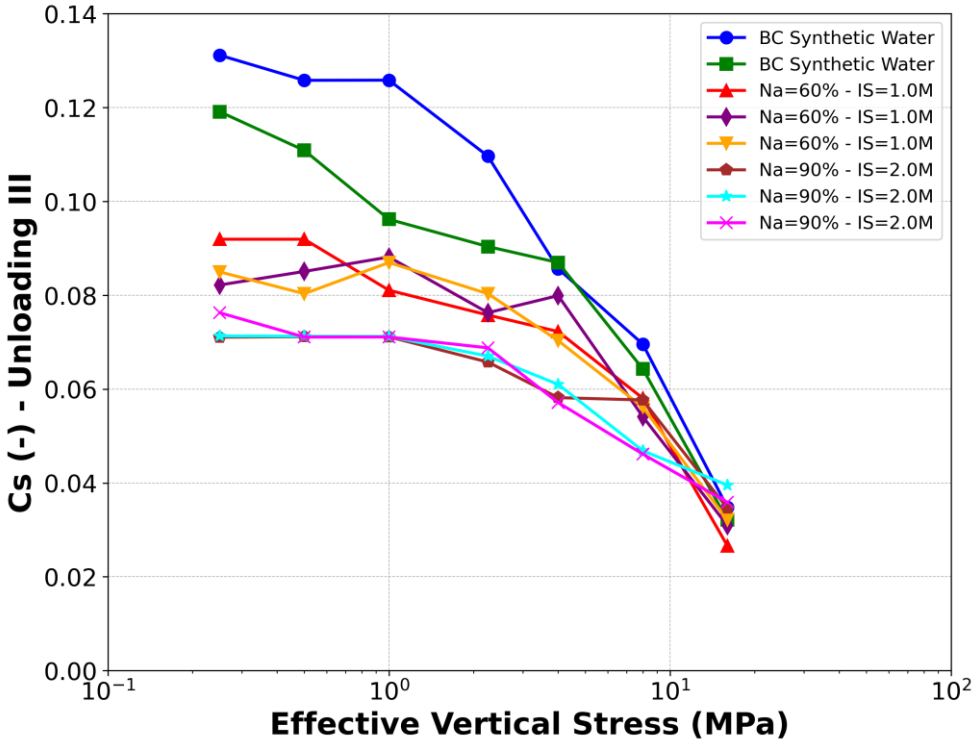

(b)

Figure 64 Variations of unloading slopes with vertical stress for (a) Unloading II and (b) Unloading III.

To further investigate the effect of saline solutions on the mechanical behavior of BC, the preconsolidation pressure was determined from the oedometer tests conducted in this study at different salt concentrations using the Casagrande method. This method involves plotting the compression curve obtained during the test and identifying the point where the curve deviates from the normally consolidated straight-line segment. The preconsolidation pressure is then determined by drawing a tangent to the steepest part of the curve in the overconsolidated range and extending a horizontal line to intersect the compression curve. The point of intersection represents the preconsolidation pressure, which indicates the maximum vertical stress the soil has previously experienced without undergoing significant yielding. This approach provides valuable insight into the soil's consolidation history and its behavior under varying saline conditions.

Figure 65 illustrates the determination method of the preconsolidation pressure of BC from test 7, which was saturated with the BC synthetic solution. The preconsolidation pressure was found to be approximately 6 MPa for samples percolated with BC synthetic water. This result is consistent with the literature, where similar

preconsolidation pressures for BC with synthetic solutions were reported (Horseman et al., 1987; Baldi et al., 1991; Awarkeh, 2023).

Additionally, the preconsolidation pressure increases with rising salt concentrations. Specifically, the preconsolidation pressure was found to increase from 6 MPa to 6.5 MPa for samples percolated with a 1.0 M solution, and to nearly 6.9 MPa for samples percolated with a 2.0 M solution. These results confirm the effect of the salt solution on the preconsolidation pressure, which is attributed to the increased stiffness and densification of the material caused by the shrinkage of the diffuse double layer.

Table 26 summarizes the variation of the main parameters, highlighting the effect of different salt concentrations (0.015 M, 1.0 M, and 2.0 M). As the salt concentration increases, noticeable changes in the compressibility and swelling behavior of Boom Clay (BC) are observed. Specifically, the preconsolidation pressure increases with higher salt concentrations, indicating an increase in stiffness. Additionally, the compression index (Cc) and swelling index (Cs) show a slight decrease as the salt concentration rises. These results align with previous studies by Deng et al. (2011) and Mokni et al. (2014). The data provide a clear comparison of how the mechanical properties of BC evolve under varying saline conditions, demonstrating the effect of saline solutions on soil compressibility and swelling behavior.

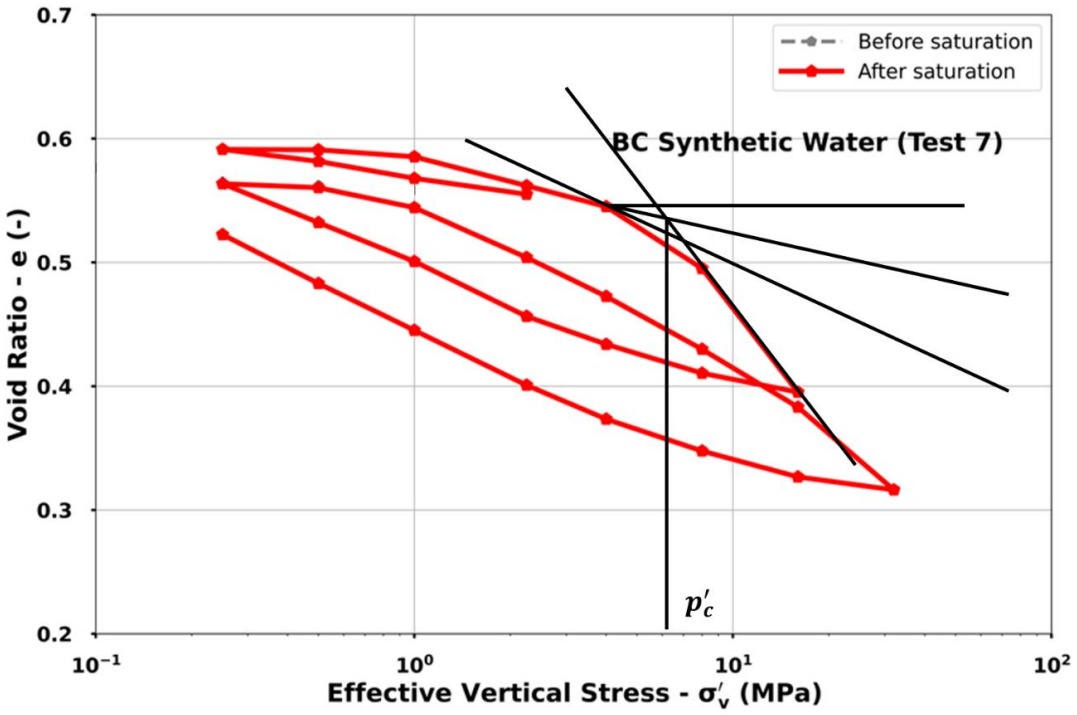

Figure 65 Determination of the preconsolidation pressure by Casagrande method.

Table 26 Table summarizing the main parameters from oedometer tests with respect to saline solutions.

Parameter	BC Synthetic water (0.015 M)	Na= 60% - IS= 1.0M	Na= 90% - IS= 2.0M
p_c' (MPa)	6	6.5	6.9
C_c (-)	0.3	0.28	0.25
C_s (-)	0.09	0.08	0.07

c. Discussion

In general, the hydro-mechanical behavior of clays is influenced by both physico-chemical and mechanical effects (Le et al., 2011; Cui et al., 2013). The term "mechanical" refers to particle interactions through direct contact, while "physico-chemical" denotes interactions through the diffuse double layer (Robinson and Allam, 1998). For each loading or unloading path, there is a threshold stress (σ_s') that divides the compression curve into two zones, each governed by one of these effects (Figure 63): (i) upon unloading, when the external stress exceeds the repulsive force associated with soil particles–water interaction (physico-chemical effect), or σ_{s3}', σ_{s4}', and σ_{s5}' for Unloading I, II, and III, only low swelling volume changes occur; otherwise, higher swelling volume changes are expected; and (ii) upon reloading, when the external stress is lower than the matric suction related to the physico-chemical effect (σ_{s1}' and σ_{s2}' for Loading I and II), this external stress balances with the repulsive force, leading to small volume decreases. In contrast, when the external stress becomes higher, the mechanical effect dominates, resulting in larger volume decreases (Cui et al., 2013; Nguyen, 2013). For the BC, the threshold stress values (σ_s') for a void ratio corresponding to in situ conditions (e = 0.55-0.6) was found equal to 1 MPa. These results align with those found by Nguyen et al. (2013).

In addition, this study observed that as the pore water salt concentration increased, the preconsolidation pressure also increased, while the values of the compression (C_c) and swelling slopes (C_s) decreased. This chemical effect was found to diminish as the vertical stress (σ_v') increasing, which is consistent with the previous studies on both natural clays (Deng et al., 2011; Nguyen, 2013) and reconstituted swelling clays (Di Maio and Fenelli, 1997; Maio, 1998; Di Maio et al., 2004; Thyagaraj and Rao, 2013).

The observed changes in compressibility and swelling behavior can be attributed to the shrinkage of the diffuse double layer as salt concentration increases. When the

concentration of salt in the pore water rises, osmotic consolidation occurs, leading to the contraction of clay particles. This shrinkage results in increased interparticle attraction, causing the formation of particle aggregates and overall densification of the soil structure. Consequently, the stiffness of the material increases, which explains the observed rise in preconsolidation pressure in Boom Clay.

5. Effect of (Na,Ca)NO_3 and Na^+ occupancy on the shear behavior of BC

a. Introduction

This section presents the effects of high-salinity (Na,Ca)NO_3 solutions and high sodium occupancy on the mechanical behavior of BC, with a particular focus on its shear response. A series of isotropically undrained triaxial tests were conducted on intact BC samples prepared from three distinct cores: R78-79W_Core 28.1, R78-79W_Core 2.2, and CG76-77W Core 13.2 (Table 27). The basic properties of the intact BC were determined in the laboratory and are presented in Table 27. The initial water content was found to be in the range of 21% to 23.5%, while the degree of saturation varied between 99% and 100%.

Three different solutions were analyzed:

- A synthetic BC solution (15 mmol/L $NaHCO_3$, IS = 0.015 M; De Craen et al., 2004),
- Two saline solutions with sodium occupancies of 60% at 1.0 M and 90% at 2.0 M (Na,Ca)NO_3.

It is important to note that these high concentrations and sodium occupancies are not fully representative of repository conditions but were chosen to detect substantial differences in the studied responses. Additionally, this study focuses solely on the salinity effect, without considering the alkalinity or pH variations. In actual geological disposal scenarios, the concentration of the (Na,Ca) nitrate plume—comprising Na, K, Mg, and Ca hydroxides, nitrates, and sulfates—expected from Eurobitum disposal is significantly lower than 1 M. High sodium

occupancies are predicted to occur only within a thin layer of the adjacent clay (Weetjens et al., 2010; Al Mais et al., 2024, 2025b).

Table 27 Dimensions, initial water content and initial void ratio of the specimens tested.

Test	Sample localization	D_0 (mm)	H_0 (mm)	ρ (g/cm^3)	W_0 (%)	e_0 (-)	S_r (-)
1	R78-79W_Core 28.1 Block4	38.3	77	2.08	21	0.539	1
2	R78-79W_Core 28.1 Block11	37	77	2.07	21.6	0.556	1
3	R78-79W_Core 28.1 Block12	38.2	77	2.05	21.3	0.569	0.99
4	R78-79W_Core 2.2 Block4	37.2	75	2.02	23.2	0.618	0.99
5	R78-79W_Core 2.2 Block7	35.5	74.6	2.13	23.5	0.536	1
6	R78-79W_Core 28.1 Block14	37.6	76.1	2.11	23.3	0.548	1
7	R78-79W_Core 13.2 Block13	37.9	76.1	2.03	23.2	0.608	1
8	R78-79W_Core 13.2 Block4	38.2	75.8	2.02	23.1	0.609	1
9	R78-79W_Core 13.2 Block3	37	76.5	2.05	23.3	0.589	1

In total, nine undrained triaxial tests were conducted, with all details summarized in Table 28. These tests investigated the effects of effective confining pressure, solute concentration of (Na, Ca)NO_3. Table 28 provides the values for the applied back pressure (BP), effective confining pressure (σ_3'), and the ionic strength (IS) of the percolated solution. The tests were conducted under three different effective confining pressures: 1.0, 2.25, and 4.5 MPa. The selection of these stress levels was motivated by the need to cover the two main volumetric strain domains - an effective confining pressure of 1 MPa (OCR = 6) was used to examine the dilatancy behavior of Boom Clay, while 4.5 MPa (OCR = 1.3) enabled the study of its contraction behavior. The intermediate confining pressure of 2.25 MPa represents the in-situ effective stress, with an OCR of 2.6, capturing the transition between contraction and dilation. The study examines the observed trends in stress-strain behavior, stress paths (p'-q), pore

pressure evolution, and overall mechanical response, which are analyzed and discussed in detail.

Table 28 Initial conditions of undrained triaxial tests.

Test No.	BP (MPa)	σ_3' (MPa)	IS (M)
1	1	4.5	2
2	1	2.25	2
3	1	1	2
4	1	4.5	1
5	1	2.25	1
6	1	1	1
7	1	4.5	0.015
8	1	2.25	0.015
9	1	2.25	0.015

b. Experimental results

i. Effect of confining pressure

The test results are discussed with reference to the mean effective stress (p') and the deviator stress (q), defined as:

(12) $$p' = \frac{\sigma_1' + 2\sigma_3'}{3}$$

(13) $$q = \sigma_1' - \sigma_3'$$

where σ_1' and σ_3' represent the vertical and lateral effective stresses, respectively.

Failure (peak) is defined as the point at which the maximum value of q is reached during compression, with the corresponding values of mean effective stress and deviator stress indexed as p_f' and q_f. In contrast, the residual deviator stress corresponds to the final value of (q) after reaching a plateau, specifically in tests conducted at lower effective confining pressures (1 MPa and 2.25 MPa) that exhibit dilative behavior. The corresponding values of (q) and p' at this residual state are denoted as q_r and p_r', respectively.

Figure 66 illustrates the results of the undrained triaxial tests, showing the variations of deviator stress (q) and pore water pressure (Δu) as function of axial strain (ε_a) under

different initial effective confining pressures. Several common features can be observed:

- The stress-strain curves indicate that the BC exhibits a typical elasto-plastic behavior. Initially, the curves display a limited linear elastic region, which continues until yielding occurs, marked by a noticeable deviation from linearity. The yield stress represents the transition between the elastic and plastic regions. After reaching the peak deviator stress (q_f), softening or contraction behavior may occur, depending on the initial conditions of each test, particularly in terms of effective confining pressure. The limited elastic zone falls in $\varepsilon_a < 1\,\%$.
- Regardless of the (Na,Ca)NO_3 concentration, it can be seen that the soil stiffness increases with increasing effective confining stress σ_3'. As illustrated in Figure 66(a), all samples were percolated with (Na,Ca)NO_3 at an ionic strength of 2.0 M. Test 1, conducted at $\sigma_3' = 4.5\,MPa$, is characterised by a peak deviator stress of 2.8 MPa, which is higher than in test 2 (2.25 MPa) and test 3 (1.4 MPa), conducted at $\sigma_3' = 2.25\,MPa$ and $\sigma_3' = 1\,MPa$, respectively. This trend is consistent with the results from other tests conducted with varying (Na,Ca)NO_3 concentrations at the same effective confining pressure, where higher effective confining pressures correlate with higher peak deviator stresses.
- The pore water pressure curves show that higher pore water pressures correspond to increased effective confining stresses. As the effective confining stress increases, the soil void ratio decreases, leading to a more rapid increase in pore pressure and overall higher values. Test 1 gives an evolution of pore pressure of 1.9 MPa at $\sigma_3' = 4.5\,MPa$, with $\Delta u = 0.51\,MPa$ for samples confined at 2.25 MPa, and $\Delta u = 0.25\,MPa$ for samples confined at 1 MPa as it is presented in Figure 66 (b).
- The stress-strain curves of the tests conducted at the highest overconsolidation ratios (OCR = 6 and 2.6 for Tests 2, 3, 5, 6, 7, and 8) show a peak followed by softening behavior. Such strain softening is more pronounced in tests performed at lower effective confining stresses ($\sigma_3' = 1.0\,MPa$). A similar trend is also reflected in the pore water pressure evolution, where a rapid increase is followed by a decrease, particularly for samples with $OCR = 6\ and\ \sigma_3' = 1.0\,MPa$.

Samples with an OCR of 1.3 (Tests 1, 4, and 9) exhibit contraction behavior, meaning that under loading, the clay tends to decrease in volume. This behavior is characterized by a rapid increase in deviator stress and pore water pressure, followed by a plateau, where further staining result in minimal changes in stress.

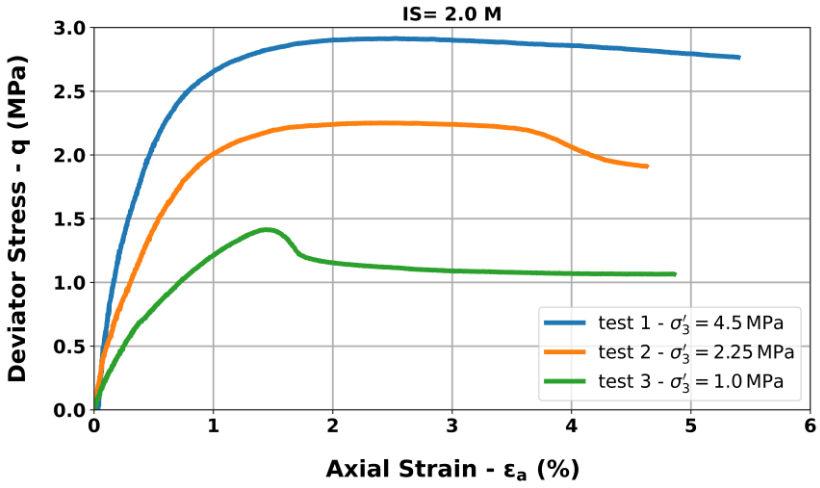

(a)

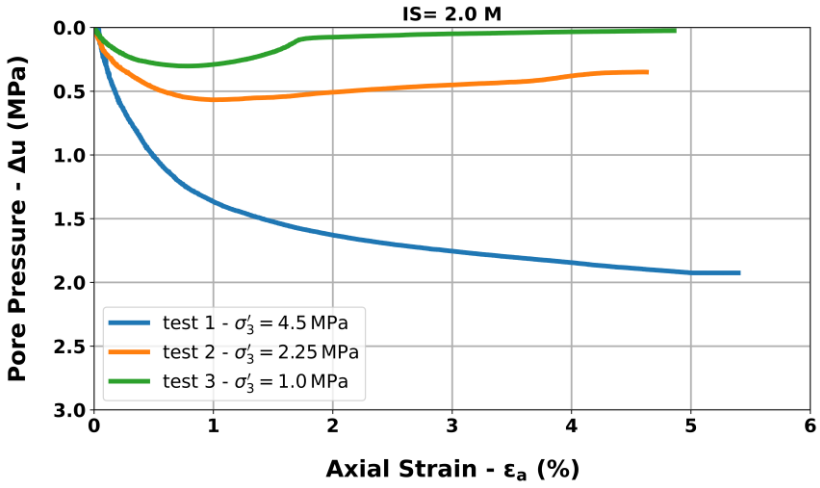

(b)

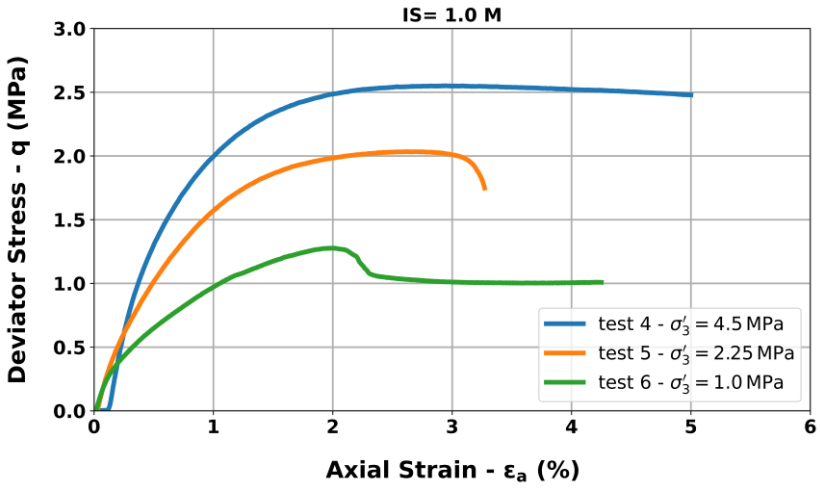
IS= 1.0 M
Deviator Stress - q (MPa)
Axial Strain - εa (%)
test 4 - σ'3 = 4.5 MPa
test 5 - σ'3 = 2.25 MPa
test 6 - σ'3 = 1.0 MPa

(c)

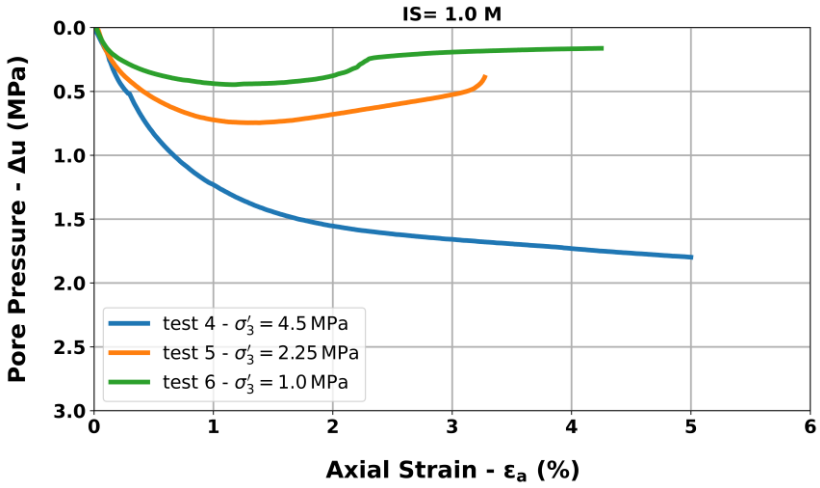
IS= 1.0 M
Pore Pressure - Δu (MPa)
Axial Strain - εa (%)
test 4 - σ'3 = 4.5 MPa
test 5 - σ'3 = 2.25 MPa
test 6 - σ'3 = 1.0 MPa

(d)

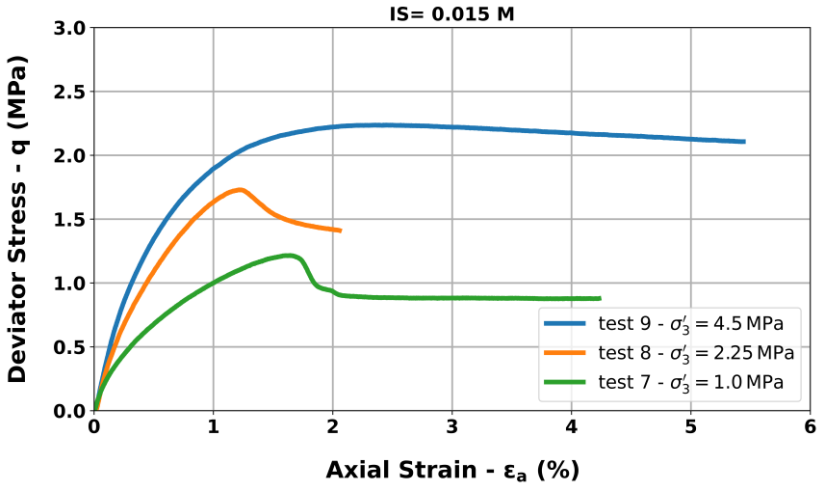
IS= 0.015 M
Deviator Stress - q (MPa)
Axial Strain - εa (%)
test 9 - σ'3 = 4.5 MPa
test 8 - σ'3 = 2.25 MPa
test 7 - σ'3 = 1.0 MPa

(e)

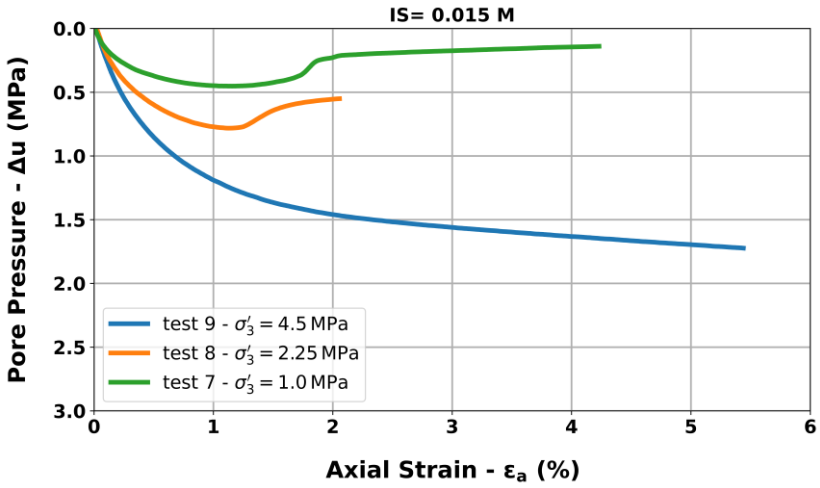

(f)

Figure 66 Stress-Strain and Pore-Pressure curves evolutions under different Ionic Strength (IS): (a, b) IS= 2.0M; (c, d) IS= 1.0M and (e, f) IS= 0.015M.

ii. Effect of solute concentration

Figure 67 shows typical results of consolidated undrained triaxial compression shear tests percolated with three different saline solutions (0.015 M; 1.0 M; 2.0 M) and subjected to three different effective confining pressures (1 MPa, 2.25 MPa and 4.5 MPa). It is worth noting that percolation of the clay with 1.0 M and 2.0 M is theoretically shown to reach 60% and 90% sodium occupancy, respectively (Figure 45 Figure 46).

For the three different effective confining stresses σ_3', the peak deviator stress (q_f) increases with higher ionic strength of (Na,Ca)NO_3 and hence also with higher sodium occupancy. As shown in Figure 67 (a), under $\sigma_3' = 4.5\,MPa$, the stress-strain curve reveals that the sample percolated with 2.0 mol/L (Na,Ca)NO_3 (IS = 2.0 M) exhibits a higher deviator stress of 2.92 MPa, compared to 2.55 MPa and 2.25 MPa for samples percolated with 1.0 mol/L (Na,Ca)NO_3 (IS = 1.0 M) and 0.015 mol/L $NaHCO_3$ (IS = 0.015 M), respectively. Similar trend is observed for samples under 2.25 MPa and 1 MPa, as shown in Figure 67(c) and Figure 67(e), respectively. Table 29 summarizes, for each triaxial compression test, the peak deviator stress (q_f), residual deviator stress (q_r), and maximum pore water pressure (Δu_{max}) in relation to the initial effective confining stress and ionic strength.

Figure 67(a) shows that lightly over-consolidated specimens with an OCR of 1.3 exhibit contraction behavior, characterized by a plateau following the peak deviator stress. This plateau indicates a stabilization in the stress response after reaching the peak.

Such behavior is typical for lightly over-consolidated clays (Baldi et al., 1991; Sultan et al., 2010).

In contrast, for the overconsolidated specimens (OCR = 2.6 and 6) shown in Figure 67(c) and (e), a different pattern emerges. These samples reach a distinct peak deviator stress, followed by a softening phase that represents a loss of strength, often associated with the initiation of failure in a clay structure. This softening response is more pronounced for highly overconsolidated clays, where accumulated stress from previous loading cycles makes them more susceptible to fail once the peak stress threshold is exceeded. The transition from peak to softening marks a shift from stable deformation to a weakening phase, leading to the formation of the shear failure plane.

This distinction in behavior between lightly and highly overconsolidated specimens underscores the impact of OCR on the mechanical response of BC. As it is widely reported in the literature, higher OCR values are associated with a greater tendency for strength loss and structural failure, whereas lower OCR values generally favor stabilization after initial deformation (Holtz et al., 1981; Burland, 1990).

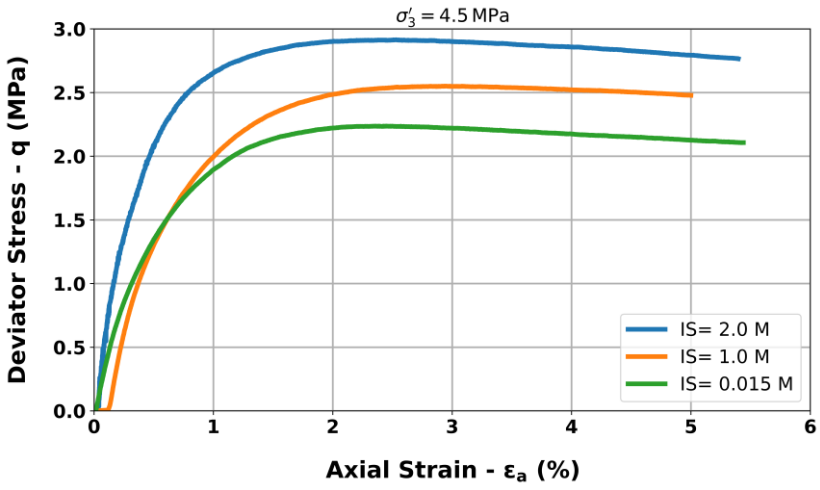

(a)

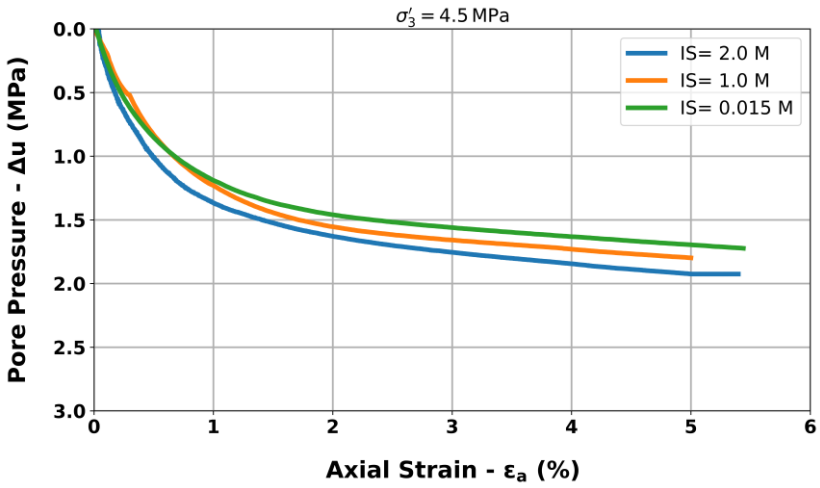
$\sigma'_3 = 4.5$ MPa
IS= 2.0 M
IS= 1.0 M
IS= 0.015 M
Pore Pressure - Δu (MPa)
Axial Strain - ε_a (%)

(b)

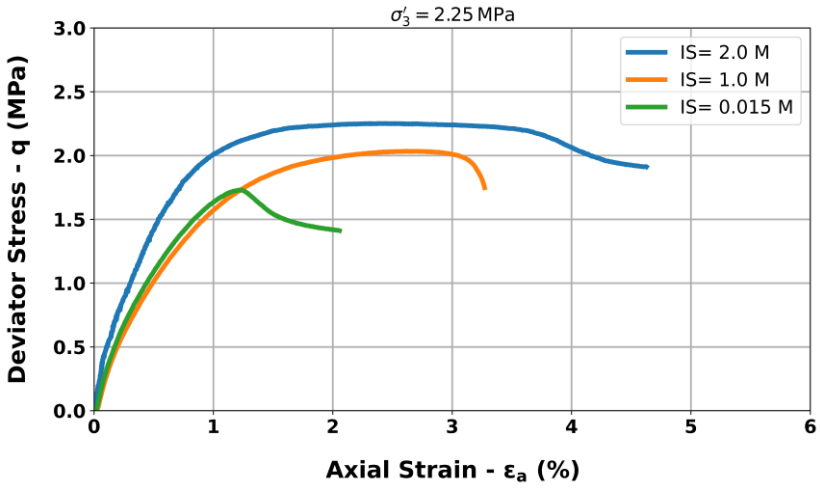
$\sigma'_3 = 2.25$ MPa
IS= 2.0 M
IS= 1.0 M
IS= 0.015 M
Deviator Stress - q (MPa)
Axial Strain - ε_a (%)

(c)

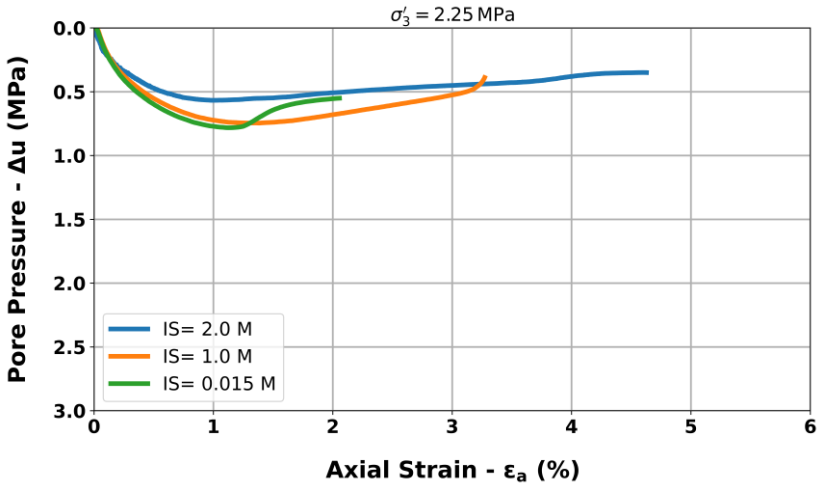
$\sigma'_3 = 2.25$ MPa
IS= 2.0 M
IS= 1.0 M
IS= 0.015 M
Pore Pressure - Δu (MPa)
Axial Strain - ε_a (%)

(d)

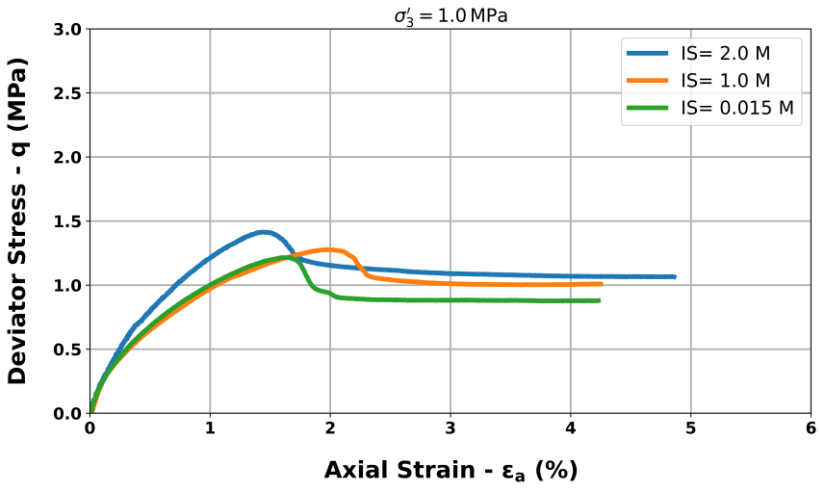

(e)

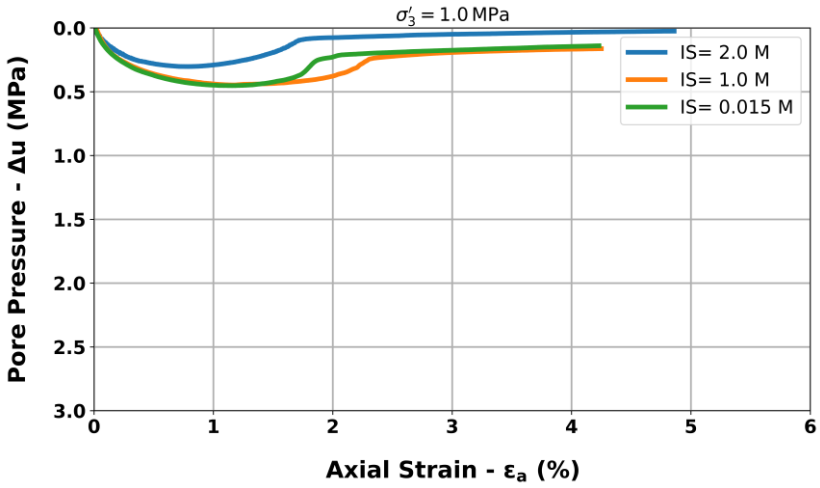

(f)

Figure 67 Stress-strain curve and pore water pressure evolution under different confining pressures: (a, b) σ'3= 4.5 MPa; (c, d) σ'3= 2.25 MPa; (e, f) σ'3= 1.0 MPa.

Table 29 Summary of test data

Test No.	σ'_3 (MPa)	IS (M)	q_f (MPa)	q_r (MPa)	Δu_{max} (MPa)
1	4.5	2	2.92	2.92	1.92
4	4.5	1	2.55	2.55	1.85
9	4.5	0.015	2.25	2.25	1.72
2	2.25	2	2.25	1.92	0.56
5	2.25	1	2	1.75	0.75
8	2.25	0.015	1.7	1.42	0.75
3	1	2	1.41	1.06	0.3
6	1	1	1.27	1	0.45
7	1	0.015	1.2	0.87	0.45

The stress paths in (p', q) space are plotted in Figure 68. They are consistent with the classical undrained stress paths typically observed for overconsolidated and lightly overconsolidated clay (Parry and Wroth, 1981; Horseman et al., 1987; Giger et al., 2018). However, Tests 4 and 9 exhibit an unusual linearity, which may be attributed to either load-control issues, where the applied load was not varied as intended, or from a technical limitation of the pore pressure transducer, which may not have fully responded to the pressure fluctuations during testing.

The anisotropic nature of BC is evident in the non-linearity of the stress paths, particularly in samples percolated with lower ionic strength solutions (0.015 and 1.0 M). This behavior reflects the inherent anisotropy of Boom Clay, as it responds differently under varying stress conditions. In contrast, samples percolated with a higher ionic strength solution (2.0 M) exhibit a more pronounced linear stress path. This linearity is likely due to the increased osmotic suction associated with the higher concentration of the percolating solution, which enhances the clay structural rigidity and reduces deformation variability.

The general leftward slope of the stress paths reflects the net increase in pore pressure, as observed in previous analyses. In the overconsolidated samples (Tests 2, 3, 5, 6, 7, and 8), the stress paths display a subtle rightward curvature both before and after failure. This behavior indicates a tendency of dilatancy under high OCR conditions (OCR = 6 and 2.6). This rightward curvature is characteristic of overconsolidated clays and reflects internal resistance to deformation after peak stress is reached.

In contrast, the samples with a lower overconsolidation ratio (OCR = 1.3) show a leftward curvature in the post-failure region, suggesting a contractive response after the peak stress. This means that once failure occurs, the soil structure collapses, leading to a continued increase in pore pressure and further volume reduction. This divergence in stress path behavior between overconsolidated and lightly overconsolidated specimens highlights the influence of OCR on the failure mechanisms and pore pressure responses.

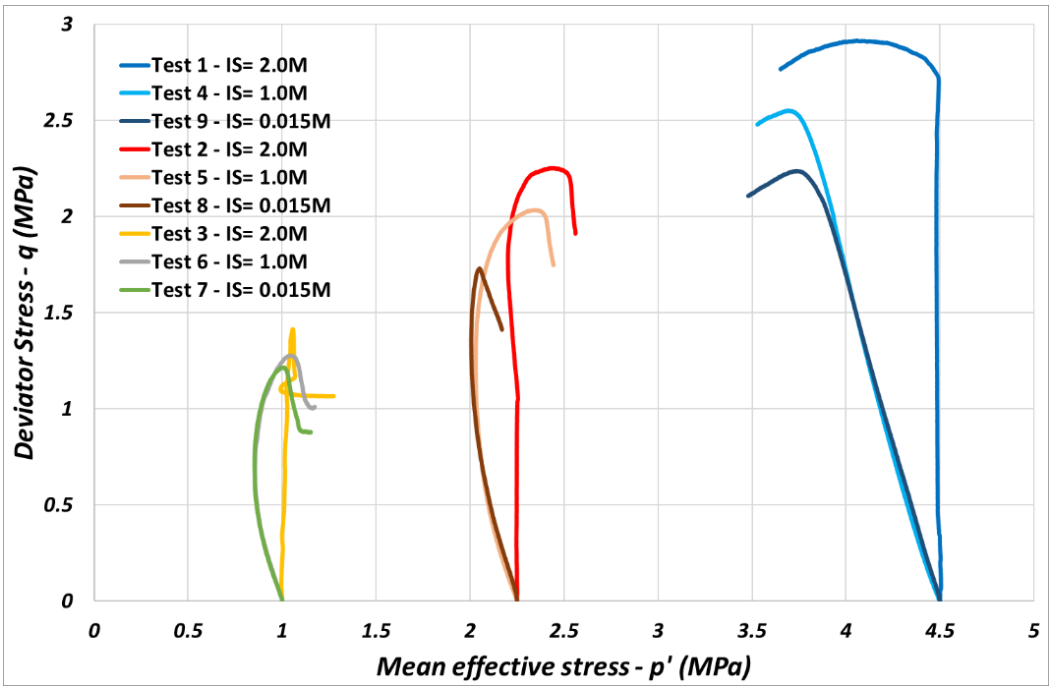

Figure 68 Stress paths in (p', q) plane for different IS.

iii. Yielding

Various approaches have been proposed in the literature to determine the yield stress, which is defined as the maximum deviator stress or the peak of the stress-strain curves (Tavenas and Leroueil, 1980). In isotropic compression tests, yield is commonly taken as the intersection of two best-fit linear segments in the (ε_v: $\ln p'$) plot. For denser soils like compacted clays, with no marked peaks, a volumetric criterion may be applied (Cui et al., 1995; Delage and Cui, 1996). Work criteria are also used to identify yield points (Leroueil et al., 1979). Sultan et al. (2010) determined yield stress based on a change in slope in linear (ε_v: $\ln p'$) plots, demonstrating that this method can reliably determine the yield stress. For Opalinus clay, Popp and Salzer (2007) and Zhang (2016) noted that the yield point could indicate the onset of microcracking, detected through shear wave velocity. However, while some shear wave velocity measurements on BC have been conducted (Neerdael and Voet, 1992; Piriyakul, 2006), there is no conclusive evidence that microfracture formation occurs beyond the yield point. Yielding in BC likely relates to modifications in microstructure or micro-fissuring, marking the transition to plastic deformation. After this yield point, BC enters a plastic deformation region, with stress increasing nonlinearly until peak stress (q_f), known as peak shear strength. After reaching the peak, all samples demonstrate a strain-softening response, with the stress-strain curve descending as shear resistance decreases due to continued plastic

shear strain. This softening response, observed by other researchers (Horseman et al., 1987; De Bruyn and Thimus, 1996; Coll, 2005), continues until the shear resistance stabilizes at the residual shear strength (q_r). Limited studies were found in literature for the determination of the yield stress and elastic zone for the undrained triaxial shear test (Vandenberghe et al., 2014; Giger et al., 2018).

In this study, a new approach is introduced to define the elastic zone and yield stress (q_y) of BC under undrained conditions. The proposed method focuses on the evolution of pore water pressure (Δu) in relation to the mean effective stress (p') during the triaxial tests. As seen in Figure 69(a), the pore water pressure initially increases in a nearly linear fashion with respect to (p'), reflecting the elastic deformation. However, as the stress increases, an inflection point occurs where the slope of the curve changes. This change in slope is indicative of the point at which the clay transitions from elastic to plastic behavior, marking the yield stress (q_y). This method is consistent with the volumetric criterion (Delage and Cui, 1996; Sultan et al., 2010). The inflection point is crucial because it signifies the onset of microstructural changes within the clay, such as the initiation of microcracking or the reorganization of clay particles. To identify the yield stress more accurately, the inflection point in the $\Delta u - p'$ curve is projected onto the stress space, specifically the (p': q) plot (Figure 69(b)) and subsequently onto the (ε_a: q) plot (Figure 69 (b)).

By using this method, the yield stress is determined based on the observable changes in the pore water pressure response, rather than just the deviator stress, offering a more comprehensive understanding of the behavior under undrained conditions. This approach also provides a more reliable means to differentiate the elastic and plastic deformation regions.

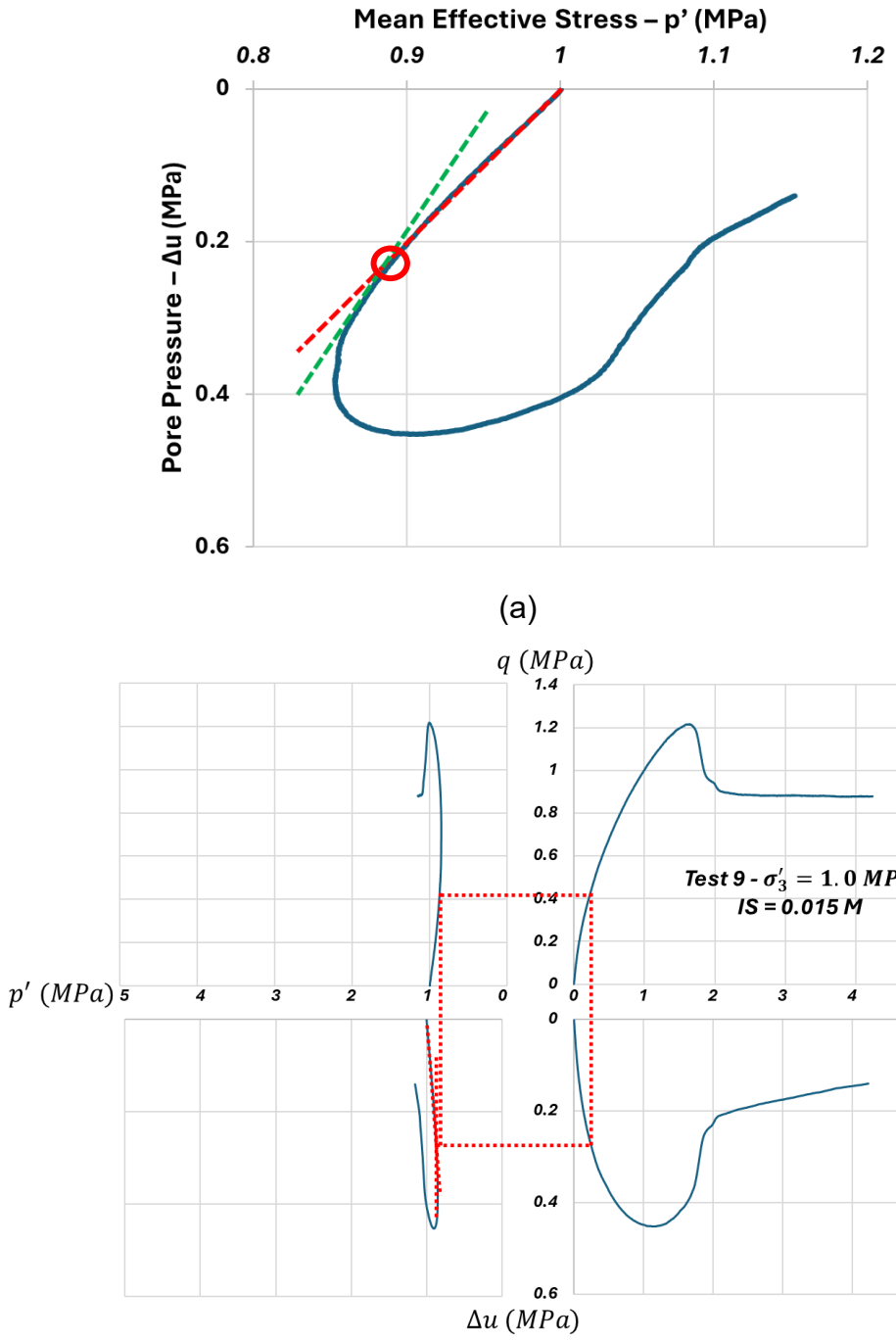

Figure 69 Yield stress determined from a semi-log plot projected in (a) $(\Delta u : p')$ plot and (b) synthetic presentation of triaxial test 9.

The results of the yield stress and the undrained tangent Young's modulus are summarized in Table 30, clearly indicating that both depend on the confining stress and salt concentration. Specifically, lower yield stress and Young's modulus values are observed at lower effective confining stresses and lower ionic strengths, as shown in

Figure 70. This trend highlights the influence of both confining stress and ionic strength on the mechanical properties.

Table 30 Yield deviator stress, effective stress and undrained Young's modulus obtained from this study.

Test No.	σ_3' (MPa)	IS (M)	q_y (MPa)	p_y' (MPa)	E_U (MPa)
1	4.5	2	1.9	4.48	600
4	4.5	1	1.25	4.1	435
7	4.5	0.015	1.0	4	340
2	2.25	2	1.0	2.25	340
5	2.25	1	0.7	2.05	290
8	2.25	0.015	0.5	2.025	280
3	1	2	0.5	1.0	200
6	1	1	0.425	0.87	195
9	1	0.015	0.40	1.0	190

The undrained Young's modulus values reported in the literature for BC vary considerably. Mair et al. (1992) found a value of approximately 1000 MPa, while Rousset et al. (1989) reported a slightly higher value of 1430 MPa. Djéran et al. (1994) who conducted a series of triaxial tests under both drained and undrained conditions, found a much lower short-term elastic modulus around 500 MPa. The differences among these values may be attributed to the differences in the testing conditions and protocols, which were not thoroughly detailed in each study, as well as the heterogeneity of the samples, since the tests were performed on specimens from different BC cores.

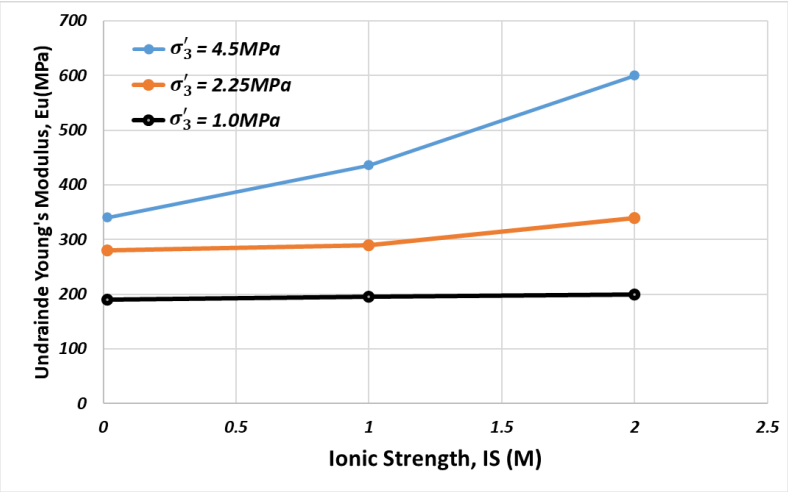

Figure 70 Undrained Young's modulus evolution versus IS under different effective confining stresses.

iv. Critical state envelope

According to the French standard NF P 94-070 (Afnor, 1994), soil failure in triaxial tests is defined at the point of the peak deviator stress (q_f). For the specimens with a low overconsolidation ratio (OCR=1.3), the failure is characterized by a horizontal plateau in the stress-strain curve; thus, for tests 1, 4, and 9, the failure is interpreted as the point where this plateau begins. In contrast, highly overconsolidated clay samples (OCR= 6 and 2.6) exhibit a peak stress followed by softening behavior. These samples reach failure as the deviator stress gradually decreases to a residual value. This residual stress, observed at the plateau following the peak, is often used to characterize the ultimate shear strength along the critical state plane for overconsolidated specimens. The resulting set of stress states at failure can be used to construct the soil failure envelope, offering a comprehensive understanding of shear strength characteristics under different conditions.

The critical state, meanwhile, represents a stable condition where further deformation does not result in additional changes in volumetric strain (for drained triaxial tests) or pore water pressure (for undrained triaxial tests). Identifying this state is important for better understanding the effect of salt concentration on the shear behavior of BC.

Regarding the chemical effects on residual shear strength, the stress states at failure for BC are presented in Figure 71 in the p': q plane. It can be observed that the failure plane for samples with higher IS lies above those with lower IS. The failure plane shifts upwards as salt concentration increases, corresponding to a higher peak deviator stress at higher salt concentrations.

It should be noted that the failure planes determined in this study display a linear trend. However, the literature reports some bilinear trends for BC (Coll, 2005; Bernier et al., 2011; Lima, 2011). Other authors (Petley, 1999) suggested that for certain clays sch as for London clay and mudrocks, a non-linear failure criterion may be more appropriate.

These failure planes provide valuable insights into the key geomechanical parameters, such as effective cohesion and internal friction angle, for varying salt concentrations and thus also sodium occupancies. Table 31 presents the evolution of the critical slope (M), effective cohesion, and internal friction angle for different IS levels. As indicated, the slope of the critical state line, which coincides with the failure plane, increases with

increasing ionic strength. Specifically, the internal friction angle increases from 14.6° at IS = 0.015 M (representing the in situ pore water of BC (De Craen et al., 2004) to 17° for samples with IS = 2.0 M, which corresponds to the theoretically estimated Na^+ occupancy of 90%. In contrast, the effective cohesion remains relatively unaffected by higher ionic strength, exhibiting only a slight increase from 0.13 MPa at IS = 0.015 M to 0.14 MPa at IS = 2.0 M. This marginal change suggests that while the friction angle is notably influenced by ionic strength, the effective cohesion remains stable with varying salt concentrations.

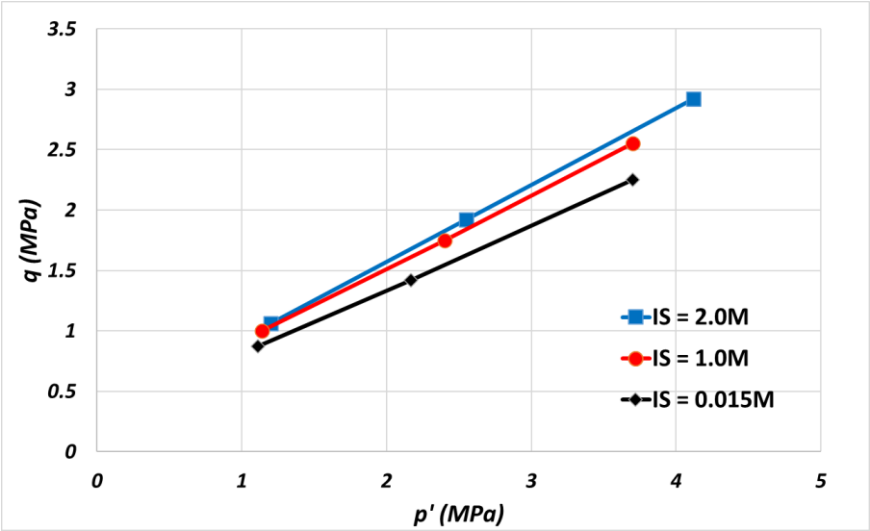

Figure 71 Failure point in the plane $(p':q)$ for the undrained triaxial tests in this study.

Table 31 Main characteristics corresponding to critical slope, effective friction angle and cohesion at different ionic strength.

IS (M)	M (-)	φ' (°)	c' (MPa)
0.015	0.55	14.6	0.13
1.0	0.60	15.8	0.135
2.0	0.65	17	0.14

Figure 72 presents the critical state strength envelope for Boom Clay at ambient temperature, incorporating the findings from this study alongside the results from various authors (Horseman et al., 1987; Baldi et al., 1991; Coll, 2005; Lê, 2007; Sultan et al., 2010; Lima, 2011; Awarkeh, 2023). All results appear consistent. The data scatter likely stems from the difference in experimental procedures, particularly during the saturation phase and sample preparation.

A single linear fit of the relationship between mean effective stress and deviator stress at the critical state suggests a slope of approximately 0.67 (Yu et al., 2018; Awarkeh, 2023). Deng et al. (2011), however, proposed a bilinear model where an intersection point near the in situ effective stress divides the envelope into two linear sections: a low-stress and a high-stress segment. In the high-stress region, a slope of 0.48 was reported. The literature suggests a general friction angle of approximately 17° and an effective cohesion of 0.2 MPa. The findings in this study are relatively close to those results with values of 14.6° and 0.55 MPa, respectively.

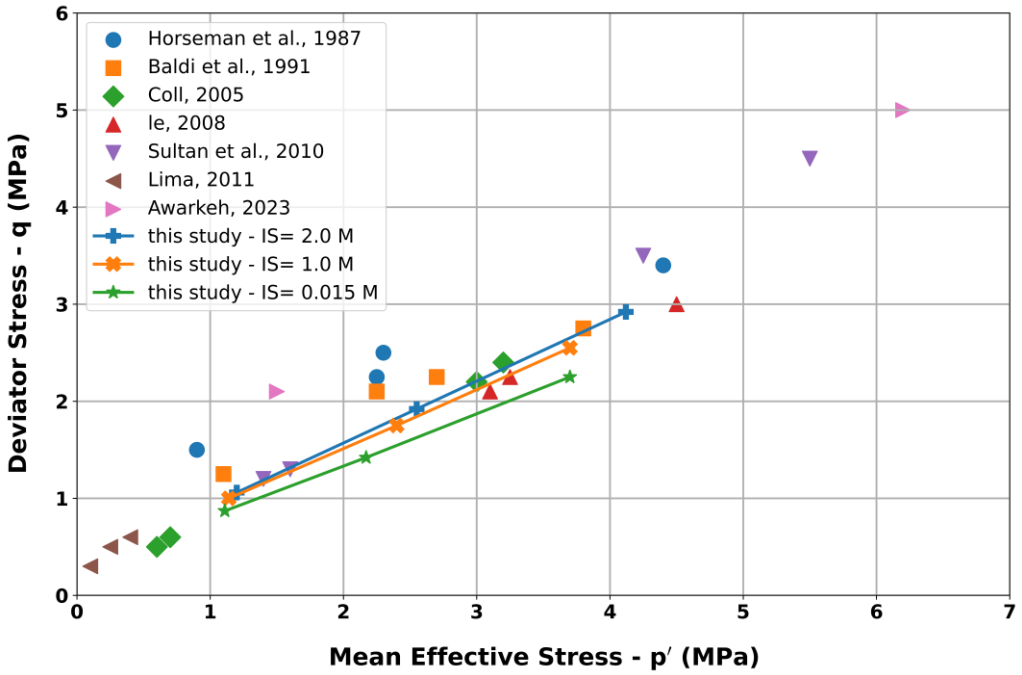

Figure 72 Failure envelopes in the p'-q plane of Boom Clay at ambient temperature.

c. Discussion

Increasing concentrations of salt ions in pore water influence the clay structure by shrinking the diffuse double layer around clay particles, which results in closer particle arrangements and increases the interparticle bonding. This process generally enhances soil stiffness (Van Olphen, 1963; Barbour and Fredlund, 1989; Mitchell and Soga, 2005; Thyagaraj and Rao, 2013).

At the clay fabric scale, initial suction in unsaturated clays primarily consists of matric suction ($u_a - u_w$) and inherent osmotic suction, which arises from the initial pore water chemistry. In fully saturated clayey soils, matric suction is negligible. When (Na,Ca)NO_3 solutions infiltrate, salts migrate into the soil pores, raising the concentration of pore

fluid. This process induces osmotic suction due to the concentration difference between the infiltrating solution and the in-situ pore water. As osmotic suction increases, the stiffness of the soil is enhanced. At the particle level, the behavior of clays is governed by the diffuse double layer (DDL), which controls both hydraulic and mechanical responses. The DDL forms around the negatively charged clay particle surface and the surrounding layer of dispersed cations (Mitchell and Soga, 2005). According to Gouy-Chapman DDL theory, the thickness of this layer inversely varies with solute concentration and cation valency, with cation exchange altering the DDL thickness (Van Olphen, 1963; Mitchell and Soga, 2005). It has been observed that under fully saturated conditions, an increase in salinity causes a slight increase of shear strength for overconsolidated and more significant increase for slightly overconsolidated soils. When a higher concentration of (Na, Ca)NO_3 infiltrates the soil, the equilibrium between the clay, water, and electrolyte is disturbed. This alteration in pore fluid concentration triggers the displacement of exchangeable cations on the clay particle surfaces by the dominant cations present in the pore fluid, i.e., Na^+ ions. Thisresults in a modification of the diffuse double layer (DDL) thickness. As Na^+ ions infiltrate through the interlayer space of montmorillonite sheets, they can cause a shrinkage of these spaces, further contributes to the increase in soil stiffness, as demonstrated in previous studies (Maio, 1998; Di Maio et al., 2004; Al Mais et al., 2024, 2025a). According to Sridharan and Prakash (1999), an increase in pore water concentration reduces the interparticle repulsive forces between clay particles while enhancing the attractive forces. This results in an increase in shear strength at the particle level. It is likely that the swelling of clays is inhibited as salt concentration increases, which in turn affects the Diffuse Double Layer (DDL). As the DDL becomes suppressed, the distance between particles decreases, leading to the increase of stiffness and thus a decrease in void ratio (i.e., a reduction in water content), contributing to the hardening of soil. Di Maio (1998), Di Maio et al. (2004), Barbour and Yang (1993), among others, showed that when clay soils are permeated with saline solutions, an increase in salt concentration results in decreased soil compressibility and higher strength. It is worth noting that these tests were performed under fully saturated conditions, i.e., suction is zero. Additionally, most of the specimens used in these studies were prepared by initially mixing the soil with distilled water and then permeating it with brine. This approach reflects a scenario where the original soil structure remains partly intact while the pore fluid is replaced, representing short-term

exposure to the salt solution. However, Di Maio (1998) and Di Maio et al. (2004) also conducted shear tests on samples initially reconstituted with brine, and an increase in shear strength was observed in these cases as well. Observations showed that the soil prepared with brine exhibited a lower void ratio, which likely contributed to the increase in strength, associated with both the increase in pore solution concentration and the compaction effect resulting from the brine exposure.

Mokni (2011) performed a series of direct shear tests on Boom Clay powder mixed with $NaNO_3$ solution. The results demonstrated that under partially saturated conditions, an increase in salinity caused a slight decrease in both compressibility and shear strength. Note that the samples prepared with $NaNO_3$ solution exhibited a reduction in water content at a given matric suction. This reduction in shear strength could be attributed to the lower water content of soil, which is equilibrated with the electrolyte at the given matric suction. Therefore, the observed decrease in strength may be primarily due to the change in water content, which influences the mechanical response of the material under these specific conditions. Barbour and Yang (1993) summarized osmotic consolidation tests conducted by Yang (1990), Ho (1985), and Barbour (1986) on remolded and undisturbed samples of glacial till and glaciolacustrine clay, exposed to various solution concentrations. The samples were subjected to specific stress levels and then equilibrated with NaCl solution through diffusion. Following this, they were reloaded to higher stresses. The results showed that when the water-saturated clay was exposed to NaCl brine, it underwent a decrease in volume. This volume change was accompanied by an apparent increase in preconsolidation stress and a decrease in compressibility, until the new preconsolidation stress was exceeded. Afterwards, the samples continued to consolidate along the same virgin compression line. Similar observations were reported by Barbour and Fredlund (1989). Ho (1985), as cited by Barbour and Yang (1993), also tested remolded samples with brine and then tested in water. A noteworthy observation was that submersion of the samples in water caused a decrease in volume under constant effective stress. Di Maio (1998) investigated the effects of exposure of water-saturated specimens of Ponza bentonite, alternately to pure water and saturated NaCl, KCl, or $CaCl_2$ solutions. Exposure to these three electrolytes produced consolidation of the specimens, large volumetric deformations, and an increase in residual shear strength. The effects of NaCl exposure were reversible in terms of ion exchange reactions when the samples were re-exposed to

pure water, while those for KCl and $CaCl_2$ were not. The irreversibility observed with KCl and $CaCl_2$ is mainly due to the stronger electrostatic interactions between the clay particles and the potassium (K^+) and calcium (Ca^{2+}) ions. K^+ ions have a lower hydration energy and are more tightly bounded to the clay particles than sodium (Na^+) ions, making their displacement less likely. Additionally, Ca^{2+} ions, being divalent, form even stronger bonds with the clay particles, further reducing the reversibility of the effects. These stronger ion-clay interactions lead to more permanent changes in the clay structure when exposed to KCl or $CaCl_2$ solutions.

6. Conclusions

This study experimentally investigated the effects of saline solutions on the hydro-mechanical behavior of intact Boom Clay (BC), considering various factors such as sodium occupancy, solute concentration and stress conditions. The findings provide valuable insights for the long-term assessment of geological disposal of bituminized and radioactive waste. The main conclusions drawn from the research are as follows:

1. **Swelling and Hydraulic Conductivity:**
    - One-dimensional swelling tests demonstrated that increasing ionic strength reduces the swelling potential of BC by contracting the diffuse double layer (DDL), leading to structural collapse and decreased swell potential.
    - Cation exchange plays a crucial role in swelling behavior. The substitution of divalent cations (e.g., Ca^{2+}) with monovalent cations (e.g., Na^+) decreases the hydrated radius, reducing swelling pressure.
    - Percolation with high-sodium concentration solutions results in an immediate increase in hydraulic conductivity due to the compression of interlayer spaces and the creation of preferential flow pathways, increasing the fraction of mobile water.
2. **Salinization and Volume Change Behavior:**
    - Under constant stresses, BC undergoes shrinkage with increasing solute concentration and sodium occupancy, while desalinization induces swelling.

- The effect of solute concentration is linked to the contraction/expansion of the DDL, whereas cation exchange modifies interlayer spacing, influencing the shrinkage behavior of montmorillonite sheets.
- Two distinct zones were identified: an elastic zone (>0.7-0.8 MPa) where volume change is recoverable and a plastic zone (<0.7-0.8 MPa) where volume change is irreversible.
- Increased solute concentration enhances osmotic suction, reducing DDL thickness, promoting particle aggregation, and forming macropores and fissures. These microstructural changes contribute to increased hydraulic conductivity.

3. **Compressibility and Preconsolidation Pressure:**
   - Percolation with high salt concentrations induces osmotic consolidation, leading to a reduction in compressibility and swelling, consistent with DDL theory.
   - The chemical influence on compressibility and swelling behavior diminishes with increasing vertical stress during loading and unloading.
   - Beyond a certain threshold concentration, chemical effects stabilize, indicating a limit to salinity-induced changes in soil behavior.
   - DDL shrinkage leads to particle densification, enhancing soil stiffness and preconsolidation pressure.
4. **Shear Strength and Undrained Behavior:**
   - The overconsolidation ratio (OCR) significantly impacts the contraction/dilatancy behavior of BC. Normally consolidated samples (OCR = 1.3) exhibit contraction, whereas overconsolidated samples (OCR = 6 and 2.6) show strain softening and failure at lower effective confining stresses.
   - Increasing salt concentration leads to shear strength enhancement due to DDL shrinkage, which tightens inter-particle spacing and increases internal friction angle and elastic modulus. However, the effect on effective cohesion remains negligible.

- Pore water pressure build-up during undrained shearing is dependent on initial mean effective stress and chemical concentration, with higher salt concentrations generating higher pore pressures under identical confining stresses.

V. Development of an elasto-plastic model for chemical effect on BC

1. Introduction

The main objective of this chapter is to develop a chemo-elasto-plastic (CEP) model, referred to as ACC2-Chem, to describe the mechanical response of Boom Clay (BC) under chemical perturbations, particularly due to variations in sodium occupancy and saline concentration. This model aims to capture the chemo-hydro-mechanical behavior of BC by extending an existing elasto-plastic model.

The base model chosen for this development is ACC-2, originally developed by Hong et al. (2016), as it was specifically formulated for Boom Clay and has demonstrated good predictive capabilities for its mechanical behavior. To adapt ACC-2 to the experimental observations obtained in this study, the model was first modified by introducing cohesion and revising the yield surface and flow rule equations to better suit in situ conditions with BC synthetic pore water.

To incorporate chemo-mechanical effects, an elasto-chemo volumetric strain formulation was developed based on the work of Guimarães et al. (2013). This formulation was implemented within the ACC-2 framework to reflect the influence of sodium occupancy and ionic strength on volumetric strain. The resulting extended model is referred to as ACC2-Chem.

The chemical extension of ACC-2 is guided by experimental findings, through which the mechanical parameters of the model are expressed as analytical functions of ionic strength. This approach allows the model to account for chemical effects in a physically consistent and predictive manner.

The development of ACC2-Chem includes (i) an analysis of the chemical perturbation mechanisms affecting BC, (ii) the mathematical formulation of the modified ACC-2 model, and (iii) the parameter calibration based on experimental data. The final model is validated through simulations of triaxial compression tests and salinization-desalinization experiments, and its performance is further assessed under in situ conditions using two-dimensional plane strain simulations with the finite element code LAGAMINE (Collin et al., 2002).

2. General overview of ACC-2

The behavior of natural Boom Clay is characterized by a limited elastic zone, a non-linear stress-strain response, and a smooth transition from elastic to plastic deformation. The conventional yield points defining the yield surface of Boom Clay are determined using the approach proposed by Wood (2004). As illustrated in Figure 73, this method identifies the yield point as the intersection of two linear extrapolations, representing the pre-yield and post-yield segments of stress-strain curves in the $(p' - \varepsilon_v)$ and $(q - \varepsilon_s)$ planes. These yield points are derived from experimental tests conducted by Baldi et al. (1991), Coll (2005), Deng et al. (2011), and Lê (2007) on Boom Clay. The collected results from the literature are presented in Figure 74.

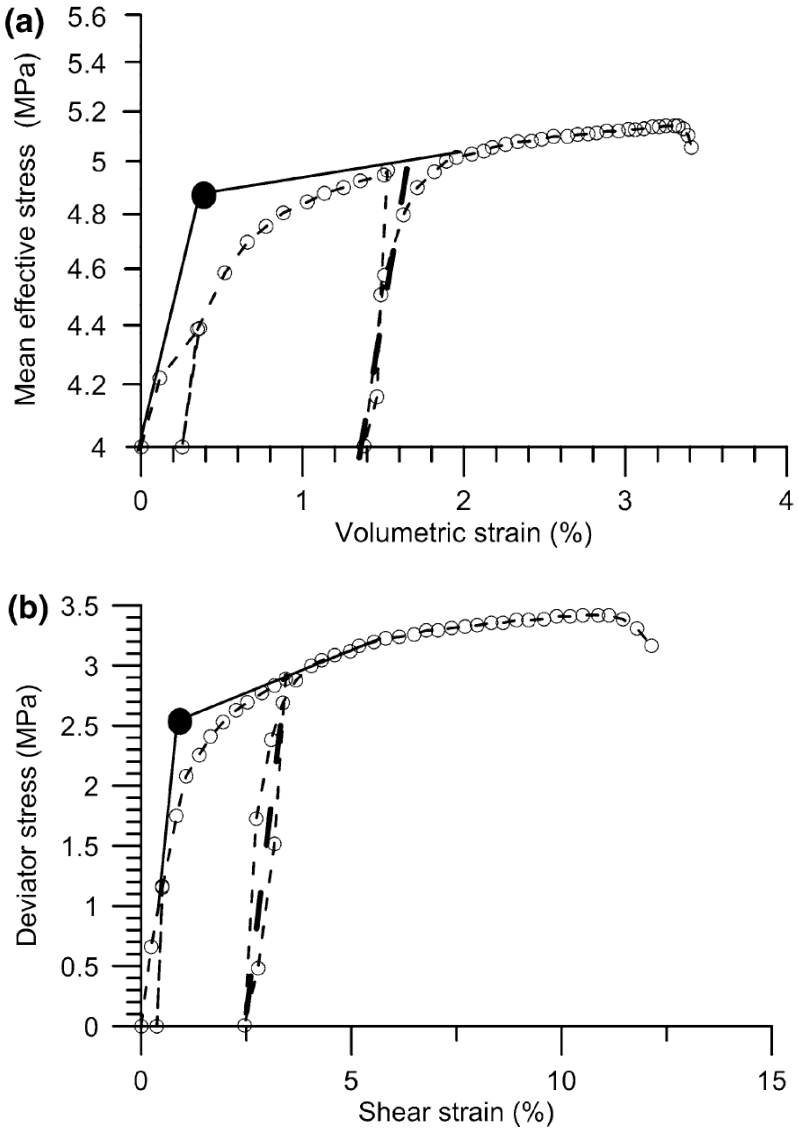

Figure 73 Conventional yield stress determination from a drained triaxial shear test: (a) $p' - \varepsilon_v$ plane, and (b) $q - \varepsilon_s$ (Baldi et al., 1991).

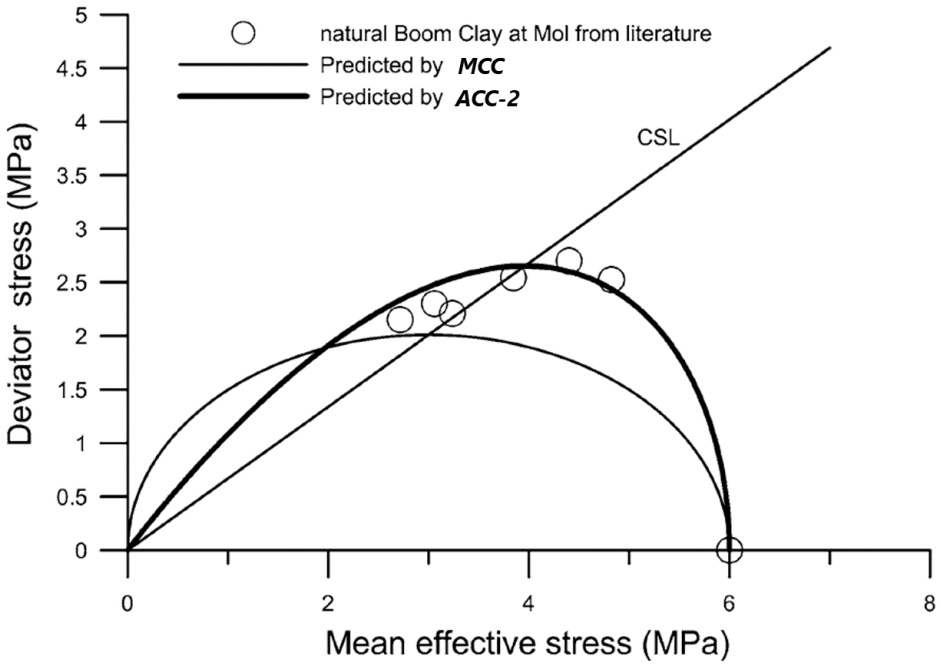

Figure 74 Conventional yield surface of natural Boom clay: experimental determination and proposed model (Hong et al., 2016).

Roscoe and Burland (1968) developed the Modified Cam Clay (MCC) model by modifying the yield curve of the original Cam Clay model, addressing the discontinuous derivative at ($q=0$) present in the original formulation. The MCC model is widely used as an elasto-plastic constitutive model to describe the behavior of soft clays. However, its evaluation on Boom Clay reveals significant limitations, as shown in Figure 74. Specifically, the MCC yield surface does not accurately capture the behavior of Boom Clay, and the model tends to predict unrealistic volumetric strains when using an associated flow rule (Valls-Marquez, 2009; Hong, 2013). Additionally, it exhibits an abrupt transition from elastic to plastic behavior, as noted by Hong (2013).

To overcome these limitations, Hong et al. (2016) developed an adapted version of the Modified Cam Clay model with two yield surfaces, referred to as ACC-2. The conventional yield surface of the ACC-2 model provides a more accurate representation of experimental results, as illustrated in Figure 74. The performance of the ACC-2 elasto-plastic (EP) model was evaluated by Hong et al. (2016) through numerical simulations of Boom Clay behavior under oedometer and triaxial loading conditions. The simulated results were compared only to experimental data from Baldi et al. (1991) and Lê (2007) on Boom Clay samples.

The constitutive model is developed and formulated in the $p' - q$ space. The mean effective stress *p'* = *p* - *u* and the deviator stress *q* are defined using the effective stress tensor $\sigma'_{ij} = \sigma_{ij} - u\,\delta_{ij}$, $i, j = \{1,2,3\}$, as follows (using the Einstein's notation repeated indices mean summation):

(14) $$p' = \frac{1}{3}\sigma'_{ij}\delta_{ij}$$

(15) $$q = \sqrt{\frac{3}{2}}\sqrt{s_{ij}s_{ij}}$$

where p refers to mean total stress, σ_{ij} is the total stress tensor, *u* is the pore water pressure; δ_{ij} is the Kronecker's symbol and $s_{ij} = \sigma'_{ij} - p'\delta_{ij}$ is the deviator stress tensor.

The elastic volumetric strain increment ($d\varepsilon_v^e$) and the shear strain increment ($d\varepsilon_s^e$) can be calculated by:

(16) $$\boldsymbol{d\varepsilon_v^e = \frac{dp'}{K}}$$

(17) $$\boldsymbol{d\varepsilon_s^e = \frac{dq}{3G}}$$

where *K* and G are the elastic bulk modulus and the shear modulus, respectively.

The bulk modulus *K* is the same as for the Cam Clay model whereas the shear modulus G is obtained with a constant Poisson's ratio $\boldsymbol{\nu}$:

(18) $$\boldsymbol{K = \frac{v_0 p'}{\kappa}}$$

(19) $$\boldsymbol{G = \frac{3(1-2\nu)K}{2(1+\nu)}}$$

where κ is the elastic slope in $(\ln p' - v)$ space and v_0 is the initial specific volume, v is the specific volume.

Yield Surfaces in the ACC-2 Model

As shown in Figure 75, two yield surfaces are introduced:

- The conventional **Yield Surface (YS)**, which represents the normal consolidation behavior.

- The **Inner Yield Surface (IYS)**, which describes yielding within the Yield Surface.

The yield stress on the Inner yield surface in the triaxial stress state is denoted by (*p′*, *q*) while ($\bar{p}'$,$\bar{q}$) is the corresponding yield stress on the conventional Yield surface.

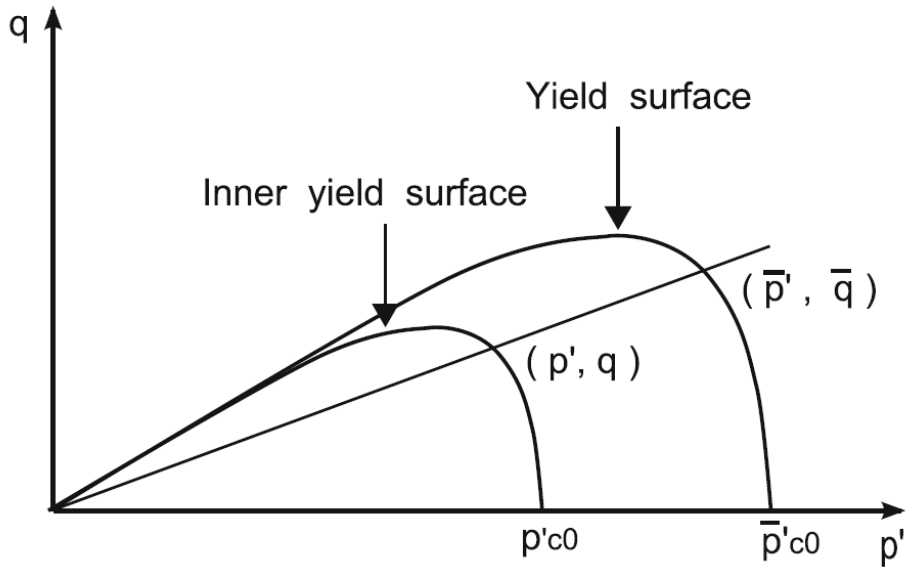

Figure 75 Yield surfaces of ACC-2 model (Hong et al., 2016).

Since the Inner yield surface is homologous to the Yield surface with respect to the origin in *p′-q* space, therefore:

(20) $$\frac{p'}{\bar{p}'} = \frac{q}{\bar{q}} = \frac{p'_c}{\bar{p}'_c} = r$$

To achieve a wide variety of yield surface shapes, a generalized yield surface proposed by McDowell & Hau (2004) is used for the Yield surface (f_Y):

(21) $$f_Y = q^2 + \frac{M_f^2}{1-k_f}\left(\frac{p'}{\bar{p}'_c}\right)^{2/k_f} \bar{p}'^{\,2}_c - \frac{M_f{}^2 p'^2}{1-k_f} = 0 \quad \textbf{(if } k_f \neq 1\textbf{)}$$

and

(22) $$f_Y = q - M_f p' \sqrt{2\,ln\left(\frac{p'_c}{p'}\right)} = 0 \qquad \textbf{(if } k_f = 1\textbf{)}$$

where M_f defines the stress ratio at the apex of the yield surface, k_f is a parameter used to specify the shape of the yield surface. For the sake of brevity but without losing generality, it is assumed that k_f does not equal 1.

A more consistent interpretation is that the inner yield surface arises by replacing the preconsolidation pressure $\bar{p}_c'$ with $r\bar{p}_c'$, leading to the following expression:

$$(23)\quad \boldsymbol{f_I = q^2 + \frac{M_f^2}{1-k_f}\left(\frac{p'}{r\bar{p}_c'}\right)^{2/k_f}(r\bar{p}_c')^2 - \frac{M_f^2 p'^2}{1-k_f} = 0}$$

The expression of the plastic potentials takes the same form as the yield surfaces. The plastic potentials associated with the Inner yield surface and the Yield surface respectively read:

$$(24)\quad \boldsymbol{g_I(p', q, \beta) = q^2 + \frac{M_g^2}{1-k_g}\left(\frac{p'}{r\beta}\right)^{2/k_g}(r\beta)^2 - \frac{M_g^2 p'^2}{1-k_g} = 0}$$

$$(25)\quad \boldsymbol{g_Y(p', q, \beta) = q^2 + \frac{M_g^2}{1-k_g}\left(\frac{p'}{r\beta}\right)^{2/k_g}(r\beta)^2 - \frac{M_g^2 p'^2}{1-k_g} = 0}$$

giving the flow rule in the case of triaxial compression based on MCC (Roscoe et al., 1958):

$$(26)\quad \frac{d\varepsilon_v^p}{d\varepsilon_s^p} = \frac{M_g^2 - \eta^2}{k_g \eta}$$

where η is the stress ratio q/p', M_g is the critical state slope defining the stress ratio at failure when there is no further volumetric strain increment, k_g is a constant parameter used to control the flow rule (the ratio between plastic volumetric strain increment and plastic shear strain increment), β is the size parameter and it can be determined by Eqt. (24) at any given stress state (p', q) using a similar procedure as done by Yu (1998). $k_g = 2$ is the case of MCC with an associated flow rule, and this parameter is not equal to 1.

Two hardening parameters $\bar{p}_c'$ and r are introduced to control the size of the Yield surface and the Inner yield surface, respectively. The internal variable $\bar{p}_c'$ depends on the volumetric plastic strain as shown in Equation (27). This equation takes the main effect of volumetric hardening into account in the evolution of the Yield surface.

$$(27)\quad \boldsymbol{d\bar{p}_c' = \frac{v_0}{\lambda - \kappa}\bar{p}_c' d\varepsilon_v^p}$$

Along with the evolution of Inner yield surface, the soil particles start to move relatively, and plastic shear strain is produced. In order to account for the contribution of this plastic shear strain to the soil hardening, the evolution law of r can be written as:

$$(28)\quad \boldsymbol{dr = \frac{v_0}{\lambda - \kappa}s(1 - r)d\varepsilon_d^p}$$

with a generalized plastic strain as follows:

$$d\varepsilon_d^p = d\varepsilon_v^p + A_d d\varepsilon_s^p \quad (29)$$

where s is a parameter to control hardening modulus evolution with plastic strain and thus describes the evolution of the slope of stress-strain curve inside YS, A_d is a parameter which controls the contribution of shear plastic strain.

3. Modification of ACC-2 for synthetic water of BC

The results of this study indicate that Boom Clay exhibits some degree of cohesion (Chapter IV), which is not accounted for in the constitutive equations of the ACC-2 model. Figure 76 presents the stress paths for Tests 7, 8, and 9, conducted with the Boom Clay synthetic solution, alongside the conventional yield surface of the ACC-2 model with a preconsolidation pressure of 6 MPa, as previously determined. It is evident that the yield surface does not accurately capture the yield points of the stress paths, as it should ideally intersect all yield points. This discrepancy was also observed in samples percolated with higher ionic strength solutions. Moreover, the constitutive model without cohesion underestimates the peak deviator strength of Boom Clay, particularly at low confining stress (1 MPa), indicating that the material exhibits additional resistance that is not captured by the original formulation.

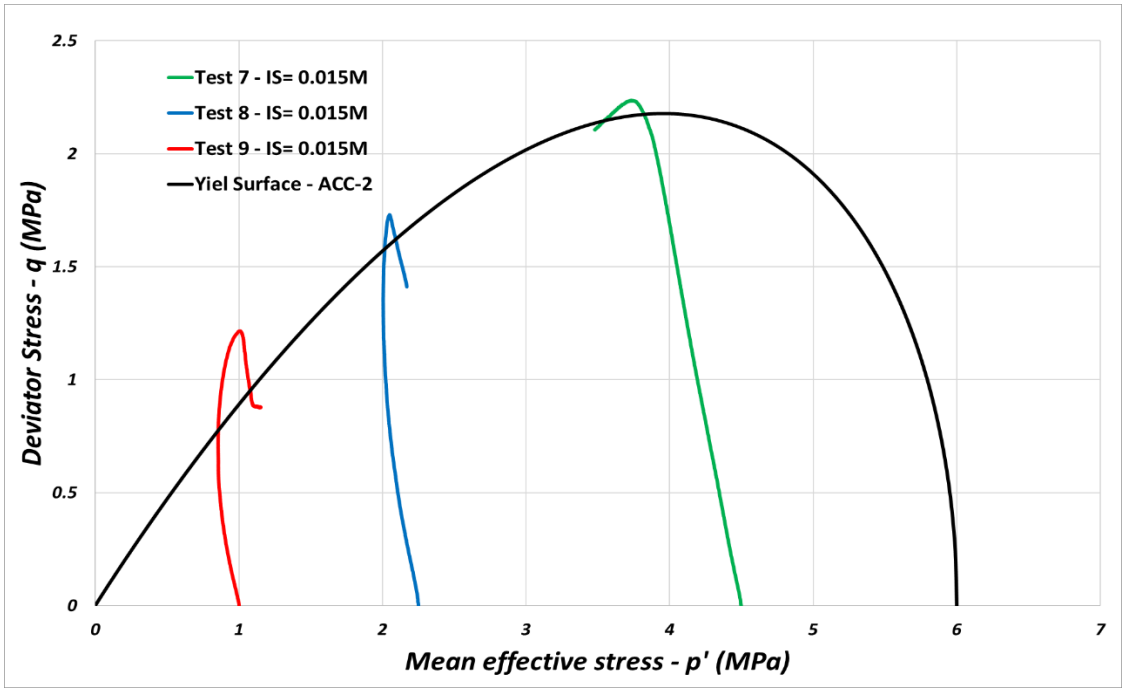

Figure 76 ACC-2 Yield Surface with triaxial test results for tests 7, 8, and 9 with BC Synthetic Water.

To address this limitation, the first modification to the constitutive model involved incorporating cohesion into both the yield surface and the inner yield surface of the ACC-2 model. This update was achieved by introducing the parameter *C*, which depends on cohesion (c') and the internal friction angle (ϕ'), with ϕ' being derived from the equation of the slope of the critical state line M, as shown in Eq. (30). The parameter *C* is mathematically described in Eq. (31).

(30) $$M = \frac{6\sin\varphi'}{3-\sin\varphi'}$$

(31) $$C = \frac{c'}{\tan\varphi'}$$

The introduction of cohesion was implemented by applying an axis translation, achieved by adding the parameter C to the yield surface. Eq. (32) presents the **Updated Yield Surface (UYS)**, incorporating this parameter. In parallel, the flow rule was also updated by introducing C into its formulation, following the same procedure used in the Modified Cam Clay (MCC) model, where C acts as an axis translation to the mean effective stress p'. The updated flow rule is represented in Eqt. (33). These modifications to both the yield surface and the flow rule improve the model's predictive capability, ensuring a better representation of the experimental results obtained in this study.

(32) $$f_Y = q^2 + \frac{M_f^2}{1-k_f}\left(\frac{p'+C}{\vec{p}_c'+C}\right)^{\left(\frac{2}{k_f}\right)}(\vec{p}_c'+C)^2 - \frac{M_f^2(p'+C)^2}{1-k_f}$$

(33) $$\frac{d\varepsilon_v^p}{d\varepsilon_s^p} = \frac{M_g^2 p'^2 + 2M_g^2 C p' + M_g^2 C^2 - q^2}{k_g q(p'+C)} = \frac{M_g^2 - \hat{\eta}^2}{k_g\hat{\eta}}$$

Where $\hat{\eta}$ is $\left(\frac{q}{p'+C}\right)$. It is important to note that the model remains fully functional with $C = 0$, in which case the yield surface reverts to its original formulation, consistent with the work of Hong et al. (2016).

Figure 77 presents the updated yield surface (solid line) and the original yield surface of ACC-2 (dashed line) in the $p' - q$ plane. The experimental stress paths from Tests 7, 8, and 9, conducted at an ionic strength of 0.015 M, corresponding to the BC synthetic water, are also shown.

It is evident that introducing cohesion in the updated yield surface improves the model's ability to reproduce the experimental results. Specifically, the original yield surface

(ACC-2) underestimates the deviator stress at low confining stresses (e.g., Test 9, $\sigma_3' = 1\ MPa$), while the updated yield surface better aligns with the experimental yield points. This highlights the necessity of incorporating cohesion to accurately capture the mechanical behavior of Boom Clay under different loading conditions.

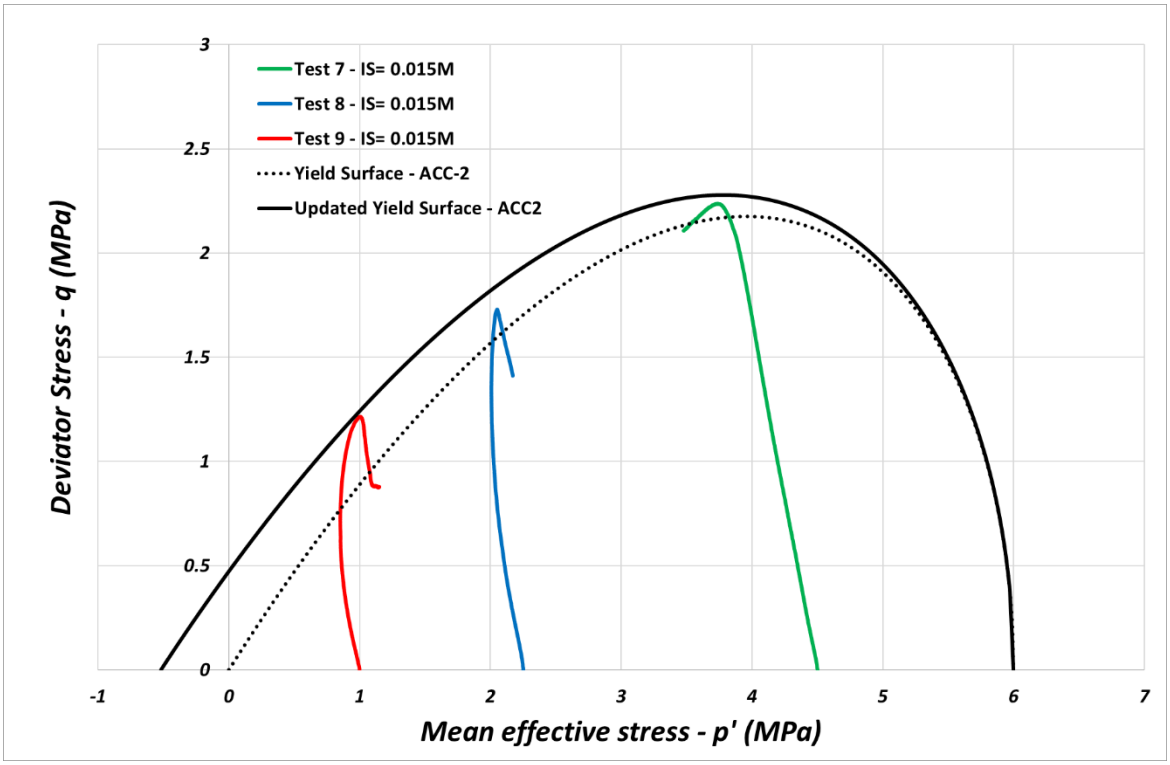

Figure 77 Updated Yield Surface vs. ACC-2 Yield Surface for tests 7, 8, and 9 with BC Synthetic Water.

4. Development of ACC-2 for chemical effect

4.1 Overview of the chemo-mechanical model

Most research on the constitutive modeling of chemo-mechanical behavior in expansive materials has focused on bentonite or unsaturated soils (Fletcher and Sposito, 1989; Hueckel, 1997; Loret et al., 2002; Gajo and Loret, 2003; Boukpeti et al., 2004; Liu et al., 2005; Guimarães et al., 2013; Navarro et al., 2017; Idiart et al., 2020; Lu et al., 2023). When establishing constitutive relationships for unsaturated expansive soils, the double-structure nature of expansive clays has been considered (Alonso et al., 1999; Dieudonné et al., 2024). To describe the elastoplastic behavior of unsaturated expansive soils under hydro-mechanical loading, several constitutive models—such as the Barcelona Expansive Model (BExM) proposed by Alonso et al. (1999)—have been developed based on the double-structure nature of expansive clays. Building on this framework, the Barcelona Expansive Chemo-Mechanical Model

(BExCM) was introduced to incorporate additional variables related to cation exchange processes. This extension of BExM has demonstrated effectiveness in describing interactions between the macrostructure and microstructure of expansive soils (Guimarães et al., 2013).

In this section, an overview of the original BExCM model developed by Guimarães et al. (2013) is presented, with the objective of outlining its key features and underlying principles; the newly developed chemo-elasto-plastic model proposed in this study will be detailed in the following section.

A key feature of BExCM is its explicit consideration of cation exchange, which plays a fundamental role in the mechanical behavior of expansive clays. However, the constitutive model was specifically developed for unsaturated soils with a bimodal pore size distribution (Guimarães et al., 2013). The conceptual framework of BExCM, as proposed by Guimaraes et al. (2013), distinguishes between two structural levels. At the microstructural level, the model captures fundamental physico-chemical interactions occurring at the clay particle scale. At the macrostructural level, it considers the assembly of particle aggregates and macropores, which together form a granular-like fabric. The total void ratio (e) is expressed as the sum of the macrostructural void ratio (e_M) and the microstructural void ratio (e_m):

$$e = e_M + e_m \tag{34}$$

Macrostructural behavior is described using concepts and models applicable to conventional soils, whereas microstructural behavior is governed by fundamental physico-chemical mechanisms at the clay particle level. A key assumption of the model states that macrostructural behavior does not influence the microstructure, whereas microstructural deformations can alter or disrupt the macrostructural arrangement, leading to irreversible deformations.

To account for the interaction between these two levels, interaction functions were introduced, ensuring a link between microstructural and macrostructural responses.

Additionally, the model assumes local hydraulic equilibrium between macrostructure and microstructure at all times. This equilibrium condition implies that total suction in the macrostructure (s_M) is equal to that in the microstructure (s_m).

$$s_M = s_m = s + s_0 \tag{35}$$

where s_m is the total microstructural suction, s_M is the total macrostructural suction, s is the macrostructural matric suction, and s_0 is the macrostructural osmotic suction.

The osmotic suction is expressed as:

$$s_0 = -\frac{RT}{v_w}\ln(a_w) \quad (36)$$

where R is the gas constant ($8.3143\ J/(mol.K)$), T is the absolute temperature (in K), v_w is the molar volume of water (m³/mol), and a_w is the activity of liquid water. In electrolyte solutions, whether dilute or concentrated, a_w depends on the concentration of dissolved salts and can be computed using a geochemical model. For saturated materials, it is assumed that the matric suction is zero.

The mathematical formulation of BExCM is based on the principles outlined earlier, integrating both hydro-mechanical and chemo-mechanical effects within a double-structure framework. At the macrostructural level, the model accounts for phenomena that influence the overall skeleton of the material and significantly affect the macroscopic response of expansive clays. This level is described using conventional constitutive models, such as the Barcelona Basic Model (BBM) proposed by Alonso et al. (1999), to represent macrostructural behavior. In contrast, the microstructural behavior is assumed to be purely volumetric and reversible. This reversibility is attributed to the fundamental physico-chemical interactions at the particle level, which are generally reversible in nature.

The effective mean stress governing the microstructural response is defined as:

$$\hat{p} = p + \chi s_m \quad (37)$$

where p is the mean net stress, s_m is the microstructural suction, and χ is a parameter that varies between 0 and 1 representing the degree of saturation. For saturated clay, $\chi = 1$:

$$\hat{p} = p + s_m \quad (38)$$

to account for the possibility that the microstructure may become unsaturated.

A mathematically convenient way to express the dependence of elastic microstructural volumetric strain on chemical and mechanical variables is:

$$\varepsilon_m^e = -\frac{\beta_m}{\alpha_m} e^{-\alpha_m \hat{p}} \quad (39)$$

This formulation was derived from diffuse double-layer (DDL) theory, which relates interparticle distances to effective stress. To account for the influence of geochemical variables on microstructural behavior, it was assumed that the material parameter α_m remains constant, while β_m depends on the concentration of exchangeable cations:

$$\beta_m = \sum_i \beta_m^i x_i \quad (40)$$

where x_i represents the equivalent fraction of exchangeable cation i, defined as:

$$x_i = \frac{concentration\ of\ exchangeable\ cation}{CEC} \quad (41)$$

where CEC is the cation exchange capacity of the clay. The equivalent fractions satisfy the constraints:

$$\sum_i x_i = 1;\ 0 \leq x_i \leq 1 \quad (42)$$

The parameters β_m^i control microstructural stiffness and must be determined for each possible exchangeable cation. According to DDL theory, β_m^i is proportional to the ionic hydrated radius and inversely proportional to the cation valence ($\beta_m^{Na^+} > \beta_m^{Ca^{2+}}$) (Mitchell and Soga, 2005).

The full differentiation of the microstructural elastic volumetric deformation Equation (39) provides the incremental form of the elastic microstructural volumetric strain:

$$d\varepsilon_m^e = \beta_m e^{-\alpha_m \hat{p}} d\hat{p} + \frac{1}{\alpha_m} e^{-\alpha_m \hat{p}} d\beta_m \quad (43)$$

This expression naturally incorporates osmotic suction into the effective stress. Equation (43) highlights a key feature of the model: cation exchange influences not only the stiffness of the microstructure in response to changes in effective stress (first term) but also directly contributes to microstructural volumetric strains (second term).

A significant implication of this formulation is that microstructural strains induced by geochemical changes depend not only on variations in osmotic suction but also on the specific type of exchangeable cations present in the clay.

The coupling between microstructural and macrostructural volumetric deformations follows the approach proposed by Alonso et al. (1999). This relationship is defined by the following expressions, which establish the link between microstructural volumetric strain (e_m) and macrostructural plastic volumetric strain (e_M):

$$d\varepsilon_M^p = f_D d\varepsilon_m^e \quad (44)$$

when the structural development (SD) mechanism is activated (microstructural expansion), and

$$d\varepsilon_M^p = f_I d\varepsilon_m^e \quad (45)$$

when the structural interference (SI) mechanism is activated (microstructural shrinkage).

The interaction functions f_D and f_I depend on the net stress ratio p/p_0, as illustrated in Figure 78.

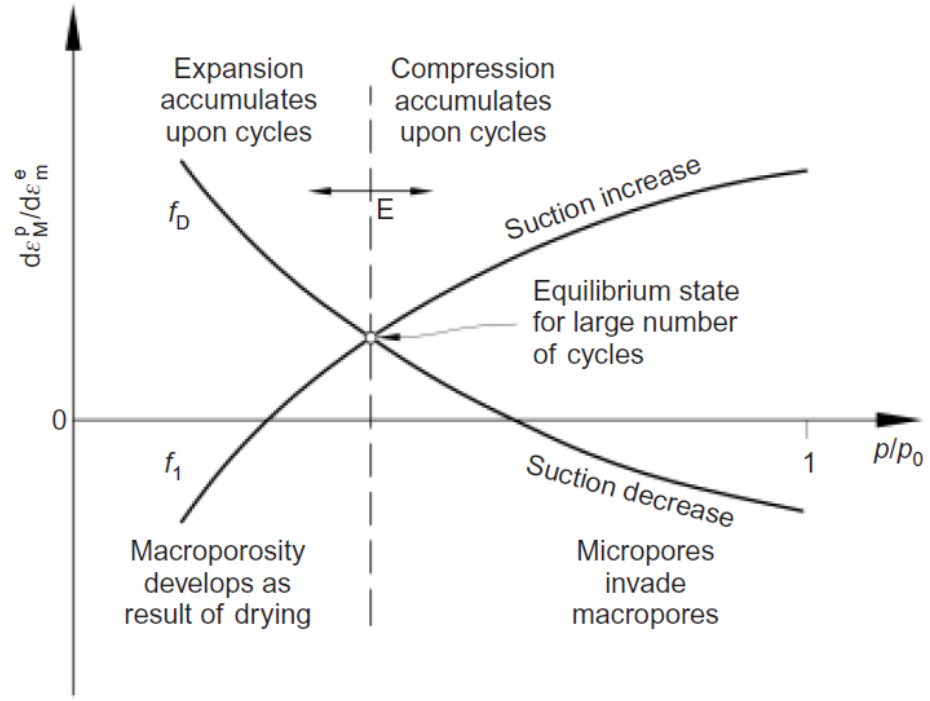

Figure 78 Schematic representation of interaction functions f_I and f_D (Guimarães et al., 2013).

The model was verified by qualitatively reproducing a series of tests on expansive clays (reference soil) subjected to both chemical and mechanical actions. The primary objective was to capture the key phenomena governing volume change in response to variations in dissolved salt concentrations and exchangeable cation content.

Figure 79 presents the model's response to multiple cycles of exposure to sodium chloride-water solutions, based on the experimental study of Di Maio (1998) conducted on Ponza bentonite. The results demonstrated that the Ponza bentonite exhibited largely reversible behavior when, after undergoing cycles of potassium chloride-water exposure, it was reintroduced to a saturated sodium chloride solution. The model

successfully reproduced the chemo-mechanical behavior observed in Di Maio (1998) study, capturing the essential features of the loading process.

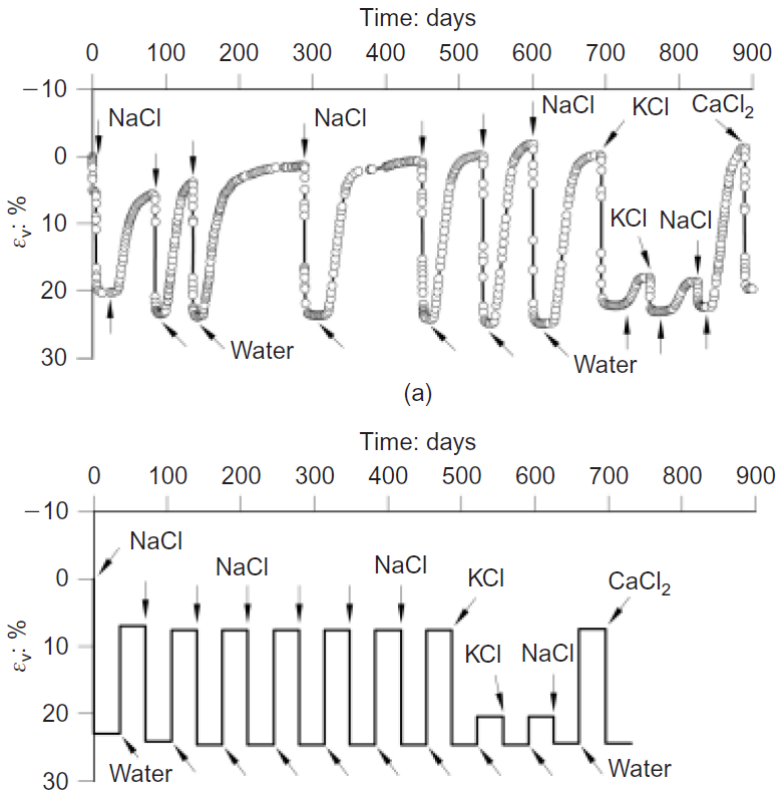

Figure 79 Cyclic exposure of sodium bentonite to saturated solutions of sodium chloride (NaCl), potassium chloride (KCl) and calcium chloride ($CaCl_2$) under axial stress of 40 kPa: (a) experimental results (Maio, 1998); (b) computed model response (Guimarães et al., 2013).

4.2 Development of chemo-mechanical model

While the BExCM model effectively integrates hydro-mechanical and chemo-mechanical effects, certain limitations must be addressed to better capture the behavior of Boom Clay. One key limitation lies in the assignment of cation occupancy, which is not well described in the current formulation of Guimarães et al. (2013). To accurately represent cation distribution, it is essential to incorporate the relative occupancy of a cation with respect to other cations existing in the medium. Additionally, the exponential form of the microstructural volumetric strain equation does not align well with the experimental results obtained in this study, indicating the need for a revised mathematical formulation. Furthermore, while the model assumes a bimodal pore size distribution, Boom Clay exhibits a unimodal porosity (Awarkeh, 2023; Al Mais et al., 2025b), necessitating a refinement of the structural framework to better reflect its microstructural behavior.

In this section, only the microstructural elastic volumetric strain model is developed and reformulated to address these limitations.

In previous studies, a bimodal pore size distribution observed in compacted bentonite and unsaturated expansive soils has justified the use of a double porosity conceptual framework. This type of model typically assumes a system consisting of two primary cations (commonly Na^+ and Ca^{2+}) and a single anion (usually Cl^-). Such a framework has been widely applied to characterize material responses to simple chemical loads and to enhance understanding of the hydro-mechanical-chemical coupling governing bentonite deformation behavior. However, given the characteristics of Boom Clay, a revised formulation of the BExCM model is necessary. In this section, we propose modifications based on experimental findings to develop a model capable of reproducing salinization and desalination test results. A key improvement introduced in this study concerns the formulation of elastic microstructural volumetric strain, ensuring better agreement with observed behavior.

In the initial model formulation (Eqt. (39)), the elastic microstructural volumetric strain ε_m^e was represented by an exponential function. However, experimental results revealed that during both salinization and desalination, the evolution of microstructural volumetric strain follows a logarithmic trend rather than an exponential one. This observation suggests that the microstructural response to changes in effective stress is better captured by a logarithmic function, leading to the modified expression:

(46) $$\varepsilon_m^e = \frac{\beta_m}{\alpha_m} ln(\frac{\hat{p}}{p_0'})$$

This revised formulation provides a more accurate representation of the observed experimental data by explicitly incorporating the dependency of microstructural strain on both the effective mean stress and osmotic suction ($\hat{p} = p' + s_o$) and the ionic occupancy β_m. This modification enhances the model's ability to describe the microstructural response of Boom Clay under varying chemical conditions, ultimately leading to better predictions of volume change behavior during salinization and desalination processes (see further).

In the previously presented model, the material parameter α_m was assumed to be constant in order to account for the influence of geochemical variables on microstructural behavior. The value of α_m was initially set by Guimarães et al. (2013)

to 2.5 MPa^{-1}, but this value was not well justified, and no clear definition was provided for its origin.

Based on the results obtained in this study, it was observed that a more accurate representation of microstructural volumetric strain requires α_m to be dependent on the mean effective stress p'. The relationship between α_m and p' was determined by analyzing the variations in $\alpha_m\ (MPa)$ with respect to p'. Figure 80 illustrates the evolution of α_m, and by fitting a trend line to the data, the following empirical equation was established:

(47) $$\alpha_m = 1051\ ln(p') + 1508$$

This modification provides a more precise definition and estimation of the α_m parameter, which now varies as a function of the mean effective stress. This dependency reflects the fact that the microstructure of Boom Clay can undergo modifications under different stress conditions, making the proposed formulation more physically meaningful and representative of the experimental findings. It is important to note that the fitting of α_m was performed to allow the model to capture the slope of the experimental salinization and desalinization curves, rather than to match the exact values of the predicted and measured strains. This approach ensures that the model can reproduce the general trend and evolution of the microstructural response under chemical loading.

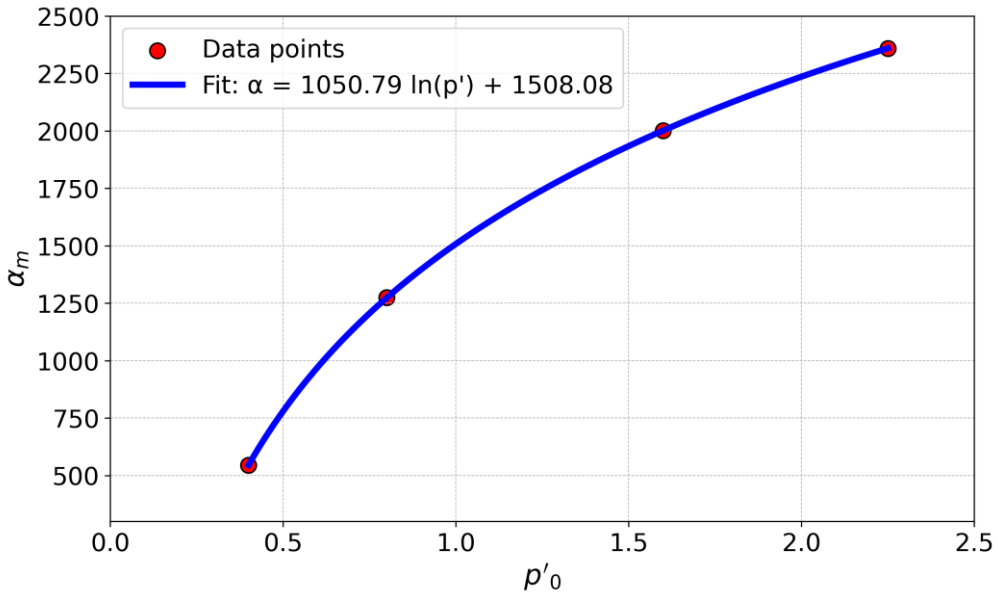

Figure 80 Evolution of parameter α_m in function of p'.

To enhance the representation of sodium (Na^+) occupancy in Boom Clay, the equations introduced account for the relative influence of calcium (Ca^{2+}) and sodium (Na^+) concentrations in the pore solution at both the initial and final stages. This improvement is necessary because the original BExCM formulation did not explicitly model cation distribution as a competitive process, whereas in reality, sodium and calcium compete for exchange sites in the clay, directly influencing its microstructural behavior.

In this formulation, C_{Na}^{A} and C_{Ca}^{A} represent the initial concentrations of sodium (Na^+) and calcium (Ca^{2+}) in the first solution at the beginning of the process. Similarly, the superscript B in C_{Na}^{B} and C_{Ca}^{B} denotes the concentrations at the final stage, after reaching equilibrium or the full concentration expected in the system. Essentially, these variables track the evolution of ion concentrations from an initial state (denoted by A) to a final state (denoted by B). This approach is similar to tracking the progression of ion concentrations from one stage to the next, comparable to moving from step i to $i + 1$ in a sequential process.

The **Sodium Adsorption Ratio (SAR)** is used to quantify the relative concentration of sodium compared to calcium in solution and is calculated separately for the initial (A) and final (B) states, based on the work of Baeyens et al. (1985):

(48) $$SAR_A = \frac{C_{Na}^{A} \times 1000}{\sqrt{\left(\frac{C_{Ca}^{A} \times 2 \times 1000}{2}\right)}}$$

(49) $$SAR_B = \frac{C_{Na}^{B} \times 1000}{\sqrt{\left(\frac{C_{Ca}^{B} \times 2 \times 1000}{2}\right)}}$$

where C_{Na}^{A} and C_{Ca}^{A} represent sodium and calcium concentrations, respectively. A higher SAR indicates greater sodium dominance, impacting the swelling and shrinkage behavior of the clay. To determine the fraction of sodium occupancy, the following empirical equation is used:

(50) $$\xi_A = \frac{-0.013 + 0.015 \times SAR_A}{0.987 + 0.015 \times SAR_A}$$

(51) $$\xi_B = \frac{-0.013 + 0.015 \times SAR_B}{0.987 + 0.015 \times SAR_B}$$

These equations, based on the work of Baeyens et al. (1985), were specifically chosen to reflect the competitive exchange between sodium and calcium, ensuring that sodium occupancy varies realistically with SAR values. Derived from experimental data, they

provide a calibrated relationship between SAR and sodium retention, maintaining physical consistency where increasing calcium concentrations reduce sodium occupancy, and at high SAR values, nearly all exchange sites become sodium-saturated.

Once ξ_A and ξ_B are computed, they are used to determine the microstructural stiffness contribution of sodium at each stage:

(52) $$\beta_m^A = \beta_{Na^+} \times \xi_A$$

(53) $$\beta_m^B = \beta_{Na^+} \times \xi_B$$

Where β_{Na^+} represents the maximum stiffness contribution of sodium at full occupancy. β_{Na^+} was taken equal to 5 based on the work of Guimarães et al. (2013), who determined this value to be appropriate for each of the potential exchangeable cations based on DDL theory. Given that osmotic suction plays a significant role in microstructural behavior, it is computed using the following equation, (Beyer et al., 2005) :

(54) $$s_o = \pi = \left(-\frac{R \times T \times \rho_l}{M_w}\right) \times \ln(a_w)$$

where R (8.31 J/(mol·K)) is the universal gas constant, T (293 K) is the temperature, M_w (18.016 Kg/mol) is the water molar mass and a_w is the water activity which is calculated using an empirical equation for sodium nitrate (Archer, 2000):

(55) $$a_w = \left(\frac{P^0_{H_2O}}{P_{H_2O}}\right)^{-1} = 1 - (w_l^s)^2$$

Where w_l^s is the mass fraction of solute ($NaNO_3$) in the liquid phase.

The sodium-induced microstructural elastic volumetric strain increment is then determined for both the initial and final stages:

(56) $$\varepsilon^e_{CON\_A} = \left(\frac{\beta_A}{\alpha_m}\right) \times \ln\left(\frac{\pi_A + p'}{p'_0}\right)$$

(57) $$\varepsilon^e_{CON\_B} = \left(\frac{\beta_B}{\alpha_m}\right) \times \ln\left(\frac{\pi_B + p'}{p'_0}\right)$$

where p' represents the effective mean stress, and α_m is a material parameter dependent on stress conditions. These equations capture the coupled effect of osmotic suction and mechanical stress on microstructural strain, ensuring a more realistic volumetric response.

Finally, the net chemo-mechanical strain change is computed as:

$$\Delta\varepsilon^{e}_{chemo} = \varepsilon^{e}_{CON\_B} - \varepsilon^{e}_{CON\_A} \quad (58)$$

This equation quantifies the net impact of sodium and calcium exchange on volume change. These refinements improve the model by explicitly considering competitive cation exchange, aligning sodium occupancy with empirical observations, refining osmotic suction representation, and enhancing strain predictions, ultimately ensuring better agreement (see further; Figure 82) with the observed behavior of Boom Clay under chemical loading conditions.

4.3 Determination of mechanical parameters of ACC-2 model

Based on the evolution of mechanical parameters shown in $Chapter\ IV$, it was found that the slope of the critical state line ($\boldsymbol{M_g}$), the stress ratio at the apex of the yield surface ($\boldsymbol{M_f}$), the cohesion ($\boldsymbol{c'}$) and the preconsolidation pressure ($\boldsymbol{p'_c}$) evolve with ionic strength (**IS**) as illustrated in Figure 81. These parameters were fitted based on the experimental data obtained in this study: specifically, the preconsolidation pressures were determined from oedometric tests on BC samples saturated with different saline solutions, while the remaining parameters were derived from triaxial tests performed on BC samples saturated with different saline solutions. Detailed procedures and results can be found in $Chapter\ IV$.

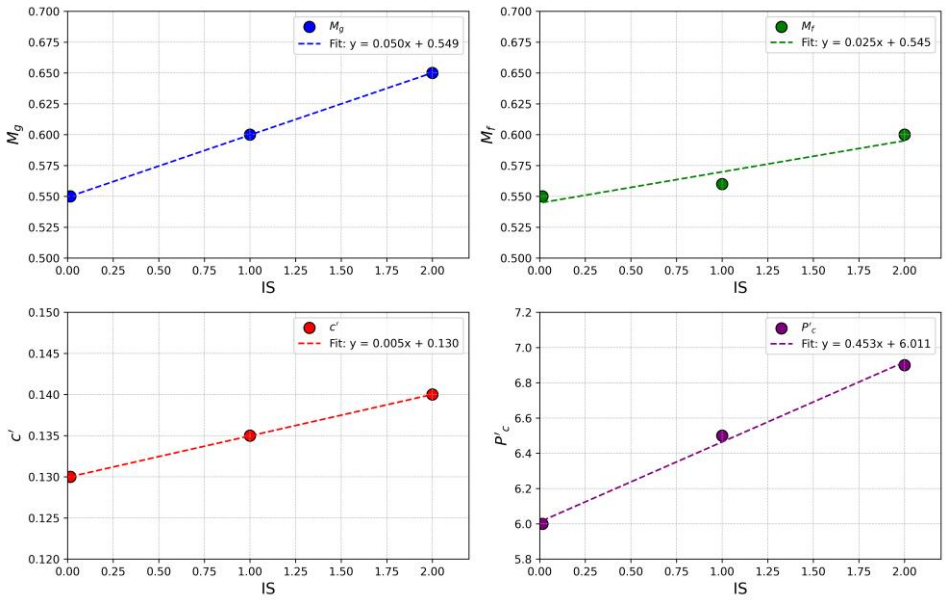

Figure 81 Linear regression of mechanical parameters with respect to IS.

To account for this dependency, analytical functions were introduced, where the subscript **0** represents the initial state before chemical interaction (i.e., IS = 0.015 M), and the subscript **IS** represents the final state after reaching full equilibrium under the influence of ionic strength. The equations governing this evolution are:

(59) $$M_{G\_IS} = M_{G\_0} + \alpha_G \times IS$$

(60) $$M_{F\_IS} = M_{F\_0} + \alpha_F \times IS$$

(61) $$c'_{IS} = c'_0 + \alpha_{c'} \times IS$$

(62) $$p'_{c\_IS} = p'_{c\_0} + \alpha_{p'_c} \times IS$$

Here, M_{G_0}, M_{F_0}, c'_0, and p'_{c_0} represent the initial values of these parameters before considering the effects of IS, while M_{G_IS}, M_{F_IS}, c'_{IS}, and p'_{c_IS} represent their final values after reaching equilibrium with the chemical environment. The coefficients α_G, α_F, $\alpha_{c'}$, and $\alpha_{p'_c}$ determine the sensitivity of each parameter to changes in IS, which itself is a function of sodium and calcium concentrations in solution. The ionic strength (**IS – (M)**) is defined as:

(63) $$IS = \frac{1}{2}\sum_i C_i Z_i^2$$

where C_i (mol/L) is the molar concentration of ion *i* in solution, and Z_i is its valence. This equation quantifies the overall ionic environment of the pore solution, directly affecting the mechanical behavior of Boom Clay. By incorporating these dependencies into the ACC2 model, a more accurate representation of chemo-mechanical coupling is achieved, ensuring that changes in ionic composition are properly reflected in the model's mechanical predictions. Table 32 presents a comprehensive summary of the parameters incorporated into the developed chemical modeling framework.

To provide a comprehensive overview of the parameters utilized in the ACC2 model and the chemo-mechanical formulation developed here, Table 33 presents the key variables and their roles. This table consolidates the essential parameters, clearly distinguishing those that remain constant from those that evolve with ionic strength (IS) to ensure clarity in their interpretation and implementation within the model.

It was observed that the parameters λ (compression index) and κ (swelling index) exhibited negligible variation with IS. This suggests that chemical interactions have minimal impact on these parameters compared to their influence on other mechanical

properties, such as the critical state parameters (M_g and M_f), cohesion (c'), and preconsolidation pressure (p'_c). Consequently, λ and κ were assumed to be independent of IS and treated as constant values in the model. This assumption simplifies the formulation while maintaining consistency with the observed experimental data.

Table 32 Summary of parameters for the developed Chemo-Mechanical model.

Parameter	Value
$\boldsymbol{\alpha_G}$ (-)	0.05
$\boldsymbol{\alpha_F}$ (-)	0.025
$\boldsymbol{\alpha_{p'_c}}$(MPa)	0.453
$\boldsymbol{\alpha_{c'}}$ (MPa)	0.005
$\boldsymbol{\beta_{Na^+}}$ (-)	5

Table 33 Summary of Parameters in the ACC2 Model for synthetic water of BC and the Developed Chemo-Mechanical Formulation.

Parameter description	Symbol	Value	Dependence on IS
Slope of critical state line	M_G (-)	0.55	Dependent
Ratio at the apex of the yield surface	M_f (-)	0.55	Dependent
Controls the shape of the yield surface	k_f (-)	0.7	Independent
Controls the flow rule	k_g (-)	0.9	Independent
Cohesion	c' (MPa)	0.13	Dependent
Preconsolidation pressure	p'_c (MPa)	6	Dependent
Compression index	λ (-)	0.10	Independent
Swelling index	κ (-)	0.04	Independent
controls the contribution of shear plastic strain	A_d (-)	1	Independent
Initial state of the inner yield surface	r_0 (-)	$\frac{p'}{p'_c}$	Independent
controls hardening modulus evolution	s	8	Independent

5. Numerical Verification

In this section, the numerical validation of the newly developed ACC2 model—an adapted Elasto-Chemo-Plastic (ECP) constitutive formulation referred to as ACC2-Chem—is presented. This model was specifically designed to capture the chemo-

mechanical behavior of clayey soils by incorporating the effects of solute concentration and cation occupancy.

To assess the performance and predictive capabilities of the ACC2-Chem model, it was implemented into the finite element software LAGAMINE (Charlier, 1987; Habraken, 1989; Collin et al., 2002), a well-established tool for coupled thermo-hydro-chemo-mechanical simulations in porous media. The numerical simulations were then compared to a comprehensive set of experimental tests, including both salinization/desalinization tests and triaxial compression tests conducted under various chemical and mechanical boundary conditions.

This chapter presents a detailed comparison between simulation results and experimental observations. The objective is to evaluate the ability of the ACC2-Chem model to reproduce the complex chemo-mechanical interactions observed in the laboratory, thereby confirming its validity and potential for predictive modeling of geo-environmental problems.

5.1 Salinization/Desalinization simulations

In this section, the verification of the developed Chemical model is presented through a comparison between its analytical zero-dimensional (0D) formulation, numerical simulations conducted using the finite element software LAGAMINE, and the experimental results obtained from salinization/desalinization laboratory tests performed under oedometric conditions (Al Mais et al., 2025b). The developed Chemical model is formulated to predict the chemo-mechanical behavior of Boom Clay under varying ionic strengths and sodium occupancies, specifically capturing the evolution of chemical volumetric strains while assuming a fully elastic and reversible response. Both the analytical and FEM-based versions of the model produce elastic, reversible results for all confining pressures considered, in line with the theoretical assumptions of the model. In analytical formulation the mean effective stress (p') was assumed to be always constant.

Figure 82 (a–d) illustrates the comparison between the three approaches across four levels of effective confining pressure: 2.25 MPa, 1.6 MPa, 0.8 MPa, and 0.4 MPa. The experimental data shown in the figures (solid lines) represent the final values of volumetric strain measured under oedometric conditions, recorded after the full percolation of the pore volume for each injected solution. These values correspond to

a complete salinization/desalinization cycle consisting of the following sequence: 0.015 M (point 0)→ 60%–1.0 M (point 1)→ 60%–2.0 M (point 2)→ 90%–2.0 M (point 3)→ 60%–2.0 M (point 4)→ 60%–1.0 M(point 5). At $p' = 2.25\,MPa$ (Figure 82a), the numerical results from LAGAMINE and the analytical model align very closely and exhibit good agreement with the experimental data. The model successfully reproduces the small, fully recoverable chemical volumetric strain observed after one complete salinization/desalinization cycle under high effective stress. The minor strain magnitude, around 0.15%, also supports the understanding that at this stress level, chemical perturbations have a limited influence due to the dominance of mechanical confinement.

For $p' = 1.6\,MPa$ and $0.8\,MPa$ (Figure 82b and Figure 82c), both the analytical and FEM simulations continue to display consistent, reversible behavior. However, a slight divergence begins to appear between the analytical and LAGAMINE results, although the overall agreement with the experimental trends remains acceptable. This minor difference between the analytical and LAGAMINE should be expected as correct boundary conditions can be applied in the FEM simulation unlike the analytical formulation, which has no spatial component.

At the lowest confining pressure of $p' = 0.4\,MPa$ (Figure 82d), the discrepancy between the analytical and FEM simulations becomes more pronounced, and both models deviate more significantly from the experimental data. Two key factors explain this divergence. First, the FEM simulation's boundary conditions prevent any lateral displacement, whereas in the laboratory tests, the clay specimen undergoes lateral contraction due to physicochemical shrinkage, particularly under low mechanical confinement. This shrinkage generates a reduction in mean effective stress (p') and induces lateral forces that are accounted for in oedometric FEM modeling. As a result, the constrained FEM conditions lead to an underestimation of the actual strain, explaining the difference between the analytical and numerical results.

Second, at such low confining pressures, the material is more susceptible to plastic deformation triggered by high ionic strength, a behavior not captured by the chemical model since it is formulated as purely elastic. The observed irreversible strain in the experimental data at 0.4 MPa is therefore beyond the scope of the model's capabilities. This limitation highlights the necessity of incorporating plasticity into the model if it is

to be used for low-stress scenarios, where chemomechanical interactions are more prominent.

It is important to note that the high ionic strengths considered in this study (1.0 M and 2.0 M) were intentionally selected to investigate the broader chemical response of Boom Clay and to deepen the understanding of its behavior under extreme chemical loading scenarios. However, recent diffusion-transport simulations (Jacques et al., 2024) have shown that the ionic strength of the saline plume diffusing from bituminized waste near the concrete liner in a geological disposal environment is unlikely to exceed 0.1 M. At such lower ionic strengths, the chemical influence on volumetric strain is minimal or even negligible, particularly under typical in situ effective stress conditions (~2.25 MPa). Consequently, although the model shows limitations under low stress and high ionic strength conditions, its underlying assumptions remain valid and applicable within the realistic boundaries of deep geological repository scenarios.

Future developments of the chemical model for broader geotechnical applications should consider extending the formulation to incorporate plastic strains to better capture the behavior observed under low-stress, high-salinity conditions. One potential approach would involve establishing a functional link between the elastic strain of the microstructure and the plastic strain of the macrostructure, as suggested by Guimarães et al. (2013), thereby enabling a more comprehensive and accurate representation of chemo-mechanical interactions in Boom Clay.

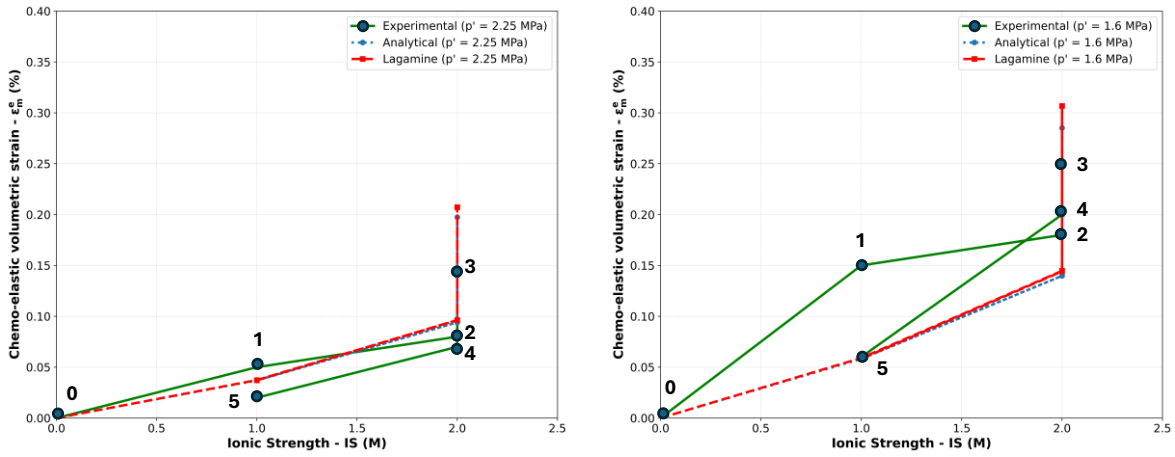

(a) (b)

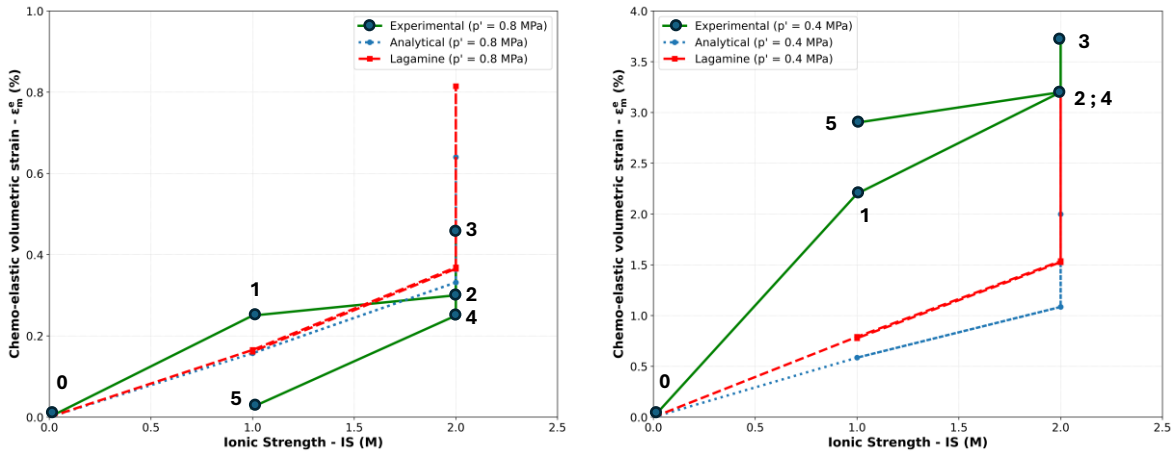

(c) (d)

Figure 82 Comparison of analytical and fem-based chemical model predictions with experimental results for salinization/desalinization cycles under oedometric conditions at various effective stresses.

5.2 Triaxial simulations

In this section, the shearing phase of the undrained triaxial experiments conducted under various final confining stresses and ionic strengths is analyzed. The results of the numerical simulations obtained using the ACC2-Chem model are presented alongside the corresponding experimental data to enable direct comparison and evaluation of the model's predictive performance.

In addition to the stress–strain responses, the stress paths followed during the shearing phase are examined with respect to their associated yield surfaces. This analysis provides further insight into the chemo-mechanical behavior of the material and serves to test the accuracy of the ACC2-Chem model in capturing the observed experimental trends under different chemical and mechanical conditions.

Figure 83(a, b) presents the results of undrained triaxial tests performed at three effective confining pressures (1.0, 2.25, and 4.5 MPa), with samples saturated using the BC synthetic solution (ionic strength: 0.015 M). Figure 83a shows the evolution of deviator stress with axial strain, while Figure Figure 83b illustrates the corresponding pore water pressure development.

The numerical predictions using the ACC2-Chem model show good overall agreement with the experimental results. Key features of Boom Clay behavior, including the initial elastic response—evident in the early slopes of both the $q - \varepsilon_a$ and $\Delta u - \varepsilon_a$ curves—and the peak values of deviator stress and pore pressure, are well captured.

However, at the lowest confining pressure (1.0 MPa), the model does not fully replicate the post-peak softening observed experimentally. The sudden drop in deviator stress is underestimated, which may be attributed to the current selection of model parameters, particularly the elastic parameter κ (slope of the swelling line) and the plastic parameter λ (slope of the compression line). Reducing the difference $\lambda - \kappa$ would enhance softening behavior, improving agreement with the observed mechanical response, as suggested by the hardening rule defined in Equation (15).

Figure 84 (a, b) and Figure 85 (a, b) extend this analysis to samples saturated with solutions of higher ionic strengths (1.0 M and 2.0 M, respectively). Across both chemical conditions, the model continues to reflect the experimental trends with a high degree of accuracy. It effectively reproduces the elastic region (for $\varepsilon_a < 1\%$) and provides coherent predictions of peak deviator stress and pore pressure values.

This consistent agreement across a range of ionic strengths highlights the robustness of the ACC2-Chem model in capturing the coupled chemo-mechanical behavior of Boom Clay. It underscores the relevance of incorporating chemical effects, such as solute concentration and cation occupancy, into constitutive modeling for geotechnical applications involving chemically active environments.

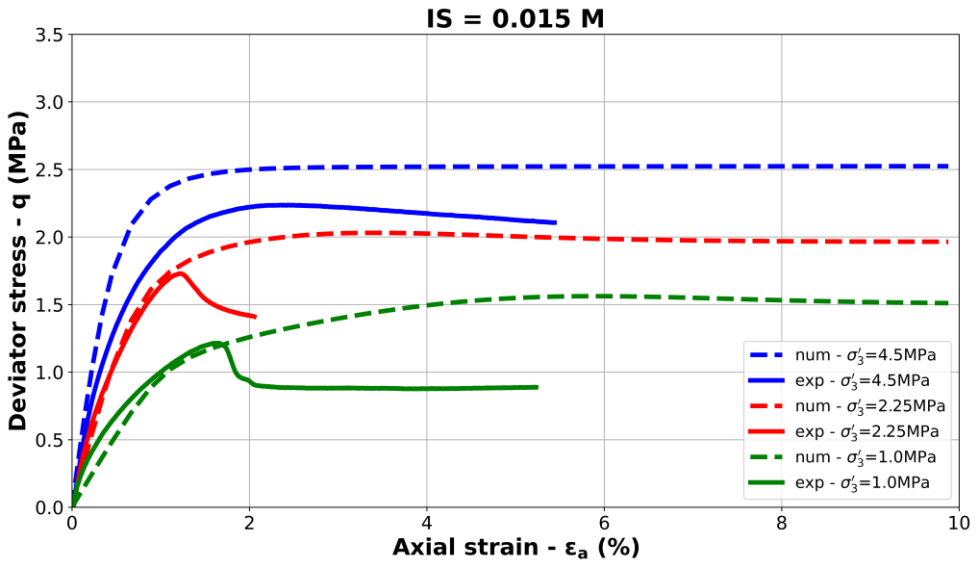

(a)

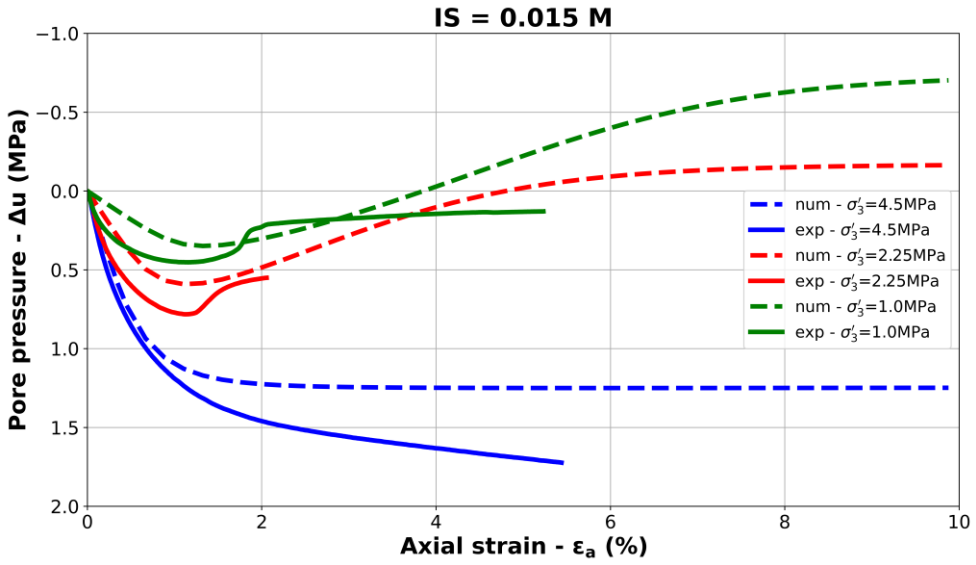

(b)

Figure 83 Comparison between experimental and numerical results for undrained triaxial tests at different effective confining pressures (1.0, 2.25, and 4.5 MPa) with BC synthetic solution (IS = 0.015 M): (a) Deviator stress vs axial strain, (b) Pore water pressure.

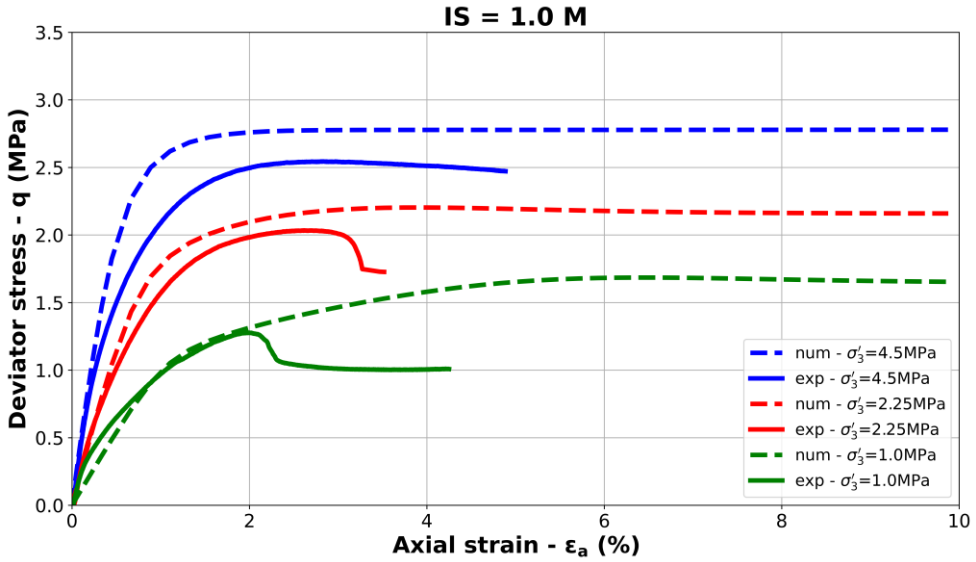

(a)

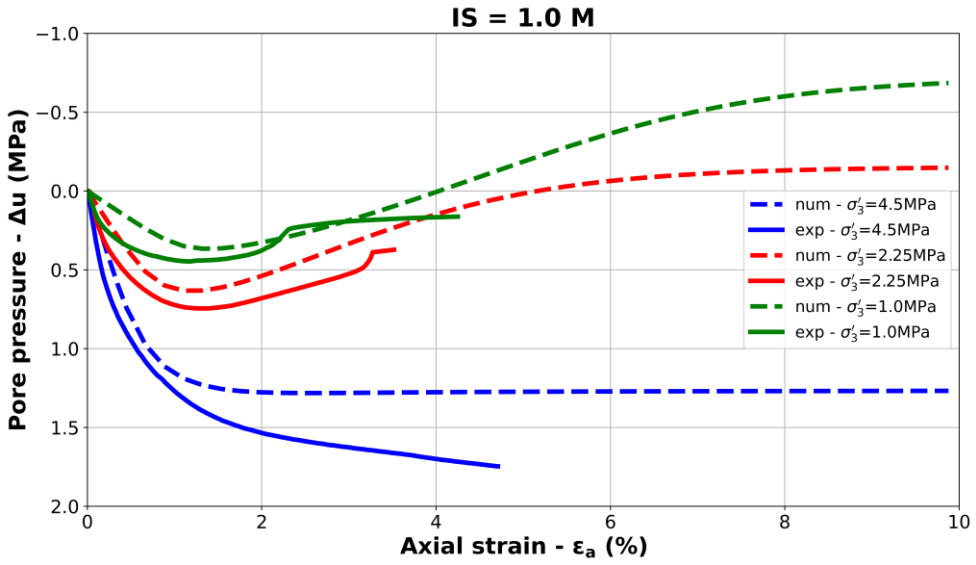

(b)

Figure 84 Comparison between experimental and numerical results for undrained triaxial tests at different effective confining pressures with BC synthetic solution (IS = 1.0 M): (a) Deviator stress vs axial strain, (b) Pore water pressure vs axial strain.

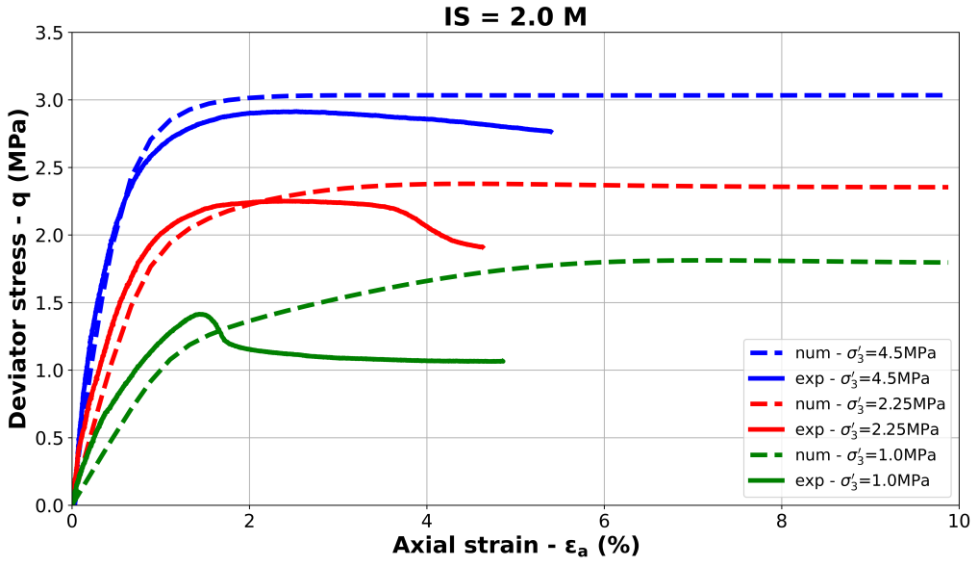

(a)

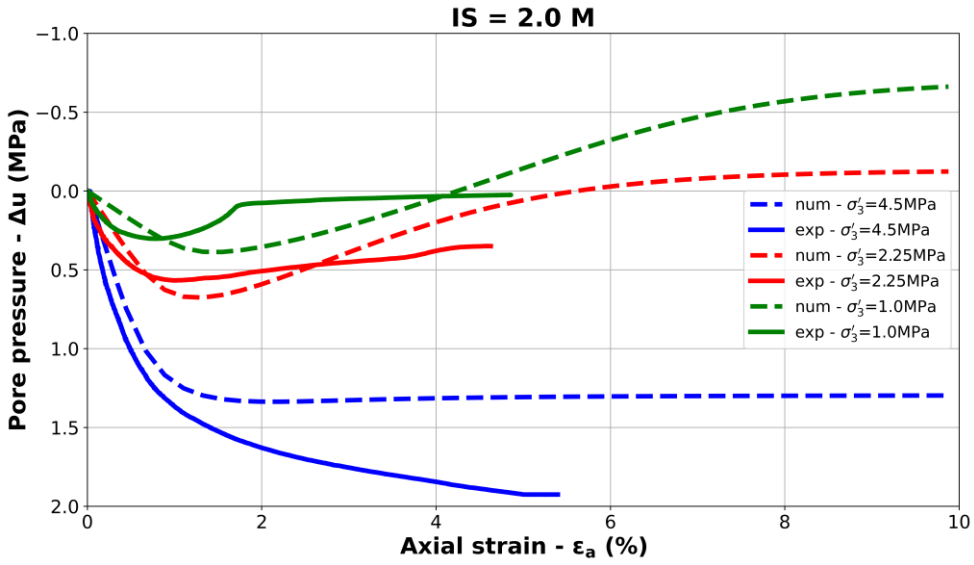

(b)

Figure 85 Comparison between experimental and numerical results for undrained triaxial tests at different effective confining pressures with BC synthetic solution (IS = 2.0 M): (a) Deviator stress vs axial strain, (b) Pore water pressure vs axial strain.

Figure 86 (a, b, c) presents the comparison between numerical simulations and experimental results of stress paths obtained from undrained triaxial tests conducted at three ionic strengths: 0.015 M, 1.0 M, and 2.0 M. Each subfigure corresponds to a specific ionic strength and includes results for three different effective confining pressures. The corresponding Critical State Lines (CSL) for each solution are also plotted as black lines.

The simulated stress paths show good agreement with the experimental data, reinforcing the ability of the ACC2-Chem model to capture the chemo-mechanical response of Boom Clay under various chemical and mechanical conditions. As expected for undrained conditions, the stress path initially follows a nearly vertical trajectory due to undrained conditions (constant volume).

The subsequent evolution of the stress path depends on the initial overconsolidation ratio (OCR) and the stress history of the sample. For overconsolidated samples ($\sigma_3' = 1.0 \,\&\, 2.25\ MPa$), a softening response is typically observed, with the stress path bending to the right before intersecting the corresponding CSL. In contrast, normally consolidated samples ($\sigma_3' = 4.5\ MPa$), exhibit a hardening response, with the stress path curving to the left before reaching the CSL. This behavior is well captured in the simulations, which reflect both the mechanical history and the influence of ionic strength on the clay behavior.

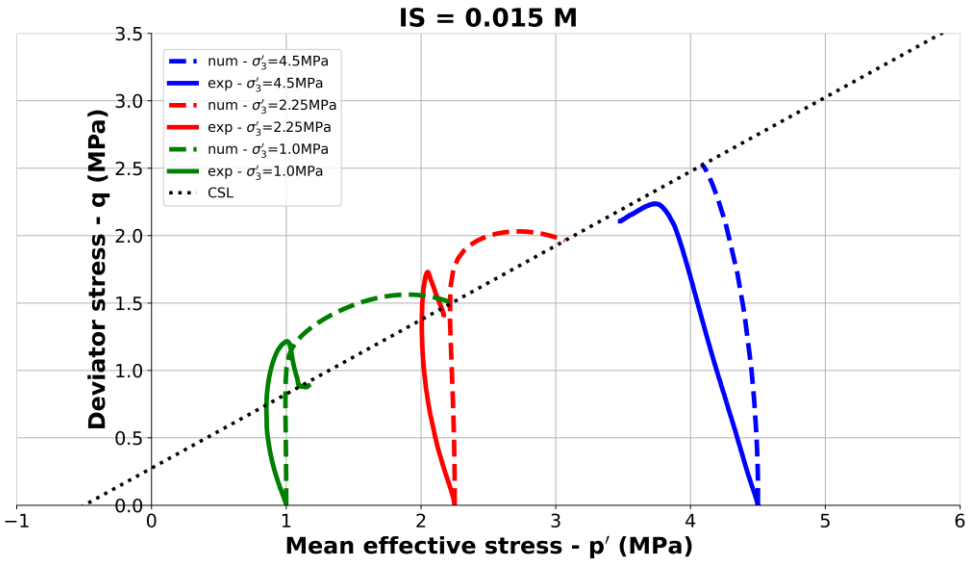
IS = 0.015 M
num - σ'_3=4.5MPa
exp - σ'_3=4.5MPa
num - σ'_3=2.25MPa
exp - σ'_3=2.25MPa
num - σ'_3=1.0MPa
exp - σ'_3=1.0MPa
CSL
Deviator stress - q (MPa)
Mean effective stress - p′ (MPa)

(a)

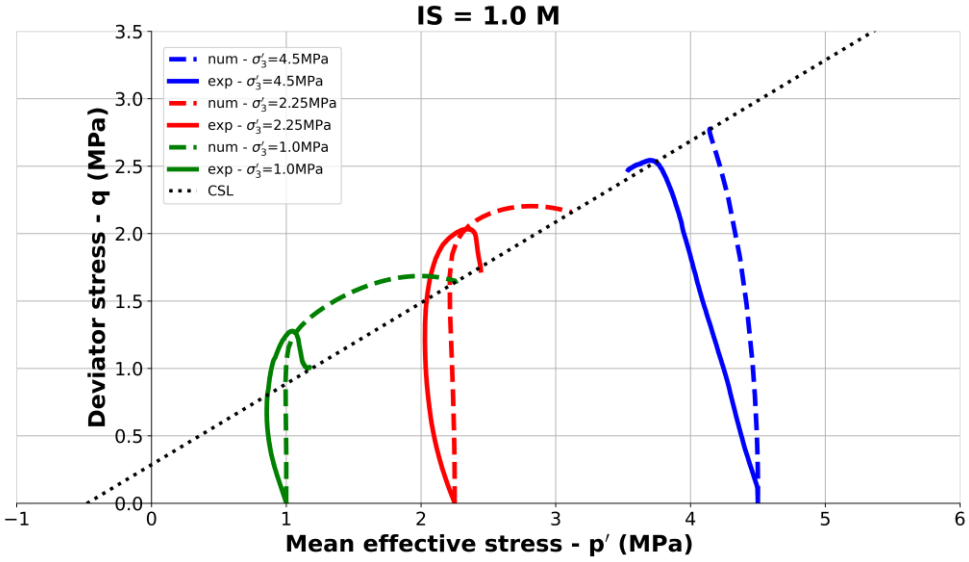
IS = 1.0 M
num - σ'_3=4.5MPa
exp - σ'_3=4.5MPa
num - σ'_3=2.25MPa
exp - σ'_3=2.25MPa
num - σ'_3=1.0MPa
exp - σ'_3=1.0MPa
CSL
Deviator stress - q (MPa)
Mean effective stress - p′ (MPa)

(b)

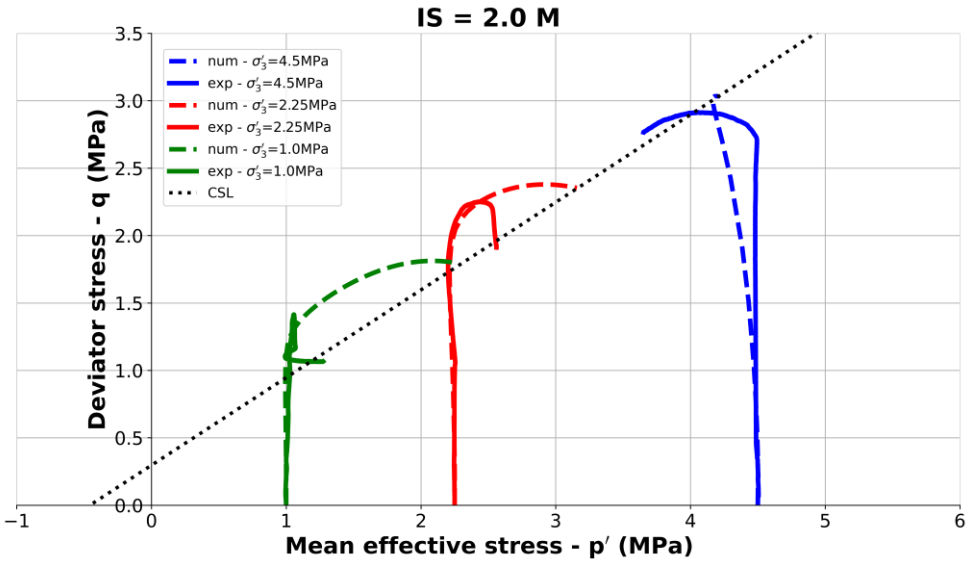

(c)

Figure 86 Comparison of numerical and experimental stress paths from undrained triaxial tests at three different ionic strengths: (a) IS = 0.015 M, (b) IS = 1.0 M, (c) IS = 2.0 M. Each figure includes results for various effective confining pressures and the corresponding CSL.

5.3 Parametric study

In this section, a comprehensive parametric study is carried out to investigate the sensitivity of the ACC2-Chem model to key non-mechanical parameters, particularly the hardening parameter s and the chemical coupling parameter A_d. The objective is to evaluate how variations in these parameters affect the model's predictive behavior and to gain deeper insight into their roles on the chemo-mechanical response of Boom Clay.

The first part of the study focuses on the influence of s, which governs the evolution of the hardening modulus with accumulated plastic strain and thus directly impacts the shape of the stress-strain curve within the yield surface. Figure 87(a–f) present the results of simulations performed by varying s across several orders of magnitude, from $s = 1$ to $s = 1000$, while maintaining $A_d = 1$ and using the BC synthetic solution with an ionic strength of 0.015 M. All other model parameters are kept constant as listed in Table 2.

Figure 87(a–d) illustrate the response in the $q - \varepsilon_a$ (deviator stress versus axial strain) and $\Delta u - \varepsilon_a$ (pore water pressure versus axial strain) planes for different values of s. As s increases, the transition between elastic and plastic behavior becomes more abrupt, resulting in a sharper and more pronounced yield point. At high values such as $s =$

1000, the model response resembles that of conventional elastic-plastic models like Modified Cam-Clay (MCC), with a distinct and immediate onset of plasticity. In contrast, lower values of s (e.g., $s = 1$) produce a much smoother transition, where plastic strains are gradually mobilized, reflecting a more progressive evolution of inelastic behavior.

Figure 87(e) and (f) focus on the post-peak softening behavior under relatively low confining pressures (e.g., 1.0 MPa). These results indicate that varying s has only a limited effect on the softening phase of the stress-strain curve. The degree of softening—observed as a reduction in deviator stress after the peak—is not significantly modified by changes in s alone. Instead, the softening response appears to be more sensitive to other parameters, particularly the swelling line slope κ, or the difference between the plastic compression line slope λ and κ. A smaller difference between these two parameters results in a softer hardening modulus and promotes more pronounced softening in the post-peak regime.

These observations suggest that while s primarily controls the sharpness of the elastic-plastic transition, it does not govern the post-peak behavior of the material. This distinction is important for the calibration of the model when targeting either yield onset or post-yield softening.

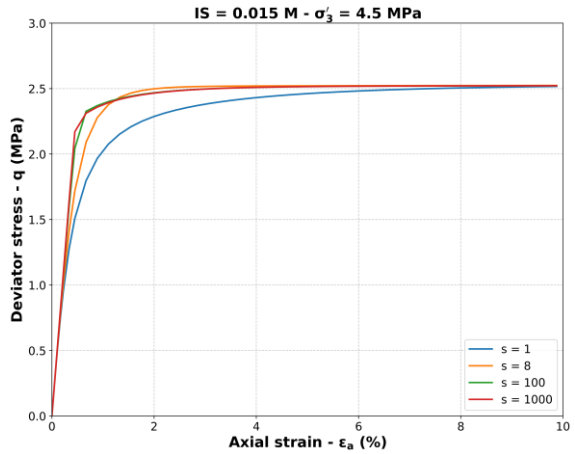

(a)

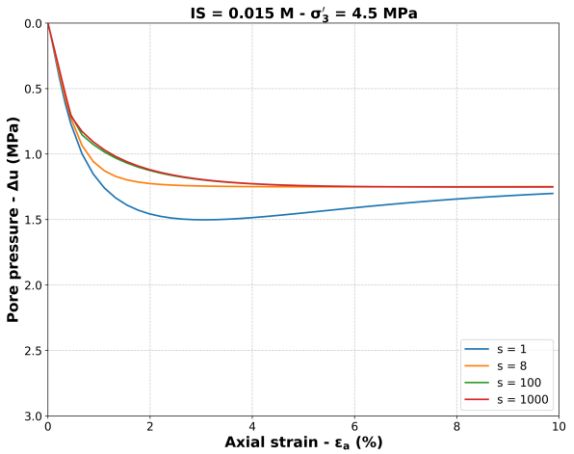

(b)

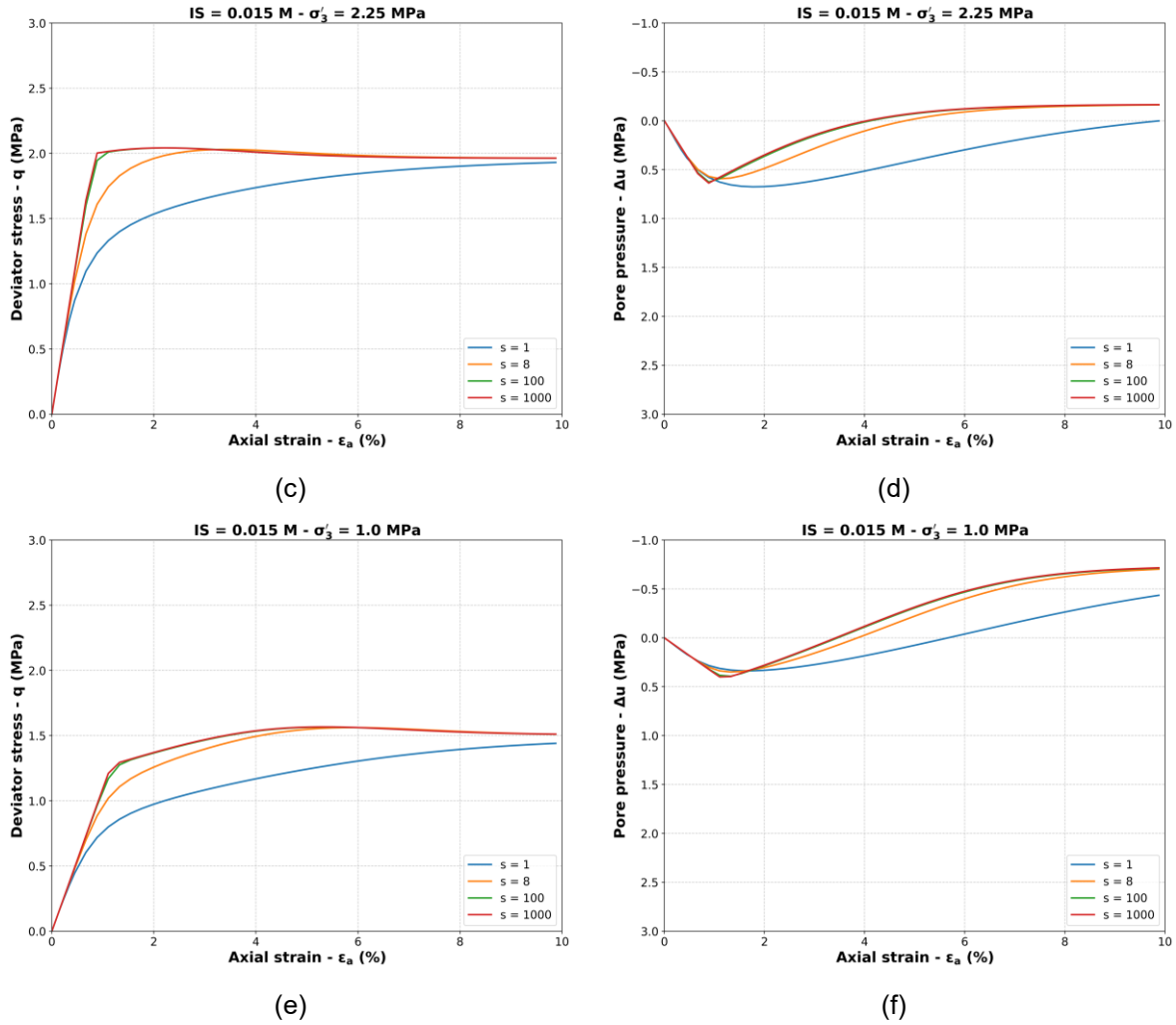

Figure 87 Influence of the hardening parameter s on the chemo-mechanical response of Boom Clay at various confining pressures ($p' = 2.25, 1.6, 0.8, and\ 0.4\ MPa$): Deviator stress–axial strain ($q-\varepsilon_a$) and pore water pressure–axial strain ($\Delta u-\varepsilon_a$) responses for varying s (1 to 1000), with fixed A_d = 1 and IS = 0.015 M.

In addition to the parameter s, the influence of the parameter A_d (which controls the contribution of deviatoric strain) on the behavior of Boom Clay is examined. A_d plays a key role in modulating the transition between elastic and plastic deformation by controlling the extent to which deviatoric strain affects the stress-strain response. To investigate the effect of A_d, simulations were performed with varying values of A_d (0.1, 0.5, 1.0, and 2.0) while keeping the parameter s fixed at 8. The simulations were conducted using the BC synthetic solution (IS = 0.015 M) and were carried out under three different confining pressures: 4.5 MPa, 2.25 MPa, and 1.0 MPa. The results of these simulations are presented in Figure 88(a–f), which shows the deviator stress versus axial strain ($q-\varepsilon_a$) and pore water pressure versus axial strain ($\Delta u-\varepsilon_a$) for each value of A_d.

At higher confining stresses (4.5 MPa), the influence of A_d is minimal. In this case, the transition from elastic to plastic behavior remains smooth across all values of A_d, with the least curvature observed for $A_d = 0.1$. This suggests that, under high confining pressure, the contribution of deviatoric strain controlled by A_d has a negligible effect on the overall stress-strain behavior. The material's response is largely governed by the confining pressure, with A_d playing a secondary role in influencing the elastic-to-plastic transition. However, at lower confining stresses (2.25 MPa and 1.0 MPa), the effect of A_d becomes more pronounced. Specifically, for $A_d = 0.1$, there is a sharp transition from elastic to plastic behavior, indicating a more abrupt shift in the material's response (see Figure 88(c-f)). In contrast, for values of A_d greater than 1.0, the transition between elastic and plastic phases becomes more gradual. This trend is particularly noticeable at 2.25 MPa and 1.0 MPa, where the parameter A_d clearly influences the smoothness of the elastic-plastic transition. Higher values of A_d result in a smoother transition, indicating a more gradual progression from elastic to plastic deformation.

The evolution of pore water pressure with respect to axial strain, shown in Figure 88(d) and Figure 88(f), further illustrates the effect of A_d. It can be observed that the pore pressure response is also affected by the value of A_d, with higher values of A_d leading to a more gradual increase in pore pressure. This is consistent with the smoother transition observed in the deviator stress response, supporting the idea that A_d governs the sharpness of the elastic-plastic transition. From these simulations, it can be concluded that A_d primarily controls the smoothness of the transition from elastic to plastic behavior, rather than significantly affecting the overall hardening or softening characteristics of the material. The value of A_d influences how abruptly or gradually the material shifts from elastic to plastic deformation under varying confining pressures, with lower values of A_d resulting in a sharper transition and higher values leading to a smoother one. However, A_d does not have a substantial effect on the material's softening or hardening behavior, particularly under typical confining pressures. Based on these results, it can be concluded that A_d = 1.0 provides a good balance for accurately capturing the elastic-plastic transition without significantly altering the material's overall stress-strain response.

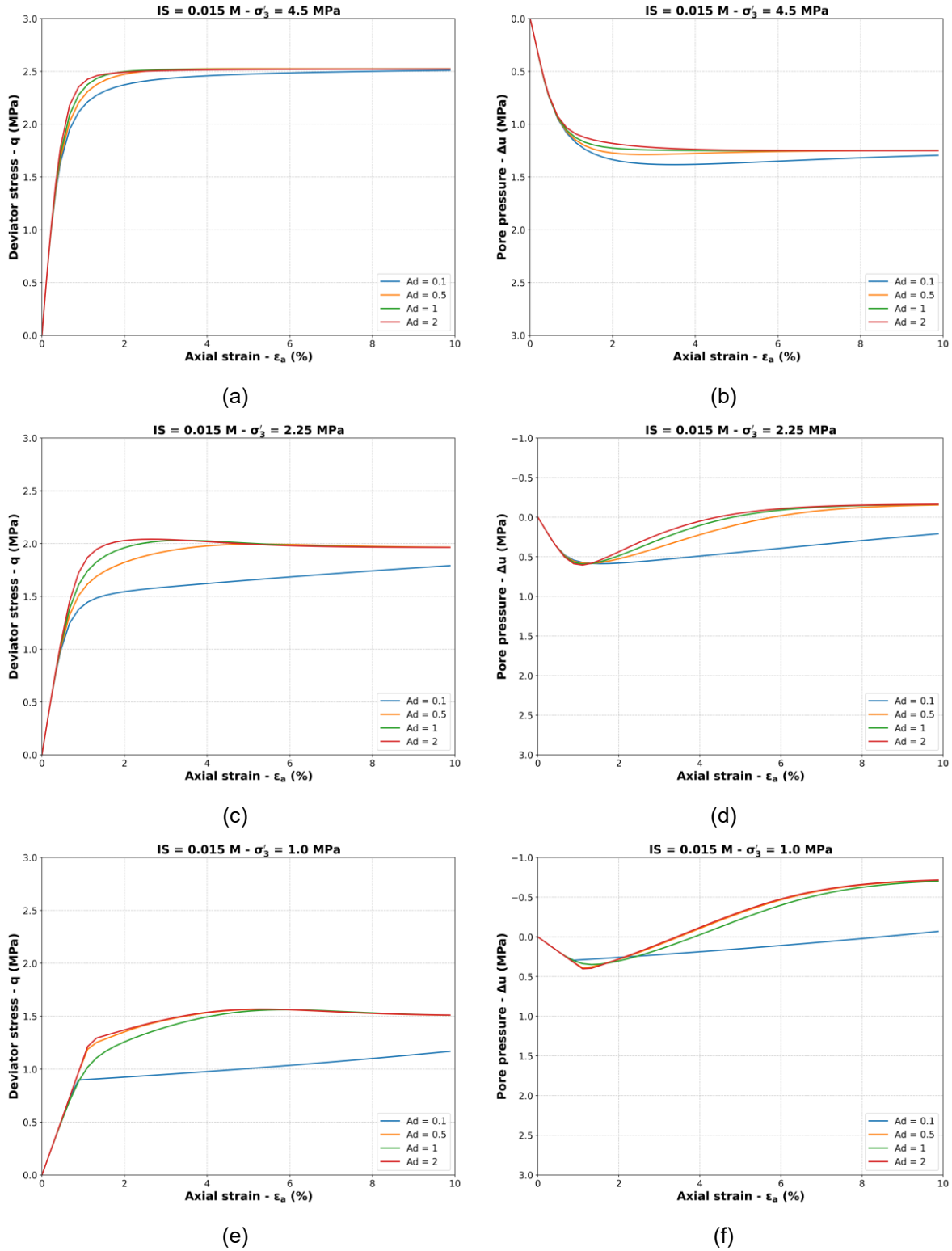

Figure 88 Influence of varying A_d values on deviator stress ($q - \varepsilon_a$) and pore water pressure ($\Delta u - \varepsilon_a$) response under different confining pressures (4.5 MPa, 2.25 MPa, and 1.0 MPa) with constant s = 8 and BC synthetic solution (IS = 0.015 M).

In order to provide a more comprehensive understanding of the ACC2-Chem model's behavior, particularly under low confining pressures, additional simulations were conducted to explore the role of the parameter κ (kappa), which represents the slope

of the swelling line. As previously discussed, at low confining stresses (e.g., 1.0 MPa), the softening behavior in the $q-\varepsilon_a$ (deviator stress versus axial strain) plane was not clearly captured (Figures Figure 83a, Figure 84a and Figure 85a). To further investigate this limitation, Figure 89(a, b) presents the results of simulations performed using three different values of κ: 0.04, 0.06, and 0.08. All other parameters were kept constant, as defined in Table 2, with the plastic compression slope λ fixed at 0.10 for all cases.

The results demonstrate that increasing κ leads to a reduction in the elastic stiffness, as evidenced by the decreasing slope of the initial elastic portion of the stress-strain curve. This trend is particularly visible when κ is set to 0.08, where the initial stiffness is noticeably lower compared to the case with $\kappa = 0.04$. More importantly, a higher κ value results in a more pronounced softening behavior in the $q-\varepsilon_a$ response. Specifically, for $\kappa = 0.08$, a clear peak in deviator stress is followed by a progressive decrease, indicating post-peak softening. This softening effect becomes more distinct as κ increases.

This behavior can be explained by considering the hardening law of the model, in which the evolution of the preconsolidation pressure p_c' is governed by the difference $\lambda - \kappa$. When κ increases while λ remains constant, the difference $\lambda - \kappa$ becomes smaller. This leads to a higher rate of hardening, as a smaller denominator amplifies the increment in p_c' for a given plastic volumetric strain. This stronger hardening contributes to the development of a clearer peak in the stress-strain curve, followed by softening. Therefore, the value of κ not only affects the elastic stiffness (i.e., the slope of the unloading-reloading line) but also plays a critical role in shaping the overall stress-strain response, especially under low confining pressures where softening is more likely to be observed. These findings highlight either a potential limitation in the constitutive model or uncertainties in the parameter calibration process, particularly regarding the definition of κ, which has a clear experimental basis and should remain within a defined confidence interval—especially in low-stress regimes where softening behavior becomes more pronounced.

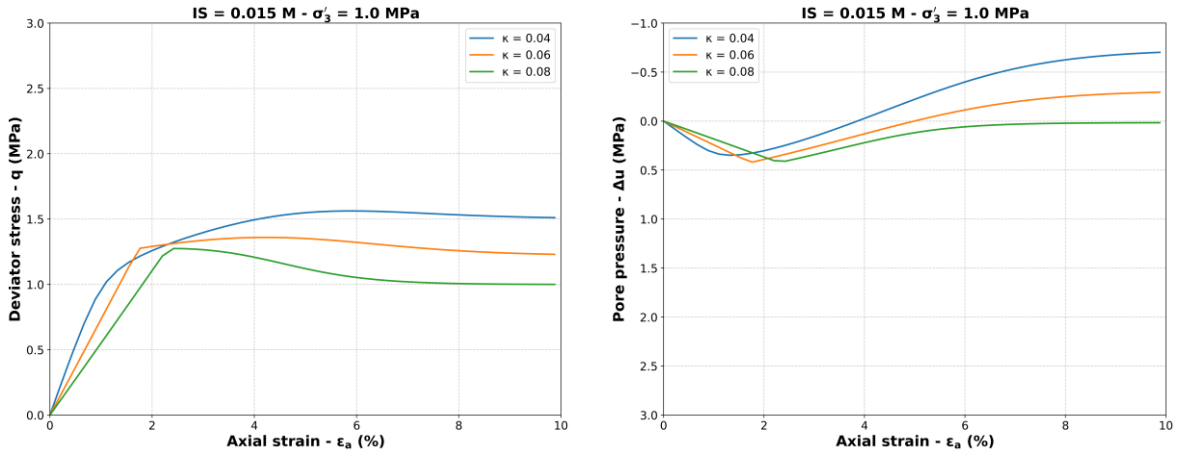

(a) (b)

Figure 89 Effect of the swelling line slope (κ) on the stress–strain and pore pressure response of Boom Clay under low confining pressure (1.0 MPa) using the ACC2-Chem model (λ = 0.1, IS = 0.015 M).

One important implication of these findings is that the parameter κ—traditionally assumed to be constant—may, in fact, benefit from being modeled as stress-dependent. Given its dual role in controlling both elastic stiffness and the hardening rate, introducing a formulation where κ evolves with confining pressure or the stress state could significantly enhance the model's ability to reproduce the observed stress–strain behavior, particularly in low-stress regimes where softening is more likely to occur. These findings also raise the question of whether the current ACC-2 framework adequately captures the volumetric response of Boom Clay. Alternatively, refining the hardening law to account for nonlinearity—by incorporating additional dependencies on stress level, strain history, or chemical conditions—could provide a more robust framework for simulating the chemo-mechanical behavior of Boom Clay. Such enhancements would allow for a more accurate representation of the transition from hardening to softening, ultimately improving the predictive performance of the ACC2-Chem model across a wider range of loading conditions.

6. Conclusion

This chapter provided a comprehensive presentation and development of the ACC-2 chemo-hydro-mechanical model, aimed at enhancing its ability to simulate the behavior of Boom Clay under combined mechanical and chemical loading conditions. The first part of the chapter offered a detailed overview of the original ACC-2 model, introducing its main constitutive equations and mechanical framework. To improve the accuracy of the yield surface and plastic flow under different stress conditions, a cohesion term was incorporated into both the yield surface and flow rule. This

modification allowed for a more realistic representation of the material's behavior, especially in scenarios where cohesive strength plays a significant role.

The chapter then introduced the chemical double-porosity model initially developed by Guimarães et al. (2013), which captures the impact of ionic strength and pore-scale chemical interactions on the hydro-mechanical behavior of clays. Limitations of this model were discussed, particularly its oversimplified representation of chemical effects on mechanical behavior. To address this, a more refined formulation was proposed, including an improved calculation of the sodium occupancy ratio and a new logarithmic expression for the chemical parameter α_m, making it dependent on both ionic strength, Na/Ca occupancy and effective stress. These enhancements allow the model to better account for chemical effects, particularly during changes in both occupancy ionic strength.

The revised chemo-mechanical model was implemented into the ACC-2 framework and integrated within the finite element code LAGAMINE. Verification of the model was carried out through simulations of experimental results, particularly focusing on salinization/desalinization tests and undrained triaxial compression tests. The model successfully reproduced the key features observed in these experiments. Notably, it was shown that the elastic chemical strain formulation is sufficient to capture the response during salinity cycles. However, for lower confining stresses, the absence of plastic chemical strains may limit the model's predictive capacity—highlighting the need for future development in this direction.

Finally, a parametric study was performed to deepen the understanding of the model's behavior and to assess its sensitivity to key parameters. The role of the non-mechanical parameters s and A_d was investigated in terms of their influence on the elastic-to-plastic transition and the hardening-softening response. The parameter s was shown to govern the sharpness of the transition, while A_d affected the contribution of deviatoric strain without significantly altering the hardening behavior. In addition, the effect of the swelling line slope κ was explored. It was observed that increasing κ enhances the softening behavior, particularly under low confining stresses. While κ is traditionally defined as a constant parameter with a clear experimental basis, these results suggest that the current formulation may not fully capture the stress-dependent volumetric response of Boom Clay. Therefore, rather than modifying κ itself, future

improvements to the model could involve adopting an alternative definition of the bulk modulus or developing a more advanced hardening law for p_c' those accounts for stress-dependent behavior. Such refinements would enhance the model's ability to represent the complex softening behavior observed experimentally.

VI. Repository scale simulations

1. Introduction

In the context of deep geological disposal of radioactive waste, particular attention must be given to intermediate-level long-lived bituminized waste (classified as Category B waste), such as Eurobitum, which contains high concentrations of soluble salts—primarily sodium nitrate ($NaNO_3$).

Figure 90 presents a schematic overview of the Belgian deep geological repository concept, as provided by ONDRAF/NIRAS. It illustrates the Engineered Barrier System (EBS) designs for both high-level (Category C) and intermediate-level long-lived (Category B) radioactive waste. The layout highlights the use of Monolith B structures for Category B waste and Supercontainers for Category C waste, each placed in separate horizontal disposal galleries. These galleries are spaced 50 meters apart for Category B waste and 120 meters apart for Category C waste, respectively, within the host formation.

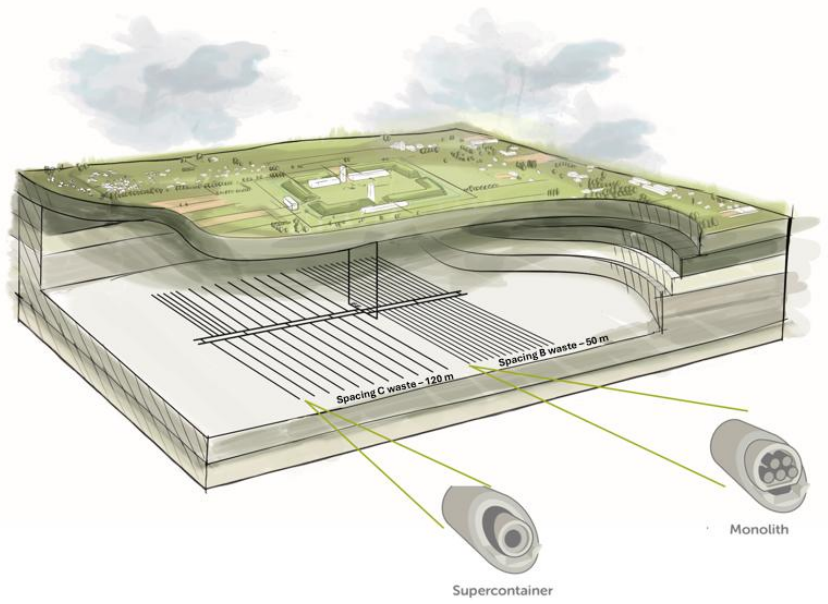

Figure 90 Schematic view of deep geological repository and the Belgian concept for the EBS of HLW and ILW (ONDRAF/NIRAS, 2020).

Over several hundred years, groundwater is expected to infiltrate the repository and come into contact with this waste, leading to significant swelling of the Eurobitum and the subsequent diffusion of a concentrated saline plume through the engineered barriers and into the surrounding Boom Clay (BC) formation. These processes are likely to induce coupled chemo-hydro-mechanical (CHM) perturbations in the host clay,

potentially compromising its integrity and barrier function around the disposal galleries. Given the importance of these long-term interactions, this chapter presents a detailed numerical investigation of the CHM effects of Eurobitum waste swelling and saline plume diffusion on the behavior of Boom Clay at the repository scale. The simulations were carried out in two dimensions using the finite element method (FEM) software LAGAMINE (Collin et al., 2002), incorporating the newly developed ACC2-Chem constitutive model introduced in the previous chapter. The analysis considers the phenomenological evolution of the repository over time, divided into four main phases: (1) the gallery excavation phase occurring over a single day; (2) a 100-year operational phase under drained conditions; (3) a 300-year post-operational equilibrium phase; and (4) a 500-year swelling phase simulating the long-term interaction between waste and surrounding clay. In the final phase, swelling is represented by imposing radial displacements on the intrados of the concrete liner to simulate the mechanical expansion of the waste. To evaluate the individual and combined effects of mechanical and chemical perturbations, several simulation scenarios were explored: one including only mechanical swelling, another incorporating both swelling and saline plume diffusion, and an additional case involving pure chemical diffusion without swelling. These variations allow for a comprehensive assessment of the influence of each component—mechanical swelling and chemical diffusion—on the hydro-mechanical behavior of Boom Clay, contributing to a better understanding of its long-term performance under repository conditions. It is important to emphasize that the release of high chemical concentrations in this model is entirely hypothetical and does not represent actual repository conditions. Chemical numerical simulations have shown that the chemically perturbed zone is limited to approximately 0.19 meters, and the maximum ionic strength observed is around 0.1 M—concentrations that are too low to significantly affect the hydro-mechanical behavior of Boom Clay (Jacques et al., 2024). Consequently, higher concentrations and a broader perturbation zone (3 meters) are intentionally used in this study to amplify the chemical effects and enable a more pronounced assessment of chemo-hydro-mechanical interactions in the model (see detailed justification in the following sections).

2. 2D plane strain modelling

2.1 Geometry

This section describes the geometry and meshing strategy adopted for the 2D plane strain simulations of the waste disposal system. The computational domain, illustrated in Figure 91, represents a vertical cross-section of a single disposal gallery used for Category B waste, as described earlier (ONDRAF/NIRAS, 2020). These galleries are part of a network spaced 50 meters apart. Due to symmetry, the model covers half the inter-gallery distance, resulting in a total width of 25 meters and a height of 50 meters. This configuration captures the essential features of the disposal system and the surrounding Boom Clay host formation.

At the lower left edge of the model lies the excavation zone representing the cylindrical waste gallery. The inner radius of this gallery, measured to the intrados of the concrete liner, is set at 1.5 meters. This dimension corresponds to the space required to accommodate five Eurobitum waste drums arranged side by side, as specified in the monolithic disposal system design (each drum having a diameter of approximately 1.885 meters; ONDRAF/NIRAS, 2020). Surrounding the gallery is a concrete liner with a thickness of 0.3 meters, resulting in an outer radius of 1.8 meters.

To represent realistic excavation and construction conditions, the model includes an over-excavation of 0.075 meters. This over-excavation accounts for the expected convergence of the Boom Clay before the concrete liner is installed. It is assumed that the liner is placed after the surrounding clay has deformed and closed this gap under in-situ stress conditions. The convergence is managed through an interface element, allowing the deformation to match the imposed over-excavation. This process is illustrated by the transition from Figure *91*a to Figure *91*b.

Surrounding the concrete liner, a 3-meter-thick *perturbated zone* is included to simulate the zone of Boom Clay expected to undergo significant chemo-mechanical alteration. This alteration results from the long-term swelling of the Eurobitum waste and the diffusion of high concentrations of dissolved salts, such as $NaNO_3$, into the surrounding clay. With the inclusion of this disturbed zone, the total modeled radius from the gallery center reaches approximately 4.875 meters.

The entire 2D domain is discretized using 1,800 quadrilateral elements, each with four nodes and four Gauss integration points. To capture the strong gradients of stress, strain, pore pressure, and chemical concentration near the excavation and in the perturbed zone, mesh refinement is applied in these critical regions. This localized refinement enhances numerical accuracy and stability, ensuring that the complex chemo-hydro-mechanical interactions are properly resolved.

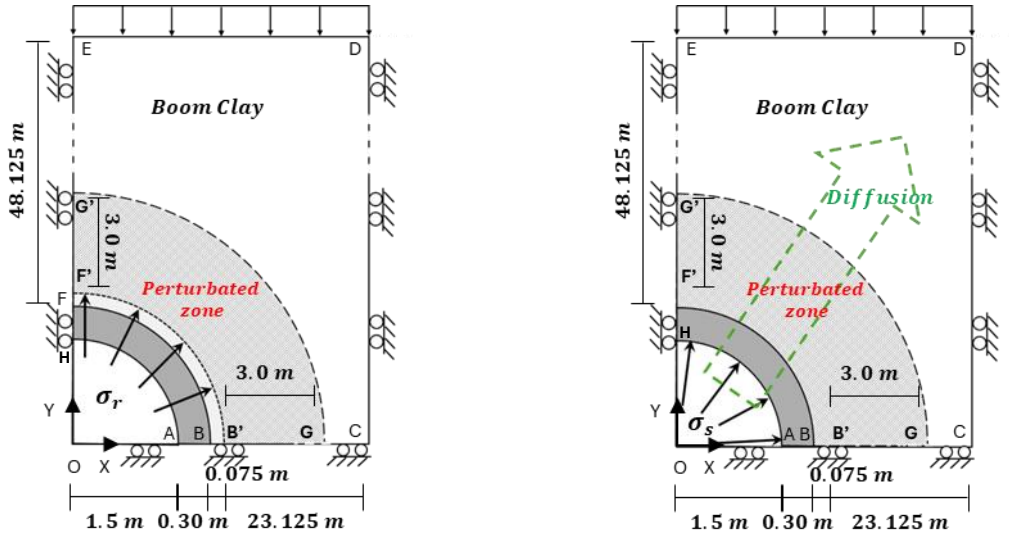

Figure 91 Geometry of the 2D plane strain model representing the disposal gallery, including the concrete liner, perturbed zone, and surrounding Boom Clay formation: a) Drainage and Equilibrium phase; b) Swelling and Diffusion phase.

2.2 Initial conditions

For the sake of simplicity, the mechanical behavior of natural Boom Clay is assumed to be both homogeneous and isotropic in this study. The disposal gallery is located at an approximate depth of 225 meters, where the groundwater level is close to the ground surface. As a result, the Boom Clay is considered to be fully saturated across the entire modeling domain.

At this depth, the total vertical stress (σ_v) is estimated to be 4.5 MPa, while the pore water pressure is about 2.2 MPa, resulting in an initial vertical effective stress of 2.3 MPa. The coefficient of earth pressure at rest (K_0), defined as the ratio of horizontal to vertical effective stresses, ranges between 0.8 and 1.0 based on laboratory and in situ investigations (Mertens et al., 2004; Bastiaens et al., 2007; ONDRAF, 2013). For the

purposes of this simulation, a K_0 value of 0.8 is adopted to represent an anisotropic initial stress state, leading to an initial horizontal effective stress of 1.84 MPa.

It is important to note that gravity is not explicitly modeled in the simulation. Instead, the initial stress field and pore pressure distribution are directly prescribed in the domain. In the concrete liner, the initial pore pressure is assumed to be 0 MPa, reflecting non saturated (atmospheric pressure) installation conditions.

The complete set of initial conditions applied in the model is summarized in Table 34.

Table 34 Initial stress state and pore pressure conditions for BC assumed in the 2D repository model.

Initial state	Boom Clay		Note
Effective stress (MPa)	$\sigma'_{yy} = \sigma'_v$	2.3	
	$\sigma'_{xx} = \sigma'_{zz} = \sigma'_h$	1.84	$\boldsymbol{K_0 = 0.8}$
Pore pressure (MPa)	$\boldsymbol{u_w}$	2.2	

2.3 Analysis sequences

The numerical modeling of the repository-scale behavior of Boom Clay in response to the excavation and long-term evolution of a disposal gallery is divided into four distinct phases, each representing a key stage in the life cycle of the repository. These phases are defined as follows:

1. Phase 1 – Excavation Phase (duration of 1 day):

   This phase simulates the excavation of the disposal gallery, assumed to be completed within one day. During this step, the pore water pressure at the gallery wall is rapidly reduced, reflecting the sudden exposure of the clay to atmospheric conditions. This decrease is imposed to replicate the stress redistribution and pore pressure drop observed in in-situ measurements. An over-excavation of 0.075 m is considered for an outer liner radius of 1.8 m, based on back-analyses and experimental data, to account for the convergence of Boom Clay before the installation of the concrete liner.

2. Phase 2 – Drained Operational Phase (duration of 100 years):

   Following excavation, the gallery enters a long-term operational period lasting 100 years. During this phase, the pore pressure at the gallery wall is held

constant, representing drainage conditions. No additional mechanical or chemical processes are introduced during this period.

3. Phase 3 – Equilibrium Phase (duration of 300 years):

   After the operational period, the gallery is assumed to be sealed, and an impervious condition is applied to the gallery wall. This stage lasts for 300 years, allowing the system to evolve under nearly undisturbed conditions. The pore pressure at the gallery wall is no longer fixed, and the clay is allowed to equilibrate gradually with the surrounding conditions.

4. Phase 4 – Swelling and Salinity Perturbation Phase (duration of 500 years):

   The final and most critical phase simulates the long-term evolution of the repository following waste degradation. This stage spans 500 years and includes three different scenarios designed to isolate and evaluate the effects of mechanical swelling and saline concentration due to the chemical diffusion of the Eurobitum waste:

   - Scenario 1 – Pure Swelling:

     A constant radial displacement is imposed on the concrete liner to simulate the mechanical swelling of the bituminized waste. A swelling rate of 0.1 mm/year is applied, reaching a maximum radial displacement of 5 cm over 500 years. In this scenario, no chemical diffusion of saline plumes is considered, and the pore pressure is maintained constant throughout the domain.

   - Scenario 2 – Pure Diffusion:

     This case considers only the chemical perturbation, simulating the diffusion of saline plumes from the bituminized waste into the surrounding Boom Clay without any mechanical swelling. The purpose is to isolate the effect of chemical transport on the hydro-mechanical behavior of the formation.

   - Scenario 3 – Coupled Swelling and Diffusion:

     This scenario represents the most realistic case, where both mechanical swelling (at 0.1 mm/year) and saline plume diffusion occur

simultaneously. The saline plumes diffuse radially from the bituminized waste, through the concrete liner, and into the 3-meter-thick perturbed zone. The evolving chemical conditions affect the hydro-mechanical response of Boom Clay. Various ionic strengths and sodium occupancy values are explored in this scenario to study their influence on the chemo-hydro-mechanical behavior (details are provided in the subsequent sections).

Each of these phases allows for a stepwise understanding of the coupled processes affecting the repository and provides insight into the long-term performance and safety of the Boom Clay host formation under repository-relevant conditions.

2.4 Hydro-Chemo-Mechanical boundary conditions

The numerical simulation applies appropriate mechanical, hydraulic, and chemical boundary conditions to realistically replicate the in-situ behavior of Boom Clay and the surrounding repository environment. The adopted boundary conditions are schematically presented in Figure 3 and are described below.

Mechanical Boundary Conditions

To ensure the stability and symmetry of the 2D plane strain model, specific constraints are applied to the model boundaries:

- Horizontal displacements are fixed (i.e., set to zero) along the vertical boundaries EH (left side) and CD (right side). This condition prevents lateral movement and simulates confinement by the surrounding formation.
- Vertical displacements are fixed along the bottom boundary AC, simulating the underlying undisturbed geological layers that provide vertical support.
- The remaining boundaries are free to deform, except where displacement control or load is applied (e.g., at the concrete liner during swelling phases).
- Contact element was imposed between the BC and concrete liner (BF).

Hydraulic Boundary Conditions

The hydraulic behavior of the Boom Clay formation is modeled under fully saturated conditions. The following assumptions and boundary settings are applied:

- Top boundary ED is maintained at a constant pore pressure, reflecting the hydrogeological setting where a sand aquifer overlays the clay layer. This implies a relatively stable hydraulic head at the interface, with negligible changes over the simulation period.
- All external boundaries (i.e., AC, CD, EH, and ED) are considered impervious, meaning no water flux is allowed through them.
- The only permeable interface is the excavated gallery wall, denoted as B′F′:
    - During the excavation phase and the drained operational phase (Phases 1 and 2), the pore pressure at the gallery wall is reduced to atmospheric pressure (0.1 MPa), simulating drainage within the open gallery.
    - In the equilibrium phase (Phase 3), the pore pressure condition at the gallery wall is released, transitioning to an undrained state representative of a sealed and impervious gallery environment.
    - During the swelling phase (Phase 4), the pore pressure throughout the domain was considered as the same condition in the previous phase (equilibrium phase). This assumption is made to isolate the effects of mechanical swelling and decouple it from the hydraulic response, thereby emphasizing the impact of the imposed radial displacements on the host clay.

Chemical Boundary Conditions

The chemical behavior is governed by the diffusion of saline plumes from the bituminized waste into the surrounding Boom Clay through the concrete liner. To represent this, the following assumptions are made:

- A 3-meter-thick chemically perturbed zone is introduced immediately beyond the concrete liner, with its outer boundary denoted as GG′.
- During the swelling and diffusion phases, saline species (e.g., Na^{+} and Ca^{2+}) are assumed to be released from the bituminized waste and migrate radially outward.
- Initially, this perturbed zone exhibits a high concentration gradient, leading to diffusion-driven transport into the surrounding clay matrix.

- Over time (hundreds of years), the chemical species are expected to gradually diffuse throughout the domain, ultimately reaching a chemical equilibrium.

This configuration allows for a realistic representation of the chemo-hydro-mechanical interactions in the system, particularly the combined influence of mechanical swelling pressure, pore pressure evolution, and saline plume transport under long-term repository conditions. It is important to emphasize that the release of high chemical concentrations in this model is entirely hypothetical and does not represent actual repository conditions. Chemical numerical simulations have shown that the chemically perturbed zone is limited to approximately 0.19 meters, and the maximum ionic strength observed is around 0.1 M—concentrations that are too low to significantly affect the hydro-mechanical behavior of Boom Clay (Jacques et al., 2025). Consequently, higher concentrations and a broader perturbation zone (3 meters) are intentionally used in this study to amplify the chemical effects and enable a more pronounced assessment of chemo-hydro-mechanical interactions in the model (see detailed justification in the following sections).

2.5 Parameters

In this study, the ACC2-Chem constitutive model is adopted to simulate the behavior of natural Boom Clay under coupled chemo-hydro-mechanical conditions. This advanced model is capable of capturing the complex interactions between mechanical deformation, fluid flow, and chemical effects in low-permeability clays. The model parameters used in the simulations were calibrated and validated based on experimental data and literature sources.

The mechanical parameters of the ACC2-Chem model, which include stiffness, strength, compressibility, and elastic-plastic behavior characteristics, are summarized in Table 35. In parallel, the chemical parameters required for modeling the influence of chemical concentration on the mechanical behavior of Boom Clay are presented in Table 36. These include chemo-elastic coupling coefficients, chemical sensitivity parameters, and other relevant factors influencing the clay's response to saline intrusion.

Table 35 Mechanical parameters of the ACC2-Chem model for Boom Clay

Parameter description	Symbol	Value
Slope of critical state line	M_G (-)	0.55
Ratio at the apex of the yield surface	M_f (-)	0.55
Controls the shape of the yield surface	k_f (-)	0.7
Controls the flow rule	k_g (-)	0.9
Cohesion	c' (MPa)	0.13
Preconsolidation pressure	p_c' (MPa)	6
Compression index	λ (-)	0.10
Swelling index	κ (-)	0.04
Poisson's ratio	ν (-)	0.15
controls the contribution of shear plastic strain	A_d (-)	1
Initial state of the inner yield surface	r_0 (-)	0.36
controls hardening modulus evolution	s	8

Table 36 Chemical parameters used in the ACC2-Chem model.

Parameter	Value
$\boldsymbol{\alpha_G}$ (-)	0.05
$\boldsymbol{\alpha_F}$ (-)	0.025
$\boldsymbol{\alpha_{p_c'}}$(MPa)	0.453
$\boldsymbol{\alpha_{c'}}$ (MPa)	0.005
$\boldsymbol{\beta_{Na^+}}$ (-)	5

In addition to the mechanical and chemical parameters, the hydraulic properties of Boom Clay and its pore water are critical for modeling fluid flow and solute transport. Table 37 presents the hydraulic characteristics of Boom Clay, including porosity and intrinsic permeability. The anisotropy of hydraulic conductivity is explicitly considered in the model, with horizontal permeability ($\mathrm{k_h}$) taken as twice the vertical permeability ($\mathrm{k_v}$), in line with in-situ observations reported by Bastiaens et al. (2007). Table 38 provides the relevant hydraulic properties of the pore water, including viscosity and chemical diffusivity, which influence transport processes during diffusion of the saline plume.

Table 37 Hydraulic properties of natural Boom Clay.

Intrinsic permeability (m^2)	$\boldsymbol{k_v}$	$\mathbf{3.0 \times 10^{-19}}$
	k_h	$\mathbf{6.0 \times 10^{-19}}$
Porosity	$\boldsymbol{n}$	$\mathbf{0.39}$

Table 38 Hydraulic and physical properties of pore water.

Fluid specific mass (kg/m^3)	$\boldsymbol{\rho_w}$	**1000**
Fluid dynamic viscosity ($Pa.s$)	μ_w	**0.001**
Liquid compressibility coefficient (MPa^{-1})	$\frac{1}{X_w}$	$\mathbf{5.0 \times 10^{-4}}$
Chemical Diffusivity	$\boldsymbol{D_{eff}}$	$\mathbf{1.0 \times 10^{-10}}$

Furthermore, the mechanical behavior of the concrete liner surrounding the gallery is also considered in the model. Table 39 presents the main geomechanical properties of the concrete material (C80/95), such as Young's modulus, Poisson's ratio, porosity and intrinsic permeability to simulate its interaction with the surrounding clay, particularly under swelling and chemically induced stress conditions.

Table 39 Geomechanical properties of the concrete liner (C80/95).

Young elastic modulus (MPa)	$\boldsymbol{E_0}$	43305
Poisson ratio [-]	$\boldsymbol{\nu}$	0.25
Intrinsic Permeability (m^2)	$\boldsymbol{k_v = k_h}$	$\mathbf{3 \times 10^{-18}}$
Porosity (-)	$\boldsymbol{n}$	0.25

This complete set of mechanical, chemical, hydraulic, and structural parameters forms the basis for the numerical simulations and ensures a consistent and realistic representation of the coupled processes affecting the performance of the repository system over time.

3. Numerical results

This section presents and analyzes the numerical results obtained for the different simulation phases described earlier. The evolution of key variables—including pore water pressure, radial displacement, as well as radial and orthoradial stresses—will be shown along both horizontal (AC; see Figure 91) and vertical (EH; see Figure 91) cross-sections of the model domain. These results provide a comprehensive view of the hydro-mechanical response of Boom Clay throughout the repository lifetime under different loading and boundary conditions.

To gain deeper insight into the underlying hydro-chemo-mechanical processes, the results will also be interpreted through the analysis of stress paths for selected points within the clay domain. In particular, the stress path is evaluated at the beginning of the 3-meter perturbated zone—specifically, at point B′ along the horizontal profile and point F′ along the vertical profile. These locations are chosen as they represent the most mechanically and chemically disturbed regions of the model, situated immediately beyond the concrete liner. The stress path analysis at these critical points allows for a detailed examination of the stress evolution under three distinct scenarios: (1) swelling of the bituminized waste alone, (2) pure chemical diffusion of saline plumes without swelling, and (3) the combined effect of swelling and increased saline concentration of chemical diffusion. Through this approach, the respective roles and interaction of mechanical swelling and chemical perturbation will be thoroughly characterized, enhancing our understanding of their impact on the hydro-mechanical behavior of Boom Clay.

3.1 Excavation phase

Figures Figure 92a and Figure 92b show the evolution of pore water pressure (P_w) as a function of radial distance from the gallery wall in both the horizontal (Figure 92a) and vertical (Figure 92b) profiles during the excavation and early drainage phases. Immediately after excavation (at 1 day), a sharp drop in pore pressure occurs at the gallery wall due to the imposed atmospheric pressure condition. This is followed by a localized increase, resulting in a pore pressure peak at approximately 4.5 to 5 meters from the wall. This peak is more pronounced in the horizontal profile, where the pore water pressure rises above the initial value of 2.6 MPa. In contrast, the peak in the

vertical profile remains close to the initial value of 2.2 MPa. This behavior is attributed to the anisotropy of in-situ stresses ($K_0 = 0.8$).

This overshoot is a characteristic response of low-permeability Boom Clay, reflecting the redistribution of pore water under sudden stress release.

A key difference between the two profiles lies in their boundary conditions. In the vertical profile, the pore pressure at the outer boundary (at R = 50 m) is fixed to simulate the natural drainage toward the overlying sandy aquifer. In contrast, in the horizontal profile, no pore pressure condition is imposed at the far boundary due to the symmetry of the model. As a result, the dissipation behavior differs between the two cases. In the horizontal profile, the pore pressure gradually recovers and reaches approximately 1.7 MPa at a distance of 25 meters from the gallery after 100 years. Meanwhile, in the vertical profile, a less pronounced reduction is observed, with the pore pressure dropping to around 2.0 MPa at 20 meters, due to the fixed pore pressure imposed by the boundary condition. These results highlight the anisotropic nature of the hydraulic response and the importance of boundary condition choices in long-term simulations.

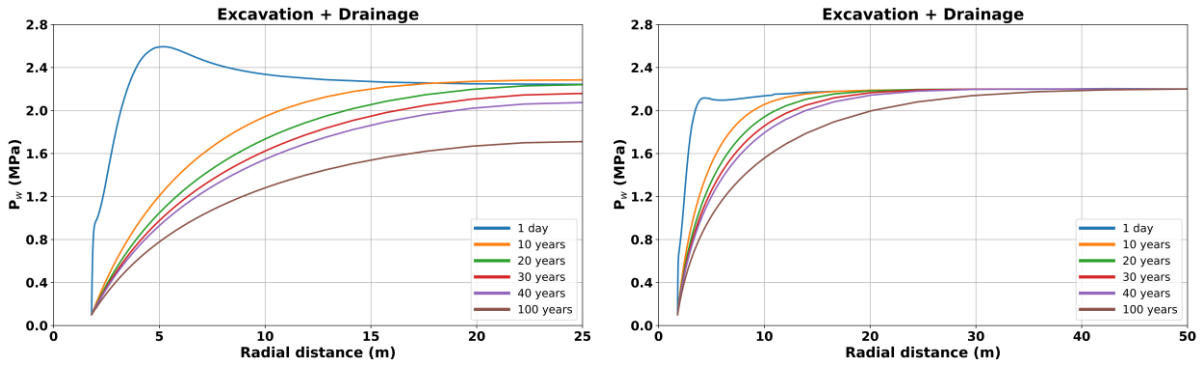

(a): Horizontal Profile (b) : Vertical Profile

Figure 92 Evolution of pore water pressure (P_w) during excavation and drainage phases: (a) horizontal profile, (b) vertical profile.

Figure 93a and Figure 93b illustrate the evolution of radial displacement with time and radial distance during the excavation and drainage phases along the horizontal and vertical profiles, respectively.

In the horizontal profile (Figure 93a), radial displacements at $R = 1.8\,m$ (at the excavated wall) and $R = 25\,m$ (along the boundary CD) remain constant throughout the analysis. This is due to the mechanical constraints imposed by the concrete liner

at the wall and the fixed horizontal displacement boundary condition at the outer edge. As pore pressure gradually dissipates during the drained phase, radial displacement increases over time, indicating a progressive mechanical response of the Boom Clay to the evolving stress field.

In the vertical profile (Figure 93b), the general trend of radial displacement evolution is similar to that observed in the horizontal profile. However, notable differences emerge due to the distinct hydraulic and mechanical boundaries conditions applied vertically, particularly the fixed pore water pressure at the top boundary. These differences result in a different spatial distribution of deformation. By the end of the drainage phase, radial displacement is more pronounced at the top boundary than at the gallery wall, reflecting a vertical settlement of the clay layer above the gallery due to pore pressure dissipation and mechanical unloading.

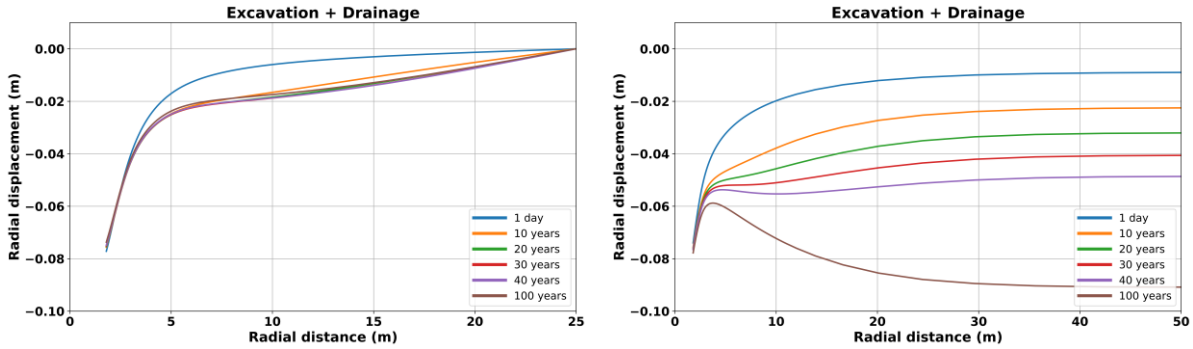

(a) : Horizontal Profile (b) : Vertical Profile

Figure 93 Evolution of radial displacement along horizontal (a) and vertical (b) profiles during excavation and drainage phase.

Figure 94a and Figure 94b show the evolution of the radial stress ($\sigma'_x \ for\ horizontal\ profile\ and\ \sigma'_y \ for\ vertical\ profile$) as a function of radial distance from the gallery wall for the horizontal and vertical profiles, respectively, during the excavation and drainage phases. Just one day after excavation, both profiles exhibit a sharp decrease in radial stress at the gallery wall, due to the sudden stress release imposed by the excavation boundary conditions. This reduction is followed by a stress redistribution in the surrounding clay, influenced by the low permeability of Boom Clay and the pore pressure gradients generated.

In the horizontal profile (Figure 94a), radial stress increases gradually with distance and reaches a relatively uniform value beyond approximately 15 m. With time, the dissipation of excess pore water pressure leads to a progressive increase in effective

stress, especially near the gallery wall. After 100 years, the radial stress recovers significantly, approaching initial in-situ levels in the outer domain.

In the vertical profile (Figure 94b), although the general trend is similar, the influence of different boundary conditions is clearly seen. The fixed pore water pressure at the top boundary accelerates drainage in that direction, leading to a more pronounced increase in radial stress near the wall. This results in a steeper stress gradient and higher stress magnitudes in the vicinity of the gallery over time, particularly at long durations (e.g., 100 years).

Overall, these results highlight the hydro-mechanical coupling in Boom Clay, where the evolution of radial stress is strongly governed by both the drainage conditions and the low permeability of the material, which control the rate of pore pressure dissipation and subsequent stress redistribution.

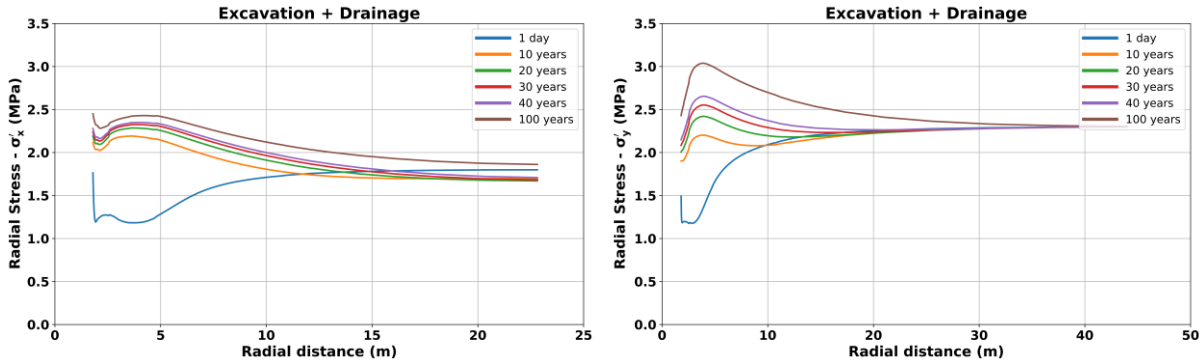

(a): Horizontal Profile (b): Vertical Profile

Figure 94 Evolution of radial stress (σ^r) during excavation and drainage phases in (a) horizontal and (b) vertical profiles.

Figure 95a and Figure 95b illustrate the evolution of orthoradial stress (σ^θ), denoted as σ'_y in the horizontal profile and σ'_x in the vertical profile, as a function of radial distance from the gallery wall during the excavation and early drainage phases. At the onset of excavation (1 day), both profiles exhibit a distinct drop in orthoradial stress at the gallery wall, resulting from the sudden release of in-situ stress due to cavity creation. This is followed by a local peak in σ^θ at approximately 2-3 meters from the wall, reflecting stress concentration caused by the redistribution of loads around the excavated cavity, particularly in a low-permeability medium such as Boom Clay.

In the horizontal profile (Figure 95a), the orthoradial stress progressively increases over time, driven by the gradual dissipation of pore water pressure and the

corresponding recovery of effective stress. After 100 years, the orthoradial stress near the gallery wall even exceeds the initial in-situ value, a phenomenon attributed to the complete drainage and the resulting increase in effective stress. This evolution underscores the slow but significant mechanical response of Boom Clay under drained conditions.

In contrast, the vertical profile (Figure 95b) exhibits a similar qualitative trend, but the magnitude of orthoradial stress increase near the gallery wall is less pronounced. This difference arises from the hydraulic boundary condition applied at the top of the vertical domain, where the pore water pressure is fixed. This condition limits drainage in the vertical direction compared to the symmetry condition in the horizontal profile, thereby restraining the recovery of effective stress.

Overall, these results highlight the anisotropic hydro-mechanical behavior of Boom Clay and the critical role of boundary conditions in governing the development of the stress field around an excavated cavity.

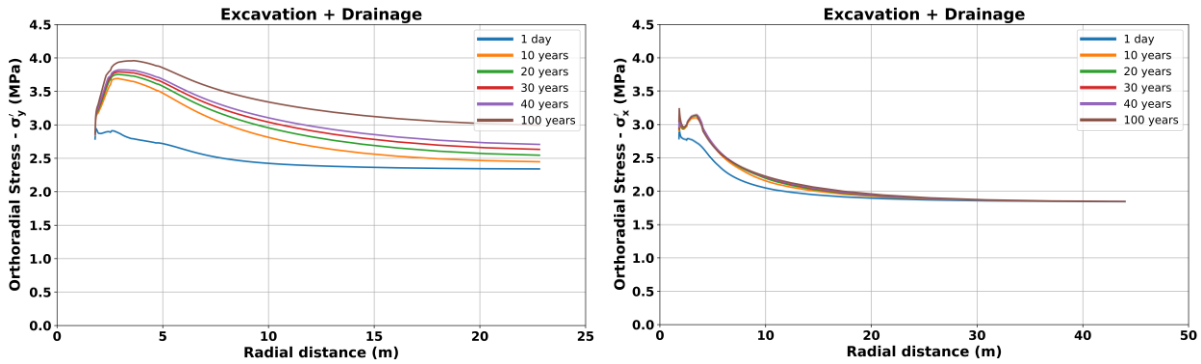

(a): Horizontal Profile (b): Vertical Profile

Figure 95 Evolution of orthoradial stress (σ^{θ}) during excavation and drainage phases in (a) horizontal and (b) vertical profiles.

3.2 Equilibrium phase

Figure 96a and Figure 96b illustrate the evolution of pore water pressure (p_w) as a function of radial distance from the gallery wall during the equilibrium phase, which spans a total duration of 300 years, in the horizontal and vertical profiles, respectively. The time legend shown in these figures corresponds exclusively to this phase. In contrast to the drainage phase, the equilibrium phase exhibits an increase in pore pressure with time, marking an opposite general trend. This increase in p_w is most

rapid during the first 10 years, after which the rate of change slows down but continues progressively.

The slow evolution is primarily due to the low permeability of Boom Clay, which significantly delays the full re-equilibration of pore water pressures. A near-final equilibrium state is approached only after approximately 300 years, although true equilibrium would theoretically require an infinite amount of time to be fully achieved.

In the vertical profile (Figure 96b), the general trend of increasing p_w with time remains consistent with that observed in the horizontal profile. However, due to the hydraulic boundary condition imposed at the top boundary (segment DE), where p_w is kept constant, the shape of the pore pressure distribution curves differs. Specifically, unlike the horizontal profile—where the p_w profiles tend to become nearly horizontal over time—the curves in the vertical profile display a sloped gradient, reflecting the influence of the fixed pore pressure at the boundary. This highlights the role of boundary conditions in shaping the evolution of pore water pressure distributions in the long term.

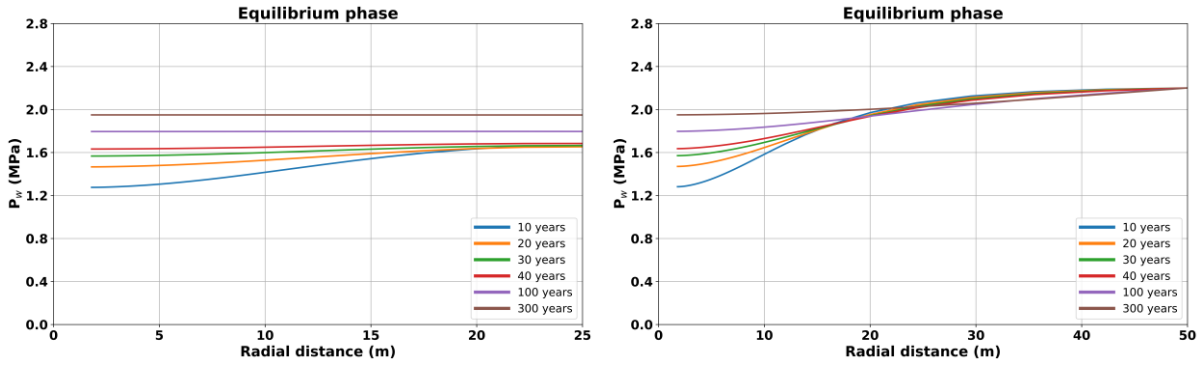

(a): Horizontal Profile (b): Vertical Profile

Figure 96 Evolution of Pore Water Pressure During the Equilibrium Phase in (a) Horizontal and (b) Vertical Profiles.

Figure 97a and Figure 97b present the evolution of radial displacement during the equilibrium phase as a function of radial distance and time for the horizontal and vertical profiles, respectively.

In Figure 97a, corresponding to the horizontal profile, the radial displacement decreases progressively with time. This behavior reflects the gradual re-equilibration of pore pressure, leading to a partial recovery of the stress field. The final accumulated displacement at the excavated wall reaches approximately 7.5 cm, which corresponds

to the initial over-excavation. At any given time, the radial displacement decreases with increasing distance from the gallery wall.

In Figure 97b, which shows the vertical profile, the displacement evolution follows a different trend due to the specific hydraulic boundary condition at the top. Here, the displacement decreases with time at the top boundary, indicating a rebound or heave of the clay layer during the re-equilibration phase.

This contrast between the two profiles highlights the impact of boundary conditions and anisotropic hydro-mechanical behavior in Boom Clay.

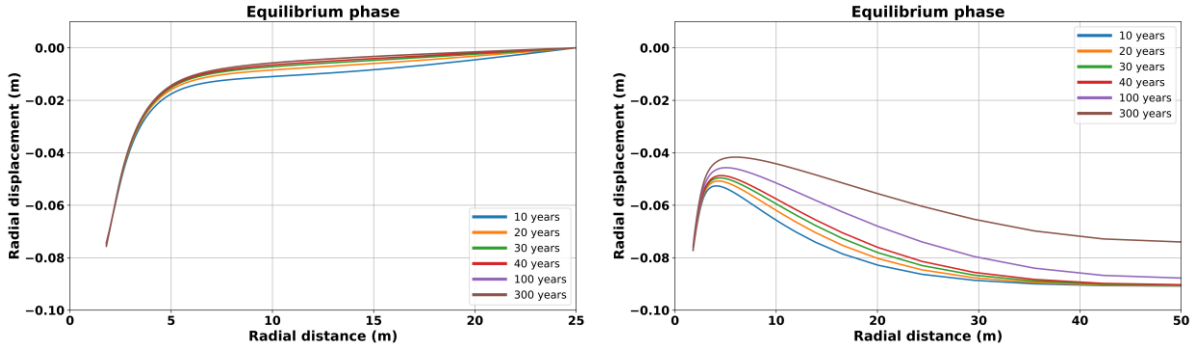

(a): Horizontal Profile (b): Vertical Profile

Figure 97 Radial displacement evolution during the equilibrium phase: (a) horizontal profile, (b) vertical profile.

Figure 98a and Figure 98b illustrate the evolution of the radial stress (σ_r') as a function of radial distance from the gallery wall and time during the equilibrium phase, for the horizontal and vertical profiles, respectively. In both profiles, a general decreasing trend in radial stress over time is observed. This reduction is linked to the gradual increase in pore water pressure (p_w) during this phase.

As water progressively re-enters the Boom Clay following the excavation and drainage phases, pore pressure rises throughout the domain. This increase reduces the effective stress according to Terzaghi's principle ($\sigma' = \sigma - u$), resulting in a noticeable drop in the radial stress with time. The most significant stress reduction occurs near the gallery wall, where the initial stress concentrations were highest and where pore pressure recovery is most pronounced.

In the horizontal profile (Figure 98a), the symmetry of the system leads to a relatively uniform dissipation and redistribution of stresses. Radial stress values decrease gradually over time, particularly within the first few meters from the gallery wall, where the system is most disturbed.

In the vertical profile (Figure 98b), although a similar decreasing trend in radial stress is observed, the evolution is slightly affected by the imposed hydraulic boundary condition at the top boundary (where pore pressure is fixed). This condition influences the redistribution of pore pressure and, consequently, the reduction of effective radial stress. As a result, the stress evolution with time is less uniform compared to the horizontal profile.

Overall, the radial stress reduction in both profiles highlights the long-term mechanical response of Boom Clay due to pore pressure equilibration in a low-permeability medium, confirming the significant influence of hydro-mechanical coupling in the post-excavation recovery process.

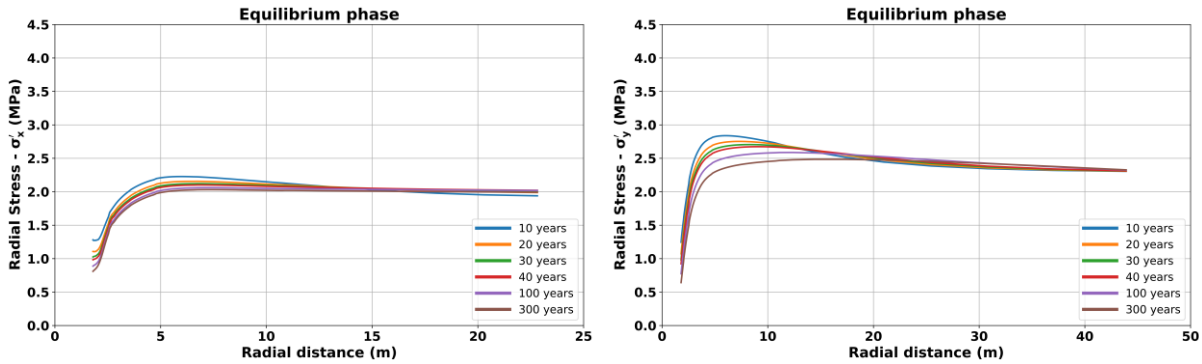

(a): Horizontal Profile (b): Vertical Profile

Figure 98 Evolution of Radial Stress during the Equilibrium Phase: (a) Horizontal Profile, (b) Vertical Profile.

Figure 99a and Figure 99b illustrate the evolution of the orthoradial stress (σ'_θ) with respect to radial distance from the gallery wall and time during the equilibrium phase. Similar to the radial stress, the orthoradial stress in both profiles shows a general decreasing trend over time, primarily due to the gradual rise in pore water pressure as the system moves toward hydro-mechanical equilibrium.

In the horizontal profile (Figure 99a), the orthoradial stress shows a progressive reduction near the gallery wall, where the mechanical perturbation caused by excavation was initially the most severe. As pore water slowly re-infiltrates the surrounding clay and pressure increases, the effective orthoradial stress correspondingly decreases, following the same mechanical principle that governs effective stress. The decrease is most notable during the first few decades of the equilibrium phase, after which the changes become more gradual.

In the vertical profile (Figure 99b), the orthoradial stress also decreases over time, though the evolution is influenced by the fixed pore pressure boundary condition imposed at the top of the domain. This condition affects how quickly and uniformly the pore pressure can recover across the vertical section, leading to a slightly different stress redistribution compared to the horizontal profile. Nevertheless, the overall trend remains the same: as pore pressure increases, the effective orthoradial stress reduces accordingly.

These observations reinforce the important role of hydro-mechanical coupling in Boom Clay and demonstrate that stress relaxation continues long after excavation, particularly under low-permeability conditions. The decreasing orthoradial stress reflects the slow and persistent nature of pore pressure equilibration in the medium, and how this influences the long-term stability and behavior of the surrounding clay formation.

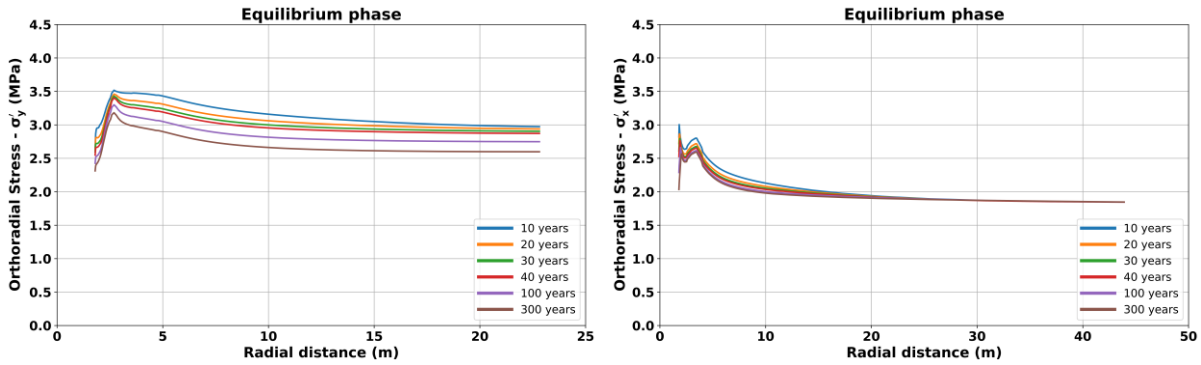

(a): Horizontal Profile (b): Vertical Profile

Figure 99 Evolution of Orthoradial Stress during the Equilibrium Phase: (a) Horizontal Profile, (b) Vertical Profile.

3.3 Swelling phase

It is important to emphasize that, in this simulation phase, only the swelling of the bituminized waste is considered—no chemical disturbance is introduced at this stage. A comparative analysis between swelling and chemical perturbation effects will be addressed in the subsequent sections.

Figure 100a and Figure 100b illustrate the evolution of pore water pressure (P_w) during the swelling phase, which spans a total duration of 500 years, in the horizontal and vertical profiles, respectively. The time legend shown in these figures corresponds exclusively to this phase. This simulation phase considers the mechanical response of Boom Clay due to the swelling of bituminized waste.

In both profiles, the observed evolution of pore water pressure is not directly caused by the swelling itself but is instead part of a continuous re-equilibration process initiated during the preceding equilibrium phase. In the horizontal profile (Figure 100a), a gradual increase in pore pressure is observed near the gallery wall. However, this increase is not a direct outcome of the applied swelling pressure but rather reflects the ongoing, time-dependent adjustment of the pore pressure field as the system approaches hydro-mechanical equilibrium.

A similar trend is visible in the vertical profile (Figure 100b), although the distribution of pressure is influenced by the different boundary conditions—particularly the fixed pressure condition at the top, which introduces slight asymmetries in the spatial evolution of P_w.

These results confirm that the increase in pore pressure during the swelling phase is not primarily driven by the swelling mechanism itself, but instead represents a continuation of the long-term equilibration behavior of Boom Clay. This interpretation will be further supported and clarified in subsequent simulation phases. The findings emphasize the importance of considering the slow hydraulic re-equilibration process when analyzing pore pressure evolution in low-permeability clays like Boom Clay.

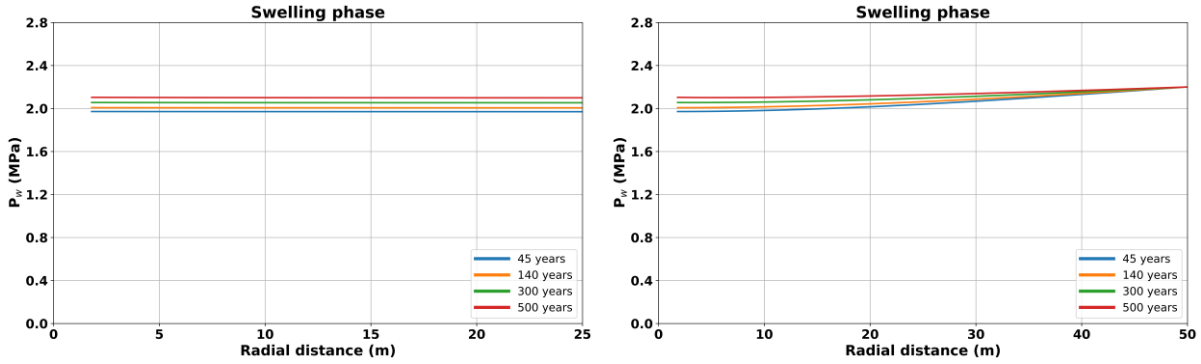

(a): Horizontal Profile (b): Vertical Profile

Figure 100 Evolution of pore water pressure during the swelling phase: (a) horizontal profile, (b) vertical profile.

Figure 101a and Figure 101b illustrate the evolution of radial displacement during the swelling phase for the horizontal and vertical profiles, respectively. In both profiles, the results show a continuous increase in radial displacement over time, driven by the swelling pressure imposed at the gallery wall as a boundary condition. In the horizontal profile (Figure 101a), the displacement is most significant at the excavated wall (R ≈

1.8 m) and gradually decreases with radial distance, reflecting the localized swelling effect and the gradual dissipation of its influence away from the source.

In the vertical profile (Figure 101b), a similar trend is observed: the radial displacement increases progressively over the 500-year simulation period. The displacement not only increases at the gallery wall but also shows a notable upward displacement at the top boundary. This behavior results from the vertical swelling propagation under constrained drainage conditions. By the end of the swelling phase (500 years), the maximum radial displacement occurs at the clay-concrete interface, with the magnitude diminishing gradually toward the boundaries, consistent with the swelling-induced deformation pattern in a low-permeability medium like Boom Clay.

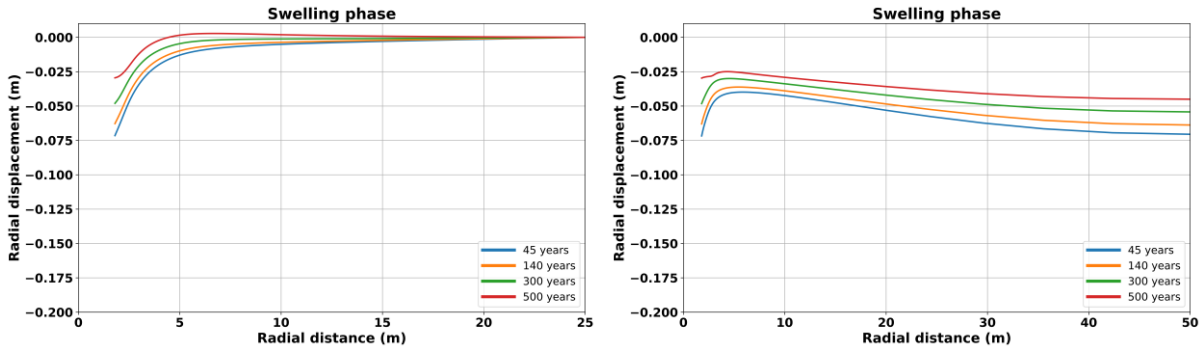

(a) : Horizontal Profile (b) : Vertical Profile

Figure 101 Evolution of radial displacement during the swelling phase for (a) the horizontal profile and (b) the vertical profile.

Figure 102a and Figure 102b illustrate the distribution of radial stress during the swelling phase for the horizontal and vertical profiles, respectively. It is important to emphasize that, in this simulation phase, only the swelling of the bituminized waste is considered—no chemical disturbance is introduced at this stage.

The observed increase in radial stress in both profiles can be directly attributed to the imposed swelling of the waste, which exerts pressure outward in the same direction as the radial stress component—along the x-axis in the horizontal profile and along the y-axis in the vertical profile. As a result, this alignment of swelling deformation with the radial stress direction leads to a progressive increase in radial stress near the concrete-clay interface.

The results show a significant increase in radial stress near the clay-concrete interface, which progressively decreases with increasing radial distance. In the horizontal profile

(Figure 102a), the stress attenuation with distance is more uniform. In contrast, in the vertical profile (Figure 102b), the influence of swelling is negligible beyond 10 meters from the gallery wall.

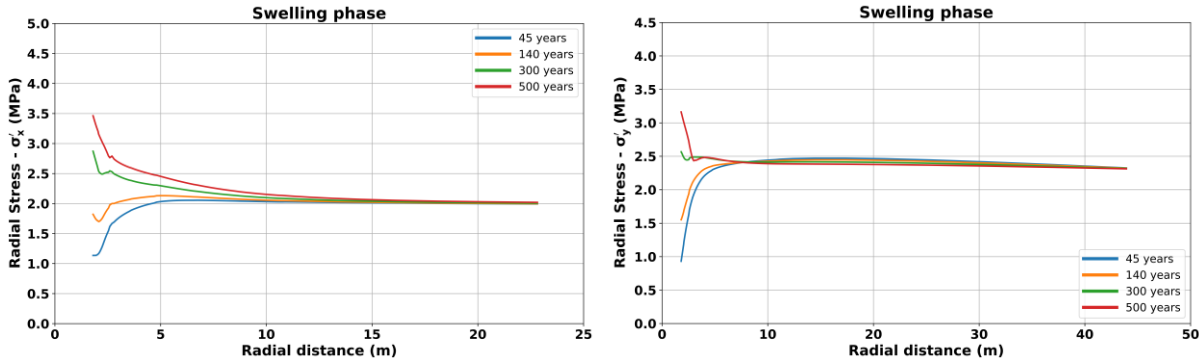

(a) : Horizontal Profile (b) : Vertical Profile

Figure 102 Evolution of Radial Stress during the Swelling Phase: (a) Horizontal Profile, (b) Vertical Profile.

Figure 103a and Figure 103b present the evolution of the orthoradial stress during the swelling phase in the horizontal and vertical profiles, respectively. In contrast to the radial stress, which increases due to the swelling-induced pressure exerted in the radial direction, the orthoradial stress exhibits an overall decreasing trend during the swelling phase, particularly in the zones closest to the gallery wall.

This behavior can be explained by the nature of the swelling boundary condition: the imposed swelling deformation acts radially outward, which effectively reduces the confinement in the orthoradial direction. Since the orthoradial stress (σ'_θ) acts tangentially around the gallery, the outward expansion of the clay causes a stress relief in this direction. As a result, a significant decrease in orthoradial stress is observed near the concrete wall (in the first few meters), with the effect becoming less pronounced further away from the gallery.

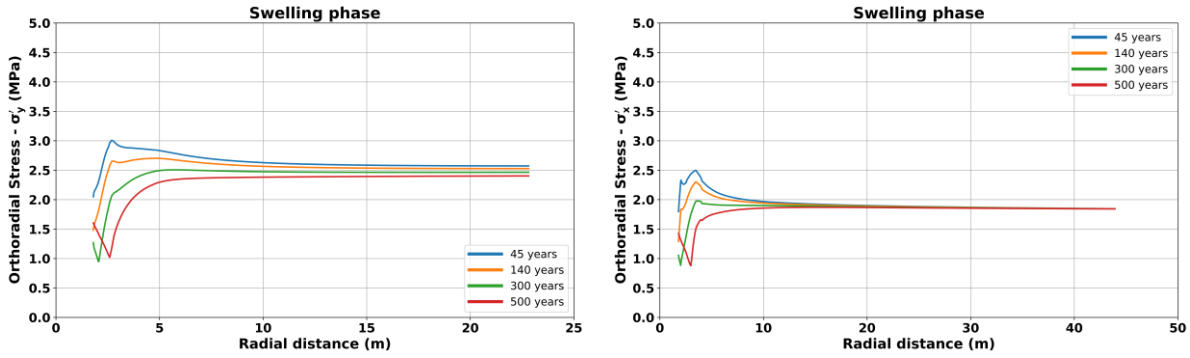

(a) : Horizontal Profile (b) : Vertical Profile

Figure 103 Evolution of orthoradial stress during the swelling phase: (a) horizontal profile, (b) vertical profile.

To gain a deeper understanding of the mechanical behavior of Boom Clay throughout the different simulation phases, Figure 104a presents the effective stress path at Point B′, located on the excavated gallery wall in the horizontal direction (see Figure 91), and Figure 104b presents the corresponding path at Point F′, located on the gallery wall in the vertical direction. These stress paths are plotted in the p′–q space, where p′ is the mean effective stress and q is the deviatoric stress.

In both horizontal and vertical profiles, the stress paths follow a broadly similar sequence of evolution through the various phases. However, distinct differences arise during the excavation phase due to the initial anisotropy in the in-situ stress conditions. In the vertical profile, the initial stress state is characterized by a higher radial stress (σ_y') compared to the orthoradial (σ_x') stress. Upon excavation, the radial stress near the cavity wall rapidly decreases due to stress release, while the orthoradial stress slightly increases. This leads to a marked drop in deviatoric stress (q), observed only in the vertical profile. As excavation progresses, a reversal in the principal stress directions occurs—orthoradial stress becomes greater than radial stress—leading to a renewed increase in q as the stress state shifts.

In contrast, in the horizontal profile, the radial stress (σ_x') increases from the outset while the orthoradial stress (σ_y') decreases, resulting in a direct and linear increase in q without the initial drop seen in the vertical profile. This linear trend reflects the undrained response of the clay under rapid loading, where the short time scale of excavation prevents significant pore pressure dissipation, leading to a buildup of shear stress. Shortly after, an elastic unloading phase occurs when the clay comes into contact with the concrete liner. This interaction causes a localized redistribution of stress, resulting in a brief decrease in q and a corresponding increase in p′, which reflects the stabilizing mechanical constraint imposed by the liner.

In the drained phase, the mean effective stress p′ progressively increases due to the dissipation of pore water pressure, reflecting the recovery of effective stress within the clay matrix. At the same time, the deviatoric stress q decreases slightly, indicating a gradual relaxation of shear stress as the soil adjusts to the evolving hydraulic conditions under drained loading.

During the equilibrium phase, the pore water pressure begins to rise again as the system tends toward long-term hydraulic re-equilibration. As a result, the mean

effective stress p′ decreases significantly, while the deviatoric stress q increases. This evolution represents a reverse trend compared to the drained phase and is driven by the slow diffusion-controlled re-saturation of the low-permeability Boom Clay. The stress path in this phase captures the delayed hydro-mechanical response under nearly undrained conditions.

In the swelling phase, the application of swelling pressure at the concrete–clay interface leads to further evolution of the stress state. Initially, there is a slight decrease in q, followed by a steady increase in both p′ and q. This reflects the mechanical effect of the clay swelling and pushing against the rigid structure. The stress path eventually reaches the inner yield surface and approaches the Critical State Line (CSL), though crossing it. This final trajectory signifies a plastic hardening behavior occurring inside the inner yield surface. The path is typical of a one-dimensional loading process, which is consistent with the simulation's boundary conditions, including fixed lateral and vertical displacements and the application of swelling pressure solely at the concrete liner.

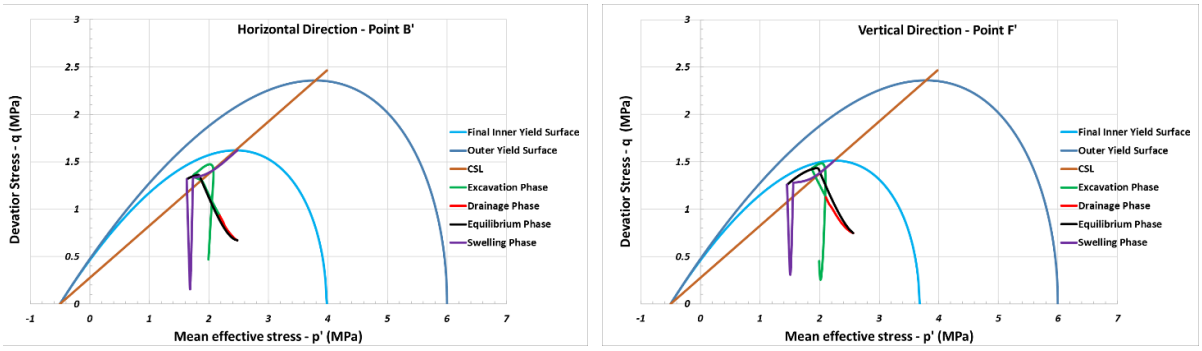

(a) (b)

Figure 104 Effective stress paths at the excavated gallery wall in (a) horizontal (point b') and (b) vertical (point f') directions across simulation phases.

3.4 Pure diffusion phase

It is important to emphasize that during this simulation phase, only the diffusion of the saline plume from the bituminized waste is considered—no swelling or mechanical disturbance is introduced. This section is dedicated solely to presenting the effect of saline solution diffusion on the hydro-mechanical behavior of Boom Clay and to demonstrate the proper functioning of the chemical model. A comparative analysis between the effects of swelling and chemical perturbation will be addressed in subsequent sections.

Figures Figure 105a and Figure 105b illustrate the evolution of pore water pressure (Pw) during the pure diffusion phase ,which spans a total duration of 500 years, in the horizontal and vertical profiles, respectively. The time legend shown in these figures corresponds exclusively to this phase.

In the horizontal profile (Figure 15a), the results indicate a gradual increase in pore water pressure near the gallery wall. It is most pronounced within the first few meters from the wall. This behavior continues from the previous equilibrium phase, where the pore pressure was still evolving, indicating that full equilibrium has not yet been reached. It is important to note that this increase in pore water pressure is not due to the diffusion of the saline plume itself, as the simulation accounts only for pure diffusion without advection. Instead, the continuous rise in pore pressure reflects the ongoing adjustment process as the system approaches equilibrium.

Similarly, in the vertical profile (Figure 15b), a comparable upward trend in pore water pressure is observed. However, the spatial distribution and magnitude differ slightly due to the hydraulic boundary conditions, particularly the fixed pore pressure imposed at the top boundary. These anisotropic boundary conditions result in a less symmetric redistribution of pore water pressure compared to the horizontal profile.

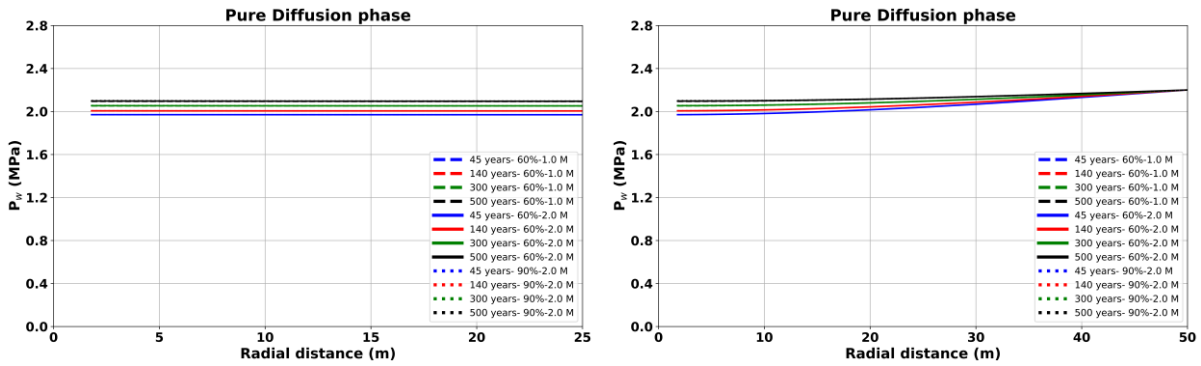

(a) : Horizontal Profile (b) : Vertical Profile

Figure 105 Evolution of pore water pressure during the pure diffusion phase: (a) horizontal profile, (b) vertical profile.

Figure 106a and Figure 106b illustrate the evolution of radial displacement during the pure diffusion phase along the horizontal and vertical profiles, respectively.

In the horizontal profile (Figure 106a), the results indicate that the solute concentration and sodium occupancy have almost no influence on the radial displacement along the radial distance. Only a very slight contraction of the clay is observed after 500 years

for the case of ionic strength (IS) = 2.0 M and 90% sodium occupancy. This minimal change suggests that pure diffusion of the saline plume does not significantly affect the mechanical deformation of the clay in the horizontal direction during this phase.

In the vertical profile (Figure 106b), a similar trend is noted: the radial displacement remains largely unaffected by the high solute concentration and sodium occupancy. However, a slight contraction is also observed after 500 years. Additionally, a notable upward displacement occurs at the top boundary. This difference compared to the horizontal profile is attributed to the boundary conditions—while lateral displacements are restricted, the clay at the top boundary is free to move upward due to the absence of displacement constraints.

Overall, the variations in radial displacement during the pure diffusion phase are minimal and mainly controlled by boundary conditions rather than chemical effects.

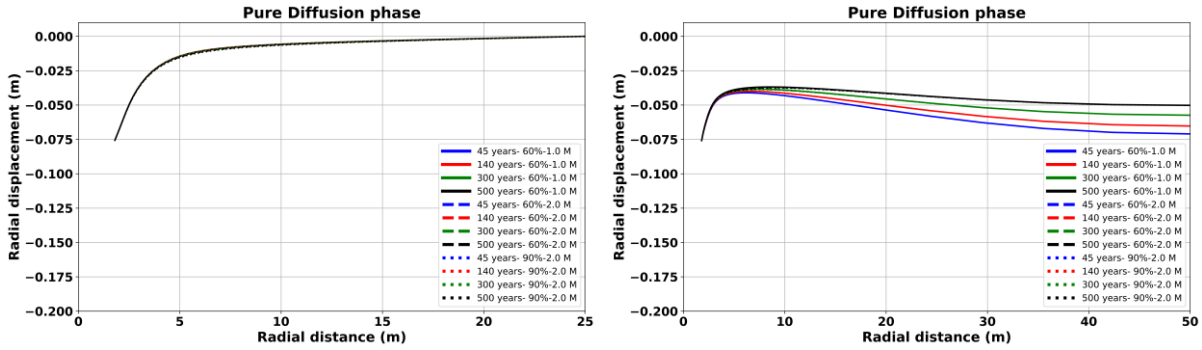

(a) : Horizontal Profile (b) : Vertical Profile

Figure 106 Evolution of radial displacement during the pure diffusion phase for (a) the horizontal profile and (b) the vertical profile.

Figure 107a and Figure 107b illustrate the distribution of radial stress during the pure diffusion phase along the horizontal and vertical profiles, respectively. It is important to highlight that in this simulation phase, only the pure diffusion of the saline plume from the bituminized waste is modeled—no mechanical loading or swelling effects are applied at this stage.

For both profiles, the results reveal only a slight influence of solute concentration and sodium occupancy on the radial stress distribution. Specifically, a minor contraction is observed after 500 years for the case with 90% sodium occupancy and an ionic strength of 2.0 M. This contraction is attributed to the shrinkage of the diffuse double layer around clay particles, caused by the injection of a high concentration of saline

solutions. The increased ionic strength compresses the electrical double layer, reducing the clay's volume and thereby slightly decreasing the radial stress.

Overall, the effect of pure chemical diffusion on radial stress is minor but consistent with the expected physicochemical interactions within the clay matrix.

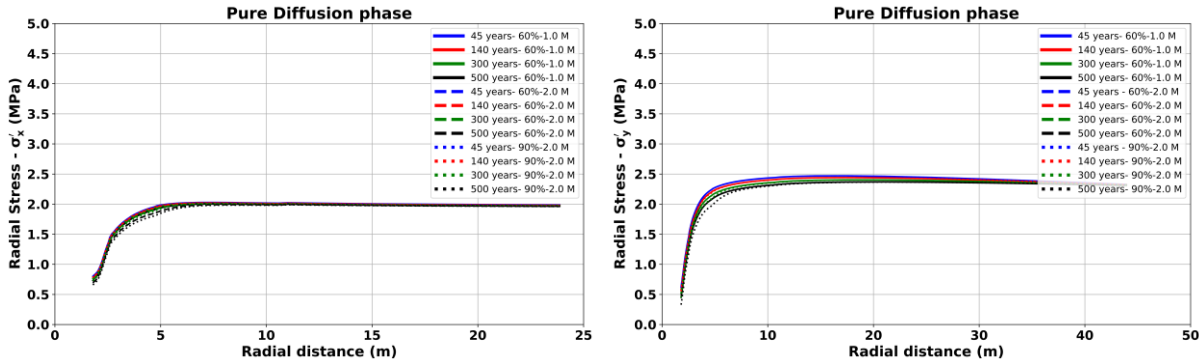

(a) : Horizontal Profile (b) : Vertical Profile

Figure 107 Evolution of radial stress during the swelling phase: (a) horizontal profile, (b) vertical profile.

Figure 108a and Figure 108b illustrate the distribution of orthoradial stress during the pure diffusion phase for the horizontal and vertical profiles, respectively. As in the previous phase, only the pure diffusion of the saline plume from bituminized waste is considered—no mechanical or swelling disturbances are introduced at this stage.

For both profiles, the results show a clear effect of solute concentration and sodium occupancy on the orthoradial stress. In particular, for the case with 90% sodium occupancy and 2.0 M concentration, a noticeable contraction of the clay is observed. This contraction results from the high concentration of the diffused saline plume affecting the clay's diffuse double layer.

Importantly, this contraction occurs in the opposite direction of the y-axis, which explains the reduction in orthoradial stress. This opposite movement leads to a clear decrease in orthoradial stress values, highlighting the sensitivity of the clay's stress response to chemical diffusion effects during this phase.

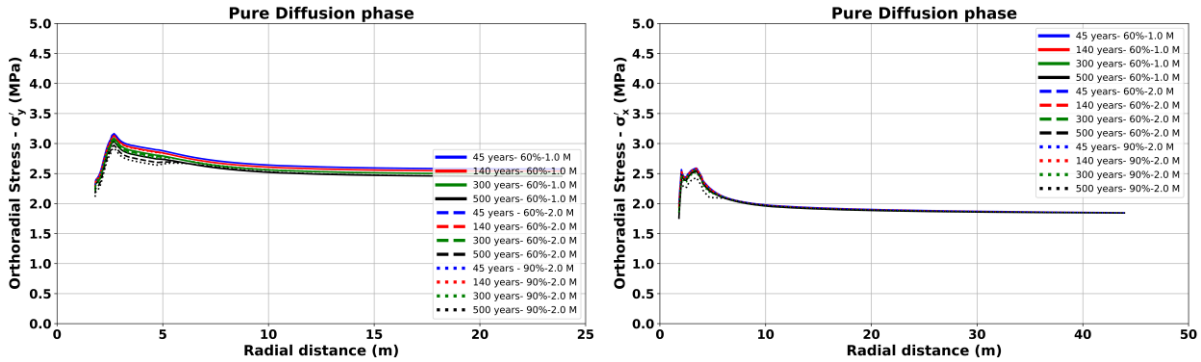

(a) : Horizontal Profile (b) : Vertical Profile

Figure 108 Evolution of orthoradial stress during the pure diffusion phase: (a) horizontal profile, (b) vertical profile.

It is important to note that, due to the negligible impact of the pure diffusion phase on the mechanical behavior of the clay, no significant change was observed in the stress path during this phase. The stress response remained almost entirely within the elastic domain, with virtually no noticeable evolution in the mean effective stress (p′) or deviatoric stress (q). As a result, the stress path remained practically unchanged and did not exhibit any meaningful deviation. For this reason, the stress path corresponding to the pure diffusion phase is not presented in this work.

3.5 Pure swelling vs pure diffusion

This section presents a comparative analysis of the hydro-mechanical responses of Boom Clay under two isolated scenarios: pure swelling of bituminized waste and pure diffusion of different saline solutions. The parameters examined include pore water pressure, radial displacement, radial stress, and orthoradial stress, with results shown for both the horizontal and vertical profiles. The objective is to clearly distinguish the contributions of swelling and diffusion processes in the global behavior of the system.

Figure 109a and Figure 109b illustrate the evolution of pore water pressure, which spans a total duration of 500 years, in the horizontal and vertical profiles, respectively. The time legend shown in these figures corresponds exclusively to this phase. The results show that there is almost no noticeable difference between the swelling scenario and the pure diffusion scenario in terms of pore water pressure distribution. This observation suggests that neither the swelling of the bituminized waste nor the diffusion of saline solutions is the dominant factor influencing pore pressure at this stage.

Instead, the continued increase in pore water pressure observed in both cases appears to be part of a progressive and ongoing process that began during the equilibrium phase. In that earlier phase, pore water pressure had not yet fully stabilized due to the slow nature of hydraulic equilibration in Boom Clay. As a result, the increase seen in the current phase reflects the natural continuation of the clay's response toward hydraulic equilibrium, rather than a direct effect of swelling pressure or solute diffusion.

This finding confirms that the evolution of pore water pressure in this phase is not driven by newly introduced mechanical or chemical perturbations, but rather by the time-dependent behavior of the clay as it seeks to reach a fully balanced pore pressure state. It also reinforces the idea that swelling and diffusion have negligible impact on pore pressure during this stage, and that the system requires a longer timeframe to complete equilibration.

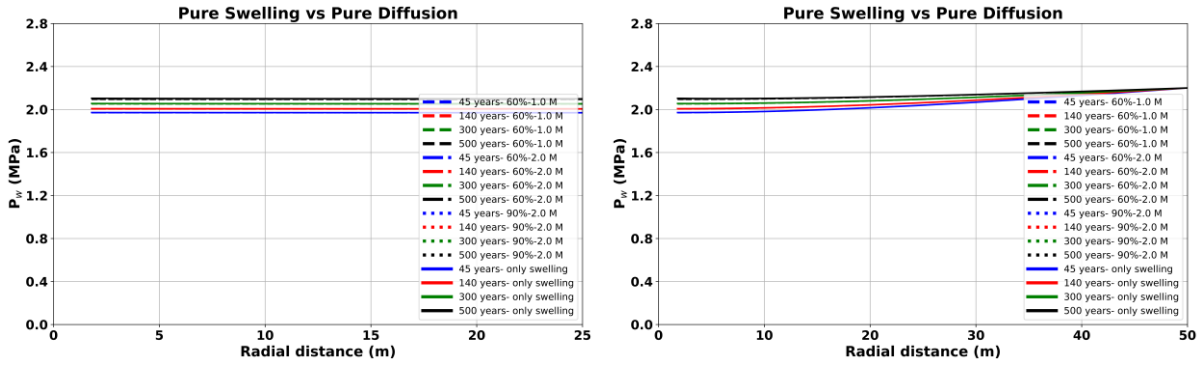

(a) : Horizontal Profile (b) : Vertical Profile

Figure 109 Evolution of pore water pressure along (a) horizontal and (b) vertical profiles during pure swelling and pure diffusion phases.

Figures Figure 110a and Figure 110b present the comparison of radial displacement evolution along the horizontal and vertical profiles during the pure swelling and pure diffusion phases. The results clearly demonstrate that swelling exerts a dominant influence on the deformation behavior of the clay.

In both profiles, the application of swelling pressure leads to a significant outward displacement of the clay matrix, especially near the gallery wall. This displacement gradually diminishes with increasing radial distance, illustrating the localized nature of the swelling-induced deformation.

Conversely, under pure diffusion conditions, the clay remains largely unaffected. The radial displacements are negligible, with only a very slight contraction observed after

500 years—specifically under the extreme chemical conditions of 2.0 M ionic strength and 90% sodium occupancy. This minor contraction results from the chemical shrinkage of the diffuse double layer, not from mechanical loading.

These findings clearly confirm that swelling of the bituminized waste is the principal driver of radial displacement, while the impact of chemical diffusion alone is insignificant in terms of mechanical deformation.

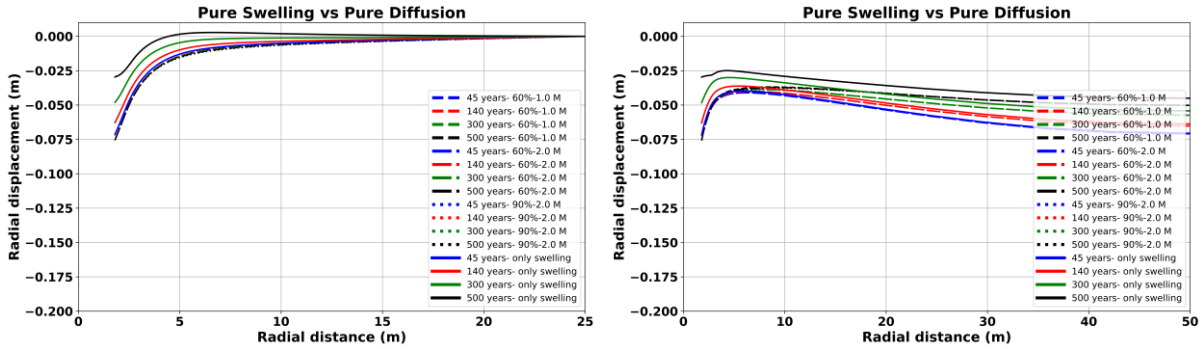

(a) : Horizontal Profile (b) : Vertical Profile

Figure 110 Comparison of radial displacement evolution under pure swelling and pure diffusion conditions for (a) horizontal and (b) vertical profiles.

Figure 111a and Figure 111b present a comparative analysis of the evolution of radial stress for both horizontal and vertical profiles under pure swelling and pure diffusion conditions.

In the case of pure swelling, a significant increase in radial stress is observed in both profiles. This increase is primarily attributed to the mechanical pressure exerted by the expanding clay matrix on the surrounding concrete liner. The maximum radial stress is located at the clay–concrete interface, and it gradually decreases with increasing radial distance into the clay body. This stress distribution reflects the progressive development of swelling pressure as the bituminized waste expands, inducing a pronounced mechanical loading on the near-field clay.

Conversely, under pure diffusion conditions, the radial stress remains largely unchanged throughout the simulation period. Only a very minor reduction or relaxation in radial stress is detected, which can be linked to the slight contraction of the clay caused by the shrinkage of the diffuse double layer under high salinity conditions (e.g., 2.0 M ionic strength with 90% sodium occupancy). However, this effect is minimal and remains highly localized near the source of chemical perturbation.

These findings reaffirm that the swelling of the bituminized waste is the dominant mechanism driving the evolution of radial stress, while the impact of saline diffusion is negligible in terms of mechanical response.

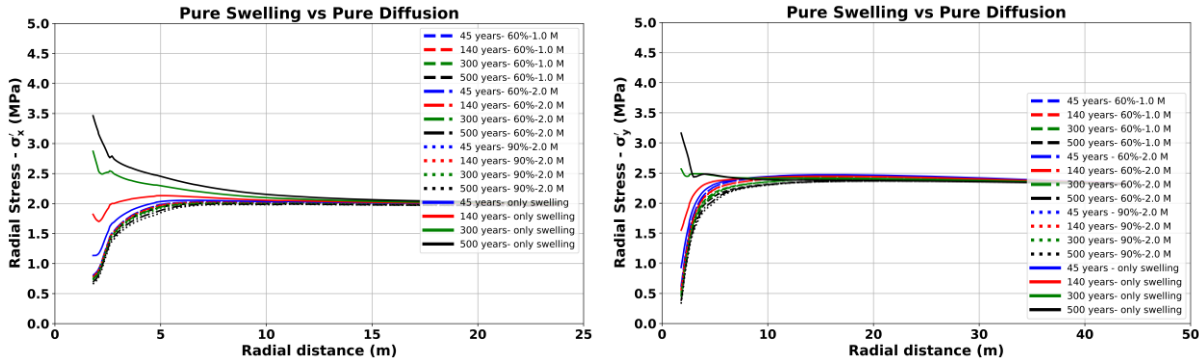

(a) : Horizontal Profile (b) : Vertical Profile

Figure 111 Comparison of radial stress evolution under pure swelling and pure diffusion conditions for (a) horizontal and (b) vertical profiles.

Figures Figure 112a and Figure 112b present the comparison of the orthoradial stress evolution for both horizontal and vertical profiles under pure swelling and pure diffusion conditions. The orthoradial stress response further illustrates the distinct effects of these two mechanisms. In the swelling scenario, a significant decrease in orthoradial stress is observed near the gallery wall, especially in the vertical profile. This reduction reflects the stress redistribution caused by the outward swelling of the clay, which relieves stress in the circumferential direction.

In contrast, the pure diffusion scenario results in only a modest reduction in orthoradial stress, particularly noticeable under the 90% sodium occupancy and 2.0 M ionic strength condition. This decrease is attributed to the inward contraction of the clay matrix, driven by the chemical shrinkage of the diffuse double layer. Since this contraction occurs in a direction opposite to the y-axis, it results in a localized stress decrease. Nevertheless, the magnitude and spatial extent of the stress changes remain limited in the diffusion case. Overall, the swelling of the bituminized waste is clearly the dominant factor influencing orthoradial stress, while diffusion-induced changes are secondary and spatially confined.

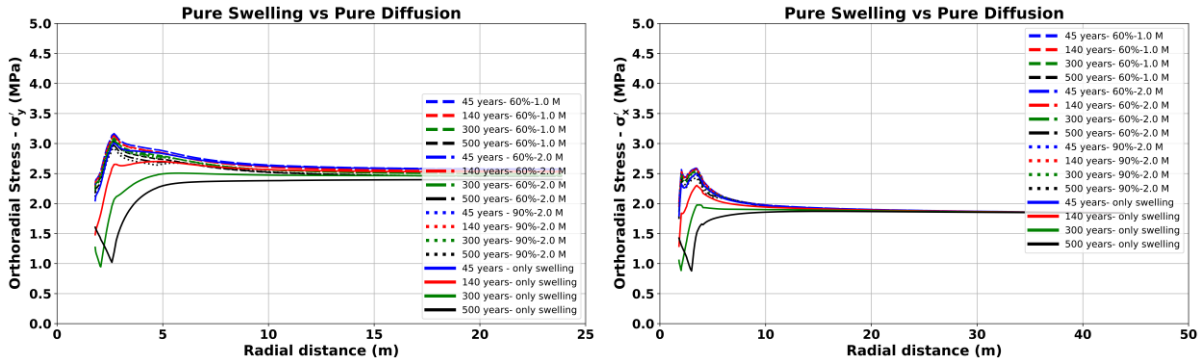

(a) : Horizontal Profile (b) : Vertical Profile

Figure 112 Comparison of radial stress evolution under pure swelling and pure diffusion conditions for (a) horizontal and (b) vertical profiles.

In summary, across all hydro-mechanical parameters and both spatial profiles, the main controlling factor is the swelling behavior of the bituminized waste. The effect of pure diffusion, even under high concentration and sodium occupancy conditions, remains secondary or negligible in terms of mechanical impact. The distinction between the two scenarios clearly highlights the mechanical dominance of swelling over chemical diffusion in the current modeling context.

3.6 Swelling + Diffusion phase

In this section, the most realistic simulation case is analyzed, involving the simultaneous effects of swelling of the bituminized waste and chemical diffusion of saline solutions through the concrete liner into the surrounding Boom Clay. It is important to note that the imposed chemical concentrations—1.0 M and 2.0 M, with 60% and 90% sodium occupancy—are hypothetical and intentionally high. These concentrations are not representative of expected in-situ values, but they were chosen deliberately to assess and highlight the potential hydro-mechanical consequences of elevated ionic strength on Boom Clay behavior. The goal is to evaluate how these extreme chemical conditions, when superimposed with swelling, might influence pore pressure evolution, deformation, and stress redistribution.

Figures Figure 113a and Figure 113b illustrate the evolution of pore water pressure (Pw) in the horizontal and vertical profiles, respectively, for the coupled case involving both swelling of the bituminized waste and chemical diffusion of saline solutions. Note that the time legend shown in these figures corresponds exclusively to this phase (500 years).

It is important to emphasize that the observed increase in pore water pressure in this phase is not directly caused by swelling or chemical diffusion. Rather, it represents a continued evolution from the previous equilibrium phase, where the system had not yet reached full hydraulic equilibrium. Due to the low permeability of Boom Clay, the re-increase of pore pressure occurs progressively as part of a long-term equilibration process.

The simulations show that whether swelling or high-concentration diffusion is present, the resulting pore pressure profiles remain nearly identical. This confirms that the pore pressure increase is primarily a time-dependent continuation of the equilibrium mechanism, not significantly influenced by either mechanical swelling or chemical effects. The contributions of these two processes to pore pressure evolution are therefore negligible, reinforcing the conclusion that hydraulic re-equilibration dominates in this phase.

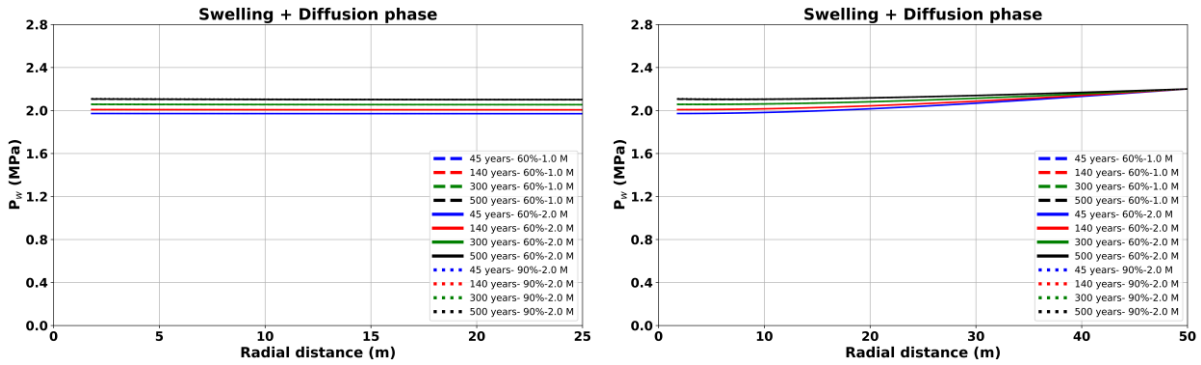

(a) : Horizontal Profile (b) : Vertical Profile

Figure 113 Evolution of pore water pressure in (a) horizontal and (b) vertical profiles during coupled swelling and saline diffusion phase

Figure 114a and Figure 114b illustrate the evolution of radial displacement in both the horizontal and vertical profiles under the combined effect of swelling and saline diffusion. The results clearly show that the dominant mechanism governing the radial displacement is the swelling of the bituminized waste, which induces a significant outward expansion of the clay matrix, particularly near the gallery wall.

A slight reduction in radial displacement is observed for the case of high salinity (2.0 M) and 90% sodium occupancy. This minor contraction can be attributed to the shrinkage of the diffuse double layer due to the ingress of high ionic strength solutions. However, this effect remains extremely limited. Although such contraction was more

visible under pure diffusion conditions, it is now largely masked by the expansive forces generated by the swelling process.

Therefore, the overall deformation profile is still predominantly controlled by the swelling mechanism. The chemical diffusion—even under highly exaggerated and hypothetical salinity conditions—contributes only marginally to the total mechanical response of Boom Clay.

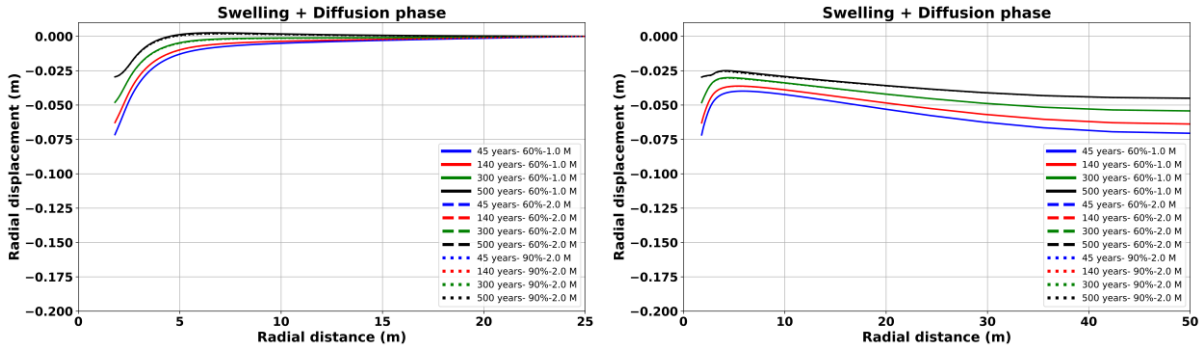

(a) : Horizontal Profile (b) : Vertical Profile

Figure 114 Evolution of radial displacement in (a) horizontal and (b) vertical profiles during coupled swelling and saline diffusion phase.

Figure 115a and Figure 115b present the evolution of radial stress in the horizontal and vertical profiles, respectively, under the combined influence of bituminized waste swelling and diffusion of highly concentrated saline solutions.

The results demonstrate that the primary contributor to radial stress is the mechanical pressure generated by the swelling clay as it pushes outward against the concrete liner. This leads to a significant increase in radial stress, especially near the clay–concrete interface, which progressively reduces with increasing radial distance from the cavity.

However, in the case of the highest salinity condition (2.0 M and 90% sodium occupancy), a slight reduction in radial stress can be observed. This localized decrease is due to the contraction of the diffuse double layer—a chemical shrinkage effect triggered by the elevated ionic strength of the diffusing solution. Despite its presence, this contraction effect remains relatively minor and localized.

Overall, the results confirm that swelling governs the mechanical response, while the influence of chemical diffusion—even at elevated concentrations—remains marginal.

The combined scenario shows that any contraction due to chemical effects is clearly dominated by the expansive mechanical behavior associated with swelling.

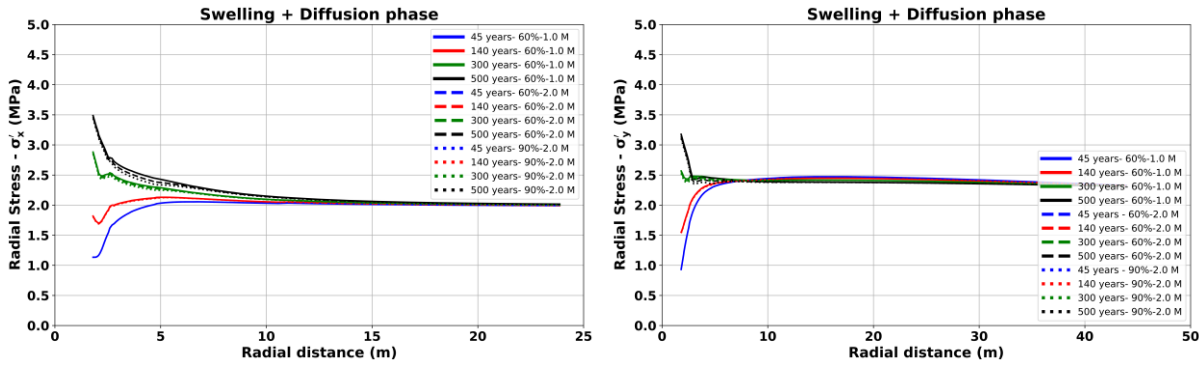

(a) : Horizontal Profile (b) : Vertical Profile

Figure 115 Evolution of radial displacement in (a) horizontal and (b) vertical profiles during coupled swelling and saline diffusion phase.

Figures Figure 116a and Figure 116b illustrate the evolution of orthoradial stress in the horizontal and vertical profiles, respectively, considering the combined scenario of swelling from bituminized waste and the diffusion of highly concentrated saline solutions.

The results show that the orthoradial stress undergoes a clear reduction, especially near the gallery wall, as a direct consequence of the swelling-induced expansion of the Boom Clay. This reduction is more pronounced in the vertical profile, where the anisotropic boundary conditions allow more vertical deformation, leading to a more evident redistribution of stress.

In addition to the dominant swelling effect, a slight additional reduction in orthoradial stress is observed under the condition of high ionic strength (2.0 M) and 90% sodium occupancy. This localized decrease is attributed to the inward contraction of the clay, driven by chemical shrinkage effects associated with the collapse of the diffuse double layer. Importantly, this contraction acts in the direction opposite to the y-axis, further reducing the orthoradial stress in that orientation.

Nevertheless, this chemical influence remains minor compared to the mechanical impact of swelling. The orthoradial stress response is still overwhelmingly governed by the swelling mechanism, while chemical diffusion introduces only a small, localized perturbation.

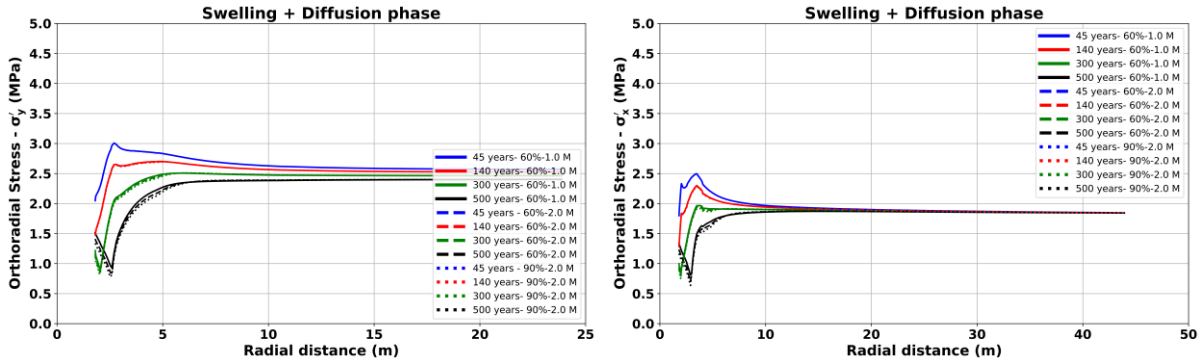

(a) : Horizontal Profile (b) : Vertical Profile

Figure 116 Evolution of radial displacement in (a) horizontal and (b) vertical profiles during coupled swelling and saline diffusion phase.

Figure 117a, Figure 117c, and Figure 117e present the effective stress path for element B′, located next to the gallery wall in the horizontal profile, while Figure 117b, Figure 117d, and Figure 117f show the stress path for element F′, situated adjacent to the excavated wall in the vertical profile. These plots illustrate the evolution of effective stress in the $q-p'$ space across all simulation phases, including the combined swelling and diffusion phase under different concentrations and sodium occupancies.

In both the horizontal and vertical profiles, the stress paths follow a broadly similar sequence of evolution throughout the different phases. However, during the excavation phase, a rapid initial drop in deviatoric stress (q) is observed only in the vertical profile, due to the sudden stress release near the cavity wall. Following this, both profiles exhibit a linear increase in q while the mean effective stress (p′) remains nearly constant—characteristic of the mechanical response of the clay under rapid unloading. Shortly thereafter, an elastic unloading phase occurs when the clay comes into contact with the concrete liner. This interaction induces a localized stress redistribution, resulting in a brief decrease in q and a corresponding increase in p′, reflecting the mechanical constraint imposed by the liner.

Shortly afterward, an elastic unloading takes place when the clay comes into contact with the concrete liner. This contact induces a localized redistribution of stresses, resulting in a brief decrease in q coupled with an increase in p', reflecting the mechanical stabilization imposed by the liner.

During the drained phase, p' progressively increases as pore water pressure dissipates, indicating a recovery of effective stress within the clay matrix.

Simultaneously, q decreases slightly, showing a gradual relaxation of shear stress as the soil adapts to the evolving hydraulic conditions under drained loading.

In the equilibrium phase, pore water pressure rises again as the system undergoes long-term hydraulic re-equilibration. Consequently, p' decreases significantly, while q increases, representing a reverse trend compared to the drained phase. This behavior is driven by the slow, diffusion-controlled re-saturation of the low-permeability Boom Clay and reflects a delayed hydro-mechanical response under nearly undrained conditions.

Finally, in the swelling and diffusion phase, the imposed swelling pressure at the concrete–clay interface and the fixed concentration in the perturbed zone cause further evolution of the stress state. Initially, q experiences a slight decrease, followed by a steady increase in both p' and q. This indicates the mechanical effect of the clay swelling and pushing against the rigid concrete structure. The stress path ultimately reaches the inner yield surface and approaches the Critical State Line (CSL), illustrating plastic hardening behavior within the inner yield surface. This trajectory is typical of one-dimensional loading and aligns with the simulation's boundary conditions, which include fixed lateral and vertical displacements and swelling pressure applied only at the clay–concrete interface.

Overall, it is evident that all stress paths share a similar trend, confirming the consistent mechanical response of Boom Clay under the combined effects of swelling and chemical diffusion across different conditions.

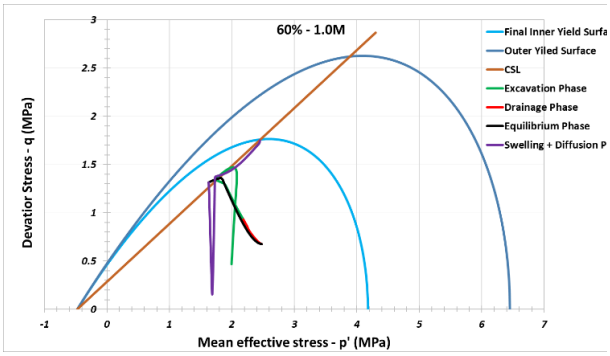

(a) : B' – Horizontal Element

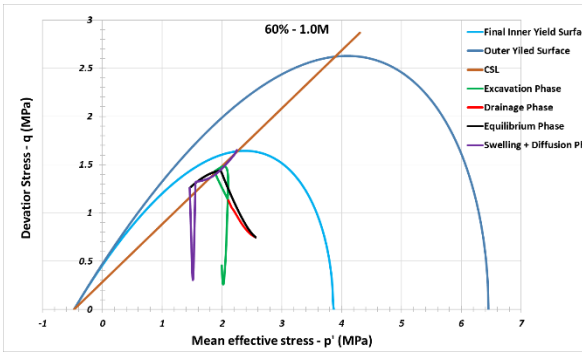

(b) : F' – Vertical Element

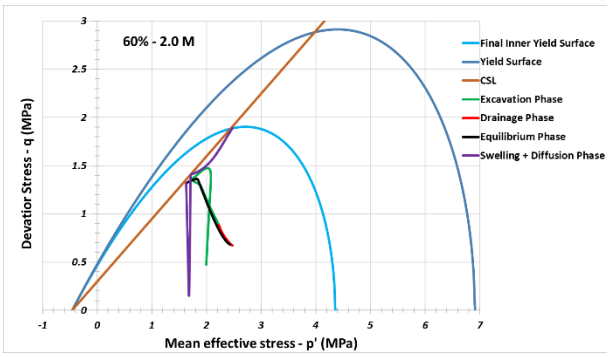

(c) : B' – Horizontal Element

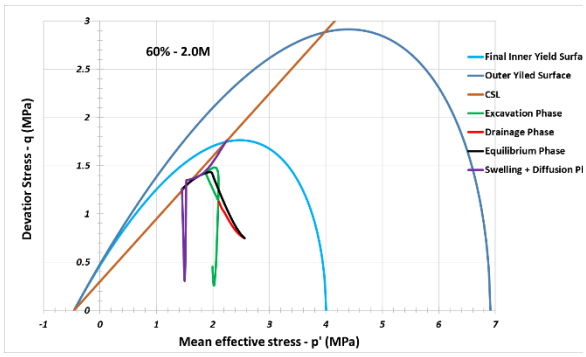

(d) : F' – Vertical Element

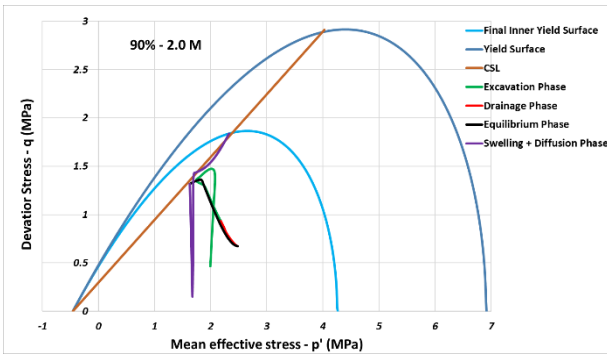

(e) : B' – Horizontal Element

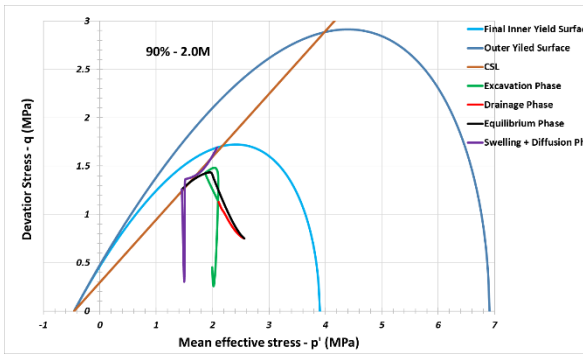

(f) : F' – Vertical Element

Figure 117 Effective stress paths (q–p') at elements B' (horizontal profile) and Fi' (vertical profile) during all simulation phases, including swelling and diffusion under varying saline concentrations and sodium occupancies.

To better understand the specific effects of sodium occupancy and ionic strength on Boom Clay behavior, Figure 118a and Figure 118b present the effective stress paths during the swelling and diffusion phase only for both horizontal and vertical element, respectively. This focused view isolates the impact of chemical conditions on the stress evolution, excluding the preceding phases.

The results reveal slight differences in the stress paths associated with higher ionic strength and sodium occupancy. Notably, an increase in shear strength is observed, which can be attributed to the hardening effect caused by the clay matrix's delayed densification resulting from chemical shrinkage. This shrinkage reduces the diffuse double layer thickness, promoting a subtle contraction in the clay structure and thus enhancing its mechanical stiffness.

Overall, these variations highlight the coupled chemo-mechanical influence of ionic concentration and sodium occupancy, where increased salinity and sodium levels induce a mild hardening effect in the Boom Clay during the swelling and diffusion phase.

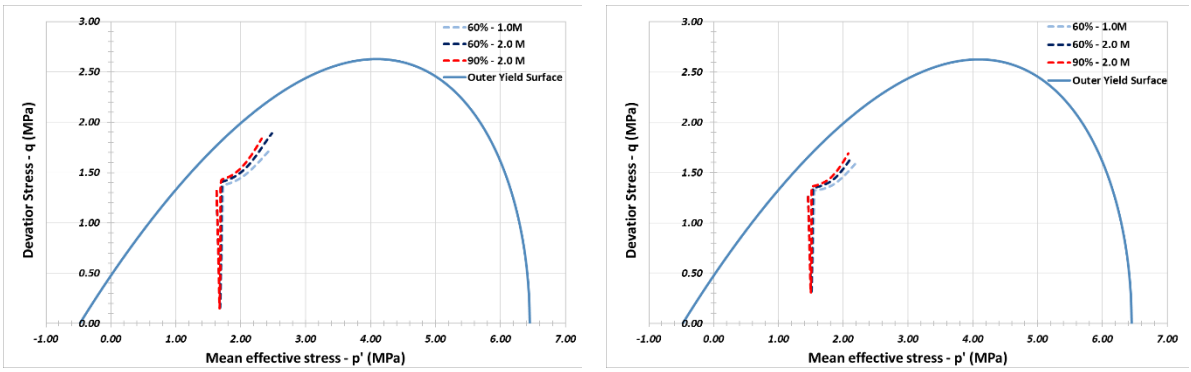

(a): Horizontal Element (b): Vertical Element

Figure 118 Stress path (q–p') during swelling and diffusion phase for different salinity conditions (1.0 m and 2.0 m, 60% and 90% na^+ occupancy): (a) horizontal element, (b) vertical element.

4. Conclusion

This chapter aimed to evaluate the hydro-mechanical behavior of Boom Clay (BC) around a single disposal gallery, representative of a larger network of galleries within a deep geological repository. A multi-phase numerical simulation framework was used to progressively isolate and then combine the effects of excavation, drainage, swelling of bituminized waste, and chemical diffusion of highly concentrated saline solutions.

The simulation of pure diffusion of saline plumes—imposed with exaggerated ionic strengths and sodium occupancies—demonstrated minimal impact on the hydro-mechanical response. Slight localized effects, such as minor contraction of the clay matrix and small changes in stress fields, were observed, particularly under the 2.0 M / 90% sodium occupancy condition. However, these effects remained within the elastic domain and produced negligible evolution in the stress path.

In contrast, the swelling of bituminized waste exhibited a dominant influence. It caused substantial outward radial displacement and increased radial stresses near the gallery wall, accompanied by a noticeable reduction in orthoradial stress due to the expansion of the clay. When swelling and chemical diffusion were combined, the swelling clearly remained the primary driver of deformation and stress redistribution. Even under the most chemically aggressive conditions, the influence of diffusion was secondary—merely modulating the local mechanical response without altering the global trends.

The radial and orthoradial stresses showed distinct patterns driven by swelling, while diffusion contributed only slight contractions or stress relaxations in high-concentration scenarios. The analysis of stress paths at critical locations near the gallery wall

revealed consistent behavior across both horizontal and vertical profiles. During excavation, Boom Clay exhibited a rapid undrained response, characterized by an initial drop in deviatoric stress (only in vertical profile) followed by a linear increase, with elastic unloading upon contact with the concrete liner. The subsequent drained phase showed recovery of effective stress as pore pressures dissipated, while the equilibrium phase featured a reverse trend: pore pressure rise led to reduced effective stress and increased shear stress due to slow hydraulic re-equilibration. The swelling phase concluded with a plastic hardening response, as the stress paths evolved toward the inner yield surface and approached the Critical State Line—typical of a constrained, one-dimensional loading condition.

Overall, this chapter demonstrates that the swelling of bituminized waste and its mechanical interaction with Boom Clay are the predominant factors affecting the hydro-mechanical state around the disposal gallery. Chemical diffusion alone introduces only minor perturbations, primarily affecting pore pressures and local stress conditions. These findings enhance our understanding of coupled chemo-hydro-mechanical processes in Boom Clay and validate the modeling approach used for simulating such interactions in engineered barrier systems.

VII. Conclusions and Perspectives

1. Conclusions

This thesis presents a comprehensive study of the chemo-hydro-mechanical (CHM) behavior of intact Boom Clay. The work combines laboratory experiments, constitutive modeling, and large-scale numerical simulations to better understand how chemical changes—especially related to sodium occupancy and ionic strength—interact with the hydraulic and mechanical behavior of Boom Clay. These investigations are conducted in the context of deep geological disposal of radioactive waste, where maintaining the integrity of the clay barrier is a key requirement.

The study begins with a review of the current state of knowledge. This review shows that the behavior of clay is influenced by many factors, including mineralogy, pore water chemistry, and applied stress. While progress has been made in understanding hydro-mechanical responses, previous research often focused on reconstituted or unsaturated materials, with limited attention to the behavior of intact Boom Clay under chemically aggressive conditions. The role of ion occupancy in percolating solutions was also underexplored.

To address these gaps, an experimental program was designed to investigate the effects of ionic strength and cation composition, with a special focus on sodium occupancy. The tests showed that high sodium concentrations and occupancies influence clay behavior by changing double-layer interactions and interparticle forces. These results clarified several mechanisms but are valid only under the conditions tested—namely high ionic strength and sodium levels—which were deliberately chosen to be more aggressive than those expected around a geological disposal facility (GDF) (e.g., $NaNO_3$ solutions up to 2 M and Na occupancies up to 90%). This approach helped assess the limits of chemical influence on Boom Clay.

One-dimensional swelling tests showed that higher ionic strength reduces swelling potential by compressing the diffuse double layer. Replacing divalent cations like calcium with sodium reduced the hydrated radius and repulsive forces between clay particles, leading to a denser structure and lower swelling pressure.

Hydraulic conductivity measurements indicated an increase in permeability under high ionic strength conditions. This trend was supported by mercury intrusion porosimetry

(MIP) results, which revealed a rise in macroporosity, suggesting the formation of preferential flow paths. It is further suggested that reduced interlayer spacing could have contributed to this increase in permeability; however, this hypothesis remains not confirmed, as interlayer distances were not directly measured or inferred from the available data. These observations highlight the coupled influence of chemical environment and mechanical state on the transport behavior of Boom Clay.

Volume change tests at constant stress revealed that the deformation of Boom Clay depends on confinement. Above a certain stress (around 0.7 – 0.8 MPa), deformations were reversible, but below this threshold, they became irreversible. This stress dependency shows that the chemical sensitivity of Boom Clay is stronger under low confinement. High Ionic Strength also caused osmotic consolidation, which reduced compressibility and increased stiffness due to microstructural densification.

Triaxial tests under various chemical and mechanical conditions showed that the overconsolidation ratio (OCR) influences failure behavior. Overconsolidated samples showed dilation and softening, while normally consolidated ones contracted more. Increasing salinity raised the internal friction angle and stiffness by shrinking the diffuse double layer and bringing clay particles closer. However, changes in cohesion were limited. Pore pressure responses during undrained loading also increased with salinity, confirming the chemical effect on transient mechanical behavior.

These experimental results confirm a strong link between chemical conditions and mechanical response. Sodium occupancy and Ionic Strength play an active role in controlling key properties such as stiffness, permeability, and deformation thresholds. Still, under realistic disposal conditions, chemical effects remained moderate. Even in highly aggressive chemical environments, Boom Clay maintained its strength and barrier properties, confirming its potential for long-term containment of radioactive waste.

Alongside the experimental work, new developments were introduced in the ACC-2 constitutive model. The ACC-2 model was first adapted to account for in-situ pore water condition through the inclusion of a cohesion term in both the yield surface and flow rule, improving its ability to reproduce observed mechanical responses. A chemo-elasto model was also developed within the ACC-2 framework to incorporate chemical effects into the elastic strain response. This model included an updated treatment of

sodium occupancy and ionic strength, along with several mechanical parameters.These additions were based on experimental results and allowed the model to simulate the reversible chemical effects observed. Chemical strain was assumed to be elastic and volumetric, without plasticity. A parametric study confirmed the model's sensitivity to chemical and mechanical parameters. The swelling line slope (κ) was also investigated. Although usually considered constant, it appeared to influence softening behavior under low stress. This suggests that κ may depend on stress level and should be reconsidered in future models, possibly by redefining bulk modulus or using a more advanced hardening law for preconsolidation pressure.

Numerical simulations of a disposal gallery at the repository scale were then carried out. These simulations showed that the swelling of bituminized waste had the greatest impact on mechanical behavior, while chemical effects were more localized and secondary. The less severe chemical conditions used in these simulations compared to laboratory tests explain the smaller influence of chemistry at repository scale. These results highlight the need to consider both mechanical and chemical processes to understand the long-term evolution of the system.

In conclusion, this work provides a detailed and integrated view of Boom Clay's behavior under chemical, hydraulic, and mechanical influences. Laboratory tests, modeling, and simulations demonstrate that Boom Clay can remain stable even under aggressive chemical conditions—worse than those expected near a GDF. These findings support its use as a host rock for radioactive waste disposal and offer a solid base for future improvements in testing methods and predictive models.

2. Perspectives

This thesis presents a detailed study of the chemo-hydro-mechanical (CHM) behavior of Boom Clay under saline conditions, with a focus on the geological disposal of Eurobitum waste. While the results provide meaningful insights, further research is needed to broaden process understanding and improve model predictions.

The findings are based on a limited number of well-controlled laboratory tests. To strengthen confidence in the observed trends, repeated experiments are recommended to confirm their consistency and reproducibility.

A key area for future research is the effect of repeated salinization and desalinization cycles. Boom Clay is considered a reference host formation in Belgium, and its response to such chemical fluctuations is critical for assessing long-term repository performance. Special attention should be given to the role of sodium, whose smaller hydrated radius reduces interlayer spacing, affecting swelling and shrinkage. The influence of other environmentally relevant cations, such as calcium and magnesium, also needs to be investigated. These cations differ in valency and hydration properties, which may impact the clay's structure and mechanical behavior. Targeted laboratory studies are necessary to better characterize these ion-specific effects.

In addition to saline environments, future investigations should also consider the impact of hyperalkaline solutions, which may be released by engineered barriers such as concrete. These high-pH fluids can diffuse into the surrounding clay and trigger mineralogical alterations or affect interparticle forces, potentially modifying the hydro-mechanical behavior of Boom Clay in ways not addressed by the current study.

Long-term creep and recovery tests under saline conditions could provide further understanding of time-dependent behavior. High salinity may increase permeability by forming preferential flow paths. It is important to observe whether these paths eventually close due to the self-sealing capacity of Boom Clay. Tracking this evolution would give valuable information on long-term hydraulic performance.

To improve predictive models, it is important to perform chemo-mechanical tests under varying chemical environments and mechanical loading paths. The current model assumes elastic and reversible chemical strains. However, some test results indicate the presence of irreversible strains, especially under low stress. Expanding the experimental dataset to cover a wider range of ionic strengths, cation compositions, and stress conditions will support the development of models that account for these complex behaviors.

Model refinements should also include the introduction of plastic chemical strain components to capture permanent microstructural changes. In addition, parameters such as swelling slope and hardening modulus should be made dependent on chemical and mechanical history, rather than treated as constant. New hardening laws reflecting this dependency would improve the model accuracy.

Integrating microstructural observations into model calibration is another important step. Techniques such as SEM, XRD, and ESEM offer detailed information on pore structure and particle arrangement. These data can help link micro-scale chemical effects to macro-scale behavior, leading to better-informed constitutive models.

The use of three-dimensional numerical simulations is also necessary. Moving from 2D to 3D enables more realistic representation of repository designs, geological features, and boundary conditions, which are needed to conduct accurate safety assessments.

Finally, time-dependent processes such as creep and chemical aging should be investigated further through coordinated experimental and modeling work. Understanding how Boom Clay evolves under long-term mechanical and chemical loads will improve the evaluation of repository performance over geological timescales.

These research directions aim to deepen the understanding of coupled chemo-hydro-mechanical processes in Boom Clay and enhance the reliability of predictive tools, ultimately supporting the long-term safety assessment of geological disposal systems.

« La patience est amère, mais son fruit est doux. »

— Jean-Jacques Rousseau

List of Figures

List of Tables

Bibliography

Adachi T, Oka F. Constitutive equations for normally consolidated clay based on elasto-viscoplasticity. Soils and Foundations 1982:22(4), 57-70.

Aertsens M, Wemaere I, Wouters L. Spatial variability of transport parameters in the Boom Clay. Applied Clay Science 2004;26:37–45. https://doi.org/10.1016/j.clay.2003.09.015.

AFNOR N. P94-078: Sols: reconnaissance et essais-Indice CBR après immersion. Indice CBR immédiat. Indice Portant Immédiat-Mesure sur échantilllon compacté dans le moule CBR, AFNOR. 1997.

Afnor NNP 94-070. Essais au labo, Essais mécanique. "Reconnaissances et essais- Essai à l'appareil triaxial de révolution. 1994.

Al Mais H, Cui YJ, Levasseur S, Valcke E, Seetharam S, Georgieva T, et al. Impact of (Na,Ca)NO3 concentration on the deviatoric mechanical behaviour of Boom Clay. Canadian Geotechnical Journal 2025a.

Al Mais H, Cui Y-J, Li X-L, Seetharam S, Valcke E, Wang L, et al. Effect of sodium occupancy and solute concentration on the swelling pressure and hydraulic conductivity of Boom Clay. Can Geotech J 2025b;62:1–17. https://doi.org/10.1139/cgj-2024-0393.

Al Mais H, Cui YJ, Li XL, Seetharam S, Valcke E, Wang L, et al. Effect of sodium occupancy and solute concentration on the swelling pressure and hydraulic conductivity of Boom Clay. Canadian Geotechnical Journal 2024:62: 1-17. https://doi.org/10.1139/cgj-2024–0393.

Al Mais H, Cui YJ, Valcke E, Li XL, Seetharam S, Georgieva T, et al. Effects of percolation of (Na,Ca)NO3 solutions on the volume change behaviour and microstructure of Boom Clay. Journal of Rock Mechanics and Geotechnical Engineering 2025c:17.

Alawaji HA. Swell and compressibility characteristics of sand–bentonite mixtures inundated with liquids. Applied Clay Science 1999;15:411–30. https://doi.org/10.1016/S0169-1317(99)00033-2.

Alonso EE, Gens A, Josa A. A constitutive model for partially saturated soils. Géotechnique 1990;40:405–30. https://doi.org/10.1680/geot.1990.40.3.405.

Alonso EE, Vaunat J, Gens A. Modelling the mechanical behaviour of expansive clays. Engineering Geology 1999;54:173–83. https://doi.org/10.1016/S0013-7952(99)00079-4.

Ammann L, Bergaya F, Lagaly G. Determination of the cation exchange capacity of clays with copper complexes revisited. Clay Miner 2005;40:441–53. https://doi.org/10.1180/0009855054040182.

Anderson DC, Crawley W, Zabcik JD. Effects of various liquids on clay soil: bentonite slurry mixtures. ASTM International; 1985.

Arasan S. Effect of chemicals on geotechnical properties of clay liners: a review. Research Journal of Applied Sciences, Engineering and Technology 2010:2(8), 765–75.

Archer DG. Thermodynamic properties of the NaNO3+H2O system. Physical and Chemical Properties Division, National Institute of Standards and Technology 2000.

Arentsen M, Van Est R, editors. The Future of Radioactive Waste Governance: Lessons from Europe. Wiesbaden: Springer Fachmedien Wiesbaden; 2023. https://doi.org/10.1007/978-3-658-40496-3.

Attard P. Electrolytes and the electric double layer. 1996:92, 1–159.

Awarkeh M. Investigation of the long-term behaviour of Boom Clay. (Doctoral dissertation, Marne-la-vallée, ENPC); 2023.

Ayininuola GM, Agbede OA, Franklin SO. Influence of calcium sulphate on subsoil cohesion and angle of friction. J Appl Sci Res 2009:5(3), 297–304.

Bache BW. The measurement of cation exchange capacity of soils. J Sci Food Agric 1976;27:273–80. https://doi.org/10.1002/jsfa.2740270313.

Baeyens B, Maes, A, Cremers, A, Henrion PN. In situ physico-chemical characterization of Boom clay 1985.

Baldi G, Hight DW, Thomas GE. A reevaluation of conventional triaxial test methods. Advanced Triaxial Testing of Soil and Rock 1988:ASTM STP, 977, 219-263.

Baldi G, Hueckel T, Peano A, Pellegrini R. Developments in modelling of thermohydro-geomechanical behaviour of Boom clay and clay-based buffer materials (volume 2) (No. EUR–13365/2). Commission of the European Communities; 1991.

Barbour SL. Osmotic flow and volume change in clay soils. (Doctoral dissertation, University of Saskatchewan); 1986.

Barbour SL, Fredlund DG. Mechanisms of osmotic flow and volume change in clay soils. Canadian Geotechnical Journal 1989:26(4), 551–62.

Barbour SL, Yang N. A review of the influence of clay–brine interactions on the geotechnical properties of Ca-montmorillonitic clayey soils from western Canada. Canadian Geotechnical Journal 1993:30(6), 920–34.

Barnichon J-D, Volckaert G. HYDRO-MECHANICAL COUPLING IN THE BOOM CLAY (MOL URL, BELGIUM): RECENT IN-SITU OBSERVATIONS, PREDICTIONS AND PERSPECTIVES 2000.

Basma AA, Husein A. Laboratory assessment of swelling pressure of expansive soils. Applied Clay Science 1995.

Bastiaens W, Bernier F, Li XL. SELFRAC: Experiments and conclusions on fracturing, self-healing and self-sealing processes in clays. Physics and Chemistry of the Earth, Parts A/B/C 2007;32:600–15. https://doi.org/10.1016/j.pce.2006.04.026.

Bernier F, Li XL, Bastiaens W. Twenty-five years' geotechnical observation and testing in the Tertiary Boom Clay format. In Stiff Sedimentary Clays: Genesis and Engineering Behaviour: Géotechnique Symposium in Print 2007 2011:223–31.

Bésuelle P, Viggiani G, Desrues J, Coll C, Charrier P. A Laboratory Experimental Study of the Hydromechanical Behavior of Boom Clay. Rock Mech Rock Eng 2014;47:143–55. https://doi.org/10.1007/s00603-013-0421-8.

Bethke CM. Geochemical and biogeochemical reaction modeling. Cambridge university press; 2022.

Beyer M, Lau S, Knoche M. Studies on water transport through the sweet cherry fruit surface: IX. Comparing permeability in water uptake and transpiration. Planta 2005;220:474–85. https://doi.org/10.1007/s00425-004-1354-y.

Blanc P, Lassin A, Piantone P, Azaroual M, Jacquemet N, Fabbri A, et al. Thermoddem: A geochemical database focused on low temperature water/rock interactions and waste materials. Applied Geochemistry 2012:27(10), 2107–16.

Bleyen E N, Hendrix, K, Moors, H, Durce, D, Vasile, M,& Valcke. Biodegradability of dissolved organic matter in Boom Clay pore water under nitrate-reducing conditions: Effect of additional C and P sources. Applied Geochemistry 2018:92, 45-58.

Bleyen N, Mrien A, Valcke E. The geochemical perturbation of Boom Clay due to the NaNO3 plume released from Eurobitum bituminised radioactive waste: status 2013. Topical report SCK CEN reports (ER-0221).; 2018.

Bolt GH. Physico-Chemical Analysis of the Compressibility of Pure Clays. Géotechnique 1956;6:86–93. https://doi.org/10.1680/geot.1956.6.2.86.

Bonino GB. Grant, J.-The Measurement Of Hydrogen Ion Concentration. 1933.

Borja RI, Kavazanjian E. A constitutive model for the stress–strain–time behaviour of 'wet'clays. Geotechnique 1985:35(3), 283-298.

Boukpeti N, Charlier R, Hueckel T, Liu Z. A Constitutive Model for Chemically Sensitive Clays. In: Hack R, Azzam R, Charlier R, editors. Engineering Geology for Infrastructure Planning in Europe, vol. 104, Berlin, Heidelberg: Springer Berlin Heidelberg; 2004a, p. 255–64. https://doi.org/10.1007/978-3-540-39918-6_30.

Boukpeti N, Charlier R, Hueckel T, Liu Z. A Constitutive Model for Chemically Sensitive Clays. In: Hack R, Azzam R, Charlier R, editors. Engineering Geology for Infrastructure Planning in Europe, vol. 104, Berlin, Heidelberg: Springer Berlin Heidelberg; 2004b, p. 255–64. https://doi.org/10.1007/978-3-540-39918-6_30.

Bradbury MH, Baeyens B. Porewater chemistry in compacted re-saturated MX-80 bentonite. Journal of Contaminant Hydrology 2003;61:329–38. https://doi.org/10.1016/S0169-7722(02)00125-0.

Burland JB. On the compressibility and shear strength of natural clays. Géotechnique 1990:40(3), 329–78.

Calvello M, Lasco M, Vassallo R, Maio CD. Compressibility and residual shear strength of smectitic clays: influence of pore aqueous solutions and organic solvents 2005.

Castellanos E, Gens A, Romero E, Lloret A. Influence of water chemistry on the swelling capacity of a high-density bentonite. In Unsaturated Soils 2006 2006:962–72.

Castellanos E, Villar MV, Romero E, Lloret A, Gens A. Chemical impact on the hydro-mechanical behaviour of high-density FEBEX bentonite. Physics and Chemistry of the Earth, Parts A/B/C 2008;33:S516–26. https://doi.org/10.1016/j.pce.2008.10.056.

CEC. "Handbook of reference medium active waste (RMA)", EUR 12482, first edition. European Commission; 1989.

Chapman DL. A contribution to the theory of electrocapillarity. The London, Edinburgh, and Dublin Philosophical Magazine and Journal of Science 1913:25(148), 475–81.

Charlier R. Approche unifiée de quelques problèmes non linéaires de mécanique des milieux continus par la méthode des éléments finis (grandes déformations des métaux et des sols, contact unilatéral de solides, conduction thermique et écoulements en milieux poreux). PhD thesis, Faculty of Applied Sciences, University of Liège, Belgium; 1987.

Chen J, Fang Y, Gu R, Shu H, Ba L, Li W. Study on pore size effect of low permeability clay seepage. Arab J Geosci 2019;12:238. https://doi.org/10.1007/s12517-019-4375-3.

Chen X, Hicks MA. Unsaturated hydro-mechanical-chemo coupled constitutive model with consideration of osmotic flow. Computers and Geotechnics 2013;54:94–103. https://doi.org/10.1016/j.compgeo.2013.06.001.

Chen Y-G, Jia L-Y, Li Q, Ye W-M, Cui Y-J, Chen B. Swelling deformation of compacted GMZ bentonite experiencing chemical cycles of sodium-calcium exchange and salinization-desalinization effect. Applied Clay Science 2017;141:55–63. https://doi.org/10.1016/j.clay.2017.02.016.

Chen Y-G, Zhu C-M, Ye W-M, Cui Y-J, Wang Q. Swelling pressure and hydraulic conductivity of compacted GMZ01 bentonite under salinization–desalinization cycle conditions. Applied Clay Science 2015;114:454–60. https://doi.org/10.1016/j.clay.2015.06.033.

Chipera SJ, Carey JW, Bish DL. Controlled-humidity XRD analyses: Application to the study of smectite expansion/contraction. 1995.

Ciesielski H, Sterckeman T, Santerne M, Willery JP. A comparison between three methods for the determination of cation exchange capacity and exchangeable cations in soils. Agronomie 1997;17:9–16. https://doi.org/10.1051/agro:19970102.

Coll C. Endommagement des roches argileuses et perméabilité induite au voisinage d'ouvrages souterrains. Université Joseph-Fourier-Grenoble I); 2005.

Collin F, Li XL, Radu JP, Charlier R. Thermo-hydro-mechanical coupling in clay barriers. Engineering Geology 2002.

Cornell RM. Adsorption of cesium on minerals: a review. Journal of Radioanalytical and Nuclear Chemistry 1993:171, 483–500.

Cui YJ, Delage P, Alzoghbi P. Retention and transport of a hydrocarbon in a silt 2003.

Cui YJ, Delage P, Durand F, Schlosser F, Wojnarowicz M. Comportement mécanique des loess sur le tracé du TGV Nord. In XIème Conférence Européenne de Mécanique Des Sols et Des Travaux de Fondations 1995:(pp. 7-45).

Cui YJ, Nguyen XP, Tang AM, Li XL. An insight into the unloading/reloading loops on the compression curve of natural stiff clays. Applied Clay Science 2013;83–84:343–8. https://doi.org/10.1016/j.clay.2013.08.003.

Cuisinier O, Javadi AA, Ahangar-Asr A, Masrouri F. Identification of coupling parameters between shear strength behaviour of compacted soils and chemical's effects with an evolutionary-based data mining technique. Computers and Geotechnics 2013;48:107–16. https://doi.org/10.1016/j.compgeo.2012.10.005.

De Beer JH. The relationship between the deep electrical resistivity structure and tectonic provinces in Southern Africa - Part 2. Results obtained by magnetometer array studies. South African Journal of Geology 1978.

De Bruyn D, Thimus JF. The influence of temperature on mechanical characteristics of Boom clay: the results of an initial laboratory programme. Engineering Geology 1996:41(1-4), 117–26.

De Craen M, Wang L, Geet MV, Moors H. Geochemistry of Boom Clay pore water at the Mol site 2004.

De La Morena G, Asensio L, Navarro V. Modelling the hydro-mechanical behaviour of GMZ bentonite. Engineering Geology 2018;239:195–205. https://doi.org/10.1016/j.enggeo.2018.03.029.

Delage P, Cui YJ. Subsidence and capillary effects in chalks. In ISRM EUROCK (Pp ISRM-EUROCK), ISRM 1996.

Delage P, Le T-T, Tang A-M, Cui Y-J, Li X-L. Suction effects in deep Boom Clay block samples. Géotechnique 2007;57:239–44. https://doi.org/10.1680/geot.2007.57.2.239.

Delage P, Lefebvre G. Study of the structure of a sensitive Champlain clay and of its evolution during consolidation. Canadian Geotechnical Journal 1984:21(1), 21–35.

Delage P, Pellerin FM. Influence de la lyophilisation sur la structure d'une argile sensible du Québec. Clay Miner 1984;19:151–60. https://doi.org/10.1180/claymin.1984.019.2.03.

Della Vecchia G, Jommi C, Lima A, Romero E. Some remarks on the hydro-mechanical constitutive modelling of natural and compacted Boom clay. Unsaturated Soils 2011:803–9.

Della Vecchia G, Musso G. Some remarks on single- and double-porosity modeling of coupled chemo-hydro-mechanical processes in clays. Soils and Foundations 2016;56:779–89. https://doi.org/10.1016/j.sandf.2016.08.004.

Deng YF, Tang AM, Cui YJ, Li XL. Study on the hydraulic conductivity of Boom clay. Canadian Geotechnical Journal, 2011:48(10), 1461-1470.

Devau N, Le Cadre E, Hinsinger P, Jaillard B, Gérard F. Soil pH controls the environmental availability of phosphorus: experimental and mechanistic modelling approaches. Applied Geochemistry 2009:24(11), 2163–74.

Di Maio C, Fenelli GB. Influenza delle interazioni chimico-fisiche sulla deformabilita di alcuni terreni argillosi. Rivista Italiana Di Geotecnica 1997:31(1), 43–59.

Di Maio C, Santoli L, Schiavone P. Volume change behaviour of clays: the influence of mineral composition, pore fluid composition and stress state. Mechanics of Materials 2004;36:435–51. https://doi.org/10.1016/S0167-6636(03)00070-X.

Dieudonné AC. Microstructure of bentonites : characterisation and evolution under mechanical and environmental loads. Université de Liège, Belgium; 2020.

Dieudonné A-C, Gatabin C, Dridi W, Talandier J, Collin F, Charlier R. Heterogeneous Swelling of an Isotropically Compacted Bentonite-Based Material: Experimental Observations and Modelling. Rock Mech Rock Eng 2024;57:4159–72. https://doi.org/10.1007/s00603-023-03476-z.

Dizier A, Chen G, Li X-L. State of the art: Thermo-hydro-mechanical behavior of the Boom Clay 2018.

DJERAN-MAIGRE I, RoUssET G, GRUNBERGER D. Experimental compaction and evolution of physical properties of fine-grained sediments. In EUROCK'94 1994:(pp. 63-69).

Dohrmann R, Kaufhold S. Three new, quick CEC methods for determining the amounts of exchangeable calcium cations in calcareous clays. Clays and Clay Miner 2009;57:338–52. https://doi.org/10.1346/CCMN.2009.0570306.

Du J, Zhou A, Lin X, Bu Y, Kodikara J. Prediction of swelling pressure of expansive soil using an improved molecular dynamics approach combining diffuse double layer theory. Applied Clay Science 2021;203:105998. https://doi.org/10.1016/j.clay.2021.105998.

Duncan JM, Chang CY. Nonlinear analysis of stress and strain in soils. Journal of the Soil Mechanics and Foundations Division 1970:96(5), 1629-1653.

Evans EA, Quigley RM. Permeation of sand-bentonite mixtures with municipal waste leachate. Geotechnical Research Centre, University of Western Ontario.; 1992.

Fang Y, Ou Z, Li B. Effect of Pore Fluid Concentration on Shear Strength of Soft Clay. Soil Mech Found Eng 2019;56:265–72. https://doi.org/10.1007/s11204-019-09601-x.

Fernandez F, Quigley RM. Hydraulic conductivity of natural clays permeated with simple liquid hydrocarbons. Canadian Geotechnical Journal 1985:22(2), 205-214.

Fletcher P, Sposito G. The chemical modelling of clay/electrolyte interactions for montmorillonite. Clay Minerals 1989:24(2), 375–91.

François B, Labiouse V, Dizier A, Marinelli F, Charlier R, Collin F. Hollow Cylinder Tests on Boom Clay: Modelling of Strain Localization in the Anisotropic Excavation Damaged Zone. Rock Mech Rock Eng 2014;47:71–86. https://doi.org/10.1007/s00603-012-0348-5.

Frederickx L, Honty M, Craen MD, Dohrmann R, Elsen J. Relating the cation exchange properties of the Boom Clay (Belgium) to mineralogy and pore-water chemistry. Clays and Clay Minerals 2018:66(5), 449-465.

Frederickx L, Honty M, De Craen M, Elsen J. Evaluating the quantification of the clay mineralogy of the Rupelian Boom Clay in Belgium by a detailed study of size fractions. Applied Clay Science 2021:201, 105954.

Gajo A, Loret B. Finite element simulations of chemo-mechanical coupling in elastic–plastic homoionic expansive clays. Computer Methods in Applied Mechanics and Engineering 2003;192:3489–530. https://doi.org/10.1016/S0045-7825(03)00355-4.

Gens A, Alonso EE. A framework for the behaviour of unsaturated expansive clays. Can Geotech J 1992;29:1013–32. https://doi.org/10.1139/t92-120.

Gera F. The classification of radioactive wastes. Health Physics 1974:27(1), 113–21.

Giger SB, Ewy RT, Favero V, Stankovic R, Keller LM. Consolidated-undrained triaxial testing of Opalinus Clay: Results and method validation. Geomechanics for Energy and the Environment 2018:14, 16–28.

Gonzalez-Blanco L, Romero Morales EE. Gas migration in deep argillaceous formations : Boom clay and indurated clays. Universitat Politècnica de Catalunya, 2017. https://doi.org/10.5821/dissertation-2117-108499.

Gouy M. Sur la constitution de la charge électrique à la surface d'un électrolyte. J Phys Théorique Appliquée 1910:457–68.

Grim RE, Guven N. Bentonites: geology, mineralogy, properties and uses. Elsevier; 2011.

Guerra AM, Mokni N, Delage P, Cui YJ, Tang AM, Aimedieu P, et al. In-depth characterisation of a mixture composed of powder/pellets MX80 bentonite. Applied Clay Science 2017:538–46.

Guimarães LDN, Gens A, Sánchez M, Olivella S. A chemo-mechanical constitutive model accounting for cation exchange in expansive clays. Géotechnique 2013;63:221–34. https://doi.org/10.1680/geot.SIP13.P.012.

Habraken A. Contribution à la modélisation du formage des métaux par la méthodes des éléments finis. PhD thesis, University of Liège; 1989.

Hara K, Yabar H. Historical evolution and development of waste management and recycling systems—analysis of Japan's experiences. J Environ Stud Sci 2012;2:296–307. https://doi.org/10.1007/s13412-012-0094-8.

Heidug WK, Wong S-W. HYDRATION SWELLING OF WATER-ABSORBING ROCKS: A CONSTITUTIVE MODEL. Int J Numer Anal Methods Geomech 1996;20:403–30. https://doi.org/10.1002/(SICI)1096-9853(199606)20:6<403::AID-NAG832>3.0.CO;2-7.

Ho YA. The effects of Brine Contamination on the Properties of Soils. (Doctoral dissertation, M. Sc. Thesis, Dept of Civil Engineering, University of Saskatohewan, Saskatoon); 1985.

Högberg L. Root causes and impacts of severe accidents at large nuclear power plants. Ambio 2013:42(3), 267–84.

Holtz RD, Kovacs WD, Sheahan TC. An introduction to geotechnical engineering (Vol. 733). Englewood Cliffs, NJ: Prentice-hall; 1981.

Hong P-Y. Development and explicit integration of a thermo-mechanical model for saturated clays. Ecole Nationale des Ponts et Chaussées, 2013.

Hong PY, Pereira JM, Cui YJ, Tang AM. A two-surface thermomechanical model for saturated clays. Num Anal Meth Geomechanics 2016;40:1059–80. https://doi.org/10.1002/nag.2474.

Honty M. CEC of the Boom Clay–a review. SCK-CEN report ER-134; 2010.

Honty M, Frederickx L, Wang L, De Craen M, Thomas P, Moors H, et al. Boom Clay pore water geochemistry at the Mol site: Experimental data as determined by in situ sampling of the piezometers. Applied Geochemistry 2022:136, 105156.

Horseman ST, Winter MG, Entwistle DC. Geotechnical characterization of boom clay in relation to the disposal of radioactive waste: final report (BGS reference: FLPU 86-12). Luxembourg: Off. for Official Publ. of the European Communities; 1987.

Horvath A, Rachlew E. Nuclear power in the 21st century: Challenges and possibilities. Ambio 2016:45, 38–49.

Hueckel T. Chemo-mechanics of geomaterials: Coupled constitutive laws. Revue Européenne de Génie Civil 2005:9(5-6), 689–711.

Hueckel T. CHEMO-PLASTICITY OF CLAYS SUBJECTED TO STRESS AND FLOW OF A SINGLE CONTAMINANT. Int J Numer Anal Meth Geomech 1997;21:43–72. https://doi.org/10.1002/(SICI)1096-9853(199701)21:1<43::AID-NAG858>3.0.CO;2-1.

Hueckel T, Hu LB. Feedback mechanisms in chemo-mechanical multi-scale modeling of soil and sediment compaction. Computers and Geotechnics 2009;36:934–43. https://doi.org/10.1016/j.compgeo.2009.02.005.

IAEA. Energy, Electricity and Nuclear Power Estimates for the Period up to 2050. International Atomic Energy Agency; 2021.

Idiart A, Laviña M, Cochepin B, Pasteau A. Hydro-chemo-mechanical modelling of long-term evolution of bentonite swelling. Applied Clay Science 2020;195:105717. https://doi.org/10.1016/j.clay.2020.105717.

Jacops E, Swennen R, Janssens N, Seemann T, Amann-Hildenbrand A, Krooss BM, et al. Linking petrographical and petrophysical properties to transport characteristics: A case from Boom Clay and Eigenbilzen Sands. Applied Clay Science 2020;190:105568. https://doi.org/10.1016/j.clay.2020.105568.

Jacques D, Liu S, Bleyens N, Valcke E. Personal communication, SCK CEN. 2024.

Jacques D, Šimůnek J, Mallants D, Van Genuchten MT. The HPx software for multicomponent reactive transport during variably-saturated flow: Recent developments and applications. Journal of Hydrology and Hydromechanics 2018:66(2), 211–26.

Karnland O. Bentonite swelling pressure in strong NaCl solutions. Correlation between model calculations and experimentally determined data (No. SKB-TR--97-31). Swedish Nuclear Fuel and Waste Management Co., Stockholm (Sweden); 1997.

Karnland O, Nilsson U, Olsson S, Sellin P. Experimental study on sealing properties of commercial bentonites related to bentonite mineralogy and water solution composition. 2005.

Karnland O, Olsson S, Nilsson U. Mineralogy and sealing properties of various bentonites and smectite-rich clay materials 2006.

Karnland O, Pusch R, Sandén T. The importance of electrolyte on the physical properties of MX-80 bentonite. Swedish Nuclear Fuel and Waste Management Company (SKB International AB), Stockholm, Sweden; 1992.

Katsumi T, Ishimori H, Onikata M, Fukagawa R. Long-term barrier performance of modified bentonite materials against sodium and calcium permeant solutions. Geotextiles and Geomembranes 2008;26:14–30. https://doi.org/10.1016/j.geotexmem.2007.04.003.

Kenney TC. Slide behaviour and shear resistance of a quick clay determined from a study of the landslide at Selnes, Norway. In Proceedings of the Geotechnical Conference Oslo 1967 on Shear Strength Properties of Soils and Rocks 1967:(pp. 57-64).

Kielland J. Individual activity coefficients of ions in aqueous solutions. Journal of the American Chemical Society 1937:59(9), 1675–8.

Komine H, Yasuhara K, Murakami S. Swelling characteristics of bentonites in artificial seawater. Can Geotech J 2009;46:177–89. https://doi.org/10.1139/T08-120.

Kurgyis K, Achtziger-Zupančič P, Bjorge M, Boxberg MS, Broggi M, Buchwald J, et al. Uncertainties and robustness with regard to the safety of a repository for high-level radioactive waste: introduction of a research initiative. Environ Earth Sci 2024;83. https://doi.org/10.1007/s12665-023-11346-8.

Labiouse V. Advanced hydro-mechanical modelling of excavations in the Boom Clay formation 1997.

Lê TT. Comportement thermo-hydro-mécanique de l'argile de Boom. (Doctoral dissertation, Marne-la-vallée, ENPC); 2007.

Le T.T., Cui YJ, Munoz JJ, Delage P, Tang AM, Li XL. Studying the stress-suction coupling in soils using an oedometer equipped with a high capacity tensiometer. 2011.

Le Trung Tinh, Cui Y-J, Muñoz JJ, Delage P, Tang AM, Li X-L. Studying the stress-suction coupling in soils using an oedometer equipped with a high capacity tensiometer. Front Archit Civ Eng China 2011;5:160–70. https://doi.org/10.1007/s11709-011-0106-x.

Lelieveld J, Kunkel D, Lawrence MG. Global risk of radioactive fallout after major nuclear reactor accidents. Atmospheric Chemistry and Physics 2012:12(9), 4245–58.

Leroueil S, Roy M, La Rochelle P, Brucy F, Tavenas FA. Behavior of destructured natural clays. Journal of the Geotechnical Engineering Division 1979:105(6), 759–78.

Levasseur S, Sillen X, Marschall P, Wendling J, Olin M, Grgic D, et al. EURADWASTE'22 Paper – Host rocks and THMC processes in DGR: EURAD GAS and HITEC: mechanistic

understanding of gas and heat transport in clay-based materials for radioactive waste geological disposal. EPJ Nuclear Sci Technol 2022;8:21. https://doi.org/10.1051/epjn/2022021.

Leverd PC. The French Underground Research Laboratory in Bure: An Essential Tool for the Development and Preparation of the French Deep GeologicalDisposal Facility Cigéo. J of Nucl Fuel Cycle and Waste Technol 2023;21:489–502. https://doi.org/10.7733/jnfcwt.2023.035.

Li X, Neerdael B, Raymaekers D, Sillen X. The construction of the HADES underground research laboratory and its role in the development of the Belgian concept of a deep geological repository. SP 2023;536:159–84. https://doi.org/10.1144/sp536-2022-101.

Li X-L, Van Geet M, De Craen M. Geological disposal of radioactive waste in deep clay formations: 40 years of RD&D in the Belgian URL HADES (No. 536). Geological Society of London Special Publications.; 2023.

Likos WJ, Wayllace A. Porosity Evolution of Free and Confined Bentonites during Interlayer Hydration. Clays and Clay Miner 2010;58:399–414. https://doi.org/10.1346/CCMN.2010.0580310.

Lima A. Some remarks on the hydro-mechanical constitutive modelling of natural and compacted Boom clay. Unsaturated Soils 2011:803–9.

Liu Z, Boukpeti N, Li X, Collin F, Radu J -P., Hueckel T, et al. Modelling chemo-hydro-mechanical behaviour of unsaturated clays: a feasibility study. Num Anal Meth Geomechanics 2005;29:919–40. https://doi.org/10.1002/nag.444.

Loret B, Hueckel T, Gajo A. Chemo-mechanical coupling in saturated porous media: elastic–plastic behaviour of homoionic expansive clays. International Journal of Solids and Structures 2002a;39:2773–806. https://doi.org/10.1016/S0020-7683(02)00151-8.

Loret B, Hueckel T, Gajo A. Chemo-mechanical coupling in saturated porous media: elastic–plastic behaviour of homoionic expansive clays. International Journal of Solids and Structures 2002b;39:2773–806. https://doi.org/10.1016/S0020-7683(02)00151-8.

Loret B, Simões FMF. A framework for deformation, generalized diffusion, mass transfer and growth in multi-species multi-phase biological tissues. European Journal of Mechanics - A/Solids 2005;24:757–81. https://doi.org/10.1016/j.euromechsol.2005.05.005.

Lu P, Ye W, He Y. A constitutive model of compacted bentonite under coupled chemo-hydro-mechanical conditions based on the framework of the BExM. Computers and Geotechnics 2023;158:105360. https://doi.org/10.1016/j.compgeo.2023.105360.

Ma Y-S, Chen W-Z, Yu H-D, Gong Z, Li X-L. Variation of the hydraulic conductivity of Boom Clay under various thermal-hydro-mechanical conditions. Engineering Geology 2016;212:35–43. https://doi.org/10.1016/j.enggeo.2016.07.013.

MacKenzie AB. Natural analogue studies in the geological disposal of radioactive wastes, volume 26. Elsevier, Amsterdam, The Netherlands; 1995.

Madsen FT, Müller-Vonmoos M. The swelling behaviour of clays. Applied Clay Science 1989;4:143–56. https://doi.org/10.1016/0169-1317(89)90005-7.

Maio CD. Exposure of bentinite to salt solution: osmotic and mechnical effects. Géotechnique 1998;48:433–6. https://doi.org/10.1680/geot.1998.48.3.433.

Mair RJ, Taylor RN. Prediction of clay behaviour around tunnels using plasticity solutions. In Predictive Soil Mechanics: Proceedings of the Wroth Memorial Symposium Held at St Catherine's College, Oxford 1992:(pp. 449-463).

Marcial D, Delage P, Cui YJ. On the high stress compression of bentonites. Can Geotech J 2002;39:812–20. https://doi.org/10.1139/t02-019.

Marcus Y. Ion properties (Vol. 1). CRC Press; 1997.

Martens E, Jacques D, Wang L, De Cannière P, Van Gompel M, Mariën A, et al. Modelling of cation concentrations in the outflow of NaNO3 percolation experiments through Boom Clay cores. Physics and Chemistry of the Earth, Parts A/B/C 2011:36(17-18), 1693-1699.

Mata Mena C. Hydraulic behaviour of bentonite based mixtures in engineered barriers: the backfill and plug test at the Äspö Hrl (Sweden). PhD thesis. Universitat Politècnica de Catalunya; 2003.

Matuso S. Microscopic study on deformation and strength characteristics of clay soil. In Proc 9th Int Conf SMFE 1977:(Vol. 1, pp. 201-204).

McDowell GR, Hau KW. A generalised Modified Cam clay model for clay and sand incorporating kinematic hardening and bounding surface plasticity. GM 2004;6. https://doi.org/10.1007/s10035-003-0152-8.

Meier LP, Kahr G. Determination of the Cation Exchange Capacity (CEC) of Clay Minerals Using the Complexes of Copper(II) Ion with Triethylenetetramine and Tetraethylenepentamine. Clays and Clay Miner 1999;47:386–8. https://doi.org/10.1346/CCMN.1999.0470315.

Mertens J, Bastiaens W, Dehandschutter B. Characterisation of induced discontinuities in the Boom Clay around the underground excavations (URF, Mol, Belgium). Applied Clay Science 2004;26:413–28. https://doi.org/10.1016/j.clay.2003.12.017.

Mesri G, Olson RE. Mechanisms controlling the permeability of clays. Clays and Clay Minerals 1971:19, 151–8.

Mesri G, Pakbaz MC, Cepeda-Diaz AF. Meaning, measurement and field application of swelling pressure of clay shales. Geotechnique 1994:44(1), 129–45.

Meunier A. Argiles. Contemporary Publishing international-GB Science publisher; 2003.

Mitchell JK, Soga K. Fundamentals of soil behavior (Vol. 3, p. USA). New York: John Wiley & Sons; 2005.

Mokni N. Deformation and flow driven by osmotic processes in porous materials. Universitat Politècnica de Catalunya.; 2011.

Mokni N, Olivella S, Valcke E, Bleyen N, Smets S, Li X, et al. Hydro-chemical modelling of in situ behaviour of bituminized radioactive waste in Boom Clay. SP 2014;400:117–34. https://doi.org/10.1144/SP400.40.

Moore R. The chemical and mineralogical controls upon the residual strength of pure and natural clays. Geotechnique 1991:41(1), 35–47.

Musso G, editor. Coupled Phenomena in Environmental Geotechnics. CRC Press; 2013. https://doi.org/10.1201/b15004.

Musso G, Romero Morales E, Gens A, Castellanos E. The role of structure in the chemically induced deformations of FEBEX bentonite. Applied Clay Science 2003;23:229–37. https://doi.org/10.1016/S0169-1317(03)00107-8.

Musso G, Scelsi G, Della Vecchia G. Elasto – plastic modelling of the behaviour of non - active clays under chemo – mechanical actions. E3S Web Conf 2020;205:04011. https://doi.org/10.1051/e3sconf/202020504011.

Nagaraj HB, Munnas MM, Sridharan A. Critical Evaluation of Determining Swelling Pressure by Swell-Load Method and Constant Volume Method. Geotechnical Testing Journal 2009;32:305–14. https://doi.org/10.1520/GTJ102051.

Navarro V, Yustres Á, Asensio L, La Morena GD, González-Arteaga J, Laurila T, et al. Modelling of compacted bentonite swelling accounting for salinity effects. Engineering Geology 2017a;223:48–58. https://doi.org/10.1016/j.enggeo.2017.04.016.

Navarro V, Yustres Á, Asensio L, La Morena GD, González-Arteaga J, Laurila T, et al. Modelling of compacted bentonite swelling accounting for salinity effects. Engineering Geology 2017b;223:48–58. https://doi.org/10.1016/j.enggeo.2017.04.016.

Neerdael B, Beaufays, R, Buyens, M, Bruyn, D de, Voet M. Geomechanical behaviour of boom clay under ambient and elevated temperature conditions 1992.

NFP 94 049-2. SOIL: SURVEY AND TESTING 1996.

Nguyen XP. Étude du comportement chimico-hydro-mécanique des argiles raides dans le contexte du stockage de déchets radioactifs. (Doctoral dissertation, Université Paris-Est); 2013.

Norrish K. The swelling of montmorillonite. Discussions of the Faraday society, 18, 120-134; 1954.

ONDRAF. Design and Construction of the Geological Disposal Facility for Category B and Category C Wastes (V3). Technical Report NIROND-TR 2017-12 E V3, NIRAS/ONDRAF, Belgian Agency for RadioactiveWaste and Enriched Fissile Materials; 2020.

ONDRAF. Research, Development and Demonstration (RD&D) Plan for the geological disposal of high-level and/or long-lived radioactive waste including irradiated fuel if considered as waste. State-of-the-art report as of December 2012. Technical Report December 2012, NIRAS/ ONDRAF, Belgian Agency for Radioactive Waste and Enriched Fissile Materials; 2013.

Palomino AM, Santamarina JC. Fabric Map for Kaolinite: Effects of pH and Ionic Concentration on Behavior. Clays and Clay Miner 2005;53:211–23. https://doi.org/10.1346/CCMN.2005.0530302.

Parkhurst DL, Appelo CAJ. Description of input and examples for PHREEQC version 3—a computer program for speciation, batch-reaction, one-dimensional transport, and inverse geochemical calculations. US Geological Survey Techniques and Methods 2013:6(A43), 497.

Parry RHG, Wroth CP. Shear stress-strain properties of soft clay. Developments in Geotechnical Engineering 1981.

Petley DN. Failure envelopes of mudrocks at high confining pressures. Geological Society, London, Special Publications 1999:158(1), 61–71.

Piriyakul K. Anisotropic Stress-Strain Behaviour of Belgian Boom Clay in the Small Strain Region. Ghent University, 2006.

Popp T, Salzer K. Anisotropy of seismic and mechanical properties of Opalinus clay during triaxial deformation in a multi-anvil apparatus. Physics and Chemistry of the Earth, Parts A/B/C 2007;32:879–88. https://doi.org/10.1016/j.pce.2006.04.022.

Potts D. Guidelines for the use of advanced numerical analysis. Thomas Telford. 2002.

Pusch R. Experimental study of the effect of high porewater salinity on the physical properties of a natural smectitic clay. Technical report. Swedish Nuclear Fuel and Waste Management Co, Stockholm, Sweden; 2001.

Rahardjo H, Rezaur RB, Leong EC, Alonso EE, Lloret A, Gens A. Monitoring and modeling of slope response to climate changes 2008.

Rao SM, Shivananda P. Compressibility behaviour of lime-stabilized clay. Geotech Geol Eng 2005;23:309–19. https://doi.org/10.1007/s10706-004-1608-2.

Rao SM, Thyagaraj T, Raghuveer Rao P. Crystalline and Osmotic Swelling of an Expansive Clay Inundated with Sodium Chloride Solutions. Geotech Geol Eng 2013;31:1399–404. https://doi.org/10.1007/s10706-013-9629-3.

Ray S, Mishra AK, Kalamdhad AS. Evaluation of equilibrium, kinetic and hydraulic characteristics of Indian bentonites in presence of heavy metal for landfill application. Journal of Cleaner Production 2021:317, 128396.

Rayment GE, Higginson FR. Australian laboratory handbook of soil and water chemical methods. Inkata Press, Melbourne; 1992.

Robinson RG, Allam MM. Effect of Clay Mineralogy on Coefficient of Consolidation. Clays and Clay Miner 1998;46:596–600. https://doi.org/10.1346/CCMN.1998.0460514.

Rolfe PF, Aylmore LAG. Water and salt flow through compacted clays: I. Permeability of compacted illite and montmorillonite. Soil Science Society of America Journal 1977:41(3), 489–95.

Romero E, Gens A, Lloret A. Water permeability, water retention and microstructure of unsaturated compacted Boom clay. Engineering Geology 1999;54:117–27. https://doi.org/10.1016/S0013-7952(99)00067-8.

Romero E, Simms PH. Microstructure Investigation in Unsaturated Soils: A Review with Special Attention to Contribution of Mercury Intrusion Porosimetry and Environmental Scanning Electron Microscopy. Geotech Geol Eng 2008;26:705–27. https://doi.org/10.1007/s10706-008-9204-5.

Roscoe K, Burland JB. On the generalized stress-strain behaviour of wet clay 1968.

Roscoe KH, Schofield AN, Worth AP. On the yielding of soils. Geotechnique 1958:8(1), 22–53.

Rousset G, Bazargan-Sabet B, Lenain R. Time-Dependent Behavior Of Rocks' Laboratory Tests On Hollow Cylinder. In ARMA US Rock Mechanics/Geomechanics Symposium 1989:(pp. ARMA-89).

Saiyouri N, Hicher PY, Tessier D. Microstructural approach and transfer water modelling in highly compacted unsaturated swelling clays. Mech Cohes-Frict Mater 2000;5:41–60. https://doi.org/10.1002/(SICI)1099-1484(200001)5:1<41::AID-CFM75>3.0.CO;2-N.

Savage D. The effects of high salinity groundwater on the performance of clay barriers. 2005.

Schneider J, Zuidema P. The ongoing Swiss site selevction: Current status, recent achievements and outlook, with special emphasis on the prominent role of safety. National Cooperative for the Disposal of Radioactive Waste (Nagra), Wettingen, Switzerland 2011:9.

Sekiguchi J. Zonal Spherical Functions on Some Symmetric Spaces. Publ Res Inst Math Sci 1976;12:455–64. https://doi.org/10.2977/prims/1195196620.

Shao JF, Jia Y, Kondo D, Chiarelli AS. A coupled elastoplastic damage model for semi-brittle materials and extension to unsaturated conditions. Mechanics of Materials 2006;38:218–32. https://doi.org/10.1016/j.mechmat.2005.07.002.

Siddiqua S, Blatz J, Siemens G. Evaluation of the impact of pore fluid chemistry on the hydromechanical behaviour of clay-based sealing materials. Can Geotech J 2011;48:199–213. https://doi.org/10.1139/T10-064.

Simons H, Reuter E. Physical and chemical behaviour of clay-based barriers under percolation with test liquids. Engineering Geology 1985:21(3-4), 301–10.

Šimůnek J, Brunetti G, Jacques D, Van Genuchten MTh, Šejna M. Developments and applications of the HYDRUS computer software packages since 2016. Vadose Zone Journal 2024;23:e20310. https://doi.org/10.1002/vzj2.20310.

Song MM, Zeng LL, Hong ZS. Pore fluid salinity effects on physicochemical-compressive behaviour of reconstituted marine clays. Applied Clay Science 2017:146, 270–7.

Song X, Menon S. Modeling of chemo-hydromechanical behavior of unsaturated porous media: a nonlocal approach based on integral equations. Acta Geotech 2019;14:727–47. https://doi.org/10.1007/s11440-018-0679-9.

Sridharan A, El-Shafei A, Miura N. Mechanisms controlling the undrained strength behavior of remolded Ariake marine clays. Marine Georesources and Geotechnology 2002:20(1), 21–50.

Sridharan A, Jose BT, Abraham BM. Determination of clay size fraction of marine clays. Geotechnical Testing Journal 1991:14(1), 103–7.

Sridharan A, Prakash K. Mechanisms controlling the undrained shear strength behaviour of clays. Can Geotech J 1999;36:1030–8. https://doi.org/10.1139/t99-071.

Sridharan A, Rao SM, Murthy N s. Compressibility behaviour of homoionized bentonites. Géotechnique 1986;36:551–64. https://doi.org/10.1680/geot.1986.36.4.551.

Sridharan A, Venkatappa Rao G. Shear strength behaviour of saturated clays and the role of the effective stress concept. Geotechnique 1979:29(2), 177–93.

Studds PG, Stewart DI, Cousens TW. The effects of salt solutions on the properties of bentonite-sand mixtures. Clay Minerals 1998:33(4), 651–60.

Sultan N, Cui Y-J, Delage P. Yielding and plastic behaviour of Boom clay. Géotechnique 2010a;60:657–66. https://doi.org/10.1680/geot.7.00142.

Sultan N, Cui YJ, Delage P. Yielding and plastic behaviour of Boom clay. Géotechnique 2010b:60(9), 657–66.

Sun W, Zhang X, Sun X, Sun Y, Cen Y. Predicting nickel concentration in soil using reflectance spectroscopy associated with organic matter and clay minerals. Geoderma 2018;327:25–35. https://doi.org/10.1016/j.geoderma.2018.04.019.

Sun WJ, Cui YJ. Determining the soil-water retention curve using mercury intrusion porosimetry test in consideration of soil volume change. Journal of Rock Mechanics and Geotechnical Engineering 2020:12(5), 1070–9.

Suzuki S, Prayongphan S, Ichikawa Y, Chae B-G. In situ observations of the swelling of bentonite aggregates in NaCl solution. Applied Clay Science 2005;29:89–98. https://doi.org/10.1016/j.clay.2004.11.001.

Suzuki S, Sazarashi M, Akimoto T, Haginuma M, Suzuki K. A study of the mineralogical alteration of bentonite in saline water. Applied Clay Science 2008;41:190–8. https://doi.org/10.1016/j.clay.2007.11.003.

Tavenas F, Leroueil S. The behaviour of embankments on clay foundations. Canadian Geotechnical Journal 1980:17(2), 236–60.

Thyagaraj T, Das AP. Physico-chemical effects on collapse behaviour of compacted red soil. Géotechnique 2014:67(7), 559–71.

Thyagaraj T, Rao SM. Osmotic Swelling and Osmotic Consolidation Behaviour of Compacted Expansive Clay. Geotech Geol Eng 2013;31:435–45. https://doi.org/10.1007/s10706-012-9596-0.

Thyagaraj T, Rao SM. Influence of osmotic suction on the soil-water characteristic curves of compacted expansive clay. Journal of Geotechnical and Geoenvironmental Engineering 2010:136(12), 1695–702.

Toll DG, Augarde CE, Gallipoli D, Wheeler SJ, editors. Water retention properties of Boom clay: A comparison between different experimental techniques. Unsaturated Soils. Advances in Geo-Engineering. 0 ed., CRC Press; 2008, p. 245–50. https://doi.org/10.1201/9780203884430-32.

Valcke E, Marien A, Smets S, Li X, Mokni N, Olivella S, et al. Osmosis-induced swelling of Eurobitum bituminized radioactive waste in constant total stress conditions. Journal of Nuclear Materials 2010;406:304–16. https://doi.org/10.1016/j.jnucmat.2010.08.060.

Valcke E, Marien A, Van Geet M. The methodology followed in Belgium to investigate the compatibility with geological disposal of Eurobitum bituminized intermediate-level radioactive waste. MRS Online Proceedings Library (OPL) 2009:1193, 105.

Valcke E, Sneyers A, Van Iseghem P. The long-term behaviour of bituminized radioactive waste in a deep clay formation, Vol. 2 of Proc. of Safewaste Conference; 2000.

Valls-Marquez M. Evaluating the capabilities of some constitutive models in reproducing the exprimental behaviour of stiff clay subjected to tunnelling stress paths. The University of Birmingham, 2009.

Van Geet M, Bruggeman C, De Craen M. Geological disposal of radioactive waste in deep clay formations: celebrating 40 years of RD&D in the Belgian URL HADES. SP 2023;536:1–10. https://doi.org/10.1144/SP536-2023-1.

Van Olphen H. Thermodynamics of interlayer adsorption of water in clays. I.—Sodium vermiculite. Journal of Colloid Science 1965:20(8), 822-837.

Van Olphen H. Clay-organic complexes and the retention of hydrocarbons by source rocks, 1963.

Vandenberghe N, Craen MD, Wouters L. The Boom Clay Geology From sedimentation to present-day occurrence A review 2014.

Vari A, Ferencz Z. Identifying remaining socio-technical challenges at the national level: Hungary. Hungarian Academy of Sciences Center of Social Science Research 2012.

Villar MV. Water retention of two natural compacted bentonites. Clays and Clay Miner 2007;55:311–22. https://doi.org/10.1346/CCMN.2007.0550307.

Villar MV. MX-80 Bentonite. Thermo-Hydro-Mechanical Characterisation Performed at CIEMAT in the Context of the Prototype Project. 2005.

Villar MV, Gómez-Espina R, Gutiérrez-Nebot L. Basal spacings of smectite in compacted bentonite. Applied Clay Science 2012a;65–66:95–105. https://doi.org/10.1016/j.clay.2012.05.010.

Villar MV, Gómez-Espina R, Gutiérrez-Nebot L. Basal spacings of smectite in compacted bentonite. Applied Clay Science 2012b;65–66:95–105. https://doi.org/10.1016/j.clay.2012.05.010.

Wahid AS, Gajo A, Di Maggio R. Chemo-mechanical effects in kaolinite. Part 1: prepared samples. Géotechnique 2011;61:439–47. https://doi.org/10.1680/geot.8.P.067.

Wang J, Chen L, Su R, Zhao X. The Beishan underground research laboratory for geological disposal of high-level radioactive waste in China: Planning, site selection, site characterization and in situ tests. Journal of Rock Mechanics and Geotechnical Engineering 2018;10:411–35. https://doi.org/10.1016/j.jrmge.2018.03.002.

Wang L, Honty M, De Craen M, Frederickx L. Boom Clay pore-water geochemistry at the Mol site: Chemical equilibrium constraints on the concentrations of major elements. Applied Geochemistry 2023:148, 105541.

Wang P, Anderko A. Computation of dielectric constants of solvent mixtures and electrolyte solutions. Fluid Phase Equilibria 2001;186:103–22. https://doi.org/10.1016/S0378-3812(01)00507-6.

Wang Q, Tang AM, Cui Y-J, Delage P, Gatmiri B. Experimental study on the swelling behaviour of bentonite/claystone mixture. Engineering Geology 2012;124:59–66. https://doi.org/10.1016/j.enggeo.2011.10.003.

Wang Y, Zhang A, Ren W, Niu L. Study on the soil water characteristic curve and its fitting model of Ili loess with high level of soluble salts. Journal of Hydrology 2019;578:124067. https://doi.org/10.1016/j.jhydrol.2019.124067.

Weetjens E, Valcke E, Mariën A. Sodium nitrate release from EUROBITUM bituminised radioactive waste-scoping calculations. SCK CEN reports (ER-146).; 2010.

Wemaere I, Marivoet J, Labat S. Hydraulic conductivity variability of the Boom Clay in north-east Belgium based on four core drilled boreholes. Physics and Chemistry of the Earth, Parts A/B/C 2008;33:S24–36. https://doi.org/10.1016/j.pce.2008.10.051.

Wong RCK, Varatharajan S. Viscous behaviour of clays in one-dimensional compression. Can Geotech J 2014;51:795–809. https://doi.org/10.1139/cgj-2013-0198.

Wood DM. Geotechnical modelling. Geotechnical modelling. CRC press. 2004.

Wood DM. Soil Behaviour and Critical State Soil Mechanics. Cambridge University Press; 1990.

Xu H, Zheng L, Rutqvist J, Birkholzer JT. Modeling of a Clay-Rock Repository for Nuclear Waste With a Coupled Chemo-Mechanical Approach. N ARMA US Rock Mechanics/Geomechanics Symposium (Pp ARMA-2017) 2017.

Ya K, Feng C, Zegong L. A New Modified Cam-Clay Model Considering Cohesion and the Difference between Yield Strengths of Tension and Compression and Its Numerical Implementation 2014.

Yan R. BBM-Type Constitutive Model for Coupled Chemomechanical Behavior of Saturated Soils. Int J Geomech 2018;18:06018023. https://doi.org/10.1061/(ASCE)GM.1943-5622.0001264.

Yang JW, Cui YJ, Mokni N, Wang H. Stress Release–Induced Suction in Unsaturated MX80 Bentonite Pellet and Powder Mixtures. Journal of Geotechnical and Geoenvironmental Engineering 2024:150(7).

Yang N. The Impact of soil structure and confining stress on the permeability of clay soils in brine environments. Masters thesis,University of Saskatchewan; 1990.

Ye W-M, Zhang F, Chen Y-G, Chen B, Cui Y-J. Influences of salt solutions and salinization-desalinization processes on the volume change of compacted GMZ01 bentonite. Engineering Geology 2017;222:140–5. https://doi.org/10.1016/j.enggeo.2017.04.002.

Ye WM, Zheng ZJ, Chen B, Chen YG, Cui YJ, Wang J. Effects of pH and temperature on the swelling pressure and hydraulic conductivity of compacted GMZ01 bentonite. Applied Clay Science 2014a;101:192–8. https://doi.org/10.1016/j.clay.2014.08.002.

Ye WM, Zheng ZJ, Chen B, Chen YG, Cui YJ, Wang J. Effects of pH and temperature on the swelling pressure and hydraulic conductivity of compacted GMZ01 bentonite. Applied Clay Science 2014b;101:192–8. https://doi.org/10.1016/j.clay.2014.08.002.

Ying Z, Cui Y-J, Duc M, Benahmed N, Bessaies-Bey H, Chen B. Salinity effect on the liquid limit of soils. Acta Geotech 2021;16:1101–11. https://doi.org/10.1007/s11440-020-01092-7.

Yong RN. Soil suction and soil-water potentials in swelling clays in engineered clay barriers. Engineering Geology 1999;54:3–13. https://doi.org/10.1016/S0013-7952(99)00056-3.

Young DA, Smith DE. Simulations of clay mineral swelling and hydration: Dependence upon interlayer ion size and charge. The Journal of Physical Chemistry B 2000:104(39), 9163–70.

Yu H, Chen W, Gong Z, Ma Y, Chen G, Li X. Influence of temperature on the hydro-mechanical behavior of Boom Clay. International Journal of Rock Mechanics and Mining Sciences 2018;108:189–97. https://doi.org/10.1016/j.ijrmms.2018.04.023.

Yu HS. CASM: a unified state parameter model for clay and sand. Int J Numer Anal Meth Geomech 1998;22:621–53. https://doi.org/10.1002/(SICI)1096-9853(199808)22:8<621::AID-NAG937>3.0.CO;2-8.

Yu L, Rogiers B, Gedeon M, Marivoet J, Craen MD, Mallants D. A critical review of laboratory and in-situ hydraulic conductivity measurements for the Boom Clay in Belgium. Applied Clay Science 2013;75–76:1–12. https://doi.org/10.1016/j.clay.2013.02.018.

Yuan S, Buzzi O, Liu X, Vaunat J. Swelling behaviour of compacted Maryland clay under different boundary conditions. Géotechnique 2019;69:514–25. https://doi.org/10.1680/jgeot.17.P.140.

Yukselen-Aksoy Y, Kaya A, Ören AH. Seawater effect on consistency limits and compressibility characteristics of clays. Engineering Geology 2008;102:54–61. https://doi.org/10.1016/j.enggeo.2008.07.005.

Yustres A, Jenni A, Asensio L, Pintado X, Koskinen K, Navarro V, et al. Comparison of the hydrogeochemical and mechanical behaviours of compacted bentonite using different

conceptual approaches. Applied Clay Science 2017;141:280–91. https://doi.org/10.1016/j.clay.2017.03.006.

Zeelmaekers E, Honty M, Derkowski A, Środoń J, De Craen M, Vandenberghe N, et al. Qualitative and quantitative mineralogical composition of the Rupelian Boom Clay in Belgium. Clay Miner 2015;50:249–72. https://doi.org/10.1180/claymin.2015.050.2.08.

Zeng Z, Cui Y-J, Conil N, Talandier J. Experimental Investigation and Modeling of the Hydraulic Conductivity of Saturated Bentonite–Claystone Mixture. Int J Geomech 2020;20:04020184. https://doi.org/10.1061/(ASCE)GM.1943-5622.0001817.

Zeng Z, Cui Y-J, Zhang F, Conil N, Talandier J. Investigation of swelling pressure of bentonite/claystone mixture in the full range of bentonite fraction. Applied Clay Science 2019;178:105137. https://doi.org/10.1016/j.clay.2019.105137.

Zhang C-L. The stress–strain–permeability behaviour of clay rock during damage and recompaction. Journal of Rock Mechanics and Geotechnical Engineering 2016;8:16–26. https://doi.org/10.1016/j.jrmge.2015.10.001.

Zhang F, Cui Y-J, Chen B. Investigation of Suction Effects Due to Stress Release with Compacted MX80 Bentonite. J Geotech Geoenviron Eng 2022;148:04022070. https://doi.org/10.1061/(ASCE)GT.1943-5606.0002849.

Zhang F, Cui Y-J, Conil N, Talandier J. Assessment of Swelling Pressure Determination Methods with Intact Callovo-Oxfordian Claystone. Rock Mech Rock Eng 2020;53:1879–88. https://doi.org/10.1007/s00603-019-02016-y.

Zhang F, Ye W-M, Chen Y-G, Chen B, Cui Y-J. Influences of salt solution concentration and vertical stress during saturation on the volume change behavior of compacted GMZ01 bentonite. Engineering Geology 2016;207:48–55. https://doi.org/10.1016/j.enggeo.2016.04.010.

Zhang F, Ye W-M, Wang Q, Chen Y-G, Cui Y. Insight into volume change behavior of GMZ01 bentonite over cyclic salinization–desalinization processes. Environ Earth Sci 2023;82:312. https://doi.org/10.1007/s12665-023-10997-x.

Zhang H-Y, Cui S-L, Zhang M, Jia L-Y. Swelling behaviors of GMZ bentonite–sand mixtures inundated in NaCl–Na2SO4 solutions. Nuclear Engineering and Design 2012;242:115–23. https://doi.org/10.1016/j.nucengdes.2011.10.042.

Zhu C-M, Ye W-M, Chen Y-G, Chen B, Cui Y-J. Impact of cyclically infiltration of CaCl2 solution and de-ionized water on volume change behavior of compacted GMZ01 bentonite. Engineering Geology 2015;184:104–10. https://doi.org/10.1016/j.enggeo.2014.11.005.

Zhu C-M, Ye W-M, Chen Y-G, Chen B, Cui Y-J. Influence of salt solutions on the swelling pressure and hydraulic conductivity of compacted GMZ01 bentonite. Engineering Geology 2013;166:74–80. https://doi.org/10.1016/j.enggeo.2013.09.001.